Development of Design Criteria for Novel 3D-printed Quadric-Surfaced Sludge Digesters for Wastewater Infrastructure

Navin Rakesh Ramroop

A thesis submitted in partial fulfilment of the requirements of the
University of the West of England, Bristol for the degree of Doctor of Philosophy

Civil and Environmental Engineering Cluster,
Faculty of Environment and Technology,
University of the West of England, Bristol.

July 2020

ABSTRACT

The quadric-surfaced sludge digester (QSD), also known as the egg-shaped sludge digester, has proven its advantages over traditional cylindrical digesters recently. A reduction in operational cost is the dominant factor. Its shell can be described as a revolution of a parabola with the apex and base being either tapered or spherical. This shape provides a surface free of discontinuities, which is advantageous regarding the efficiency during mixing. Since the shape does not produce areas of inactive fluid motion within the tank, sludge settlement and an eventual grit build-up are avoided. The stresses developed in the shell of the sludge digester, vary along the meridian and equatorial diameters. A non-dimensional parameter, ξ, defines the height-to-diameter aspect ratio which is used to delineate the parametric boundary conditions of the shell's surface. Three groups of analyses were conducted to determine the orthogonal stresses in the shell of the QSD. The first-principles numerical models ran reasonably quickly, and many iterations were made during the study. The results showed that they were in within the range 5.34% to 7.2% to 2D FEA simulations. The 3D FEA simulations were within the range of 8.3% to 9.2% to the MATLAB time-history models. This is a good indicator that the first principles numerical models are an excellent time-saving method to predict the behaviour of the QSD under seismic excitation. Upon examining the criteria for the design, analysing the results for the 2D FEA simulations showed that the fill height is not a significant variable with sloshing however the 3D FEA showed that the hydrostatic pressure is a significant variable. The maximum principal stress was found to be 5.457 MPa whilst the maximum Von Mises stress was found to be 22.73 MPa With the maximum tensile stress of the 3D-printed ABS being 24.4 MPa, the overall maximum stress of 5.45 MPa, the criteria for design has been developed for the Serviceability and Ultimate limit states. Hence the material can be a viable option for the use of QSD construction in small island developing states (SIDS). A design guide has been developed that will aid the structural engineer to size the QSD as well as design against the failure criteria.

Keywords: quadric-surfaced, egg-shaped sludge digester, 3D printing, wastewater reactor, shell structures, hydraulic infrastructure

ACKNOWLEDGEMENTS

I want to convey my sincerest gratitude to my Director of Studies, Dr Kiran Tota-Maharaj (Head of Civil and Environmental Engineering at the University of the West of England, Bristol), for his continuous support, patience and motivation during this PhD study. His knowledge was an invaluable asset during the research phase and writing of this thesis. I could not imagine having a better advisor and mentor for this undertaking. I would also like to thank my second supervisor, Prof. Chad Staddon from the International Water Security Network, for his guidance, encouragement and advice he has provided throughout my time as a PhD student.

I greatly appreciate the support received from the University of Trinidad and Tobago (UTT), Unit for Project Management and Civil Infrastructure. The commitment by UTT for small island development through research has been the cornerstone for this undertaking. I would also like to thank the directors of Statiker Limited, who have unfailingly provided financial assistance which made pursuing doctoral studies possible for me.

I thank my parents (Krishna and Deokie Ramroop) and my sister and her family (Renita and Khaimraj Singh) for their tremendous encouragement; not only during this PhD but for all the times when the academic life has taken a toll on me. Their commitment to always seek my best interest is overwhelmingly appreciated.

Finally, I wish to thank my better half, Dr Nekisha Dattoo for her encouragement, patience and love during these years. The kind support and understanding she has provided me with, has been a light during times when hope became seemingly elusive.

Navin Ramroop

2020

No problem can withstand the assault of sustained thinking ~ Voltaire

TABLE OF CONTENTS

LIST OF FIGURES

LIST OF TABLES

1.0 Introduction

1.1 Overview

1.1.1 Introduction

Water conservation is a crucial objective in water resource management across the globe. Climatic changes have redistributed rainfall intensities causing smaller islands to look closer at water quantities accounting. The reuse of wastewater has now become essential in areas where low potable water levels are existent. Traditionally, domestic wastewater across small island developing states (SIDS), have been treated via localised septic tanks. In much low-income residential and rural communities, pit latrines are still being utilised. There is a degree difficulty for assessing proper functionality of these structures since little or no maintenance usually occurs during the life of these hydraulic structures. Hence, groundwater contamination in the indigenous aquifers becomes a high possibility. Centralised wastewater treatment facilities can eliminate groundwater contamination hence not only ensuring the non-pollution of groundwater but also providing reuse of treated water for commercial activities. Some SIDS are heavily dependent on tourism and are reliant on using water for activities such as landscaping (Hutchinson, 2010). Wastewater reuse can be a supplemental alternative for water resources when compared to the reliability of rainwater harvesting. The secondary treatment phase offers removal of bacteria and sludge from the effluent, preparing it for the final or tertiary stage of disinfection.

Within the secondary treatment stage, anaerobic digestion of the sludge usually takes place in a sludge digester. These tanks are typically cylindrical. The problem with this shape is that due to improper mixing, dead zones (see Figure 1) develop, leaving a build-up of scum and grit on the tank walls (Zingoni, 2001). This inefficiency causes the plant operations to be temporarily halted to facilitate cleaning of the digesters. Recommencing operation of the tanks usually requires time and energy for the bacteria to develop which results in further delays. With the advent of the quadric surfaced sludge digester, the efficiency of mixing is increased, thus eliminating the scum build-up, hence reducing the overall costs associated with operation and maintenance.

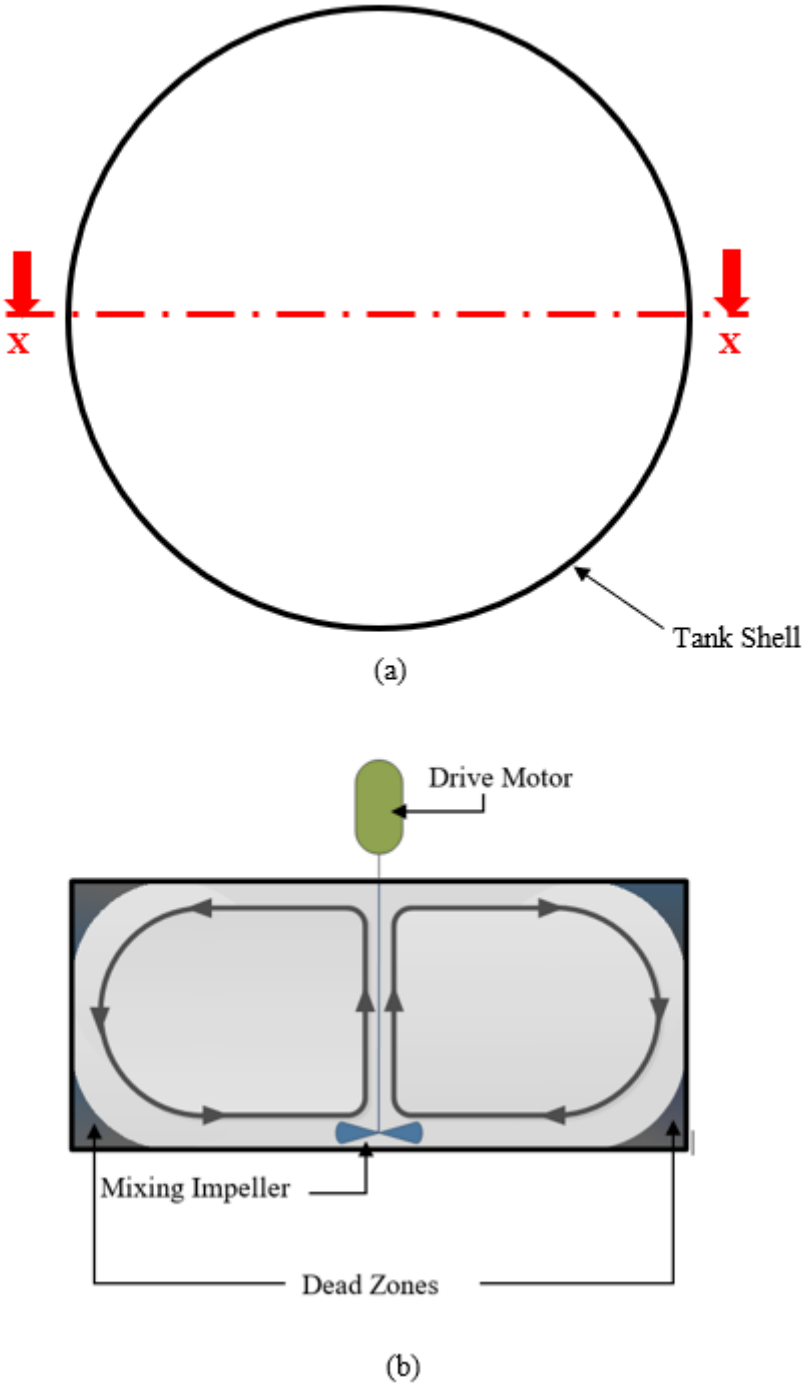

Figure 1 (a) Plan of cylindrical tank. (b) Section X-X showing mixing pattern in a typical cylindrical digester showing dead zones

The quadric-surfaced sludge digester (QSD) has seen few iterations in design since its initial development. Although the benefit of lower maintenance cost outweighs the initial cost of construction, this has not been an attractive reason for adoption in Caribbean small island developing states (SIDS).

It is due to the lack of construction expertise and procurement of special purpose-made formwork and other equipment that comes at a high cost. A reduction in this cost can provide a means for SIDS to adopt the QSD for integration in their wastewater treatment facilities. Replacing the primary material with a 3D printed polymer can provide rapid off-site production of the QSD in a modular manner, which can be shipped and assembled on-site with semi-skilled labour. This research examines the possibility of using acrylonitrile butadiene styrene (ABS) as the primary material and 3D fused deposition manufacturing as the main construction method. This study conducts various numerical analyses to determine the applicability of using 3D printed ABS for QSDs under seismic loads. The analyses conducted measured the load effects of hydrostatic and dynamic pressures on different height-to-diameter ratios of a parabolic ogival form for the QSD.

The QSD replaces the typical cylindrical sludge digester within the secondary stage of the treatment process (see Figure 2). During the primary treatment stage, undissolved solids removal which is settled

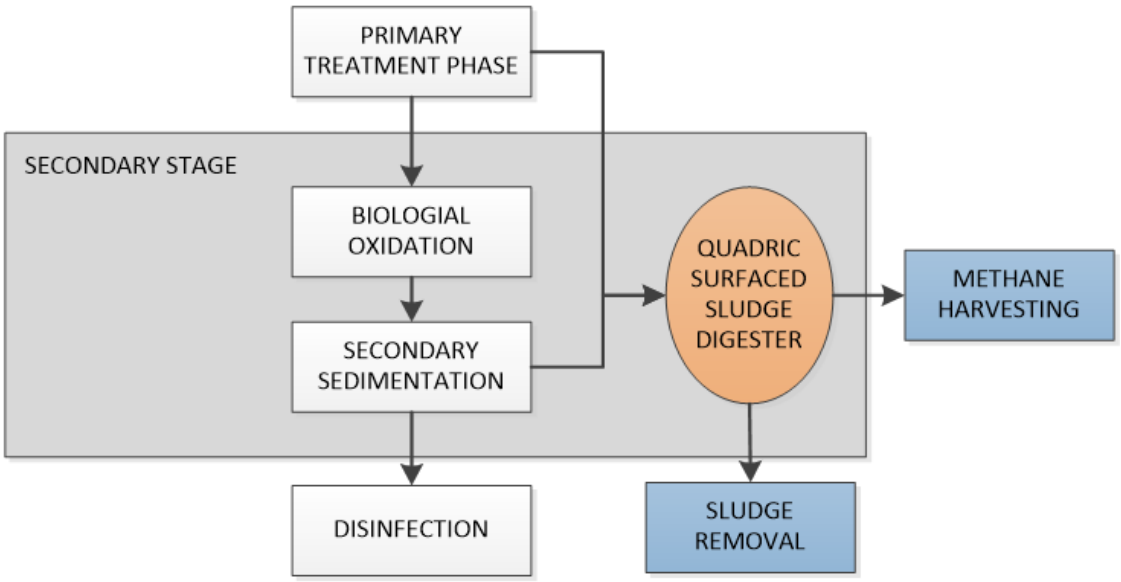

Figure 2. Schematic of the secondary treatment process

in primary sedimentation tanks. These are removed and sent for treatment in the secondary stage. Similarly, the undissolved coagulated solids that settle during the secondary sedimentation, in the secondary treatment stage, is also removed and sent for further treatment. Both are placed in a sludge

digester where anaerobic digestion stabilises the sludge. This digestion process utilises various anaerobic bacteria that produce biogas (Priadi *et al*., 2013) including methane which can be harvested and used as an alternative source of energy for various plant activities thus reducing the power consumption. The digestion process also degrades harmful bacteria by depriving them of oxygen since the most present gas is methane. Hence the methane sterilises the digested sludge which makes it safe for use as fertilisers post-treatment.

1.1.2 The Form

The quadric surfaced digester's basic form can be described as a revolution of a parabola where the polar regions are either curved or conical (Zingoni, 2002) (see Figure 3).

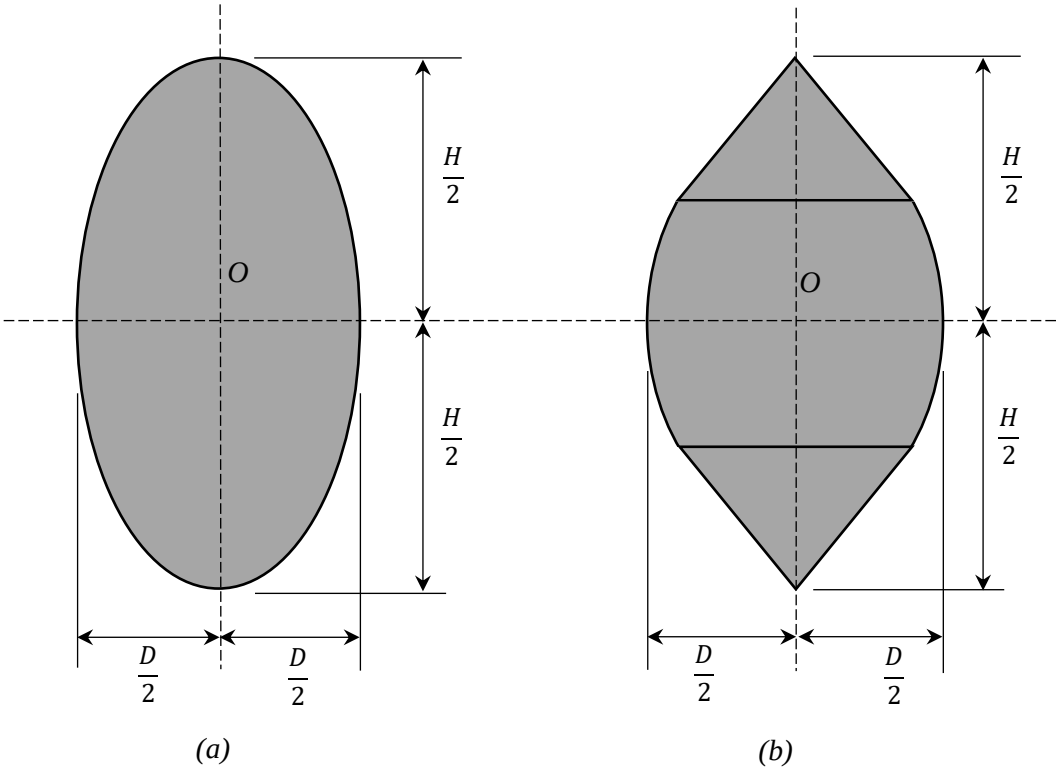

Figure 3. (a) Spherical ogival shell with spherical closures, (b) Parabolic ogival shell

The quadric-surfaced sludge digester must have smooth transitions, where there are changes radii along the meridional axes. It ensures optimal stress distribution throughout the shell, along these axes thus

minimising stress accumulation. The shell's general form can be described as a vertical revolution of a parabola that tapers at each apex. This study utilises the parabolic ogival form since it contains no shell discontinuities. Zingoni (2001), has demonstrated parametric stress distribution due to hydrostatic loading. The aspect ratio is defined by the non-dimensional parameter:

$$\xi = \frac{H}{D} \tag{1}$$

Where: H is the height of the tank and D is the diameter of the tank.

This parameter was used to analyse various forms of the digester (see Figure 4).

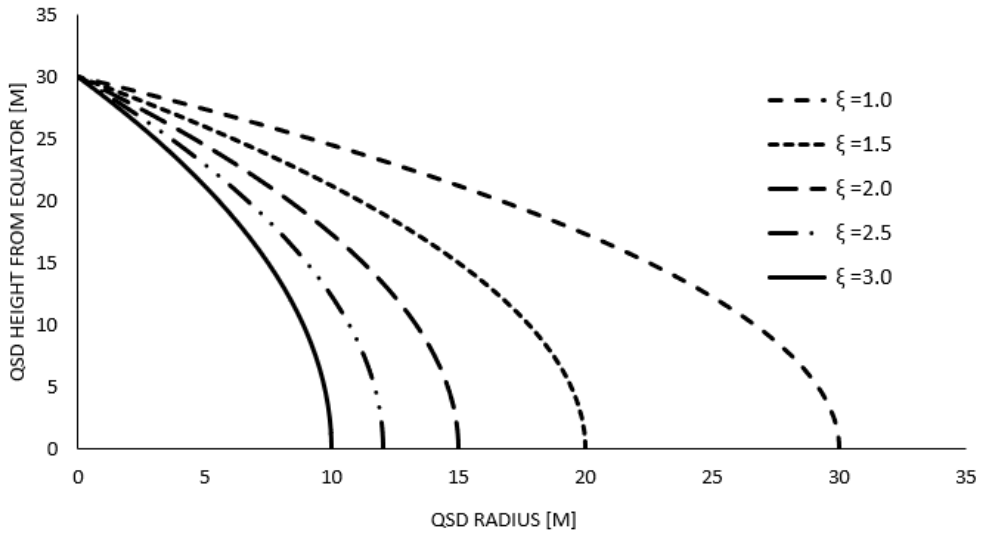

Figure 4. Parabolic ogival QSD quarter profiles with ξ ranging from 1.0 to 3.0

According to the Cohn-Vossen theorem, from differential geometry, inextensional deformation of the shell is not possible unless the lengths on the surface changes. Stiffness can be further increased at points of contact were the QSD is supported and connected to the foundation. Structurally, this is an advantage when designing QSDs to resist hydrostatic and hydrodynamic loads. This study utilises a shell of 3D printed acrylonitrile butadiene styrene as the primary material for the structural element.

1.1.3 Material

1.1.3.1 Traditional Materials

QSD shells can be constructed from various materials as the. Table 1 shows seven cities that utilise this technology for their secondary treatment. The two types of construction materials used are pre-stressed concrete and welded steel.

Table 1. QSDs Primary Shell Material from around the world. (Lia *et al.*, 2007).

Country	Location	Number of tanks	Volume [m^3]	Primary Material
Australia	Pertyh	2	2700	Prestressed Concrete
Austria	Fritzens	2	2700	Prestressed Concrete
Germany	Bottrop	4	5000	Prestressed Concrete
Japan	Kumamoto	2	3300	Prestressed Concrete
Singapore	Kranji	3	10000	Prestressed Concrete
USA	Baltimore	2	11350	Prestressed Concrete
USA	Utah	2	6245	Welded Steel

In the 1960s, a 15,000 m^3 pre-stressed QSD, the largest one of the bonded Prestressed QSDs constructed in the world, was designed and built successfully in Germany (Li, *et al*., 2007). After that, the trend of QSDs followed globally with Japan, Singapore, China and Europe furthering study and construction of concrete QSDs. In the United States, steel was the preferred material (Sutter, 1996).

Prestressed concrete implores the use of reinforced concrete, which is embedded with post-tensioning tendons that are arranged both vertically and horizontally and which are anchored in the lower lifts and foundations. Construction progresses as horizontal layers are cast and the horizontal tendons are stressed incrementally until the concrete is poured and cured in the final layer. The vertical tendons are then stressed. Reinforcing steel that is used in this type of construction is mainly to assist in confining concrete, should have strains limited to about 0.1 % (i.e. 200 MPa stress), under ultimate loads. Also to resist primary tie (tension) forces should have stresses limited to about 250 MPa under service loads (Rogowsky and Marti, 1996). Associated temperature and shrinkage effects are accounted for with the placement of reinforcing steel bars. Figure 5 shows a prestressed concrete QSD under construction.

Figure 5. Prestressed Concrete QSD under construction Back River Wastewater Treatment Plant Baltimore, Maryland, USA. (Photograph courtesy Crom Corporation).

Structural steel plates that are welded together is another type of construction method used to build egg-shaped sludge digesters (see Figure 6). These types of QSDs are quite fewer since the construction becomes more complicated. Each steel plate has a synclastic curvature that is uniform only in the lateral direction. In the vertical direction, the plate may develop multiple radii depending on the vertical placement of the panel. Alternatively, single vertical strips can be welded together creating a similar

form. This, however, does not maintain the circumferential curvature, as with other construction methods, and results in a reduction of efficiency due to the development of dead mixing zones, at each plate junction, within the tank.

Prestressed concrete is a preferred choice between the two primary materials described above. Despite the high cost in fabrication and erection of specialised formwork, it still outweighs the cost of fabricating steel panels with the required synclastic double curvature.

Figure 6. Structural Steel QSDs at Newtown Creek Wastewater Treatment Plant, Brooklyn, New York, USA. (Photograph courtesy Newton Creek WWTP).

1.1.3.2 Proposed 3D Printed Polymer

The novel 3D printed polymer QSD employs acrylonitrile butadiene styrene as the shell material. The strength characteristics vary from raw ABS (see Table 2) since extrusions during the 3D printing process creates voids within the material (see Figure 7a) which reduces the net cross-sectional area. Hence the longitudinal direction would be that of the extrusion paths of the 3D printed material. Raw ABS has the same stress and strain properties in both longitudinal and transverse (perpendicular to the longitudinal direction) directions since the material is isotropic.

Table 2. Yield strength and strain values raw and 3D printed ABS (Rodríguez, 2001)

Mesostructure	**Longitudinal (MPa)**		**Transverse [MPa]**	
	Stress	**Strain**	**Stress**	**Strain**
Raw ABS	31.2	0.0154	31.2	0.0154
3D Printed ABS	24.4	0.0145	13.6	0.0104

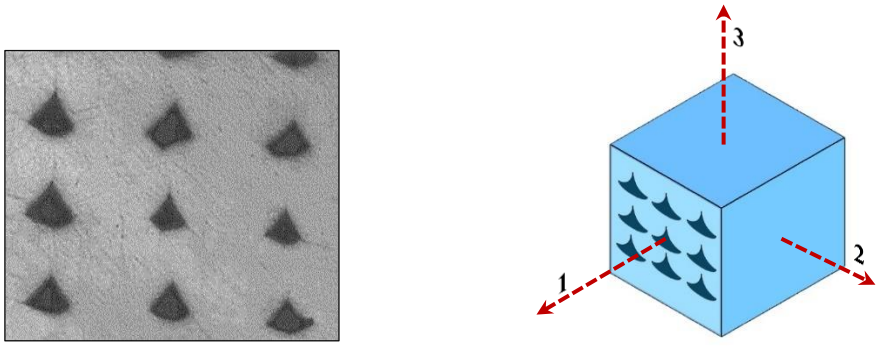

(a) (b)

Figure 7. (a) A cross-sectional sample of the mesostructure magnified for 3D printed acrylonitrile butadiene styrene (b) orientation of 3 axes of 3D printed ABS. (Adapted from Rodríguez, 2001)

Hence the 3D printed ABS material carries lower longitudinal stress of 24.4 MPa and longitudinal strain of 0.0145 MPa. The transverse stress and strain for raw ABS are the same as that of the longitudinal. Since the strength characteristics differ in each axis orientation (see Figure 7b), the longitudinal direction (axis 1) is chosen to run parallel to the equatorial circumference. The filament orientation was chosen to accommodate the most significant forces of the QSD, which are hoop forces that would develop under full load.

1.14 Analyses and Experiments

The study was conducted in two phases. The first examined the mechanical properties of the 3D printed polymer, and the second investigated the overall dynamics of the QSD utilising the properties of the 3D printed material.

Phase 1

3D printed samples were fabricated and examined for the basic mechanical properties, i.e. flexure, shear and torsion. Experimental work was conducted in the laboratory to investigate these properties. Numerical finite element analyses, which replicated the experiments, verified the results.

Phase 2

Finite element analysis (FEA) models were analysed in ABAQUS CAE. The height, H, of the tanks vary from 1 metre to 20 metres with shell thicknesses varying from 100 mm to 500mm. Further the equatorial diameter, D, varied utilising the aspect ratio with ξ =1.5, ξ =2.0, ξ =2.5 and ξ =3.0. Here the simulated tanks were subjected to a ground motion of 5 Hz and the results were recorded. A second numerical study where the tanks were analysed via first principles. This was used to verify the previous FEA results. Finally, a 6 degree of freedom (DOF) FEA model was created and was subjected to realtime earthquake time history ground accelerations.

All the results were examined and comparisons made to determine the suitability of using 3D printed polymers in QSD construction.

1.2 Aim and Objectives

Aim

The aim of the study is to design novel quadric-surfaced sludge digesters applicable to wastewater treatment works with the primary shell material being a 3D printed polymer that can be used in small island developing states (SIDS) in the Caribbean region.

This was achieved by conducting the following objectives:

Objective 1

To verify the mechanical properties of 3D printed polymers, specifically, ABS.

Objective 2

To investigate the global behaviour of the QSD under hydrostatic loads while utilising a chosen 3D printed polymer from objective 1.

Objective 3

Upon completing the first two objectives, the third objective was to determine the behaviour of a 3D printed polymer QSD under seismic conditions (Most of the earthquakes occurring in the Caribbean are either tectonic or volcanic in origin) that would make it fit for use within the wastewater sector in the Caribbean. Models of various scales were analysed to determine the optimum size.

1.3 Research Novelty

This study examines modern materials that are commonly used in the light manufacturing industry. 3D printing for the construction sector is a niche market where new research is now being explored. The current materials of choice are the traditional reinforced concrete and steel. 3D printed polymers are utilised for household and general consumer products, many of which are still novelty items. The marriage of 3D printed polymers and the construction of large-scale civil engineering infrastructure is

in itself a novelty. In terms of previous research, the literature review did not substantiate any prior studies in this field.

Another novel characteristic of this study is the use of QSDs in the Caribbean. As mentioned in section 1.1.1, the current types of wastewater infrastructure currently used are where the stakeholders continue to use out of comfort and lack of information about the behaviour of such structures in the region. This study addresses this concern thereby bridging the gap with its novelty.

1.4 Thesis Outline

This thesis is structured into six (6) chapters:

Chapter 1: Introduction

This chapter starts by introducing the reader to the QSD and the reason for its superiority over traditional cylindrical digesters. It continues to briefly describe the form and its geometry. The materials proposed to be examined is also introduced and the aim and research objectives are defined. Here the novelty of the study is also rationalised.

Chapter 2: Literature Review

In this chapter, all necessary elements that are required for carrying out the research objectives, were investigated. Firstly, the geometry of the parabolic ogival QSD shell is developed. Sloshing dynamics of the fluid inside liquid retaining structure were explored which is an essential part of the dynamic behaviour of any such structure subjected to seismic excitation. Finally, the 3D printed material was examined and the development of the mechanical properties were studied.

Chapter 3: Methodology

This chapter describes the processes followed for the experimental and numerical investigation of the mechanical properties of 3D printed polymers. Then the methodology for modelling the tank in first principles is developed. Thereafter the finite element modelling is established.

Chapter 4: Results

This chapter describes the results from the experimental and numerical studies performed on 3D printed polymers. Results from the first principles analyses are then shown followed by those of the finite element analyses. A comparison of all the results for the QSD is then discussed.

Chapter 5: Discussion

This chapter discusses the results from the experimental and numerical studies performed on 3D printed polymers. Results from the first principles analyses are then discussed followed by those of the finite element analyses. A comparison of all the results for the QSD is then discussed together with the failure criteria for QSD design.

Chapter 6: Conclusions and Future Work

This section brings to a close the thesis. It pronounces the final conclusions from the stud which includes the lessons learnt. The sub-section on future work, briefs the reader with some of the work that can be continued on this topic in the future since there are many facets that can be considered.

The undermentioned quick-guide flowchart maps the structure of the thesis.

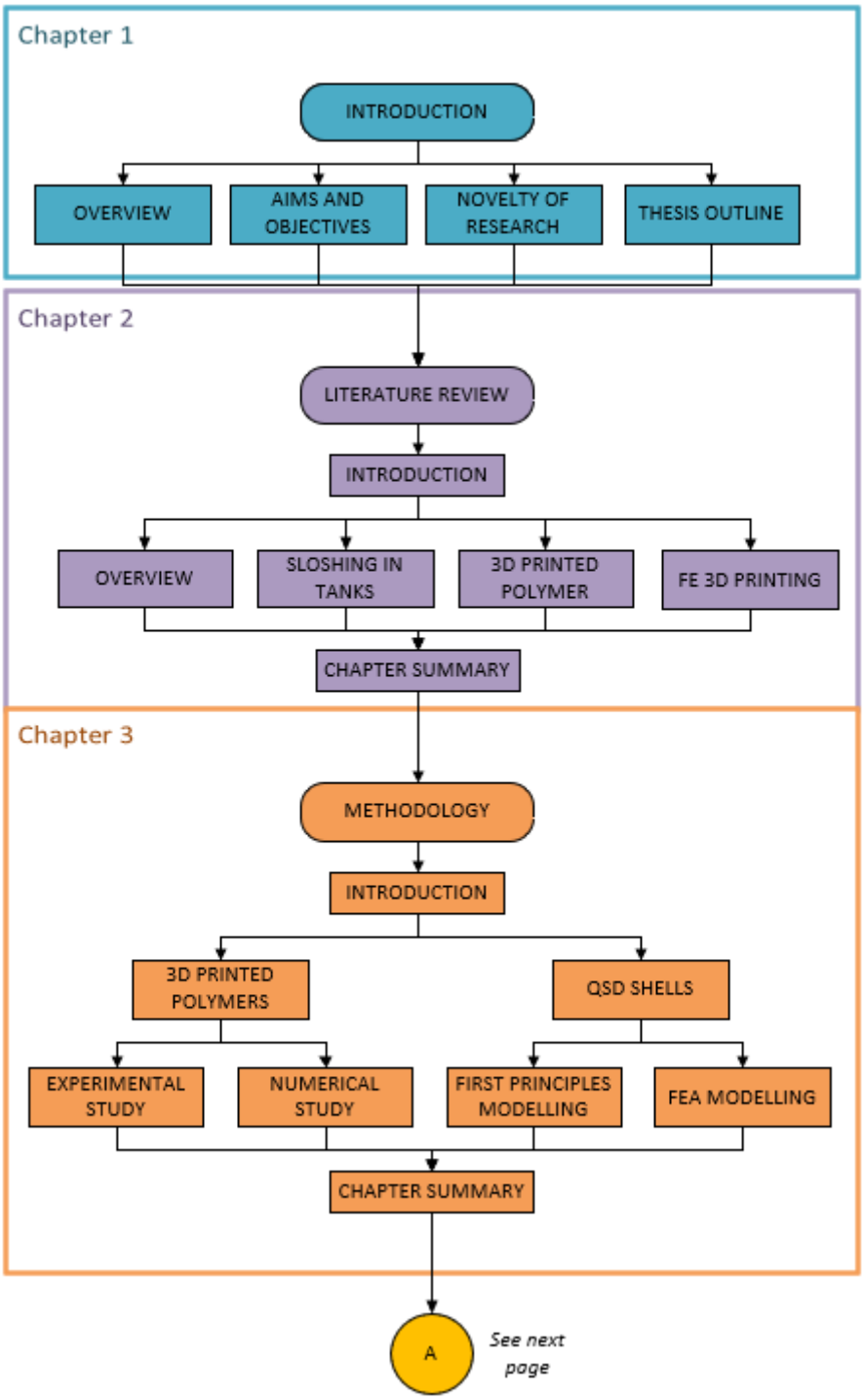
Chapter 1
INTRODUCTION
OVERVIEW
AIMS AND OBJECTIVES
NOVELTY OF RESEARCH
THESIS OUTLINE
Chapter 2
LITERATURE REVIEW
INTRODUCTION
OVERVIEW
SLOSHING IN TANKS
3D PRINTED POLYMER
FE 3D PRINTING
CHAPTER SUMMARY
Chapter 3
METHODOLOGY
INTRODUCTION
3D PRINTED POLYMERS
QSD SHELLS
EXPERIMENTAL STUDY
NUMERICAL STUDY
FIRST PRINCIPLES MODELLING
FEA MODELLING
CHAPTER SUMMARY
A
See next page

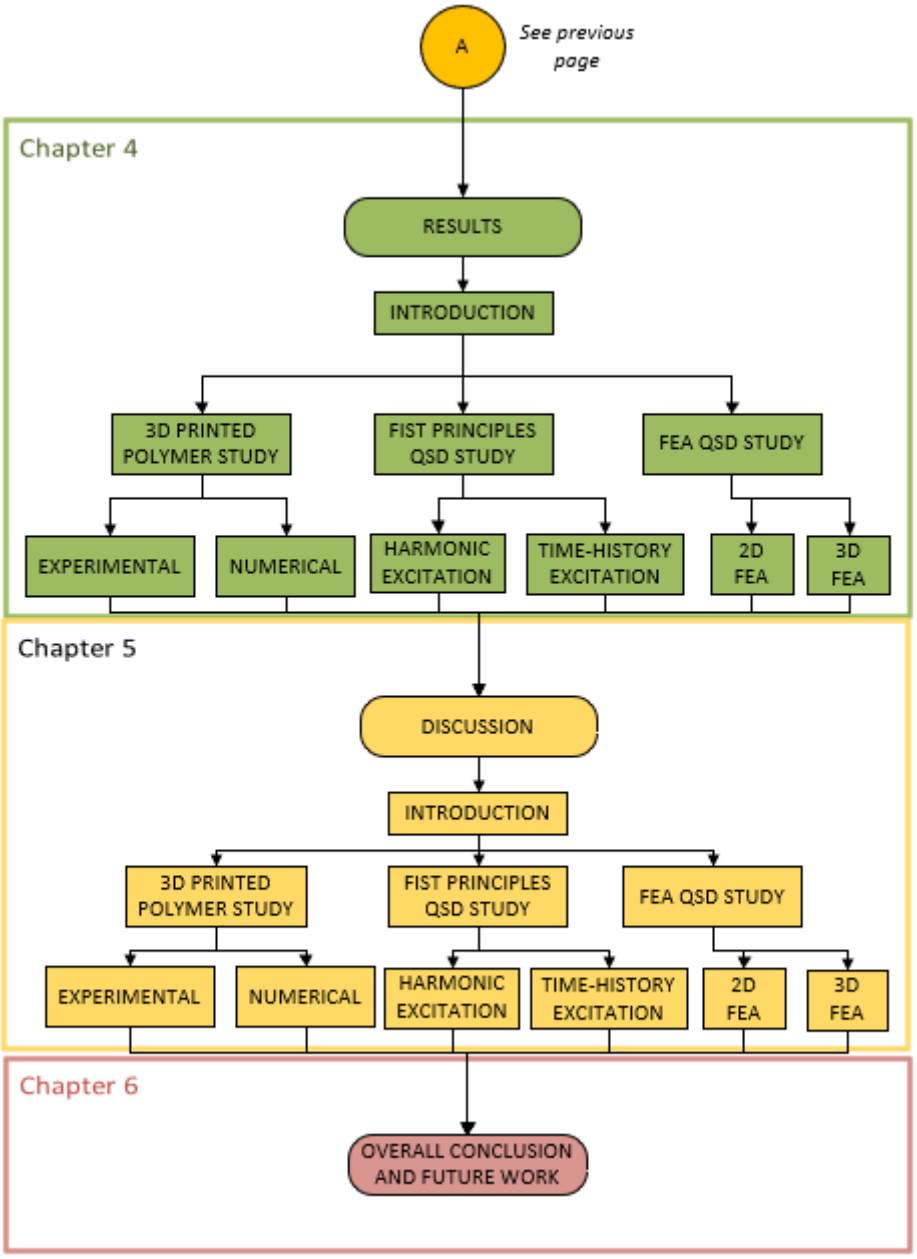

Figure 8. Flowchart of Thesis Structure

2.0 Literature Review

2.1 Introduction

The literature review examined four main areas. The first investigated quadric-surfaced shells where the relevant principles were developed and its application to the QSD. In particular the parabolic ogival shell. The second section examined linear and non-linear sloshing dynamics as it pertains to liquid retaining structures. Thereafter the literature review investigated the numerical analyses for liquid sloshing. Finally, the mechanical properties of 3D printed polymers were examined.

2.2 Quadric-surfaced Shells

2.2.1 Introduction

In civil engineering, shell structures have been established as a refined building element that utilises maximum efficiency of distributing forces throughout their cross-sectional areas for such elements. Reinforced concrete and structural steel have been the materials of choice for constructing shell structures. Shells are defined as the solid material enclosed between two doubly curved surfaces (Gibson 1965). As seen in Figure 9, the distance between the curved surfaces is the thickness, *t*. Shells are classified as either thick or thin. This is based largely on the proportions of the overall dimensions of the element in proportion with the thickness.

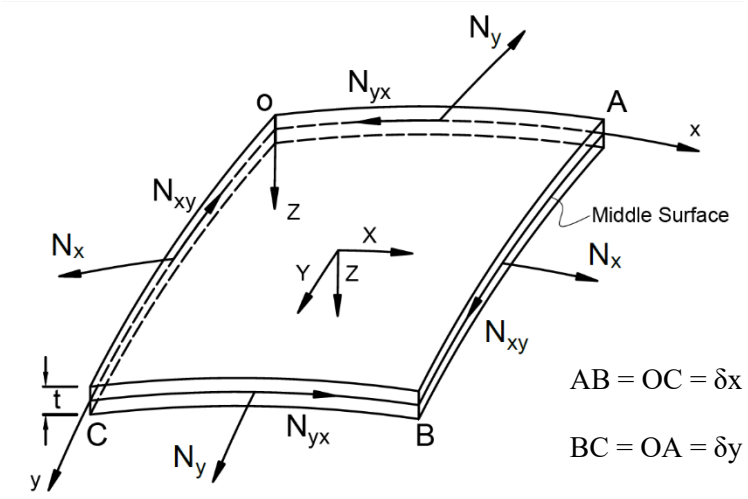

Figure 9. Diagram showing membrane stress resultants for a shell element. Adapted from Gibson, (1965)

New materials and manufacturing techniques are now being explored for use in shell construction. One such technique is the fused deposition manufacturing process (FDM), more commonly known as 3D printing. Various materials can be used with this method; however, the most common materials are polymers. Glass transition temperatures during the FDM process alter the properties of polymers thus varying the rigidity, Rodriguez, *et al* (2001). During the process, voids are created between each layer of 3D printed material. These voids can enhance or reduce the strength of the product. The problem then arises with deformations of the shell due to its flexibility. This chapter examines literature on the various deformation types within shell structures, namely the Saint-Venant shell deformations for use within the FDM quadric-surfaced sludge digester shell. It starts by defining the terminologies used in general plate/shell theory. The stress resultant equations as well as the equilibrium equations are then developed. The application of these equations is then shown on the parabolic ogival quadric-surface shell. The failure criteria are then examined based on the maximum stress resultants. Finally, the deformations of the Saint-Venant problems are reviewed based on the equations developed in the previous sections.

2.2.2 Plate Element Definitions

Shell theory is subdivided into two main categories when external forces are applied. These are: (i) membrane action and (ii) bending action. Before these can be explained, reference is made to Figure 9, where the element defines the reference axis within a three-dimensional co-ordinate system. Element OABC has a reference plane (defined as the middle surface in the *xy* plane) which is located at $t/2$. Each side of the element is parallel to the opposing side and parallel to the *xz* and *yz* planes respectively.

The shell undergoes membrane action. When external forces applied, they are transmitted by internal forces within the surface of the shell only. This means that the element resists forces axially. As can be seen in Figure 9, stress resultants N_x and N_y are normal to edges AB and BC respectively. The sense is also positive indicating that they are tensile in nature. These stress resultants are forces acting on the sides of the element and have the units *force per unit length*. Shear forces, N_{xy} and N_{yx}, carry the same units as stated above and run perpendicular to the stress resultants. The user coordinate system (UCS) located in the middle of the

element denote the positive directions of applied external forces in the x, y and z directions. These are area loads and the units are defined as *force per unit area*.

In addition to membrane action the shell also experiences flexure where in order for equilibrium to be achieved, this bending must be resisted by internal bending moments induced within the shell element. Figure 10 shows bending moments M_x and M_y, at the edges, which rotate about the y and x axes

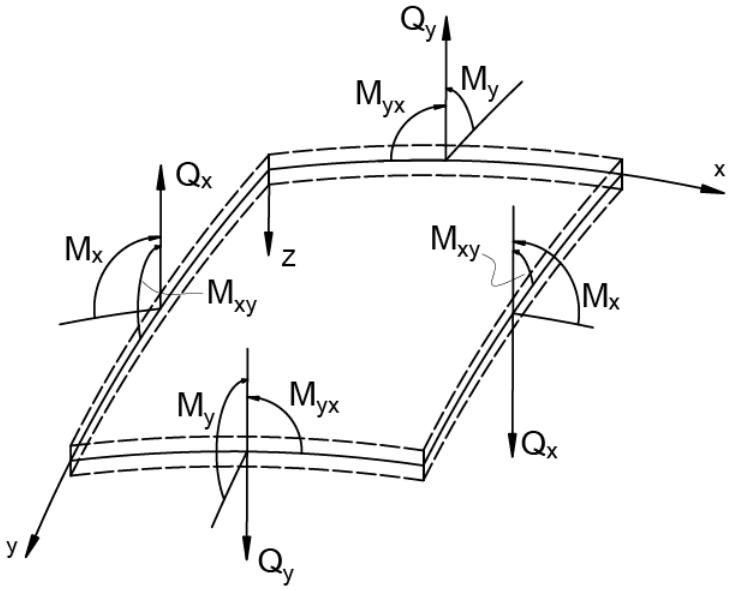

Figure 10. Diagram showing bending stress resultants for a shell element. Adapted from Gibson, (1965)

respectively. These are *moment per unit length*. Torsional moments are the combined M_x and M_y moments, namely M_{xy} and M_{yx} which rotate about the x and y axes respectively. Q_x and Q_y are the transverse shear forces per unit length which act along the z-axis.

Gibson (1965) explains that the determination of the resultant stress and moment resultants becomes complex since the use of static equilibrium equations alone are inadequate. Therefore, strain and displacement equations would have to be considered for the solution. Since the bending and membrane actions are co-dependent, solutions should not involve them independently. However, in some cases separate solutions were found to lead to accurate results.

2.2.3 Shells of Revolution

The element as described in section 2.2.1 now has to be revolved about a main axis in order to generate a full surface. Various radii of curvature define the boundaries of each element (see Figure 11). The first main principal radius of curvature, r_1, defines the meridian. The second principal radius, r_2, is the length of the normal to the surface at point A. The intersections of radius r_2 governed by φ and

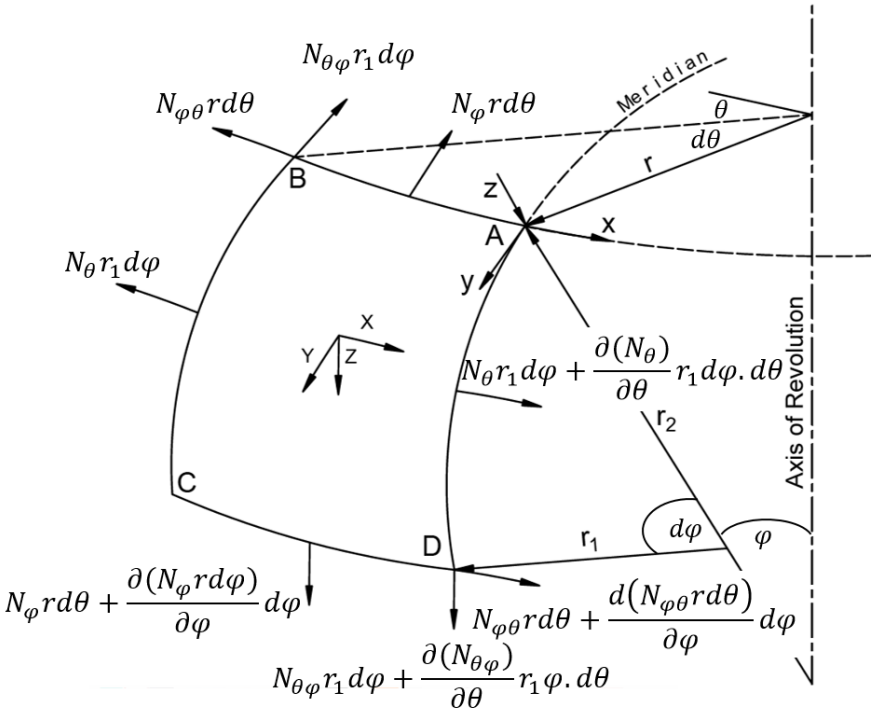

Figure 11. Diagram showing membrane stress resultants for a shell of revolution. Adapted from Gibson, (1965)

θ, defines a point on the surface of the element. If the element is bounded by 2 meridians and two parallel circles (which make up ABCD), the lengths of AB on the element is rdθ and AD become $r_1 d\varphi$. In relation to Figure 9, the element ABCD defines the middle surface of the shell of thickness t. Also the subscripts of φ and θ now replace x and y in Figure 9, thus the stress and shear resultants are presented analogously in Figure 11. As the stress resultant increases (from edge AB to CD) the term:

$$\frac{\partial(N_{\varphi}rd\theta)}{\partial\varphi} \cdot d\varphi \qquad (2)$$

is added. The partial derivative of the stress resultant function is found so that the angle, θ, remains constant while r_1 moves downwards from AB to CD. This small change in force correlates to a small change in the angle φ of the latitudinal circles. Hence, this increase is summed to create:

$$N_{\varphi} r d\theta + \frac{\partial (N_{\varphi} r d\theta)}{\partial \varphi} \cdot d\varphi \tag{3}$$

Similarly, the term:

$$\frac{\partial (N_{\varphi\theta} r d\theta)}{\partial \varphi} \cdot d\varphi \tag{4}$$

is added to the shear resultant from AB to CD, thus producing:

$$N_{\varphi\theta} r_1 d\varphi + \frac{\partial (N_{\varphi\theta} r d\theta)}{\partial \varphi} \cdot d\varphi \tag{5}$$

Here again the angle, θ, remains constant while r_1 increases.

2.2.4 Equations of Equilibrium

The equations for the solutions of the stress and shear resultants (Eq. (3) and Eq.(5)) must now include additional components of $N_{\varphi\theta}$ and $N_{\theta\varphi}$ respectively, to achieve equilibrium. The statically determinate problem can be deduced as follows:

From Figure 11, The meridional tangents at A and B intersect at a point P, on the axis of revolution with an internal angle dα and lengths AP=BP=$r_2 \tan\varphi$ dα. With r = $r_2 \sin\varphi$, angle dα can be written as:

$$d\alpha = d\theta \cos\varphi \tag{6}$$

With AD =BC = dα/2, the total horizontal (x-direction) stress resultant is

$$2N_{\varphi\theta}r_1 d\varphi \sin\left(\frac{d\alpha}{2}\right) \approx N_{\varphi\theta}r_1 d\varphi d\alpha \tag{7}$$

Substituting Eq. (6) into Eq. (7)

$$N_{\varphi\theta}r_1 d\varphi d\theta cos\varphi \tag{8}$$

By using the static equilibrium equation, $\xrightarrow{(+ve)} \sum F_x = 0$ and summing all the horizontal forces (see Figure 11):

$$\begin{aligned} N_{\varphi\theta}rd\varphi + \frac{\partial(N_{\varphi\theta}rd\theta)}{\partial\varphi}\cdot d\varphi - N_{\varphi\theta}rd\theta + N_\theta r_1 d\varphi + \frac{\partial(N_\theta)}{\partial\theta}r_1 d\varphi . d\theta - N_\theta r_1 d\varphi \\ + N_{\varphi\theta}r_1 d\varphi d\theta cos\varphi + Xr_1 d\varphi rd\theta = 0 \end{aligned} \tag{9}$$

Where X is the external load applied to the shell element. Equation (9) can now be simplified into the final equation which yields:

$$\frac{\partial}{\partial\varphi}\left(N_{\varphi\theta}r\right) + \frac{\partial N_\theta}{\partial\varphi}r_1 + N_{\varphi\theta}r_1 cos\varphi + Xrr_1 = 0 \tag{10}$$

which is the equilibrium equation to solve for the stress resultant in the x-direction. The solutions for the y and z directions are similar in principle and the final equations are:

$$\frac{\partial}{\partial\varphi}\left(N_\varphi r\right) + \frac{\partial N_{\theta\varphi}}{\partial\varphi}r_1 - N_\theta r_1 cos\varphi + Yrr_1 = 0 \tag{11}$$

And,

$$\frac{N_\theta}{r_2} + \frac{N_\varphi}{r_1} + Z = 0 \tag{12}$$

2.2.5 Application to the parabolic ogival quadric surface shell

In the previous section, the aforementioned equations of equilibrium give rise for solutions of resultant stresses due to applied external forces on a generically revolved shell element. The application of this to the quadric surfaced sludge digester (QSD) is examined from studies conducted by Zingoni (2002). The general shape of the QSD is a revolution of a parabola (see Figure 12).

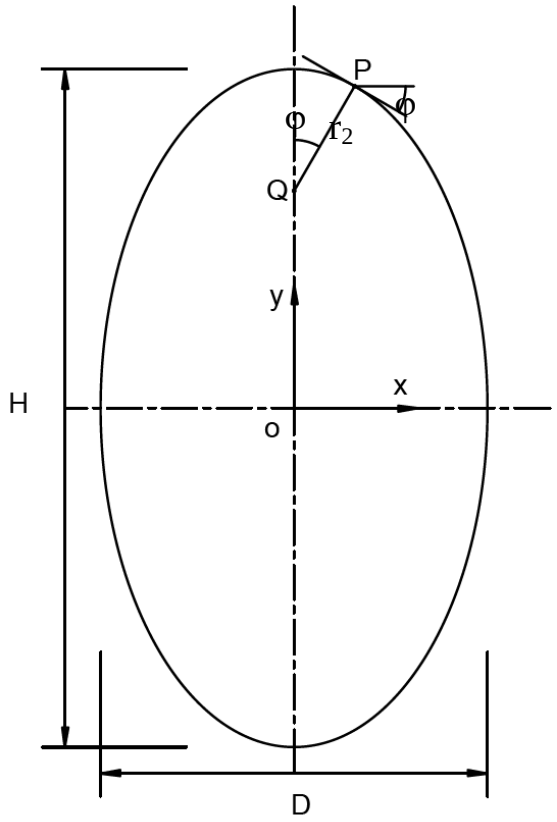

Figure 12. Geometric parameters of the parabolic ogival quadric surface shell. Adapted from Zingoni, (2002)

Here, unlike spherical shells where the radii in both the meridional and latitudinal profiles are constant. In the parabolic ogival shell the radius, r_2, changes constantly. Hence calculating the stress resultants, r_1 and r_2, become functions of the height, H and diameter, D. According to Zingoni (2002), r_1 now becomes:

$$r_1 = \frac{H^2}{4D\sin^3\varphi} \tag{13}$$

and r_2 now becomes:

$$r_2 = \frac{4D^2 sin^2\varphi - H^2 cos^2\varphi}{8D sin^3\varphi} \tag{14}$$

By means of substituting equations (13) and (14) into equation (10) and simplifying, the solution of the stress resultant becomes:

$$N_\varphi = \frac{XH^3}{16D^2}\left(\frac{sin\varphi}{4D^2 sin^2\varphi - H^2 cos^2\varphi}\right)\left[-\frac{D(4D^2+H^2)}{sin^2\varphi} + \frac{DH^2}{2sin^4\varphi}\right.$$
$$- H(4D^2+H^2)\left(\frac{cos\varphi}{sin\varphi}\right) + \frac{H}{3}(4D^2+H^2)\left(\frac{cos\varphi}{sin^3\varphi}\right)(1+2sin^2\varphi) \tag{15}$$
$$\left. - \frac{H^3}{15}\left(\frac{cos\varphi}{sin^5\varphi}\right)(3+4sin^2\varphi+8sin^4\varphi) + C\right]$$

Where C is a constant derived from the partial deferential equation. By applying a boundary condition at the apex of the shell, the angle φ becomes 0. Hence N_φ=0, thus:

$$C = \frac{D(4D^2+H^2)}{sin^2\varphi_0} - \frac{DH^2}{2sin^4\varphi_0} + H(4D^2+H^2)\left(\frac{cos\varphi_0}{sin\varphi_0}\right)$$
$$- \frac{H}{3}(4D^2+H^2)\left(\frac{cos\varphi_0}{sin^3\varphi_0}\right)(1+2sin^2\varphi_0) \tag{16}$$
$$+ \frac{H^3}{15}\left(\frac{cos\varphi_0}{sin^5\varphi_0}\right)(3+4sin^2\varphi_0+8sin^4\varphi_0)$$

The stress resultant N_θ can now be calculated with N_φ known:

$$N_\theta = (4D^2 sin^2\varphi - H^2 cos^2\varphi)\left[\frac{X(2HD^2 sin\varphi - H^2 cos\varphi}{32D^2 sin^4\varphi} - \frac{N_\varphi}{2H^2}\right] \tag{17}$$

Now with the known stress resultants and the thickness, t, of the shell, the stresses in both the meridional and latitudinal directions can be found, hence:

$$\sigma_{\emptyset} = \frac{N_{\varphi}}{t} \quad \text{and} \quad \sigma_{\theta} = \frac{N_{\theta}}{t} \tag{18}$$

2.2.6 Failure criteria

The development of the stresses in the previous section can now lead to the discussion on the failure criteria for the FDM ABS polymer shells. Since the polymer is extruded in adjoining layers, voids between each extrusion are created, thus this type of (3D-printed) material is known to have directional properties and hence anisotropic with the polymer being linearly elastic. Doyle (2001) stated that elastic constitutive relations become apparent where deformations occur such that the rotations and/or displacements are large while the strains are quite small in comparison. Hence, approximations are made which does not influence the accuracy of the analysis of results when calculating the stress resultants.

The criteria for failure can be characterised in three areas. These are (i) the maximum principal stresses, (ii) the energy of distortion and (iii) the maximum shear stresses. The maximum principle stress is based on Rankine's theory and assumes that failure will occur at any point that reaches a value equal to the tensile stress in tension at failure. Thus inequalities for the principle stresses:

$$\sigma_1 \geq \sigma_f \quad \text{and} \quad \sigma_3 \leq -\sigma_f \tag{19}$$

where σ_f is the failure stress due to a single tensile force in one direction. While this is not a good predictive method for failure in most materials, it has proven to yield satisfactory results in brittle materials (Doyle 2001). Hence, in the event of FDM ABS becoming brittle due to ultraviolet ray exposure, this criterion will be useful. The energy distortion theory idealises the total strain energy the dilation of energy and the distortion of energy. The first is associated with the change of volume due to hydrostatic pressure whilst the latter deals with the deformation of the body. In both cases this particular criterion is not a good measure for failure of FDM materials since it is associated with isotropic linear elastic materials (Doyle 2001). FDM materials are anisotropic, mainly due to the existence of voids that are created along the extrusion path-line. The maximum shear stress theory compares maximum yield during shearing of the material and the maximum shear stress at yield of a sample undergoing a uniaxial tensile test. The failure criterion for the maximum shear is give as:

$$\tau_{max} \geq \frac{1}{2}\sigma_Y \tag{20}$$

In the shell of liquid retaining structures, the shear usually is zero. Henceforth under hydrostatic loading, where the load is distributed along the surface area of the shell, this yield criterion will not be suitable for use. However since its applicability is good for predicting failure in ductile materials, it can still be used when examining failure due to various Saint-Venant deformations.

2.2.7 Saint-Venant Deformations

The Saint-Venant's principle allows for replacing complex stress distributions or weak boundary conditions (BCs) with ones that are simpler to solve, as long as that boundary is geometrically short (Naghdi and Yongsarpigoon 1985). In other words if the distance between two loads become large, the high order momentum of mechanical load decays quickly (at a rate of $1/r^{i+2}$, where r is the rate of decay) so that they never need to be considered for regions far from the boundary. Thus the difference between the effects of two different but statically equivalent loads becomes negligible.

This principle is very useful in aiding the solutions of various types of deformations that can occur in shell structures. Axelrad (1987) explains that this principle can be applied to the solution of deformations in shell structures by prescribing only the load on an edge and not its distribution along the element's edge or boundary contour. This application now reduces the three dimensional problem into a single dimension.

According to Fried (1985) there are several applications for the Saint-Venant principle to flexible shell problems. These can be categorised as (i) rotationally symmetric problems and (ii) lateral and space bending problems. The latter does not have any significant application to the parabolic ogival quadric-surfaced sludge digester since the continuous shell surface does not give rise to such deformations occurring. Only if the design would accommodate geometrical discontinuities (other than increasing/decreasing the shell thickness) in the surface area, such as penetrations, then this would be of significant relevance to the study. In the case of rotationally symmetric problems, the deformations produced are axisymmetric in nature and

hence the shell of revolution remains axisymmetric as well. In such cases, the shell elements are in a state where flexure is 100% of the element's force carrying capacity. The problem eliminates all shear resultant stresses and strains. Therefore, the three equations of equilibrium are satisfied (Eq. (9), (10) and (12)). The equilibrium equations for bending (given by Gibson 1965):

$$\frac{d(N_\varphi r)}{d\varphi} - N_\theta r_1 cos\varphi - Q_\varphi r_2 sin\varphi + Y r_1 r_2 sin\varphi = 0 \tag{21}$$

$$\frac{d(Q_\varphi r)}{d\varphi} + N_\theta r_1 sin\varphi + N_\varphi r_2 sin\varphi + Z r_1 r_2 sin\varphi = 0 \tag{22}$$

$$\frac{d(M_\varphi r)}{d\varphi} - M_\theta r_1 cos\varphi - Q_\varphi r_1 r_2 sin\varphi = 0 \tag{23}$$

where: Q is the transverse shear stress resultant and M is the resultant moment about the meridional element boundary, denote the equilibrium equations for flexure in the X, Y and Z-axes respectively. These equations become dominant in the Saint-Venant solutions since the load must act along the meridional axis, hence this assumption is made and the solution to calculate the displacements and forces are conducted.

A second type of rotationally symmetric Saint-Venant deformation that is of interest to the QSD, relates directly to an axisymmetric torsional force, that rotates about the axis of the shell of revolution. With the introduction of this torsional force the six equations of equilibrium are satisfied. This is because the structure remains axisymmetric and the general form of the shell remains intact. Therefore, the shell elements experience pure shear strain, hence a stain energy equation needs to be introduced for solution of this type. Consider the axisymmetric introduction of torsional force applied to the shell element in Figure 11. The displacement of point A translates to A' and D to D' (see Figure 13). If point A displaces at a distance v,

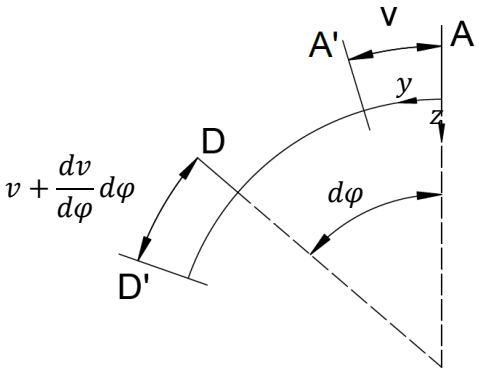

Figure 13. Diagram showing displacement of shell surface. Adapted from Gibson, (1965)

then point D will have a displacement of $v + (dv/d\varphi\ d\varphi)\ d\varphi$. In the z-direction, AD will also be displaced, hence:

$$A'D' - AD = (r_1 - w)d\varphi - r_1 d\varphi = w\ d\varphi \tag{24}$$

Where w is the displacement along the z-direction.

Thus by the principle of superposition, the displacements of points A and D in both the y and z-directions can be summed to get:

$$\frac{dv}{d\varphi} d\varphi - w d\varphi \tag{25}$$

Recognising that the arc length $AD = r_1 d\varphi$, the strain at the meridian will be:

$$\varepsilon_\varphi = \frac{dv}{r_1 d\varphi} - \frac{w}{r_1} \tag{26}$$

The circumferential strain is formulated by the new radius, $r' = r - rwsin\varphi + vcos\varphi$. Analogous to the solution for ε_φ given above, the solution for the strain in the latitudinal direction, ε_θ, would be:

$$\varepsilon_\theta = v\cos\frac{\varphi}{r} - w\sin\frac{\varphi}{r} = \frac{(v\cot\varphi - w)}{r_2} \quad (27)$$

Hence, equations (26) and (27) can now be used to solve the final Saint-Venant torsional displacement problem.

2.2.8 Summary

In this section, it can be seen that previous studies in the geometry of QSDs are minimal. The development of stress resultant equations (equation (18)), for the parabolic ogival shell, by Zingoni (2002), is a continuation of studies conducted by Gibsom (1965). Axelrad also developed these equations from first principles as well however his work was based on scalar matrices. Doyle's work was also based on a method utilising scalar matrices. The solutions for the rotationally symmetric Saint-Venant shell distortion problems that can occur in QSDs were also examined even though the literature available did not conclude of any actual case studies with this type of failure. However, the literature can prove valuable when developing design code parameters for QSD shell design.

2.3 Sloshing Dynamics in Liquid Retaining Structures

2.4 Sloshing Dynamics

2.4.1 Introduction

Sloshing is the dynamic behaviour of the free liquid's surface, which is initiated by any disturbance to the liquid retaining structure. Sloshing is of significant importance and is one of the major concerns in the design of liquid retaining structures and fuel tankers for carriers. Abramson (1967) mentioned that for several years, this subject had been a significant concern for scientists, engineers and mathematicians. According to Ibrahim (2006), the free liquid's surface can experience different motions comprising of simple planar, nonplanar, symmetric, asymmetric, rotational, irregular beating, quasi-periodic and chaotic,

all depending on the type of disturbance, amplitude and frequency of seismic excitation, properties of the liquid, height of liquid and the geometry of the retaining liquid container. When the frequency of the motion and the natural frequencies of liquid sloshing are close to each other, the resulting amplitudes of the sloshing wave would be very large increasing the sloshing dynamic forces on the shell surfaces of the container. The high hydrodynamic forces produced by the sloshing waves on the inner surface of the container affects the overall response of the container and causes a complex Fluid-Structure Interaction (FSI) phenomenon between the two materials concerning the liquid properties and retaining container properties.

The difficulty of sloshing involves the assessment and estimation of the hydrodynamic pressure distribution on the container's surface, moments, forces and natural frequencies of the system and the liquid surface. As cited by Ibrahim (2006), the non-linear phenomena of sloshing dynamics have an infinite number of natural frequencies where the lowest frequency is excited by concentrated seismic action which, directly affects the dynamic stability and performance of liquid retaining structures. This nonlinear phenomenon of sloshing results in the maximum response frequency being different from the linear natural frequency and is reliant on amplitude. Nonlinear effects encompass of amplitude jumps, chaotic liquid motion, parametric resonance and nonlinear sloshing mode interaction due to the occurrence of internal resonance between the liquid sloshing modes. For this reason, previous studies focused on investigating forced harmonic oscillations near the lowest natural frequencies that are computed by the fluid field linear equations.

Challenges of sloshing dynamics are encountered in a wide array of engineering applications. In the design of high-performance automobiles, stationary liquid retaining structures and the reduction of noise due to fuel sloshing is becoming an increasingly significant consideration. A more pressing concern, according to Godderidge *et al*. (2012) is the effect of fuel slosh on the stability of road vehicles during sudden acceleration and deceleration. However, this would not be examined in this study. In large buildings, fluid sloshing in tuned liquid dampers counteracts earthquake or wind-induced motions and vibration. The water tower, reservoir and dam design also include sloshing concerns.

Previous research of sloshing has a long history and presently continues to grasp the importance because of its significance in the application of structural and aerospace engineering. After several decades of research, several effective approaches for researching have been proposed. However, because of its extreme

nonlinear effects, solving the dynamics of sloshing is still a great challenge and a vast amount of work is still essential to develop and confirm theories and fully grasp the understanding of sloshing dynamics under seismic excitation.

2.4.2 Linear Sloshing Dynamics

2.4.2.1 Fluid field equations and Modal analysis of rigid tanks

The theory of dynamic sloshing in liquid retaining structures is based on understanding the derivation of fluid field equations that are used to approximate the hydrodynamic shell forces and moments induced by sloshing waves. Solutions for simple geometry retaining structures such as the upright cylindrical and rectangular containers are possible by explicit analysis. Modal analysis is a linear dynamic response process which illustrates and evaluates the dynamic response and superimposes the free vibration mode shapes to characterise the displacement. Ibrahim, (2006) mentioned that by conducting a modal analysis on a rigid shell liquid retaining structure eliminates the boundary value problem for the dynamic response characteristics to seismic excitations, the natural frequencies of the sloshing mode shapes. The natural frequencies of sloshing are kinematic and dynamic on the fluid-structure boundaries rather than in form of the fluid continuity equation.

For a tank geometry, which is open to the atmosphere, the BCs typically specify the value of the field at all nodes on the liquid's boundary surface or the normal gradient to the container surface and sometimes both. According to Morse and Fesbach (1999), the BCs mentioned below, where each group has its appropriate equations associated with its boundary condition.

i. Dirichlet BCs, which fix the value of the field on the surface.
ii. Neumann BCs, which fix the value of the normal gradient on the surface.
iii. Cauchy conditions, which fix both value of the field and normal gradient on the surface.

The variational formulation proposed and used by Lawrence *et al.* (1958) is based on Hamilton's principle as illustrated by Equation (28) and is observed as a powerful tool for developing the fluid field equations. As mentioned by Ibrahim, R. (2006), Hamilton's principle states that the actual path in the configuration

space yields the value of the finite integral stationary with respect to all arbitrary variations of the path between two instants of times, t_1 and t_2, provided the path variations vanish at these two endpoints. Budiansky (1958) modified Hamilton's principle and developed an integral equation for tanks with a curved geometry such as spherical tanks and horizontal cylindrical tanks. The variational approach is based on deriving the superlative of a function that describes the system behaviour. The Lagrangian, L=T-V, has to be minimised or maximised, where T and V are the kinetic and potential energies of the system, respectively. Hamilton's principle is defined as;

$$\delta I = \delta \int_{t_1}^{t_2} (T - V) dt = 0 \tag{28}$$

Studies were carried out by Trotsenko (1967), where the liquid oscillations in cylindrical containers with annular baffles were investigated. Further studies were done by Lamb *et al.* (1970) with respect to sloshing for an inclined cylindrical container geometry with axial symmetry where they computed the normal modes and natural frequencies of sloshing and concluded that for spherical containers, solving sloshing shell forces would be a problem because the six degrees of freedom model would be analytically complex. For this complication, Leonard and Walton (1961), experimentally measured the natural frequencies and mode shapes in spheroidal containers with respect to different orientations. The dependence of the measured natural frequencies of the first three sloshing modes on the fluid depth ratio, h/2b or h/2a, or the three tank orientations and the respective plots in Figure 14.

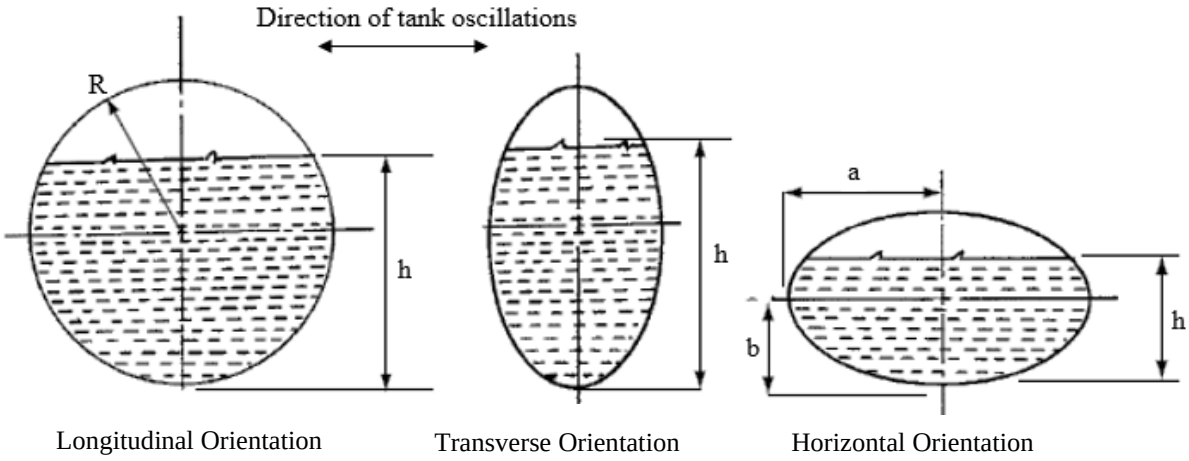

Figure 14. Dependence of liquid natural frequencies on depth ratio for three orientations of a spheroidal tank. (Leonard and Walton, 1961).

For the horizontal orientation case, the natural frequency of the free surface, computed from Equation (29), is compared with the measured results of a liquid in an upright circular cylindrical tank of radius, r, equal to the radius of the liquid surface and a liquid depth, hc, which yields the same liquid volume.

$$\omega_n = \sqrt{\frac{g\xi_n}{r}\tanh(\frac{\xi nhc}{r})} \tag{29}$$

where

ω_n – sloshing frequency of order n

g – gravitational acceleration

ξ – coordinate transformation function $= \frac{x}{\propto R}$, where x is the coordinate on x-axis

R – radius of curvature of the free surface

$\propto$ - factor $= \propto = \frac{a}{R} < \propto \leq 1$, where a is half the width of the free surface on the x-axis

Investigating the natural frequency of horizontal circular cylinders and spherical containers, Barnyak and Barnyak (1996) determined the normal mode frequencies of viscous liquid partially filling a horizontal cylinder. Lamb (1995) presented an energy approach to determine the natural frequency of the first transverse mode of the liquid's free surface in a half-filled horizontal cylinder, that is, h = -R. He obtained Equation (30) which is an expression for the velocity potential function.

$$\Phi(r,\theta) = \frac{1}{2}\omega r^2 \sin 2\theta - \sum A_{2n+1}\, Sin(2n+1)\theta \left(\frac{r}{R}\right)^{(2n+1)} \tag{30}$$

where

$$A_{2n+1} = (-1)^{n+1}\left(\frac{\omega R^2}{\pi}\right)\left\{\left(\frac{1}{2n-1}\right) - \left(\frac{2}{2n+1}\right) + \left(\frac{1}{2n+3}\right)\right\} \tag{31}$$

where

Φ – velocity potential

ω – sloshing frequency

n – order of operation

R – radius of curvature of the free surface

r – cylindrical tank of radius

θ – angular coordinates

The kinetic energy, T, of sloshing undergoing small oscillations is given by Equation 46 below.

$$T = \frac{1}{2}\,\pi\rho R^4 \left(\frac{4}{\pi^2} - \frac{1}{4}\right)\omega^2 \tag{32}$$

where ρ is the density of the fluid.

From this expression, the effective mass moment of inertia, $I_{o(eff)}$, of the liquid about the centre of the cylinder is given by Equation (33).

$$I_{o(eff)} = \pi\rho R^4 \left(\frac{4}{\pi^2} - \frac{1}{4}\right) \tag{33}$$

The potential energy, U, is given by Equation (34).

$$U = \frac{1}{3}\rho g R^3 \theta^2 \tag{34}$$

Bauer, (1964) analysed the liquid's free surface oscillations in a partially filled tank and also with respect to the annular cross-section where he concluded that for both cases, the natural frequency of the liquid's free surface displayed the same expressions as the cylindrical tank but with different roots of the Bessel

function. Mclver and Mclver (1993) investigated the liquid sloshing dynamic frequencies for different tank geometries, and Bauer and Eidel (1999) investigated the different configurations of cylindrical containers.

Numerical studies of two-dimensional sloshing in rectangular geometry containers, Ibrahim (2006) mentioned that the natural frequency of sloshing depends on the liquid's depth to width ratio and also stated that as the mode increases, the effect of liquid depth is reduced. Graham and Rodriguez (1951), solved the three-dimensional velocity potential for which the natural frequency depends on the three significant dimensions' axis of the fluid. Ibrahim (2006) mentioned that the nonlinear dependence of the natural frequencies on the wave motion amplitude was resolved and the influence of damping on the natural frequency resulted for higher viscosities of kinematic viscosity v = 2.5 poise and the resonance frequency is slightly higher than the predicted value for an ideal liquid.

The variational formulation approach is mainly used to attain the boundary value to solve the boundary value problem in one treatment. The modal analysis of sloshing is formulated for different tank geometries which resulted in the estimation of the velocity potential function given by Equation (35),

$$\Phi(r,\theta,z,t) = \sum_{m=0}^{\infty}\sum_{n=1}^{\infty}[A_{mn}\cos 2m\theta]\sin(\omega_{mn}t)\left\{\frac{\cosh\left[\frac{\xi_{mn}(z+h)}{R}\right]}{\frac{\cosh\xi_{mn}h}{R}}\right\}J_{2m}\left(\frac{\xi_{mn}r}{R}\right) \qquad (35)$$

where

Φ – velocity potential

ω_{mn}– sloshing frequency of order m and n

A_{mn} – integration constants

m – mass of liquid in the tank

R – radius of curvature of the free surface

r – cylindrical tank of radius

θ – angular coordinate

ξ_{mn} – sloshing amplitude of order m and n

h – upper level of liquid volume

t – time

J – first order Bessel function

The natural frequencies of sloshing given by Equation (36) and the corresponding wave height are given by Equation (37). Figure 15 illustrates the notations of a cylindrical tank.

$$\omega_{mm}^2 = \frac{g}{R}\xi_{mn}\tanh\left(\frac{\xi_{mn}h}{R}\right), \qquad m,n = 0,1,2,\ldots.n \tag{36}$$

$$\frac{1}{g}\sum_{m=0}^{\infty}\sum_{n=1}^{\infty}[A_{mn}\cos 2m\theta]\omega_{mn}\cos(\omega_{mn}t)\left\{J_{2m}\left(\frac{\xi_{mn}r}{R}\right)\right\} \tag{37}$$

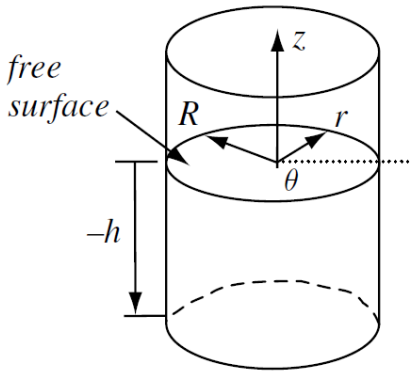

Figure 15. Cylindrical Tank. (Ibrahim, 2006)

2.4.2.2 Linear Forced Sloshing

In the previous section, the fluid field equations were developed, and the natural frequencies were estimated from the free surface boundary conditions. The knowledge of natural frequencies with respect to sloshing is essential in the design of all liquid retaining structures subjected to seismic excitations. Ibrahim, (2006) mentioned that it is crucial to have the natural frequencies of sloshing away from all normal and nonlinear resonance conditions when designing these types of structures. The types of excitation that can be expected are impulsive, periodic, sinusoidal or random excitations and concerning geometry orientation, they can be lateral, parametric, pitching, roll or a combination. Ibrahim, (2006) also mentioned that under forced

excitation, it is vital to determine the hydrodynamic loads acting on the container, and their phase with respect to this excitation. The hydrodynamic shell forces and moments are computed by integrating the pressure distribution over the wetted area. The free-surface wave height which affects the location of the centre of mass should also be determined. For resonance, the liquid's free surface experiences different types of nonlinear behaviour.

Trembath, (1957) attained a solution for sloshing in cylindrical and rectangular geometry containers undergoing small horizontal oscillations and pitching. The solution contained integrals which are evaluated either algebraically or numerically depending on the problem. A general treatment of an arbitrary tank geometry undergoing forced motion was given in terms of the velocity potential function by Brooks, (1959). A Lagrangian formulation was developed by Budiansky (1958), to observe sloshing dynamics under horizontal excitation of spherical and circular horizontal tanks. This section deals with the liquid response to lateral and pitching excitations for an upright cylindrical and rectangular tank configuration.

2.4.2.2.1 Upright Cylindrical Containers

Widmayer and Reese (1953) studied the analytical problem of liquid forced oscillations in an upright circular cylindrical tank of uniform depth experiencing horizontal and pitching motion. This study aid in the estimation of the liquid's effective mass moment of inertia, the forces and moments acting on the tank, and the sloshing wave height. In this section, the liquid hydrodynamic shell forces and moments acting on the container geometry are estimated under translational and pitching excitations. Ibrahim, (2006) states that under roll excitation, the fluid does not participate in the tank motion since it is assumed to be inviscid. However, if the fluid viscosity is considered, then the Navier–Stokes equations must be used to determine the thickness of the fluid contributing to sloshing.

2.4.2.2.2 Lateral Excitation

For an upright circular tank, as shown in Figure 16, under sinusoidal excitation along the x-axis, where X_o and Ω are the excitation amplitude and frequency, respectively.

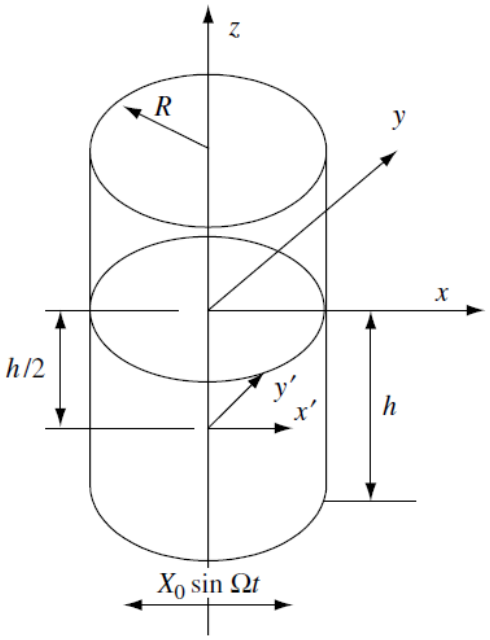

Figure 16. Cylindrical tank under sinusoidal lateral excitation, (Ibrahim 2006)

Under the assumption that the amplitudes of liquid excitation and the respective fluid responses are small, the linearised fluid field dynamic and kinematic equations for free surface conditions are given by Equations (38) and (39) respectfully.

$$0 = g\eta - \frac{\partial \Phi}{\partial t} + \ddot{X} r \cos\theta \ , \qquad at\ z = \eta(r, \theta, t) \tag{38}$$

$$-\frac{\partial \Phi}{\partial t} = \frac{\partial \eta}{\partial t} \ , \qquad at\ z = \eta(r, \theta, t) \tag{39}$$

where

g – gravitational acceleration

η – wave height

$\ddot{X}$ – second derivative of the excitation amplitude

r – cylindrical tank of radius

t – time

θ – angular coordinate

$\partial\Phi$ and $\partial\eta$ – change in potential velocity and wave height respectively

∂t – change of potential velocity and wave height with respect to the time taken for that change to occur

The maximum wave height occurs, η_{max}, at r = R, θ = 0 and $\Omega t = \pi/2$ and is given by Equation (40)

$$\eta_{max} = \frac{X_0 \Omega^2}{g} \left\{ R + \sum_{n=1}^{\infty} \frac{2R}{(\xi_{1n}^2 - 1)} \frac{\Omega^3}{(\omega_{1n}^2 - \Omega^2)} \right\} \quad (40)$$

where

R – radius of curvature of the free surface

Xo and Ω – the excitation amplitude and frequency respectively

g – gravitational acceleration

ξ – sloshing amplitude

ω – sloshing frequency

The maximum pressure occurs on the wall at r = R, θ = 0 and $\Omega t = \pi/2$ and is given by Equation (41)

$$p = \rho \frac{\partial \Phi}{\partial t} = \frac{p_w}{\rho g R \left(\frac{X_0}{R}\right)} \quad (41)$$

Where

g – Gravitational acceleration

R – Radius of curvature of the free surface

$\partial\Phi$ – change in potential velocity

∂t – change of potential velocity with respect to the time taken for that change to occur

Xo – the excitation amplitude

ρ – Density of the fluid

p_w – pressure at the top of the wall

p_b – pressure at bottom of tank

The pressure distribution on the bottom at z = -h, $\theta = 0$ and $\Omega t = \pi/2$ and is given by Equation (42)

$$p = \rho \frac{\partial \Phi}{\partial t} = \frac{p_b}{\rho g R \left(\frac{X_0}{R}\right)} \quad (42)$$

According to Ibrahim (2006) and Abramson (1961), Figure 17 illustrates the wall pressure distribution for liquid depth ratio h/R = 2 and for different values of excitation frequency parameter. According to literature provided by Abramson (1961), the lower third of the fluid behaves as a rigid mass, while most of the sloshing effects occur near the surface.

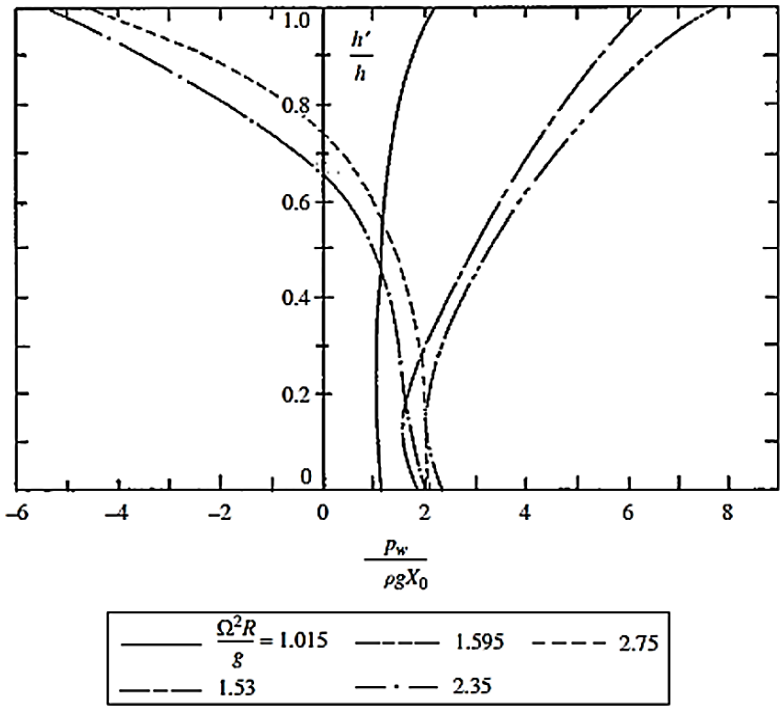

Figure 17. Wall pressure distribution in a circular tank under lateral excitation for h/R = 2 (Ibrahim, 2006)

Abramson (1961) directed a series of experimental tests to compare the analytical results given by Equations (41) and (42) mentioned above with those found experimentally. Note that the analytical results do not include any damping effects.

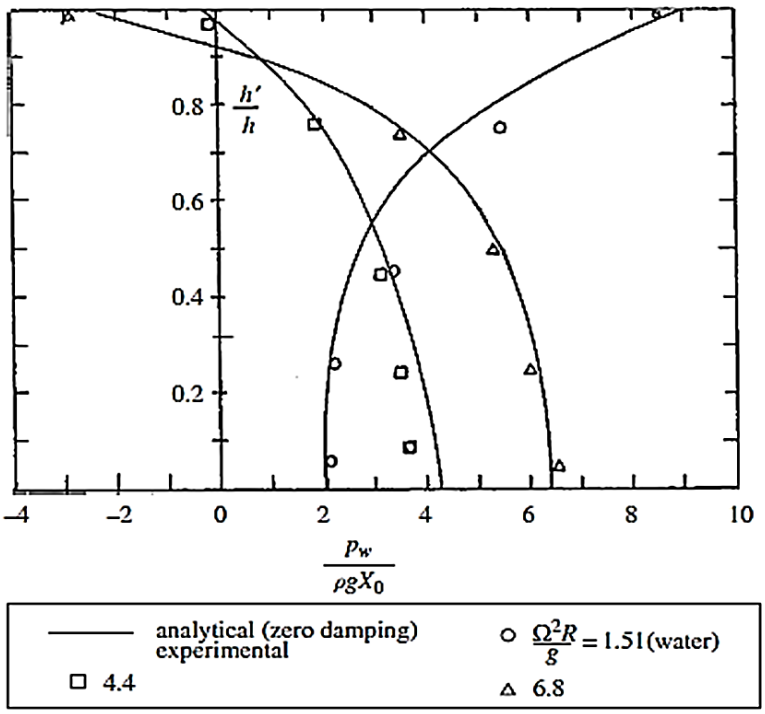

Figure 18. Comparison between analytical and measured wall distribution for h/R = 2. (Ibrahim, 2006)

As seen in Figure 18, an interesting phenomenon occurs over the frequency range between the first mode natural frequency and the frequency at which the net force vanishes. The pressure distributions over the first and second modes indicate that the pressures near the surface are one hundred and eighty degrees (180^{o}) out of phase with those adjacent to the bottom surface.

2.4.3 Nonlinear and Parametric Sloshing Dynamics

2.4.3.1 Weakly nonlinear lateral sloshing

Ibrahim, R. (2006) mentioned that the linear theory for liquid sloshing is acceptable for determining the natural frequencies and wave height of the liquid's free surface. Under translational excitation, the linear theory is useful for predicting the shell's liquid hydrodynamic pressure, forces, and moments. This holds true only when the free surface maintains a planar shape with a nodal diameter that remains perpendicular to the line of excitation, and does not take into consideration the importance of vertical displacement with respect to the centre of gravity of the liquid for large amplitudes of sloshing. Ibrahim (2006) also mentioned that the linear theory fails to predict complex surface phenomena observed experimentally near resonance. These phenomena include the nonplanar unstable motion of the liquid's free surface associated with chaotic sloshing and rotation of the nodal diameter also called rotary sloshing.

According to an investigation done by Abramson and Garza (1965), concerning the nonlinear effects of lateral sloshing in compartmented containers, they concluded that the measured natural frequencies of the liquid's free surface are dependent on the excitation amplitude. Under the hydrodynamic force amplitudes at each resonant peak, the liquid's free surface shape is no longer planar and its upward displacement is larger than the downward displacement. Thus, for excitations near resonance, the nonlinear analysis is essential to determine the shell's hydrodynamic forces. This phenomenon can be uncovered using the theory of weakly nonlinear oscillations for quantitative analysis and the modern theory of nonlinear dynamics for

stability analysis. The main source of nonlinearity in the fluid field equations is contributed by the free surface BCs.

2.4.3.2 Rotary Sloshing

Rotary sloshing for deep liquid retaining structures, Berlot (1960) states that under lateral harmonic excitation, the liquid's free surface may exhibit two types of nonlinearities. The first is large amplitude response, and the second involves different forms of liquid behaviour resulted by instabilities of various sloshing modes. The most important of these is the rotary sloshing, which usually occurs at the lowest sloshing natural frequency.

Weiss and Rogge (1965), reported three types of fluid motion in circular cylindrical tanks:

i. Stable planar.
ii. Stable nonplanar.
iii. Unstable motion near resonance.

Stable planar motion is associated with constant wave height and a stationary single nodal diameter perpendicular to the direction of excitation. Stable nonplanar motion is associated with a constant wave height connected with a single nodal diameter that rotates at a constant rate around the tank vertical axis and an unstable motion near resonance never attains a steady-state harmonic response. The liquid motion displays a softening restoring characteristic in the stable planar motion and a hardening effect in the nonplanar regime.

For rotary sloshing in shallow liquid retaining structures, with low liquid depth, all the liquid takes part in the dynamic response to lateral excitation. There's a critical liquid depth where the free liquid's surface exhibits the ''hard-soft'' spring characteristics of a rotating wave.

2.4.3.3 Dynamics Sloshing Impact

An impulsive acceleration to liquid influences a hydrodynamic pressure impact on the container shell walls. According to Stephens (1965), methods for estimating the liquid impact and its hydrodynamic pressure are not well developed and are only recognised by experimental studies. According to previous experimental studies provided by Stephens (1965) and Ibrahim (2006), they noticed that when hydraulic waves are present, extremely high impact pressures could occur on the container walls. A hydraulic wave occurs when the container undergoes an oscillatory motion when the liquid height is shallow, and the excitation frequency is close to the natural frequency of sloshing.

According to Chester (1964), the hydraulic wave is a nonlinear phenomenon, similar to the shock waves that would be displayed in a one-dimensional gas flow under analogous resonance conditions. Also, the effect of dispersion is to introduce higher harmonics into the spectrum of liquid oscillations. The movement of hydraulic wave affects the stability of liquid retaining structures. Under these conditions, there is a strong coupling between the dynamics of the container and the movement of the hydraulic wave. In the case of deep liquid storage, the flow resonates and hits the top of the tank, which consequences in substantial impact pressure. Sloshing can be more severe longitudinally than laterally if no transverse baffles are introduced. The longitudinal acceleration peaks are more significant than the lateral ones. For some container geometry, the sloshing impact is probably more severe to the structure for longitudinal than for lateral sloshing.

2.4.4 Sloshing Structure Interaction

2.4.4.1 Introduction

Ibrahim (2006) states that the linear theory cannot be used for dynamic analysis of shell elements undergoing elastic deformation that is analogous to its wall thickness and if the liquid's free surface amplitude is large. Nonlinear resonance conditions that cause complex response characteristics will result in the occurrence of nonlinearities within FEA model. The core complications in nonlinear problems of

shell liquid systems is that the boundary conditions are nonlinear knowing that the strain state of an elastic shell and the shape of the liquid's free surface are not known a priori. He also stated that the nonlinear interaction of a liquid shell interaction is a non-classical boundary-value problem and depends on the mechanics of deformable solids, fluid dynamics and nonlinear mechanics.

Experimental work was done by researchers as explained by Ibrahim (2006) and concluded that, under external periodic excitation of cylindrical shells, it was observed that the specific steady conditions of dynamic deformation in which the lines of nodes representing the sloshing wave moves in the azimuthal direction with respect to time. Analytically, the dynamic deflection of the shell is usually represented as a single standing wave, considered in combination with an axisymmetric form with twice the number of harmonics along the shell surface generator. The presence of an axisymmetric form must be reflected by predominant inward deflection.

2.4.4.2 General Equations of Motion

Using Donnell's nonlinear theory of shallow shells that is based on the assumptions of neglecting in-plane inertia, transverse shear deformation and rotary inertia, the governing equation for large deformation is shown in Equation (43).

$$D\nabla^4 w + c\hat{t}\dot{w} + \rho_c \hat{t}\ddot{w} = \frac{1}{R}\frac{\partial^2 F}{\partial z^2} + \frac{1}{R^2}\left(\frac{\partial^2 F}{\partial \theta^2}\frac{\partial^2 w}{\partial z^2} - 2\frac{\partial^2 F}{\partial z \partial \theta}\frac{\partial^2 w}{\partial z \partial \theta} + \frac{\partial^2 F}{\partial z^2}\frac{\partial^2 w}{\partial \theta^2}\right) + f(t) - p - N_z(t)\frac{\partial^2 w}{\partial z^2} \quad (43)$$

where;

$$D = \frac{E\hat{t}^3}{12(1-\nu^2)} \quad \& \quad N_z(t) = N_0 + N(t) \quad (44)$$

where

ω– sloshing frequency

z – axial dimension

R – radius of curvature of the free surface

θ – angular coordinate

t – time

E = Young's modulus

Figure 19 illustrates a partially filled shell container (with reference coordinates z, r, θ) with an incompressible fluid to a depth h.

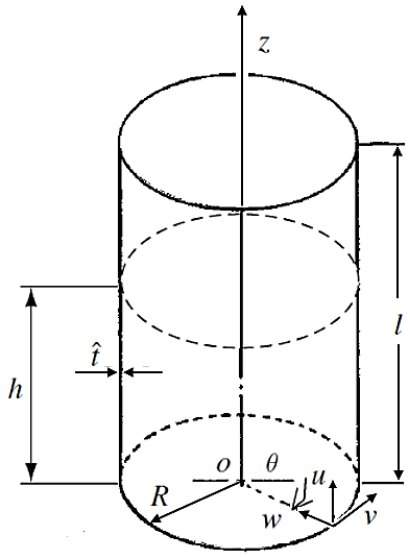

Figure 19. Partially filled Cylindrical Container. (Ibrahim 2006)

The origin, O placed at the centre of container base and the displacement of a point on the middle surface of the shell are denoted as u, v, w in the axial, z, circumferential, θ, and radial, r, directions, respectively. The radial displacement, w, is taken to be positive towards the shell centre. The applicability of Donnell's theory is dependent on the following statement, shell thickness, t, must less than the shell radius, R.

where;

$$D = \frac{E\hat{t}^3}{12(1-\nu^2)} \quad \& \quad N_z(t) = N_0 + N(t) \tag{45}$$

where;

D = flexural rigidity

E = Young's modulus

Y = Poisson's ratio

ρc = shell density

c = damping coefficient

p = internal hydrodynamic pressure acting on the wetted wall

f(t) = external excitation acting on the shell

Nz (t) = dynamic excitation acting along the shell edges

In Equation (43), the dot denotes differentiation with respect to time, and F is the in-plane stress function obtained by solving Equation (45).

$$\frac{1}{E\hat{t}}\nabla^4 F = \frac{1}{R}\frac{\partial^2\omega}{\partial z^2} + \frac{1}{R^2}\left(\left[\frac{\partial^2\omega}{\partial z\partial\theta}\right]^2 - \frac{\partial^2\omega}{\partial z^2}\frac{\partial^2\omega}{\partial\theta^2}\right) \tag{46}$$

where

$$\nabla^4 = \left(\frac{\partial^2}{\partial z^2} + \frac{1}{R^2}\frac{\partial^2}{\partial\theta^2}\right)^2 \tag{47}$$

where

ω– sloshing frequency

z – axial dimension

R – radius of curvature of the free surface

θ – angular coordinate

t – time

E = Young's modulus

2.5.2.3 Parametric Excitation of a Shell-Liquid System

As stated by Ibrahim (2006), the modal equations of motion can take the form of Equations (48) and (49) and used the averaging method to determine the steady-state response A and B as shown in Equations (50) and (51).

$$\ddot{A} + (\omega_1^2 - N\cos\Omega t)A + \gamma_1(A^2 + B^2)A = 0 \tag{48}$$

$$\ddot{B} + (\omega_1^2 - N\cos\Omega t)B + \gamma_1(A^2 + B^2)B = 0 \tag{49}$$

$$A(t) = a(t)\cos\left(\frac{\Omega}{2}t + \vartheta_1(t)\right) \tag{50}$$

$$B(t) = b(t)\cos\left(\frac{\Omega}{2}t + \vartheta_2(t)\right) \tag{51}$$

where

$$N = \frac{N_z \left(\frac{m\pi}{l}\right)^2}{\rho_c (1 + m_{01})} \tag{52}$$

and

N_z – in-plane restraint stresses generated at the end of the shell

ω – sloshing frequency

Ω – the frequency of the tank motion

h – upper level of liquid volume

t – time

m – sloshing mass

ϑ – angular coordinate

γ – surface tension

ρ – density of the fluid

This method results in two possible solutions. The unimodal response a and b are shown as Equations (53) and (54).

$$a^2 = -\frac{4}{3\gamma_1}\left\{\omega_1^2 - \frac{\Omega^2}{4} \pm \frac{N}{2}\right\}, \qquad b = 0 \tag{53}$$

$$b^2 = -\frac{4}{3\gamma_1}\left\{\omega_1^2 - \frac{\Omega^2}{4} \pm \frac{N}{2}\right\}, \qquad a = 0 \tag{54}$$

The mixed mode response a and b are as Equations (55) and (55).

$$a^2 = -\frac{1}{\gamma_1}\left\{\frac{\Omega^2}{4} - \omega_1^2 \mp N\right\} \tag{55}$$

$$b^2 = -\frac{1}{\gamma_1}\left\{\frac{\Omega^2}{4} - \omega_1^2 \pm N\right\} \tag{56}$$

The domain of existence of this solution is bounded by the frequency band as shown in Equation (57).

$$\Omega < \Omega^* = 2\sqrt{\omega_1^2 - N} \tag{57}$$

2.4 Numerical Analysis

2.4.1 Introduction

Currently, numerical simulation is being utilised for solving complex Finite-difference methods (F-DM) and Finite Element Methods (FEM) complications in engineering and science by conducting experimental investigations and examining theories to provide knowledge on complex dynamic analysis and can even contribute to the discovery of a new theory. F-DM and FEM are numerical grid methods, which solve complex Computational Fluid Dynamics (CFD) and Computational Solid Mechanics (CSM) problems. The significant consequences of these grid-based methods are based on the time taken to create and regenerate the mesh which is a costly process especially when required to regenerate a quality mesh for accurate analysis with respect to problems with free surfaces, deformable boundary, moving interface (for FDM) and tremendously large deformation (for FEM).

Liu and Liu (2009), mentioned that meshfree methods are being used to solve complex engineering problems and in time will be superior to conventional grid F-DM and FEM in many applications. One of the modelling techniques utilises a FEM software (ABAQUS) where the Smoothed Particle Hydrodynamics (SPH) method would be adopted. The reasons for this method are listed as follows:

i. SPH is capable of producing accurate results about problems with a free surface, deformable boundary, moving interface as well as large deformation.

ii. Previous research and enhancements to the SPH method increased the accuracy of results and stability of model have reached a threshold level for investigating the complex complications, especially for the phenomena of sloshing.

2.4.2 Meshing Methods for Numerical Fluid-Structure Analysis

There are several techniques used to determine the complexity of fluid-structure interaction problems. As mentioned by Papadrakakis *et al.* (2011), the following non-linear finite element techniques, can cope with large deformations of the liquid's free surface. The structure, hence generating precise results for the hydrodynamic pressures due to impulsive fluid motion effects and seismic impacts within the internal wall and roof. In some instances, some methods cannot cope with large deformations.

2.4.2.1 Smooth Particle Hydrodynamics Method

A finite element technique to analyse fluid-structure complications is called the Smooth Particle Hydrodynamics (SPH) method, which is a meshless Lagrangian procedure, used to model the liquid conditions under applied motion. In this method, the fluid region is represented by particles, which convey information about mass conservation, hydrodynamic and thermodynamic performance. Since this is a meshless technique, problems that involve large-amplitude fluid motion and complex geometries can be solved very easily producing more accurate results as opposed to the grid numerical methods mentioned in the previous section, without having the limitations of volumetric meshing. This method is computationally expensive for both memory and CPU time because analysis requires a large number of particles to simulate the actual phenomena of FSI problems. The more particles modelled the result accuracy will increase.

Complications in CFD are commonly solved by the conventional grid numerical methods such as the FEM, F-DM and Finite Volume Method (FVM). Liu and Liu (2009) mentioned that the critical feature of these techniques is a grid that corresponds to the Eulerian Algorithm (for F-DM and FVM) or Lagrangian Algorithm (for FEM) that is essential for the computational structure to provide spatial discretisation for the governing equations.

The problems concerning significant mesh element distortion, moving material interfaces, deformable boundaries and free surfaces cannot be resolved by FEM and the Eulerian methods. As a result attempts have been made to combine features of the F-DM and FEM by using CEL and ALE which are two-grid systems. In these methods, the computational information is replaced by mapping or a distinct interface treatment among the two types of grids. These approaches are complicated but work well for numerous problems. However, they can cause a level of inaccuracy in numerical analysis for the mapping process.

Brackbill *et al.* (1988) mentioned that the SPH method is used to simulate complex dynamic fluid flows. Liu and Liu (2009) explained that by discretising the Navier-Stokers equations spatially, the SPH formulation derived would contain several ordinary differential equations with respect to time, which can then be solved through time integration calculations. This method can, therefore, treat large deformation, tracking moving interfaces or free surfaces and obtaining the time history of the field variables due to its pure Lagrangian nature.

In this chapter, the SPH approximations are given, which comprise the strategy of the SPH method, the kernel approximation and the discretised particle approximation.

2.4.2.2 SPH Concept

The SPH procedure can understand hydrodynamics intricacies whose arrangement appear as a Partial Differential Equations (PDE) for field factors such as the density, velocity and energy. Acquiring expository solutions for such an arrangement of PDEs is not frequently conceivable, aside from not very many straightforward cases. For numerical arrangements, one needs first to discretize the problem area where the PDEs are characterised so that the technique can give an estimate to the estimations of the field capacities and their derivatives at any point.

The function approximation is then applied to the PDEs to create an arrangement of ODEs in a discretised form with respect only to time. This arrangement of discretised ODE can then be solved utilising one of the standard integration procedures of the conventional FDM.

In the SPH strategy, the accompanying vital thoughts are utilised to accomplish the previously mentioned task.

i. **Meshfree –** The problem space is represented by an arrangement of subjectively appropriated particles if the area is not yet as particles. No connectivity for these particles is required.

ii. **Integral function representation** – The integral representation procedure is used for field function estimations. In the SPH method, this is designated as the kernel approximation.

iii. **Compact support** – The kernel approximation is then further approximated using particles. In the SPH method, this is designated as particle approximation. This process is carried out by replacing the integration in the integral representation of the field function and its derivatives with summations over all the comparing values at the neighbouring particles in a local domain called the support domain.

iv. **Adaptive** – The particle estimation is completed at every time step, and consequently, the utilisation of the particles relies upon the present local appropriation of the particles.

v. **Lagrangian** – The particle estimations are performed to all related field functions terms in the PDEs to produce a set of ODEs in a discretised form with respect to just time.

vi. **Dynamic** – The ODEs are then solved using an explicit integration process to achieve fast time stepping to obtain the time history of all the field variables for all the particles.

2.4.2.3 SPH Formulation

2.4.2.3.1 Kernel Approximation of a Function

The SPH formulation consists of two essential steps where the first step relating to the kernel approximation of field equations and the other relating to the particle approximation of the equation. During the first step of the SPH formulation in finite element analysis, integration of an arbitrary equation and smoothing kernel equation produces an integral representation of the kernel approximation of the SPH function. The integral representation of this function is computed based on nearby interacting particles, which then results in the particle approximation of the SPH function of a discrete particle within the model.

As explained by Liu and Liu (2009), the kernel approximation of a function f(x) is illustrated as Equation (58).

$$< f(x) >= \int_{\Omega} f(x')\, W(x - x', h) dx \tag{58}$$

where

< > – angled brackets represent the kernel approximation operator

f – function of the three-dimensional position vector x

Ω – volume of the integral that contains x

W – smoothing kernel function.

x – three-dimensional position vector

In the smoothing kernel function, h, is the smoothing length defined by the influenced area of the smoothing kernel function, W. According to Monaghan (1992), a suitable kernel must have the following two properties illustrated in Equation 78 and Equation 79, where, W should be an even function and satisfy unity (Equation (59)), Delta function property (Equation (60)) and the compact condition (Equation (61)).

$$\int_{\Omega} W(x - x', h) dx' = 1 \tag{59}$$

where

Ω – volume of the integral that contains x

W – smoothing kernel function

h – the smoothing length

x – three-dimensional position vector

$$\lim_{h\to 0} W(x-x',h) = \delta\,(x-x') \tag{60}$$

where

δ – Dirac delta function = $\delta(x-x') = \begin{cases} 1 & x=x' \\ 0 & x\neq x' \end{cases}$

$$W(x-x',h) = 0\ when\ \ |x-x'| > kh \tag{61}$$

where

k – is the constant of the smoothing function for a point, x, and defines the effective area of the smoothing kernel function.

2.4.3 Smoothing Kernel Function

Liu and Liu (2009) mentioned that the smoothing function plays a significant role in the SPH estimations because this determines the accuracy of the kernel approximation and efficiency of the computation.

2.4.3.1 Quadratic Smoothing Kernel Function

Johnson *et al.* (1996) used the following quadratic smoothing kernel function as illustrated in Figure 20 and Equation (62) to simulate the high-velocity impact problem.

$$W(R,h) = \alpha_d\left(\frac{3}{16}R^2 - \frac{3}{16}R + \frac{3}{4}\right) \qquad 0 \le R \le 2 \tag{62}$$

where

R – the relative distance between two particles at points x and x' = $R = \frac{r}{h} = \frac{|x-x'|}{h}$

r – the distance between the two points

α_d – with respect to one, two and three-dimensional space.

$$\alpha_d = \frac{1}{h} \quad , \alpha_d = \frac{2}{\pi h^2} \quad , \alpha_d = \frac{5}{4\pi h^3}$$

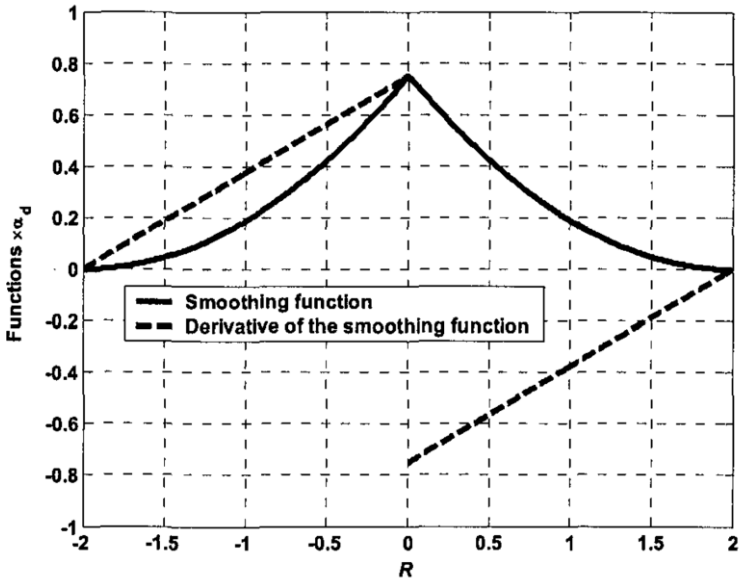

Figure 20. The quadratic smoothing function and its first derivatives. (Johnson et al. 1996)

Johnson *et al.* (1996) mentioned that the difference with this smoothing function to the other smoothing functions proposed in the past is that the derivatives of the quadratic smoothing kernel function increases as the particles move closer, and decreases as the particles move apart hence resolving the problem of compressive instability and producing more accurate results with respect to numerical simulations.

2.4.4 Particle Approximation

Since the entire model of the problem, the domain is represented by a finite number of particles, the particle approximation, which is an essential operation to provide accurate information for mass, individual space occupied. The equivalent discretised process of summation of the particles is generally known as particle approximation in most SPH literature.

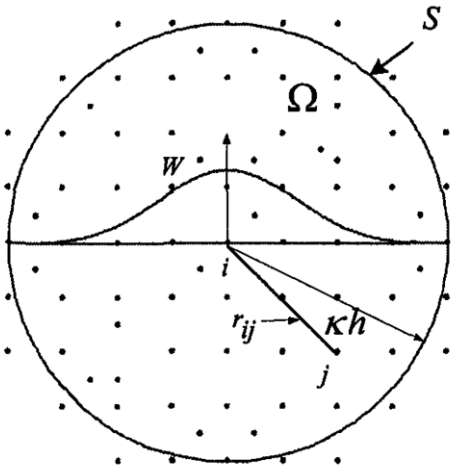

Figure 21. Particle approximations using particles within the support domain of the smoothing function W for particle i. (Liu and Liu 2009)

According to Liu and Liu (2009), understanding Figure 21, equation (63) states that the value of a function at the particle, i, is approximated using the average of those values of the function at all the particles in the support domain of particle, i, weighted by the smoothing kernel function. The particle approximation for a function at the particle, i, is written as:

$$< f(x_i) >= \sum_{j=1}^{N} \frac{m_j}{\rho_j} f(x_j).W(x_i - x_j, h) \qquad (63)$$

where

< > – angled brackets represent the kernel approximation operator

f – function of the three-dimensional position vector x

W – smoothing kernel function

x – three-dimensional position vector

j – the location of a particle

ρ_j – density of the particle

N – is the number of particles within the support domain of particle j

m_j – mass of the particle

2.4.5 Lagrangian Navier-Stokes Equations

The governing equations of fluid dynamics are based on the subsequent three fundamental physical laws of conservation.

i. Conservation of mass
ii. Conservation of momentum
iii. Conservation of energy

The physical governing equations are described by two methods known as the Eulerian and Lagrangian algorithm where one is a spatial description, and the other is a material description respectfully. According to Liu and Liu (2009) study, the fundamental difference between these two descriptions is that the Lagrangian algorithm uses the total time derivative as the combination of local derivative and convective derivative.

The SPH governing equations (64) to (66) for dynamic fluid flows are partial differential Navier-Stokes equations in the Lagrangian algorithm, which states the conservation of mass and momentum and energy. The superscripts α and β are used to denote the coordinate directions, the summation in the equations is taken over repeated indices, and the total time derivatives are taken in the moving Lagrangian frame.

The Continuity Equation:

$$\frac{D_\rho}{D_t} = -\rho \frac{\partial v^\beta}{\partial x^\beta} \tag{64}$$

where

σ – total stress = $\sigma^{\alpha\beta} = -p\delta^{\alpha\beta} + \tau^{\alpha\beta}$

τ – viscous stress = $\tau^{\alpha\beta} = \mu\varepsilon^{\alpha\beta}$

p – isotropic pressure

α and β – used to denote the coordinate directions

The Momentum Equation:

$$\frac{D_\rho}{D_t} = -\rho \frac{\partial v^\beta}{\partial x^\beta} \tag{65}$$

The Energy Equation:

$$\frac{De}{D_t} = \frac{\sigma^{\alpha\beta}}{\rho} \frac{\partial v^\alpha}{\partial x^\beta} \tag{66}$$

For Newtonian fluids, the viscous shear stress is relative to the shear strain rate denoted by ε through the dynamic viscosity μ.

Where

$$\varepsilon^{\alpha\beta} = \frac{\partial v^\beta}{\partial x^\alpha} + \frac{\partial v^\alpha}{\partial x^\beta} - \frac{2}{3}\left(\frac{1}{\delta V}\frac{D(\delta V)}{Dt}\right)\delta^{\alpha\beta} \tag{67}$$

And: δV – the infinitesimal fluid cell control volume

2.4.5.1 SPH formulations for Navier-Stokes Equations

2.4.5.1.1 Approximation of Particle Density

The approximation of the particle density is essential with the SPH method since the density controls the particle distribution and smoothing length evolution. The approach of particle approximation for density is the continuity density, which approximates the density according to the continuity equation using the concepts of SPH approximations plus some transformations. Transformation of the right-hand side (RHS) of the continuity Equation (66) leads to the formulation of the **conservation of mass** Equation (68) as illustrated by Liu and Liu (2009).

$$\frac{D_{\rho_i}}{D_t} = \rho_i \sum_{j=1}^{N} \frac{m_j}{\rho_j} v_{ij}^{\beta} . \frac{\partial W_{ij}}{\partial x_{ij}^{\beta}} \tag{68}$$

where

$$v_{ij}^{\beta} = (v_i^{\beta} - v_j^{\beta}) \tag{69}$$

and

W – smoothing kernel function

j – the location of a particle

ρ_j – density of the particle

N – is the number of particles within the support domain of particle j

m_j – mass of the particle

α and β – used to denote the coordinate directions

v – velocity

2.4.5.1.2 Approximation of Particle Momentum

Liu and Liu (2009) derived the equation by directly applying the SPH particle approximation concepts to the gradient on the RHS of the momentum Equation (65) which results in the conservation of momentum Equation (70). The advantage of this equation is that it decreases errors arising from the problem of particle inconsistency.

$$\frac{Dv_i^{\alpha}}{Dt} = \sum_{j=1}^{N} m_j \frac{\sigma_i^{\alpha\beta} + \sigma_j^{\alpha\beta}}{\rho_i \rho_j} \frac{\partial W_{ij}}{\partial x_i^{\beta}} \tag{70}$$

where

σ – total stress = $\sigma^{\alpha\beta} = -p\delta^{\alpha\beta} + \tau^{\alpha\beta}$

τ – viscous stress = $\tau^{\alpha\beta} = \mu\varepsilon^{\alpha\beta}$

p – isotropic pressure

α and β – used to denote the coordinate directions

W – smoothing kernel function

j – the location of a particle

ρ_j – density of the particle

N – is the number of particles within the support domain of particle j

m_j – mass of the particle

v – velocity

μ – dynamic viscosity

2.4.5.1.3 Approximation of Particle Energy

The energy equation depends on the conservation of energy, which illustrates the first law of thermodynamics. The equation expresses that the change of time with respect to the change of the rate of energy inside a minuscule liquid particle should equal to;

i. The sum of net heat flux into the fluid particle.
ii. The time rate of work done by the body and surface forces acting on the particle.

If neglecting the heat flux, and the body force, the time rate of change of the internal energy, e, of the minuscule liquid particle consists of the following two parts.

i. The work done by the isotropic pressure multiplying the volumetric strain.
ii. The energy dissipation due to the viscous shear forces.

Therefore, the particle energy equation can be written as follows;

$$\frac{De_i}{Dt} = \frac{1}{2}\sum_{j=1}^{N} m_j \frac{p_i + p_j}{\rho_i \rho_j} v_{ij}^{\beta} \frac{\partial W_{ij}}{\partial x_i^{\beta}} + \frac{\mu_i}{2\rho_i} \varepsilon_i{}^{\alpha\beta} \varepsilon_j{}^{\alpha\beta} \tag{71}$$

where

σ – total stress = $\sigma^{\alpha\beta} = -p\delta^{\alpha\beta} + \tau^{\alpha\beta}$

τ – viscous stress = $\tau^{\alpha\beta} = \mu\varepsilon^{\alpha\beta}$

p – isotropic pressure

α and β – used to denote the coordinate directions

W – smoothing kernel function

j – the location of a particle

ρ_j – density of the particle

N – is the number of particles within the support domain of particle j

m_j – mass of the particle

v – velocity

ε – strain rate

μ – dynamic viscosity

The method chosen to analyse fluid-structure complications of this investigation is the Smooth Particle Hydrodynamics (SPH) method. Since this is a meshless technique, problems that involve large-amplitude fluid motion and complex geometries can be solved very easily producing more accurate results as opposed to the grid numerical methods, without having the limitations of volumetric meshing. This method is computationally expensive with respect to both memory and CPU time because analysis requires a large number of particles to simulate the actual phenomena of FSI problems. The more particles modelled the result accuracy will increase. For this reason, this method will be adopted as the methods for the FEA analysis to investigate dynamic sloshing of the QSD.

2.5 The Mechanical Properties of 3D Polymers

2.5.1 Introduction

The Mechanical properties investigated in this study are those commonly considered in structural members. These properties are strength, ductility, hardness, impact resistance and fracture toughness. Most structural materials show anisotropic properties; it was observed that the mechanical properties of a component would differ depending on the type of manufacturing process used to produce the component. This review focuses on the type of manufacturing process known as additive manufacturing (AM) or more commonly referred to as 3D-printing (3DP). AM is a process where the material is added to the desired location, building up the desired shape in layers rather than cutting from a larger piece of material. This type of manufacturing opens several design possibilities. FDM is a type of AM which allow for manufacturing of complicated geometries with ease, by simple means of developing a CAD drawing. The CAD file is converted

to a compatible file format, sliced and prepared to be printed on available platforms. 3D-printers based on fused deposition modelling principles are commonly available platforms that offer a user-friendly interface and produce relatively accurate print jobs. FDM works by feeding polymer materials through an extrusion nozzle that heats the material to a semi-liquid form that is then deposited along the extrusion path. The word fused explains the bonding process that the polymer material undergoes as the newly deposited material is placed on previous layers (Berman, 2015).

Most FDM platforms are limited to polymer materials, hence the interest in developing new polymer composites for use in structural applications. Polymers are modern materials developed from crude oil and natural gas, which are produced in large amounts. The raw materials used to make polymers are low-molecular-weight substances (Kratochvil, 1989). Making these materials worth considering for use in structural applications due to their strength to weight ratio. Polymers are also available as composite materials. These are materials that use a polymer base resin as its matrix and are reinforced by fibres or other additives. The result is the change of the mechanical properties as discussed in Torrado, (2015) and Gray IV, (1998).

Prediction of material behaviours under different types of loading is of high importance in structural design. Structural engineers must be able to predict these behaviours to ensure that their designs meet the required design standards. An exact type of analysis used to achieve this is Finite Element Analysis method (FEA). FEA has been used by Henry, (1985) to study the performance of glass-reinforced bridge decks of different configurations. The study indicated that the design is almost always controlled by the deflection limit state rather than the strength limit state. This information proved to be accurate and is still used when designing fibre reinforced polymer systems to date. In this review, the use of FEA software gave some accurate approximations of strength, stiffness and stability behaviours of FDM manufactured components found in studies by Rodriguez, (2003). Tensile, compression and dynamic test have been simulated using FEA software utilising information obtains from experimental research by Sayre, (2014). This paper reviews the previous research done to analyse the applicability of 3DP polymers for structural engineering applications.

2.5.2 Fused deposition technology

The concept of fused deposition printing originates in the way the technology constructs geometries. The process uses polymer-based materials which are fused to form one solid object. The word fused describes how the extruded layers bond to each other. There are two elevations in temperatures to consider when using this technology, the glass transition temperature (Tg) and the melting temperature (Tm). Tg is the temperature in which a polymer material cools and becomes hard. Tm is the temperature where the polymer material melts to become liquid. These temperatures differ among polymers and do show a relationship between their mechanical properties (Stansbury, 2015; Torrado, 2014). However there are some defects discovered in parts printed using FDM technology as observed by Tekinalp, (2014), who found triangular void formation along the build direction of 3D-printed ABS material caused by the elliptical shape of the extruded filament. Tekinalp stated that the deformation occurred during the transition from the Tm to Tg, which caused the top of the filament to form round edges. This manufacturing flaw may contribute to the anisotropic properties of the 3D-printed polymer.

Hossain *et al.* (2013), found that by modifying the build parameters of FDM technology leads to the reduction in the gaps formed like the ones in Tekinalp's research. Their research focused on obtaining a method in which to modify build parameters to improve the mechanical properties of Polycarbonate (PC) specimens. This research showed that by modifying build parameters flaws in the 3DP-polymers can be reduced, which gives FDM technology potential in structural applications. The build parameters modified in this research were raster angle (RA), raster width (RW), contour width (CW), raster to raster air gap (RRAG) and layer height as seen in Figure 22.

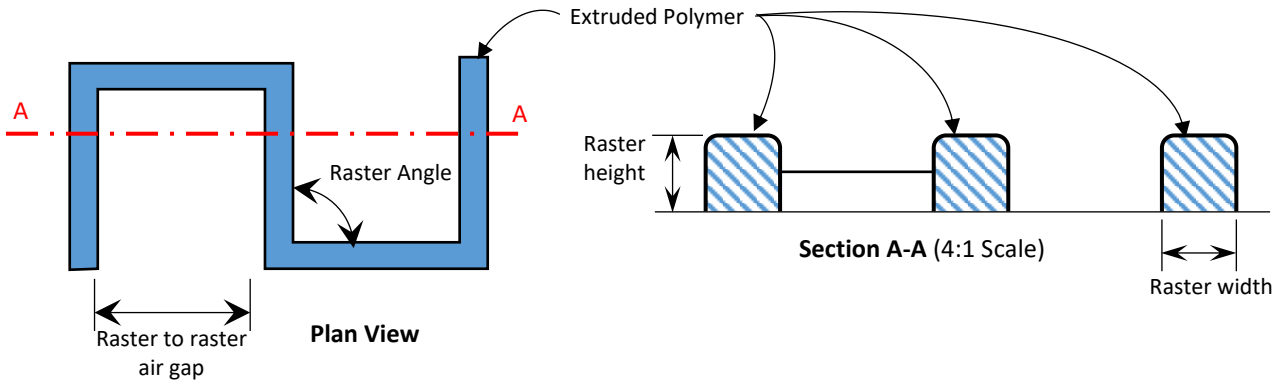

Figure 22. Build parameters in FDM platforms adapted from Hossain *et al.* (2013)

Two methods for modifying build parameters which involved considering the tool path operations and examining low-magnified optical images were developed. These modifications were then named Insight revision method and Visual feedback method; the layer height was set at 0.254 throughout the experiment. The 3DP platform used was a Fortus 900 mc with a build chamber of 914mm ×610 mm × 914 mm. Table 3 shows the parameters used in this study.

Table 3. Modified build parameters (Hossain et al. 2013)

Build orientation	**Raster angle**	**Default Parameter (mm)**			**Insight revision method (mm)**			**Visual feedback method (mm)**		
		CW	**RW**	**RRAG**	**CW**	**RW**	**RRAG**	**CW**	**RW**	**RRAG**
XYZ	0º/90º	0.508	0.508	0	0.432	0.432	0	0.432	0.432	-0.013
	30/-60	0.508	0.508	0	0.432	0.432	0	0.432	0.432	-0.013
	45/-45	0.508	0.508	0	0.432	0.432	0	0.432	0.432	-0.013

The visual feedback method showed the most promising results with the introduction of negative raster to raster air gap (RRAG). The modification led to the removal of air gaps in the specimen tested. These parameters can be used when modelling geometries for structural application as they resulted in an overall increase in the ultimate tensile strength (UTS) of the samples. Negative RRAG were also proven to be successful in increasing the tensile strength of ABS material as conducted in previous studies by Ahn et al. 2002, who used RRAG of -0.003 in with a raster angle (RA) of 0º/90º which showed an increase in UTS of about 30%. The author explained that negative RRAG led to the production of denser structures which increased UTS. However in a similar study conducted by Sood, (2010) revealed that a reduction in UTS of about 19% was observed when the RA was changed from 30º/-60º to 90º/0º. The reason for this reduction as stated by the author was that at 90º/0º RA the longest rasters were produced which developed an accumulation of stress along that direction resulting in distortion and weak bonding. This was reflected in

Hossain, (2013) study which showed relative increases in UTS using modified parameters that can be seen in Table 4.

Table 4. Percentage of relative UTS increases from that of the default method (Hossain, 2013)

Raster angle	Insight revision method	Visual feedback method
0°/90°	4%	15%
30°/-60°	6%	19%
45°/-45°	5%	13%

The visual feedback method showed the highest increase in UTS when using RA of 30°/-60°. These results reflect the previous research done by Ahn (2002). However, not much comparison was made in this study that showed any difference in the mechanical properties when varying the layer thickness. This information is essential for structural application in that it determines the build time of components. Sood (2010) mentioned that by changing the layer thickness from 0.127 mm to 0.254 mm, no significant changes to the UTS were observed. However, this is not true when comparing the results of Sayre (2014) who tested Acrylonitrile Butadiene Styrene at 2 mm layer thickness and 4mm layer thickness and saw that there was a change in the tensile strength of 4,307 psi and 4,090 psi respectively. This was backed by Hossain, (2013) who stated that the lack of difference of UTS in Sood (2010) study was a result of changing RA's in successive layer thickness, resulting in a delta angle being the change of RA's between adjacent layers. Saying that *"the directional effect of one layer might be nullified by the delta angle of the adjacent layer"*.

2.5.2.1 Fuse deposition polymer resins

Most FDM printers are capable of reaching temperatures of up to 300° C; this results in a limit to the type of polymer materials compatible with FDM technology. The most common materials available are ABS and Poly-lactic Acid (PLA). Over the years, new materials have been advanced to exhibit dimensional stability, relatively low glass transition and melting temperatures that can be compatible with the FDM platform. Materials like Polycarbonate and Polyvinyl Alcohol (PVA) are some of these materials (Torrado, 2014). Table 5 shows the relative temperatures of these materials.

Table 5. Tg and Tm for FDM compatible polymers. (Schimd, 2008)

Material name	Tg (ºC)	Tm (ºC)
ABS	110	-
PLA	60	175
PC	145	230-260
PVA	85	170

The effect that these temperatures have on polymer materials deserves some attention; the Tg affects how the parts shrink as the material solidifies. This effect may contribute to warp and warping may lead to the anisotropic behaviour of 3DP polymers. The Tm, on the other hand, contradicts the extrusion temperature (Te) of the FDM utilised platform. This determines the ease of extrusion, the difference between the Te and the Tg give us an idea of the time taken for the extruded material to solidify (alternatively affecting the print time).

Among the polymers chosen, ABS and PC show the highest mechanical properties in terms of toughness and ductility. ABS has an Ultimate tensile strength (UTS) in the range of about 28-55Mpa and PC of about 55-70Mpa (Schimd, 2008). When compared to that of traditional structural materials like grade 36 steel which UTS is about 200 GPa, It may seem challenging to characterise applications for these polymer materials. However, this characteristic alone does not fully define the usefulness of these materials. Among the advantages of polymer materials are their resistance to corrosion, strength to weight ratio and modification capabilities. All of which are desirable characteristics of structural materials. Due to these characteristics, polymers have some applications as structural materials such as armour in the defence industry where the need for lighter, stronger and more durable components are appropriate (Wu, 2006). However, these applications are for traditional manufacturing processes and not necessarily FDM technology which does show some strength limitations associated with 3DP polymers. One way to solve these limitations is the development of Polymer Matrix Composites (PMC). PMC's are polymer-based materials reinforced with particles or fibres such as iron particles or glass fibres. By using FDM compatible polymers as the matrix material and reinforcing with fibre or glass composites a change in the mechanical properties is obvious. Blends of ABS and PC can be used as the composite matrix due to their compatibility with FDM platforms and their relatively easy and cheap production process. It can be seen that 3DP polymer

composites are not only limited to improving material strength; it can also be modified to exhibit specific characteristics such as being flame-retardant.

To further improve the strength characteristics of 3DP components, the development of new materials designed to display high levels of isotropic properties may serve as a viable solution. Research by Torrado, (2015), examined a total of six additives to ABS in an attempt to reduce the anisotropic mechanical properties found in FDM printed specimens. The best results in terms of anisotropic reduction were found in the blend of ABS with styrene ethylene butadiene styrene (SEBS) and ultra-high molecular weight polyethylene (UHMWP). However, even though the results showed a reduction in the anisotropic properties of the polymer blend of 75:25:10 by weight ratio of ABS: UHMWPE: SEBS. This came at the expense of the ultimate tensile strength UTS, which resulted as (14.7+/- 0.63 MPa) as opposed to (33.96 +/-1.74 MPa) for sample printed in ABS alone. The anisotropic reduction was determined by examining the samples which show that failure occurred within the printed raster and not at the raster to raster boundary. This discovery may prove useful for the development of polymer matrices that display low levels of anisotropy. These matrices can then be reinforced to increase the tensile properties hence generally producing FDM compatible material with desirable mechanical and physical properties.

2.5.2.2 Reinforced polymer for fused deposition technology

Reinforced polymers are commonly known as polymer composites. These composites are usually a combination of low cost, lightweight and environmentally resistant polymer matrices with high strength and high stiffness fibres (e.g. as glass, carbon or aramid fibres). These advanced engineering materials used in structural applications such as bridges, piers, and retaining walls exposed to salts and chemicals. Their application has proven to be efficient due to their light-weight, corrosion resistance and high energy absorptions capabilities (which makes them suitable for seismic applications). They also hold an economic advantage based on load capability per unit weight which is said to eliminate transportation issues, high labour cost and energy consumption according to Head, (1996).

Tekinalp, (2014) and Zhong, (2001) Investigated the potential for using short fibre (0.2–0.4 mm) reinforced ABS composites for the production of load-bearing components using FDM technology. The samples produced using FDM technology was compared with the conventional technique, Compression Moulding Process (CMP). Their study aimed at revealing the improvements needed for both the FDM technology and compatible polymer material to produce high-quality structural components. Mixtures of ABS with Chopped Hexcel AS4 carbon fibres; 10, 20, 30, and 40% weight ratio (wt.) were tested using ASTM D638 type-V dog-bone. The results acquired showed a dramatic increase in both modulus and tensile strength with the specific strength reaching (52.9 kN m/kg) higher than Aluminium 6061-0 which is (45.9 kN m/kg). This result shows that there is potential for FDM technology in structural applications. Voids within the FDM-printed beads increased relative to an increase in fibre content while voids between the beads decreased. These voids/gaps may lead to high concentration of stress formation at their location causing the component to fail at lower stresses. FDM-printed samples showed lower porosity and high fibre orientation in the printing direction "coming close to perfect orientation" as stated by Tekinalp, (2014). However, the CM specimens showed higher results in comparison to the FDM samples, proving that porosity controls over fibre orientation. The same study showed that fibres had pulled out of the matrix, indicating a poor interfacial connection between the fibres and the matrix as seen in Figure 23.

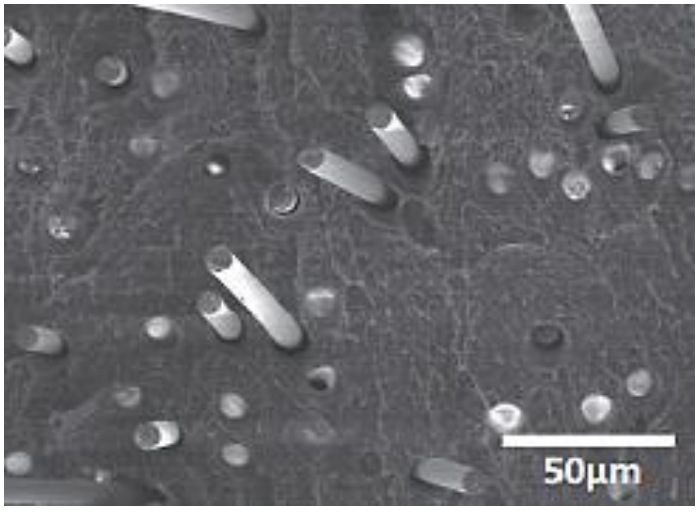

Figure 23. Fibres pulled out following failure. (Tekinalp, 2014)

This study revealed that the FDM process displays high fibre orientation and excellent dispersion capabilities. It also showed that by using fibre reinforcements with ABS has dramatically improved the tensile capabilities of the specimens and hence shows that the process has the potential for application in the production of structural members.

Tekinalp, (2014) made suggestions to further improve the FDM process by stating that, pore formation during printing and fibre breakage during compounding must be minimised, as well as improving bonding between fibres and matrix through surface modification.

2.5.3 Experimental work

The use of 3D-printed fused deposited ABS polymer for structural applications depends significantly on the strength of the polymer after extrusion. Rodríguez, (2001) conducted studies on these properties of fused deposited ABS polymer. Tensile and torsional tests were performed on specimens of ABS monofilament feedstock. The tensile tests were conducted on specimens with a length of 380mm using a screwdriven load frame at constant crosshead speeds ranging from 0.00381mm/s to 0.381 mm/s providing strain rates in the range of 10±5 to 10±3 l/s. Tensile modulus, E, strength, σys, and strain, εs, values were obtained from the stress-strain data. E corresponds to the slope of the stress-strain curve at zero strain, σys is taken as the maximum stress reached during the test (Brown, 1986), and εs the corresponding strain at maximum stress. Torsion tests were performed on specimens with lengths of 1,228mm using the device shown in Figure 24.

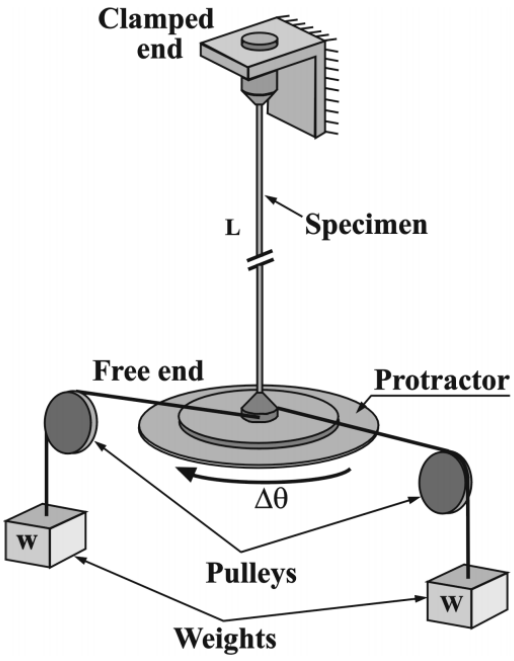

Figure 24. Torsion test apparatus, Rodríguez, (2001)

Various weights were hung and the change in angle measured with a protractor at the free end of the specimen. Geometries were constructed using a Stratasys FDM1600 system with process parameters shown in Table 6. Three mesostructures were examined; an aligned and a skewed configuration with raster width 25.4 μm and another skewed pattern with raster width 76.2μm as shown in Figure 25.

Table 6. FDM process variable settings (Rodríguez, 2001)

Extrusion temperature	270ºC
Envelope temperature	70ºC
Normalised flow rate	20 (mils)
Extruded fibre height	0.254mm
Extrusion nozzle diameter	0.305mm
Nozzle transverse speed	12.7mm/s

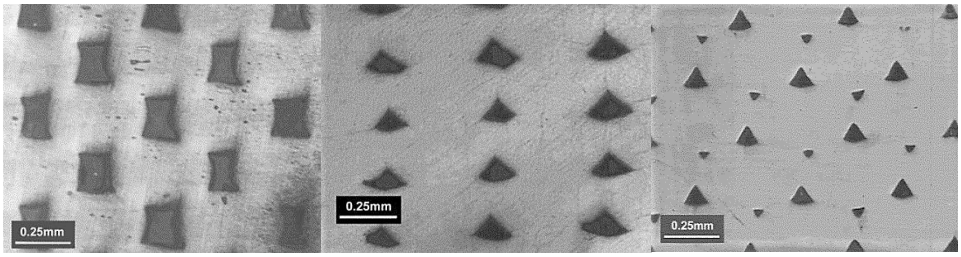

(a) (b) (c)

Figure 25. Photographs showing the three mesostructures examined
(a) Skewed with 76.2μm (b) aligned -25.4 (c) Skewed with -25.4 μm. (Rodríguez, 2001)

Rodríguez, (2001) tested the three mesostructures of 3D-printed ABS polymer with an MTS servo-hydraulic test system at strain rates of 10^{-2}, 10^{-3}, 10^{-4}, and 10^{-5}. This was done to test the influence of strain rate on the strength as well as the microcracking. An off-axis tensile test was used at angles 10^{o}, 30^{o}, 45^{o} and 60^{o} to determine the shear modulus. These specimens were then used to estimate the shear strengths. The orthotropic material symmetry assumption used by the authors assumes four elastic constants defined in equations (72) and (73) below.

$$E_1 = \frac{1}{\varepsilon_x^L}\frac{P}{A}, E_2 = \frac{1}{\varepsilon_x^T}\frac{P}{A}, v_{12} = -\frac{\varepsilon_y^L}{\varepsilon_x^L} \tag{72}$$

$$G_{12} = \left[2\frac{v_{12}}{E_1} + \frac{1}{sin^2\emptyset\, cos^2\emptyset}\left(\frac{1}{E_x} - \frac{cos^4\emptyset}{E_1} - \frac{sin^4\emptyset}{E_2}\right)\right]^{-1} \tag{73}$$

Where:

- P is the applied load in the (x) direction.
- A is the cross-sectional area
- ε_x^L is the longitudinal strain
- ε_x^T is the transverse strain
- The subscripts *1, 2* indicate the material direction while E_x is the tensile modulus in the direction of the loading.
- $\emptyset$ is the angle between the rasters and loading.
- v_{12} is the Poisson's ratio
- G_{12} is the classical error propagation analysis equation.

To consider FDM 3D-printed ABS components suitable for structural applications Table 7 and Table 8 show the results of the FDM ABS material compared to that of ABS monofilament. The results show a decrease in the moduli and the strength of the ABS material after extrusion owing part to the formation of air voids at a mesostructural level. It shows that the skewed structure with 76.2 μm yields the lowest results.

Table 7. ABS monofilament moduli value (Rodríguez, 2001)

E, [MPa]	2,230 ± 15
G, [MPa]	833± 7.6
ν	0.34±0.02

Table 8. Fused deposited ABS moduli value(Rodríguez, 2001)

Property	**Aligned -25.4μm**	**Skewed -25.4μm**	**Skewed 76.2μm**
$E_{1,}$ [MPa]	1972 ± 21	1986 ± 21	1807 ± 11
E_2, [MPa]	1762 ± 24	1701 ± 24	1400 ± 24
ν_{12}	0.376 ±0.013	0.386 ±0.012	0.357 ± 0.016
G_{12} [MPa]	676 ± 99	675 ± 152	612 ± 57

Table 9. Yield strength and strain of monofilament & printed ABS at strain rate (0.0005 s-1) (Rodríguez, 2001)

	Longitudinal [MPa, 1]		**Transverse [MPa, 1]**	
Mesostructure	σ_{ys}	ε_{ys}	σ_{ys}	ε_{ys}
ABS Monofilament	31.2	0.0154	-	
Aligned, g = -25.4μm	24.4	0.0145	13.6	0.0104
Skewed, g = -25.4μm	21.6	0.0146	13.4	0.0107
Skewed, g = 76.2μm	17.9	0.014	13.4	0.0131

2.5.4 Numerical modelling

Numerical models of fused deposition 3DP ABS materials were developed by Rodriguez, (2003) who used these models to estimate the mechanical behaviour of the specimens through the method of finite element analysis, modelled in a finite element software. Materials with three different mesostructures were explored in this study and results showed a 10% difference in the relative moduli when compared to experimental

data. This may be an acceptable range for which the behaviour of structural material can be predicted. The authors modelled the elastic moduli of the material using the strength and elasticity based approach. FDM materials show isotropic properties as such these materials were modelled as 3 dimensional homogeneous linear elastic orthotropic continua (i.e. materials with continuous air voids). The method used by the authors to model the problem was to define the represented volumetric element (RVE) as explained by Nemat-Nasser, (1993). After which a mathematical homogenisation theory was used to represent the constitutive characteristics of the ABS materials to display equivalent global behaviour.

The mathematical modelling of the specimens were developed using the constitutive equation seen in Jones, (1999) where the effective moduli depend on the density of voids and moduli of the raw material. Where symmetry of compliance tensor is implied (Equation (73)), resulting in nine independent elastic moduli that can be determined to establish the elastic mathematical equation for the 3DP ABS material. These equations are as follows:

$$[e] = [S][\sigma] \tag{74}$$

where in full matrix form:

$$\begin{Bmatrix} \mathbf{e}_{11} \\ \mathbf{e}_{22} \\ \mathbf{e}_{33} \\ \mathbf{e}_{23} \\ \mathbf{e}_{13} \\ \mathbf{e}_{12} \end{Bmatrix} = \begin{bmatrix} \frac{1}{\tilde{E}_1} & -\frac{\tilde{\nu}_{21}}{\tilde{E}_2} & -\frac{\tilde{\nu}_{31}}{\tilde{E}_3} & 0 & 0 & 0 \\ -\frac{\tilde{\nu}_{12}}{\tilde{E}_1} & \frac{1}{\tilde{E}_1} & -\frac{\tilde{\nu}_{32}}{\tilde{E}_3} & 0 & 0 & 0 \\ -\frac{\tilde{\nu}_{13}}{\tilde{E}_1} & -\frac{\tilde{\nu}_{23}}{\tilde{E}_2} & \frac{1}{\tilde{E}_1} & 0 & 0 & 0 \\ 0 & 0 & 0 & \frac{1}{\tilde{G}_{23}} & 0 & 0 \\ 0 & 0 & 0 & 0 & \frac{1}{\tilde{G}_{13}} & 0 \\ 0 & 0 & 0 & 0 & 0 & \frac{1}{\tilde{G}_{12}} \end{bmatrix} \times \begin{Bmatrix} \sigma_{11} \\ \sigma_{22} \\ \sigma_{33} \\ \sigma_{23} \\ \sigma_{13} \\ \sigma_{12} \end{Bmatrix}. \tag{75}$$

$$\frac{\tilde{\nu}_{ij}}{E_i} = \frac{\tilde{\nu}_{ij}}{E_j}, \qquad for\ i,j = 1,2,3 \tag{76}$$

where

- $\mathbf{E_1, E_2, E_3}$ are effective young moduli in the directions of **1,2,3** as shown in Figure 7b
- $\tilde{\nu}_{ij}$ are the effective Poisson's ratio for the transverse strains in the $\mathbf{j^{th}}$ direction when stressed in the $\mathbf{i^{th}}$ direction.
- $\mathbf{G_{12}, G_{23}, G_{13}}$ are the effective shear moduli in the 1-2,2-3and 1-3 planes

To obtain the useful properties of the FDM ABS material, the authors investigated two approaches. The mechanic of material approach assumes that the characteristic description of the voids present in 3D-printed specimens can be defined. The void density is assumed to be uniform on each plane in the solid; this density is considered a tensor with a magnitude that is dependent on the plane associated with any given point. The following equations (77) to (83) were used to obtain the effective properties:

$$E_1 = (1 - \rho_1)E \tag{77}$$

$$E_2 = E_3 = \left(1 - \rho_1^{1/2}\right)E \tag{78}$$

$$G_{12} = G_{13} = G\frac{(1 - \rho_1)(1 - \rho_1^{1/2})}{(1 - \rho_1) + (1 - \rho_1^{1/2})} \tag{79}$$

$$G_{23} = \left(1 - \rho_1^{\frac{1}{2}}\right)G \tag{80}$$

$$v_{12} = v_{13} = (1 - \rho_1)v \tag{81}$$

$$v_{23} = \left(1 - \rho_1^{\frac{1}{2}}\right)v \tag{82}$$

$$v_{21} = v_{31} = v_{32} = \left(1 - \rho_1^{\frac{1}{2}}\right) v \tag{83}$$

Where, E, G, ν and ρ_1 are the elastic properties and void density of the ABS material respectively.

The second approach used to obtain the effective properties is the asymptotic theory of homogenisation; this is used for solids with periodic mesostructures as seen in Figure 25. This approach assumes that the periodicity characteristic of the material affects the displacement, stress and strain relatively. Figure 26 shows a representation of this theory where **x** is the global scale of the material of where effective properties must be found. While **y** represents the micro-scale of the material accounting for the periodicity of the material.

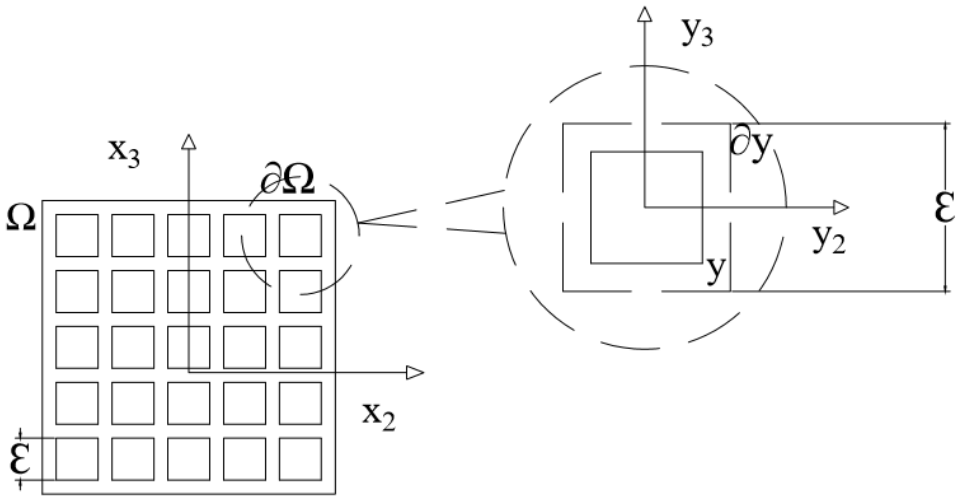

Figure 26. The periodic body considered in Rodriguez, (2003)

To find the effective properties the following equation must be solved for $\mathbf{u}^{(1)}(\mathbf{x}, \mathbf{y})$ in the micro-scale for six microscopic strain states $\mathbf{E}(\mathbf{u}^{(0)}(\mathbf{x})) = \nabla \mathbf{u}^{(0)}$ which describes the pure elongation and shear.

$$\frac{\partial}{\partial y_j}\left[C_{ijkl}\left(\frac{\partial}{\partial y_l} u_k^{(0)}(x,y) + \frac{\partial}{\partial x_l} u_k^{(0)}(x)\right)\right] = 0 \tag{84}$$

The authors found effective properties by solving equation (84) using the finite element method with triangular elements. The authors constrained the nodes on opposite sides of the voids so that displacement would be the same to account for the boundary conditions of the periodicity as stated in the code. The geometry chosen for the FEM simulation were taken from a sample of microimages which four voids were taken and digitised. In order to determine a suitable mesh, a study of FEM solutions was conducted where a mesh system of 900 nodes was chosen for the aligned configurations and 1900 nodes for skewed. The calculated results were then compared to experimental data conducted by Rodrıguez, (2001), which showed that both numerical methods displayed similar performances for predicting the effective elastic properties. See Table 10.

Table 10. Comparison of predicted elastic moduli to experimental data (Rodriguez, 2003)

Mesostructure	Property	Experiment	Strength of materials	Percent	Homogenization	Percent
	E_1(Mpa)	1972	2076.8	5.1	2075.8	5.3
Aligned	E_2(Mpa)	1762.7	1645.5	-6.7	1830.2	3.8
g: -25µm	v_{12}(1)	0.377	0.315	-16.9	0.339	-10
	G_{12} (Mpa)	676.6	686.7	13.4	677.7	0.2
	E_1(Mpa)	1986.6	2129.2	7.2	2119.1	6.7
Skewed	E_2(Mpa)	1707.6	1755.9	3.2	1884.9	10.8
g: -25µm	v_{12}(1)	0.385	0.323	-16.1	0.338	-12.1
	G_{12} (Mpa)	675.9	719.8	6.5	708.3	4.8
	E_1(Mpa)	1807.7	1934.3	7	1963.9	8.6
Skewed	E_2(Mpa)	1400.8	1418	1.2	1374.3	-1.9
g: 76.5µm	v_{12}(1)	0.357	0.293	-17.9	0.338	-5.4
	G_{12} (Mpa)	659.5	612	-7.2	629.3	-4.6

2.5.5 Structural geometries

Structural geometry is the study of shapes, sizes, patterns and position in space concerning load transfer through structural members. It has assisted engineers in predictions of structural forms since early times through interpretations of the physical world. Dealing with the configuration of geometric forms such as

points, lines and circles structural engineers can improve structural system utilising orienting shapes of desired structural properties. Structurally suitable geometries can be obtained using the shape optimisation method as studied by Allare, (2002). This method may be used to develop algorithms that can modify a particular geometry to obtain a minimum weight which can still adequately serve its function. In a study conducted by Stava, (2012), that was aimed at developing a method to detect structural issues of 3D-printed geometries. The author utilises FEM analysis with quadratic tetrahedral elements found in Hughes, (1987) to calculate stresses in the 3D-printed geometry derived from a pinch grip.

Using the equation:

$$K\mathit{d} = F \tag{85}$$

where K is the stiffness matrix developed from the material properties and the tetrahedral mesh. *d* is the deformation caused by F which is the forces both external and internal. The author considered the boundary condition to be fixed vertices of the mesh with a *d* equal to zero. The forces F are expressed as a sum of elemental contributions

$$F = \sum f^e \tag{86}$$

Where :

$$f^e = \int_{\Omega e} N^T b \, d\Omega + \int_{re} N^T t \, dr \tag{87}$$

Where Ω_e is the tetrahedral element, r_e is one face of the tetrahedron, N is the matrix of quadratic functions, t is the surface load at the face of the element and b is the body force on the element. Using the calculated stress and displacements derived from the analysis the author was able to equate the need for thickness, hollowing or strut addition required along the medial axis of the geometry hence resolving structural issues found in 3D-printed geometries.

2.6 Large Scale Testing on QSDs

Li et al., (2007), performed large scaled shaking table tests on prestressed concrete QSDs. The QSD tested was modelled from a prototype which was to be built in Xiamen, China. Based on similitude laws, the 1:8 scaled test model had an equatorial diameter of 2.75 metres and a height of 4.9 metres with a shell thickess that varied between 0.06 and 0.08 metres (see Figure 27). The tests involve three stages including the empty model digester which subjected to accelerations of relatively small peak ground acceleration (0.1g) , the model digester filled with 50% water was subjected to accelerations of medium ground acceleration and the empty model digester with water taken out subjected to acceleration with accelerations up to a large value (0.8g). According to the site condition and seismic background, two scaled ground motion accelerations, the recorded El Centro acceleration and the artificial acceleration adopted in Guangzhou, are employed as the seismic excitations.

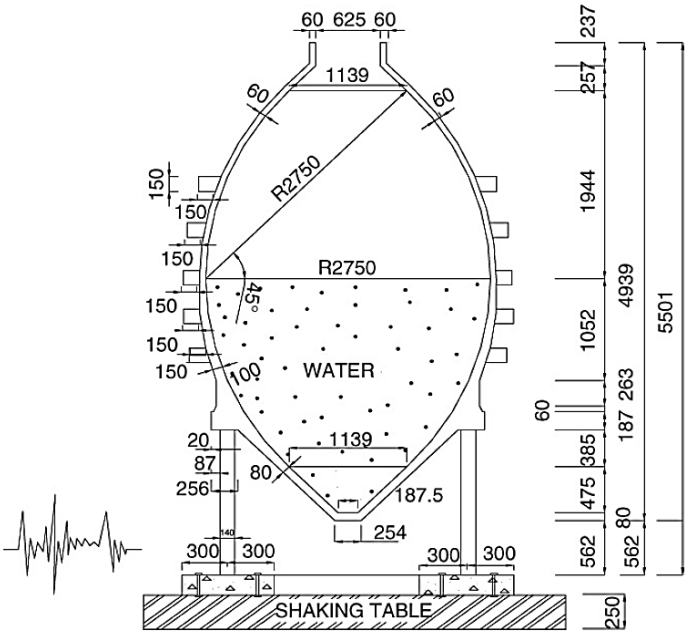

Figure 27. Schematic of 1:8 Prestressed QSD model for shaking table test (Li et al., 2007)

The test measured various strain responses on the surface of the shell.

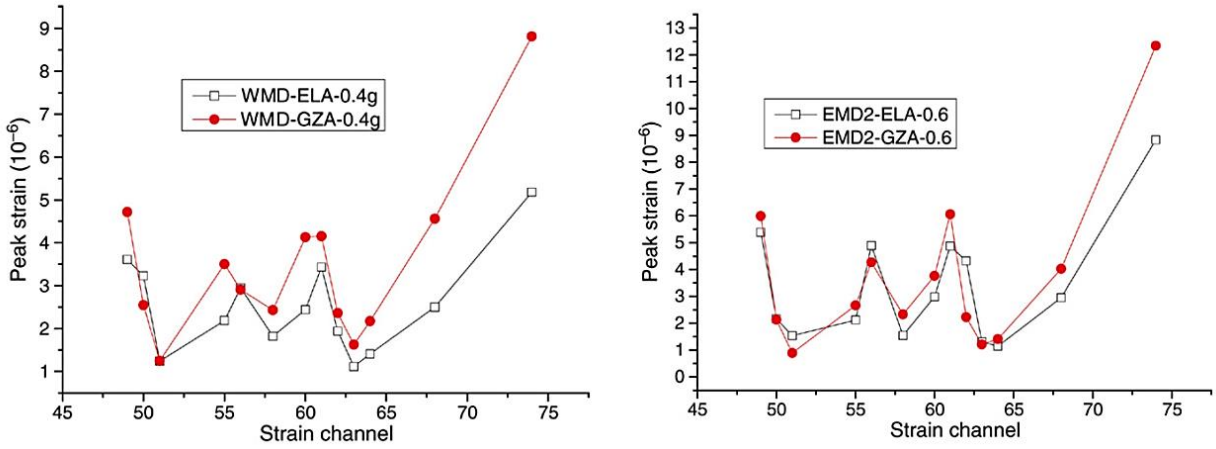

(a) (b)

Figure 28. The resulting peak strain of the: (a) 50% filled tank and (b) Empty tank, both subjected to acceleration with PGA of0.4g. (Li et al., 2007)

Figure 27Figure 28 Figure 27shows the peak strain of the 50% filled QSD model (labelled WMD) and the empty QSD model (labelled EMD) both subjected to El Centro acceleration (ELA) and the artificial acceleration (GZA) respectively. It is seen that for the WMD, the peak strains under the artificial acceleration are much larger than those under ELA, the maximal discrepancy reaching 70% in the midriff. For the EMD2, in general peak strains under GZA are also larger than those under ELA with the maximal discrepancy reaching 40% in the midriff.

The study concluded that the model behaved in the linear-elastic range and the natural frequency has minor variations with the PGA. It was also found that when subjected to strong earthquake excitations, localised non-linearity appeared at various areas where discontinuities in the shell occurred.

2.7 Summary

2.7.1 Quadric-surfaced Shells

In this section, it can be seen that previous studies in the geometry of QSDs are very limited. The development of stress resultant equations (equation (18)), for the parabolic ogival shell, by Zingoni (2002), is a continuation of studies conducted by Gibsom (1965). Axelrad also developed these equations from first principle as well however his work was based on scalar matrices. Doyle's work was also based on a method utilising scalar matirces. The solutions for the rotationally symmetric Saint-Venant shell distortion problems that can occur in QSDs were also examined even though the literature available did not conclude of any actual case studies with this type of failure. However, the literature can prove valuable when developing design code parameters for QSD shell design.

2.7.2 Sloshing Dynamics

Sloshing is of significant importance and is one of the major concerns in the design of liquid retaining structures and fuel tankers for carriers. Abramson (1967) mentioned that for several years, this subject has been a major concern for scientists, engineers and mathematicians. According to Ibrahim (2006), the free liquid's surface can experience different motions comprising of simple planar, non-planar, symmetric, asymmetric, rotational, irregular beating, quasi-periodic and chaotic, all depending on the type of disturbance, amplitude and frequency of seismic excitation, properties of the liquid, height of liquid and the geometry of the retaining liquid container. When the frequency of the motion and the natural frequencies of liquid sloshing are close to each other, the resulting amplitudes of the sloshing wave would be very large increasing the sloshing dynamic forces on the shell surfaces of the container. The high hydrodynamic forces produced by the sloshing waves on the inner surface of the container affects the overall response of the container and causes a complex FSI phenomenon between the two materials with respect to the liquid properties and retaining container properties.

The linear theory of dynamic sloshing in liquid retaining structures is based on understanding the derivation of fluid field equations that are used to approximate the hydrodynamic shell forces and moments induced by sloshing waves. Ibrahim (2006) mentioned that the linear theory for liquid sloshing is acceptable for

determining the natural frequencies and wave height of the liquid's free surface. Under translational excitation, the linear theory is useful for predicting the shell's liquid hydrodynamic pressure, forces, and moments. Only applicable when the free surface maintains a planar shape with a nodal diameter that remains perpendicular to the line of excitation, and it does not take into consideration the importance of vertical displacement with respect to the centre of gravity of the liquid for large amplitudes of sloshing.

Ibrahim, (2006) also mentioned that the linear theory fails to predict complex surface phenomena observed experimentally near resonance. These phenomena include the non-planar unstable motion of the liquid's free surface associated with chaotic sloshing and rotation of the nodal diameter also called rotary sloshing. He also states that the linear theory cannot be used for dynamic analysis of shell elements undergoing elastic deformation that is analogous to its wall thickness and also if the liquid's free surface amplitude is large. Nonlinear resonance conditions that cause complex response characteristics will result in the occurrence of nonlinearities within FEA model.

The SPH procedure can understand hydrodynamics intricacies whose arrangement appear as a PDE for field factors such as the density, velocity and energy. Acquiring expository solutions for such an arrangement of PDEs is not frequently conceivable, aside from not very many straightforward cases. For numerical arrangements, one needs first to discretise the problem area where the PDEs are characterised so that the technique can give an estimate to the estimations of the field capacities and their derivatives at any point.

2.7.3 The Mechanical Properties of 3D Polymers

Studies has proven that the adaptation of FDM in its current development has shown some potential for structural applications as Ahn, (2002) and Berman, (2015) mentioned, displaying capabilities for the production of complex geometries. Stava, (2012) has added to discovering defects in 3D-printed geometries through FEM analysis with tetrahedral elements. However, the voids which are formed due to the deformation of beads caused by the cooling effect of printed rasters reduces the structural integrity of the printed components. Hossain's, (2013) solution to reduce these voids by modifying built parameters seems to be a viable option when modelling geometries for experimental data. Rodriguez, (2003) has provided a

workable procedure in which results from experimental data can be modelled in FEM software to provide accurate analysis of structural geometries. The discovery of FDM compatible PMCs aids the development of a multi-material geometry suitable for a specified structural application where high strength and low weight is desired. For this application, the properties of Tekinalp, (2014) test sample can be used due to the favourable increase in tensile strength observed. To improve the bond between the fibres and the associated matrix, surface modification seems to be the solution in addition to changing the geometry of the fibre. E.g. using a curved fibre may reduce the ability for fibres to pull out of the matrix.

Based on previous research, the porosity of FDM specimens concerning CMP specimens appears lower which results in lower structural properties. A solution may be to reduce the raster height while printing which results in denser structures. ABS and PC show the most desired material and structural properties are considered as the material choice of geometries. Both glass and carbon fibres improved the mechanical properties of FDM printed components and will also be considered for investigation. Honeycomb structures of various densities are suitable geometries for high compression members as well as impact resistance as discussed in Mroszczyk, (2014). This seems to be logical for structural applications such as slabs and aircraft wings

3.0 Methodology

3.1 Introduction

This chapter is divided into two main areas. The first provides the methodology for investigating the mechanical properties of the 3D printed polymer. This was further sub-divided into experimental studies and numerical simulations.

3.2 Material Characterisation

3.2.1 Introduction

The research methodology is quantitative; it attempts to collect and convert data into a numerical form for finite element analysis. The purpose of this research is to determine the structural applicability of 3D printed polymer.

This research seeks to answer the following questions:

- What are the structural material properties of the 3D printed polymer?
- What is a suitable approach to modelling the material using FEA software?
- How does 3D printed polymer material behaviour under tensile, bending and torsional forces?
- What are some suitable structural applications?

To determine suitable structural applications for 3D printed polymers, the structural properties of such polymers must be investigated. To do this Finite Element Analysis software, ABAQUS, was used to analyse the relationship between the stress in the material and the corresponding strain within the elastic limit. Both experimental and numerical modelling was chosen as the investigation tools that provided two sets of data for comparison. Experimental investigations determined the material properties needed to characterise the material for numerical modelling. The numerical results were compared to those of the experiments. After which the various geometries were modelled and analysed to test the applicability of the developed constitutive model.

Based on the nature of the application for the 3D printed polymers, cost of analysis and simulations become a significant factor for design. FEA software packages require the mesh size and aspect ratio have desirable densities and sizes so that satisfactory results are obtained. Hence it is essential to satisfy these conditions to obtain a reasonable mesh size. Therefore, reducing the time and computational power for simulating the part loading conditions is one of the goals of this study. It was achieved with the assumption that the 3D printed polymer is a material with material properties that are dependent on the 3D printed technology and other parameters. The 3D printed polymer material has properties similar to that of the bulk material, but with deviations from the bulk material. One deviation is that the 3D printed material will not remain isotropic, even if the parent material is isotropic. The material moduli were obtained from experiments that enabled use their basic equations.

The approach starts by first investigating the characteristics of the material (obtaining the properties of the material by experimental tests). Samples were obtained from the 3D system's cube pro which utilises fused deposition technology. A total of three tests were conducted tensile, bending and torsion; these tests represent some of the loadings structural elements usually undergo. These tests were used to determine the independent moduli for the numerical models. Then a study of the characteristic equations was conducted in order to determine the mechanical constants. These constants were used to estimate the stress, strain and deformation in the material when loaded. The constitutive mechanics of material approach was used to model the properties of the material. This chosen approach allowed the assumption that the material is solid with aligned prismatic voids. It theoretically described the 3D printed polymer material and allowed the modification of the material properties by the implementation of the void density variable. Afterwards the results of the numerical analysis and the experimental work were compared to verify the correctness of the results.

3.2.2 Material Description

The 3D printed material was described using experimental methods to probe and measure the material structure and properties. The configuration of the layers is [0,90] respective to the perpendicular axis of the extruded tool path. Considering that the material is made up of layers of extruded fibres, it's idealisation is a composite laminate. However, Mamadapur (2007) revealed that the layer to layer bound

properties differs from that of the raw material, whereas the laminate theory assumes perfect bonding. Another theory to the material description is by assuming that the material exhibits a particular case of orthotropy. It is due to the effect that the layer configuration has on the relative effective properties. According to Mamadapur (2007), Young's moduli of the two perpendicular directions, and the corresponding Poisson's ratios are the same on two of the materials plane. However, the corresponding shear modulus is still independent of Young's modulus or the Poisson's ratio. Hence the 3D printed material was described as being a transversely isotropic material using engineering constants. These constants were obtained using the Mechanics of materials approach to constitutive modelling.

The rule of mixtures was used to predict the longitudinal modulus of FD-3D printed ABS polymer. Three constants (C, ζ, k) were included, which considered fibre contiguity, bonding strength and miss alignment of the voids formed after extrusion. Each constant was applied to the properties that were affected and were measured differently on its respective axis.

The development of the effective properties was done based on a mixture model. Where every point of the material, is associated with the void density on that plane. Hence, using equations (77) to (82), the effective elastic properties were obtained. Where E, G, v are the elastic material properties of the raw material.

3.2.3 Experimental Technique

All test specimens were constructed using the 3Dsystems cube pro FDM type 3D-printer with parameters described in Table 6. Two types of low-cost polymer materials were examined in these experiments; acrylonitrile butadiene styrene (ABS) and polylactic acid (PLA). It is important to note that any warping during the manufacturing process will affect the results. Hence, to prevent unwanted warp from accruing specimens were created in an environmentally controlled workspace. The temperature parameters were recommended by *FOJO Design Company*, based on their experience using the mentioned 3D printing platform.

The printer extrudes filament rasters in an [0,90] orientation, as shown in Figure 22. Build parameters in FDM platforms adapted from Hossain *et al.* (2013) This is because of the algorithm the printer's software uses to perform a 100% infill print job. Hence, the material properties obtained from these experimental test are only valid for geometries created using the 3Dsystem's cube pro FDM type 3D-printer with printed raters of [0,90] configuration.

3.2.3.1 Printer settings

The specimens were then examined to obtain the mesostructural properties for obtaining the effective material constants. The acquisition of these properties makes it possible to describe the material in the form of engineering constants. This was done by taking a sample of the FD-3D print and removing a cross-section using a diamond blade saw to obtain a smooth surface. The samples were then washed, cleaned and probed to be examined using the microscope. Photographs were then obtained from the apparatus, displaying the characteristic shape of the mesostructure shown in Figure 29.

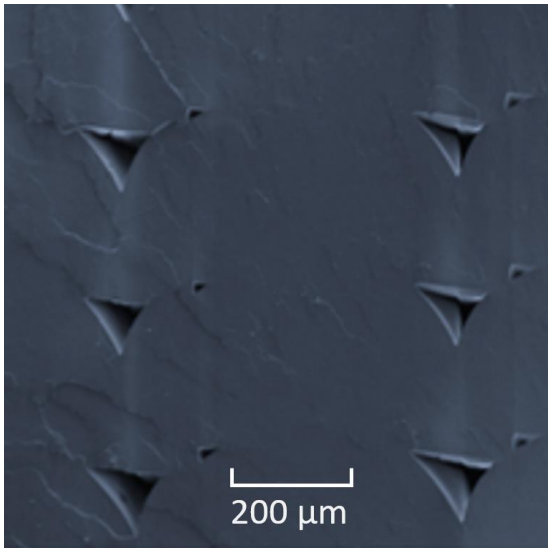

Figure 29. Photograph of mesostructure of 3D printed ABS at a zoom of 200µm

The specimens were printed at a scale of 200µm which required a microscope magnification of 200µm. The photographs were then exported and digitised into AutoCAD. Tensile, torsion and flexural tests were performed to examine the behaviour of the 3D printed material in an attempt to characterise the

structural properties. Upon investigation no tests were found explicitly tailored for 3D printed material. Hence, the ASTM tests were chosen based on the recommendation obtained from an overview by Forster, (2015).

$$\rho_i = \frac{Void\ Area}{Cross - section\ Area} \tag{88}$$

Equation (88) was utilised to calculate two ρ values; ρ_1 which is the ratio of the effective load carrying material, ρ_2 which count's the potential load-carrying dimension (see Figure 30), i.e. ratio of bond length to overall dimension Longmei (2001).

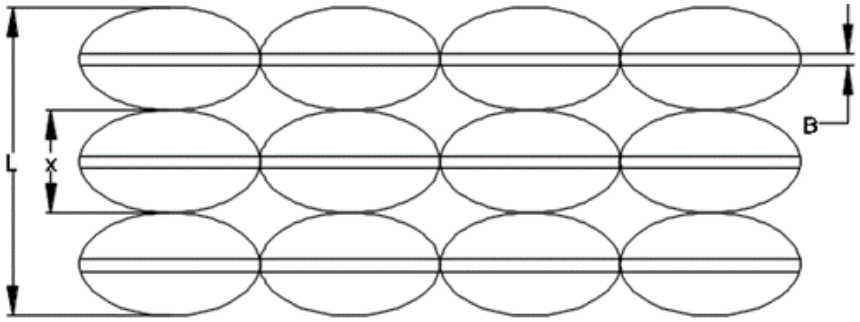

Figure 30. Typical projection of load-carrying material for calculating void density

ρ_2 was introduced to obtain the effective elastic modulus for the transverse direction (E_2, G_{12}). Once the geometric properties of the mesostructure were obtained, equations (89) and (90) were used to calculate the void density (ρ_1, ρ_2).

$$\rho_1 = 1 - \sum_{l} {}^{B_l}/_{L} \tag{89}$$

$$\rho_2 = \frac{X - B}{X} \tag{90}$$

The material constants [C, ζ, k] as explained by Longmei (2001) are obtained from the tensile experiments. The bond strength ζ is taken as the deference of yield strength of the bond and the extruded monofilament. It was observed that there is a difference in bond strength of bead to bead and layer to

layer bonds. This may be caused by the extrusion path and time taken for the material to be laid. The contiguity was applied between two extreme cases where $C = 0$ is if fibres are isolated and $C = 1$ when all sides incased.

The molecular orientation phenomenon was examined through thermal shrinkage measurements. PLA and ABS samples for raw material and extruded material were cut into lengths of 100mm and placed in an oven for 6hrs at 110^{o}C. After which the amount of shrinkage was measured using a digital calliper. A comparison of the raw material properties and the reduced properties are displayed in Table 11. The results clearly showed a difference in shrinkage and confirmed the need to reduce the stiffness and strength of the raw FD-3D polymers as suggested by Rodríguez, (2001).

Table 11. Property reduction percentages used in numerical calculations

Property	**Reduction**
Stiffness	4%
Strength	15%

Table 12. Comparing the Original ABS properties with Modified ABS properties

Property	**Original**	**Modified**
Young's modulus "*E*"	2230 MPa	2140 MPa
Shear modulus "*G*"	833 MPa	708 MPa
Poison's ratio "*v*"	0.34	0.19

3.2.4 Tensile test

A tensile test was performed on an MTS 100 Kip testing machine (Figure 31).

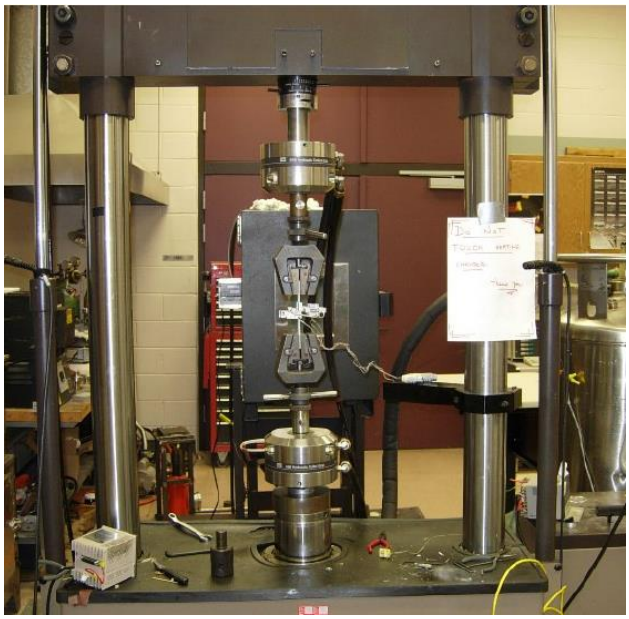

Figure 31. Tensiometer with ASTM D638 type-V dog-bone Sample. University of the West Indies, Tested on 6/10/2016.

Three sets of readings were obtainable from the tests apparatus; the load value, the axial strain and the transverse strain. 10 test specimens were fabricated as per ASTM D638 standard for tensile testing of rigid plastics (ASTM, 2002) (see Figure 32).

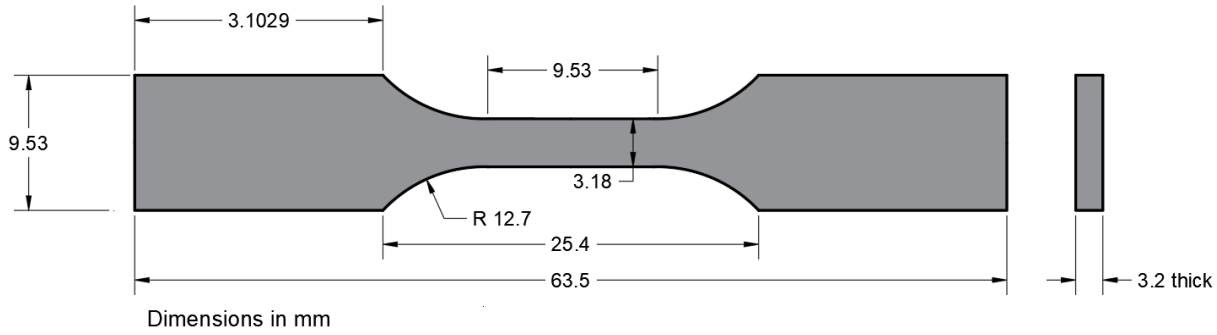

Figure 32. ASTM D638 type-V dog-bone Sample used in test

The test was performed by controlling the displacement where the axial and transverse strains were collected in mm/mm, and the corresponding loads were collected in kg. The loads were then converted to (engineering) stresses by dividing the load values by the original area of cross-section of the specimen. Stress vs axial strain curve was obtained for each specimen, and the corresponding elastic modulus was obtained as the slope of the linear elastic portion of the curve. The axial strain and the

transverse strain were plotted against the applied load, and the corresponding Poisson's ratio was obtained as the ratio of the slopes of the two straight-line curves in accordance with the definition of Poisson's ratio. The yield strengths of different specimens were also obtained from their stress vs. axial strain plots.

3.2.5 Torsion

Torsion tests were conducted using a Gunt WP500 torsional tester shown in Figure 33. The FD-3D polymer test bars are torqued until failure. The test torque and the angle of twist were obtained during this process. The test torque is applied manually using a hand wheel and a worm gear. Measurements were recorded with a strain gauge torsion shaft, the deformation of which is compensated. The measurement was taken in Nm from the digital display. The angle of twist was recorded by an incremental encoder and digitally displayed at the measuring amplifier.

The FD-3Dpoymer specimens were fabricated in accordance with the ASTM E143 standard test method for shear modulus at room temperature (ASTM, 2002). 10 test specimens were fabricated with hexagonal ends to grip firmly in the torsion apparatus. The testing diameter was 10mm and the shaft length was 80 mm. A total of 10 samples were tested. A graph of Torque/Polar moment of inertia (T/J) vs angle of twist (Φ) was plotted for all specimens. Its shear modulus was obtained as the linear portion of the curve and the resulting slope.

Figure 33. Gunt WP500 torsional tester at University of the West Indies.

3.2.6 Flexure

The three-point bending tests were executed using an Instron 4411 bending apparatus (**Error! Reference source not found.**4). This apparatus generated the loading in force units N.mm and the corresponding deflection data. A 1000 lb load cell was used which was built into the apparatus. The apparatus provided an adjustable support span which was set at 50.80 mm. Hence the specimen dimensions used. The rectangular specimen must be 6 times the depth of the sample recommended by

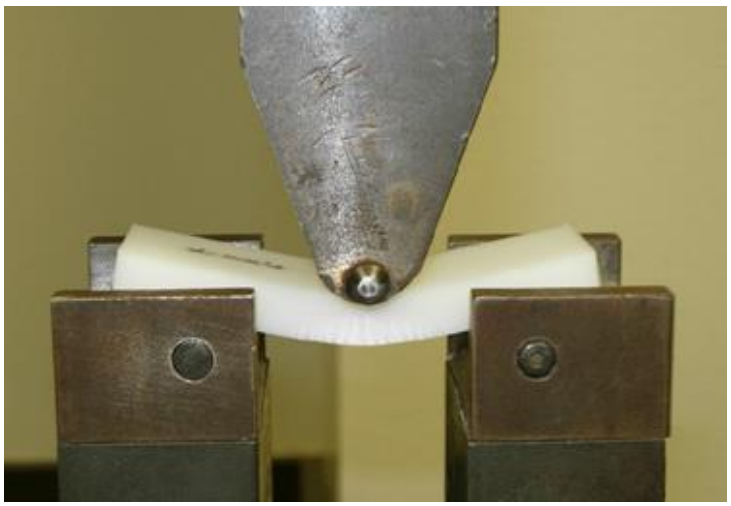

Figure 34. Sample loaded in Instron 44113-point bending apparatus. University of the West Indies.

the ASTM standard.

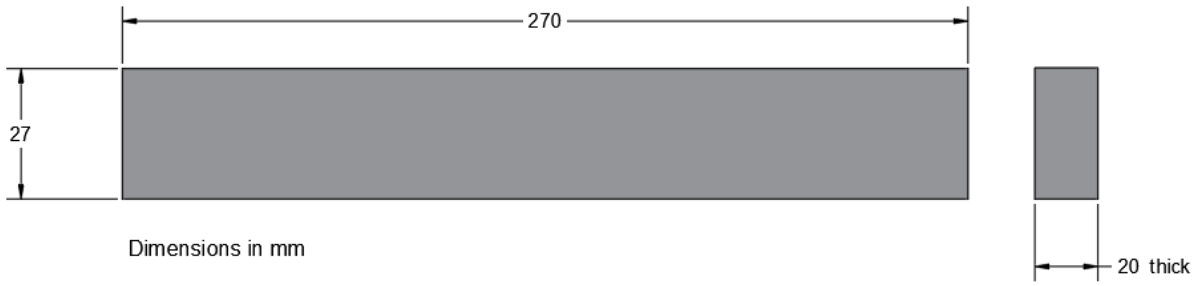

Figure 35. ASTM D790 type-V Sample used in test

The radius of the loading nose was 6.35 mm, and the support radius was 6.35 mm (

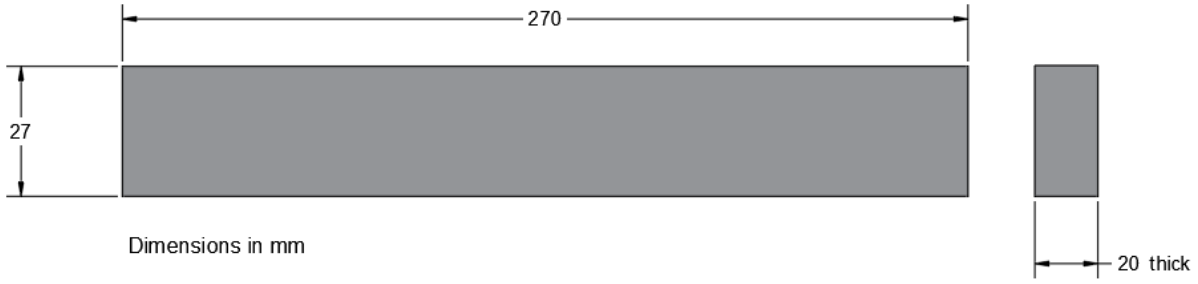

Figure 35). The FD-3D polymer specimens were fabricated in accordance with the ASTM D 790 Standard Test Methods for Flexural Properties of plastics (ASTM, 2002). A deflection vs curve graph was plotted for all specimens. Its flexural modulus was obtained as the linear portion of the curve and the resulting slope.

3.2.7 Numerical Modelling

FEM analysis provides the prediction of displacements through three types of relationships; equilibrium equations, compatibility conditions, and constitutive relations. The geometries examined in this study were three-dimensional parts subjected to static loading. The equilibrium equation can be obtained from the summation of the forces and moment on the respective plane. The compatibility conditions relate to the deformed part ensuring the shape of the deformation is continuous. The constitutive relations

describe the relationships between the stresses and strains of the part in accordance with the stress-strain properties of the FD-3D polymer material. The constitutive relations is the link between the equilibrium equations and compatibility conditions that is necessary to predict the load-deformation relationships for the FD-3D polymer part.

The geometries and properties were designed by determining the sufficient stiffness so that the model can be used to predict the structural behaviours of the parts. The loading direction and longitudinal direction of filaments were used to define the filament orientation. Models were constructed using the constitutive relations for the case of special orthotropic, where $\theta = 0$ (or 90^{o}), the constitutive relations are expressed in the form of material constants..

The stiffness matrix [K] describes the material through nine (9) constants, which represents the effective Elastic modulus (Ei), effective Poisson's ratio (vi) and Shear modulus (Gi). The Matrix [σij] represents the stress in the respective plane and [eij] is the strain in the corresponding plane.

The parameters for the material tests (both experimental and numerical) were benchmarked by compairing the results obtainted from similar experimental and numerical studies done by Rodriguez, (2001).

3.2.7.1 Tensile FEA Model

The tensile geometry was constructed identically to the ones used in the experimental test. ABAQUS FEA software was used to conduct the analysis for a 3D-solid geometry. The experimental values were obtained from physical testing while the calculated values were obtained using expressions derived by Rodriguez, (2003).

The calculated material constants used to represent the stiffness of the global FD-3D polymer material can be seen in Table 13.

Table 13. Experimental material constants compared to calculated constants

No	Property	Experimental	Calculated
1	$E_{1\ (MPA)}$	1636	1528
2	$E_{2\ (MPA)}$	1636	1528

3	$E_{3\ (MPA)}$	1197	1129
4	v_{21}	0.39	0.37
5	v_{32}	0.37	0.33
6	v_{31}	0.39	0.37
7	$G_{13\ (MPA)}$	645	532
8	$G_{23\ (MPA)}$	645	529
9	$G_{12\ (MPA)}$	676	669
10	$UTS_{1\ (MPA)}$	18	17.8
11	$UTS_{2\ (MPA)}$	18	17.8
12	$UTS_{3\ (MPA)}$	15.2	15.8
13	Yield Stress 1	16	17.2
14	Yield Stress 2	15.8	16.2
15	Yield Stress 3	13.1	13.2

Equations 77 to 83 (pages 77-78) were used to calculate properties 1 to 9**.** Properties 10 to 15 (the ultimate and yield stresses) were benchmarked and adopted from Rodriguez, (2001).

These material constants were oriented according to the local coordinate system (CSYS). Since the material was described as a particular case of orthotropic material, it can be considered as anisotropic with its respective material constants well known. Once the material orientation matches that of the experiments, it is assigned to the section, and BCs applied.

The BCs for the tensile specimens describe the condition of the experimental work in numerical form. The base of the specimen was kept fixed in both displacement and rotation. This was achieved by making the degree of freedom equal to 0 at each node at the grip area. The other end needed to be displaced along the longitudinal axis. This was achieved by releasing the nodes at the area of the grip along the y-axis in the software.

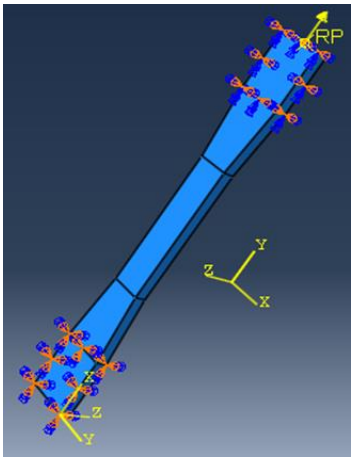

Figure 36. Tensile specimen showing loading and boundary conditions

The tensile force applied to the numerical model was obtained as the yield tensile force recorded from the experimental investigation. It was inputted as a negative value to describe the direction of action. The nodes at the area of the free section were constrained to a reference point at the face of the section and the force applied to that node to ensure uniform movement.

The element size and density are important in numerical modelling as it determines the time taken to complete the analysis and the accuracy of the results obtained. The aspect ratio for the mesh sizes was chosen based on five factors; the geometry of the part, element type, degree of accuracy, boundary conditions and type of loading. The size and type of mesh was derived from the characteristics of the RVE. The mesh was of adequate size to cover the cross-sectional area of four aligned filament rasters as shown in Figure 37 as such the hexahedron element type was chosen with an aspect ratio of 0.1 to 1 for the mesh.

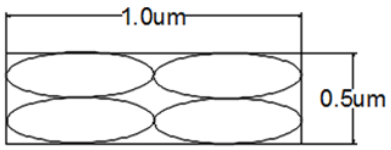

Figure 37. RVE of the numerical geometries

3.2.7.2 Flexure FEA Model

The bending geometry was constructed identically to the ones used in the experimental test. The ABAQUS modelling variables were identical to the tensile numerical model.

The boundary conditions for the bending specimens describe the condition of the experimental work in numerical form. The support pins and the load pin were constructed using rigid shell part types. The rigid shell part type is used because there are no deformation calculations to consider hence less analysis time. One support pins was tied to the test specimen allowing rotation around the pin. This boundary condition is considered a roller constraint and has a degree of freedom equal to two. The other was fixed such that it simulated a pinned connection. The support pins were kept in-cased to restrict horizontal displacement. The loading pin, however, was assigned a degree of freedom 1 free to move along the y-axis. A tie constraint was used between the load pin and the specimen to simulate contact (see Figure 38).

The mesh elements used were the Continuum solid element (8-node brick, C3D8). The mesh optimisation methods varied for the test sample and support/load pins. For the test sample, the structured meshing technique was used since this generates structured meshes using simple predefined mesh topologies. Abaqus/CAE transforms the mesh for the cuboid shaped region, into cube, onto the geometry of the region. For the pins, the algorithm used was the advancing front which generates quadrilateral elements at the boundary of the region and continues to generate quadrilateral elements as it moves systematically to the interior of the region. The failure criteria was added to the deformation plasticity in the properties section in Abaqus. This value was 18, 18 and 15.2 MPa (as stated in Table 12)

The bending force applied to the numerical model was obtained from the experimental investigation. The force that yielded the highest deflection values were used in the analysis. This force was applied to ta reference point at the centre of the face of the loading pin and that point tied to the nodes of the loading pin. This was done for the loading pin to distribute a uniform force equal to that of the concentrated load applied.

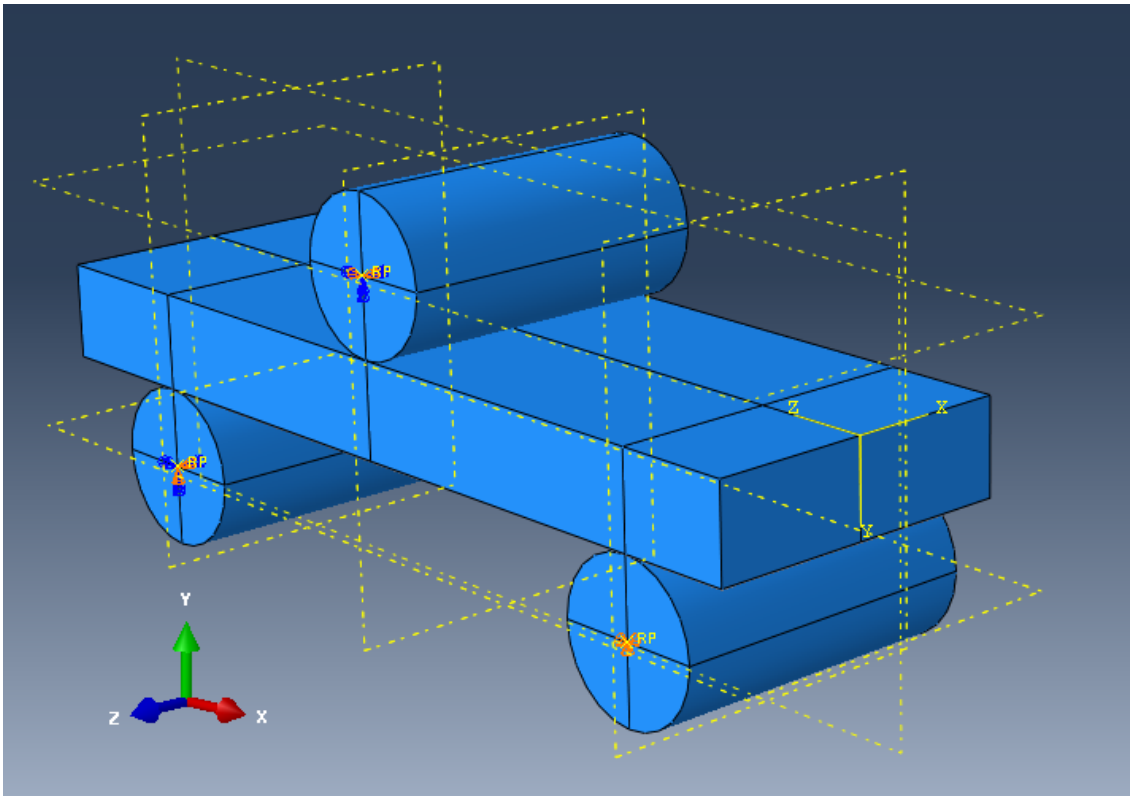

Figure 38. Showing the 3 points bending Flexure FEA Model with boundary conditions

3.2.7.3 Torsional FEA Model

The torsion geometry was constructed identically to the ones used in the experimental test. See Figure 39. The ABAQUS modelling variables were identical to the two previous models.

The BCs for the torsion specimens describe the condition of the experimental work in numerical form. Two sleeves were constructed 1mm larger than the torsion specimen itself and was constructed as a rigid shell element. The reason for this is that there are no deformation calculations to be considered for the analysis hence, less analysis time. The sleeve was connected to the gripping section of the geometry using a tie constraint that allowed rotation in the clockwise direction. The base of the specimen was kept in-cased with a degree of freedom equal to 0. The rotational end was assigned boundary condition that allowed rotation about the XY plane.

The load was applied as the torsional force used in the experimental work conducted. The force used was a moment force and was assigned to the rotating sleeve at the rotating end of the specimen. Seeing that the sleeve was already tied to the specimen the nodes of the specimen covered by the sleeve will displace simultaneously with the sleeve. The rotation angle was set at 180 degrees and was assigned as the angle of freedom of the constraint.

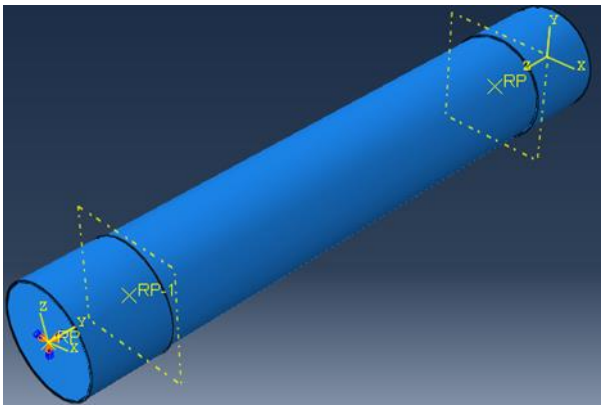

Figure 39. Showing the Torsion FEA Model

3.3 Numerical Modelling of the QSD

3.3.1 Introduction

Two types of numerical modelling were performed. The first was a group of 2-dimensional SPH models and the second was a 3-dimensional SPH model (see Figure 40).

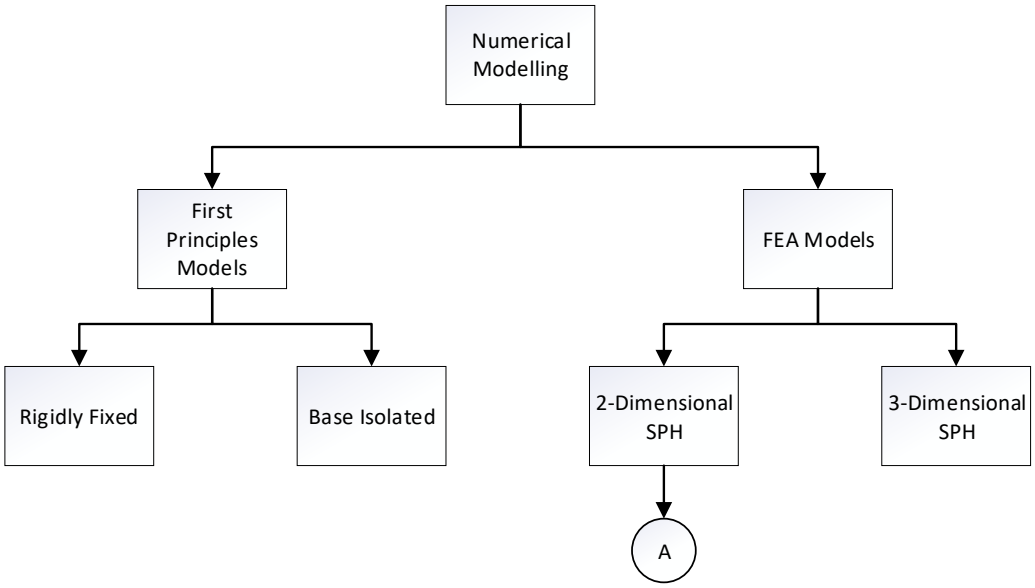

Figure 40. Flowchart for numerical modelling structure.

Note: Labels A to C are expanded below.

The first principles models examined the QSDs under various loading parameters. A digester of 25m height and wall thickness of 500mm was modelled and analysed with varying fill levels of 10%, 25%, 50%, 75% and 90% (see Figure 41). All models were each categorised based on varying fill levels, as shown in Figure 42. The second group of analyses are a series of 2D FEA models, and finally a 3D FEA model was analysed.

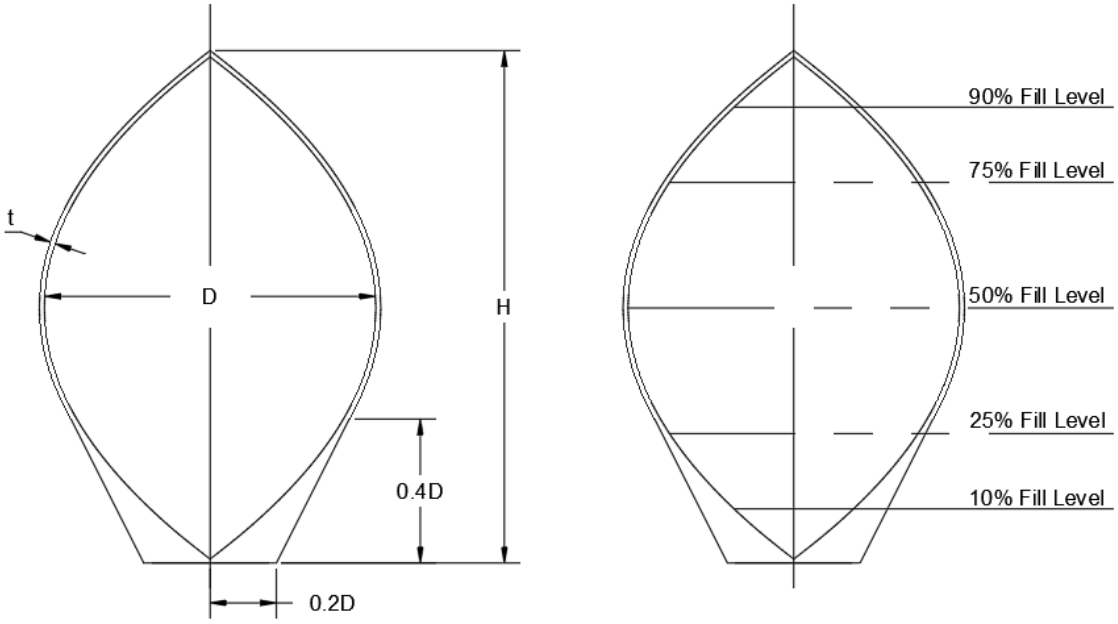

Figure 41. QSD dimensions and fill levels

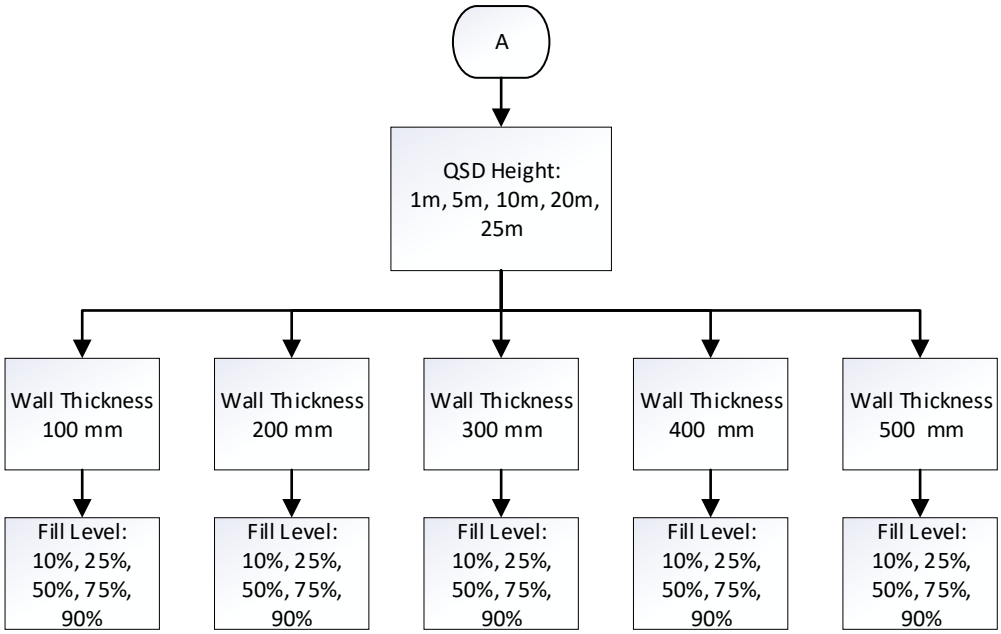

Figure 42. QSD modelling geometrical and loading parameters. This is a continuance from section A evolving from Figure 40.

3.3.2 First Principles Modelling

When a horizontal seismic displacement applied to the QSD, the hydrodynamic sloshing force that develops and interacts with the shell can decompose into two constituents. The first element is a

convective force directly related to the fluid sloshing movement. The second is an impulsive force where the motion of the fluid has zero relative acceleration relative to the QSD shell. Consequently, the total hydrodynamic pressure applied to the inside of the QSD shell also has a correlating impulsive and convective components.

The sloshing motion is a superposition of few eigenmodes of the fluid motion. In general, each eigenmode generates a hydrodynamic wall pressure of different distribution, but not all of these modes contribute to the development of a nonzero horizontal force on the tank. The eigenmodes, responsible for the generation of a nonzero horizontal hydrodynamic force, influence the horizontal motion of the tank structure. These are few that exhibit free-surface antisymmetry to a plane parallel to the tank axis of symmetry. The convective masses, M_{cn}, are related to the sloshing modes n=1,…,∞. This and the impulsive mass, MI, are related via the principle of conservation of mass as:

$$M = M_1 + \sum_{n=1}^{7} Mc_{n_i} + M_{cn} \tag{91}$$

where *M* stands for the entire liquid mass. The total horizontal hydrodynamic force, *F*, applied on the tank due to the liquid motion is:

$$F(t) = M_1 \ddot{x}(t) - \sum_{i=1}^{7} M_{Cn_i} \omega_{Cn_i}^2 u_{Cni}(t) - M_{Cn} \omega_{Cn}^2 u_{cn}(t) \tag{92}$$

where $x(t)$ is the acceleration of the tank structure and $u_{Cni}(t), u_{cn}(t)$ is the response of an SDOF system, with frequency $\omega_{Cn_i}, \omega_{Cn}$, which is computed using as forcing input the acceleration of the tank.

The liquid in mas of the tank is modelled as an MDOF system since the liquid behaves as an MDOF oscillator. Therefore, the convective mass M_{Cn} of each sloshing mode is equal to an effective modal mass computed,

$$M_{Cn_i} = \left(L_{Cn_i}\right)^2 / M_{n_i} \tag{93}$$

where:

$$M_n = \{\phi\}_n^T [M] \{\phi\}_n \tag{94}$$

is the generalised mass of eigenmode n =8, and

$$L_{Cn} = \{\phi\}_n^T [M] \{I\} \tag{95}$$

with $\{I\}$ being the unit vector in the direction of the seismic excitation.

For arbitrary tank geometries, the corresponding heights can be calculated via a straightforward numerical integration of the fluid pressure distribution and subsequent positioning of the resultant force using standard procedures. Similarly, the total hydrodynamic pressure distribution on the tank wall can be decomposed, into impulsive and convective parts of the fluid, the total hydrodynamic force can also be divided into an axisymmetric part, associated with the axisymmetric eigenmodes of the fluid motion which do not contribute to the total horizontal force:

$$p(\phi,\varphi,t) = p_I(\phi,\varphi,t) + \sum_{i=1}^{7} p_{Cn_i}(\phi,\varphi,t) + p_{Cn}(\phi,\varphi,t) \tag{96}$$

where θ and φ are the azimuths and meridian angles, respectively (see Figure 43).

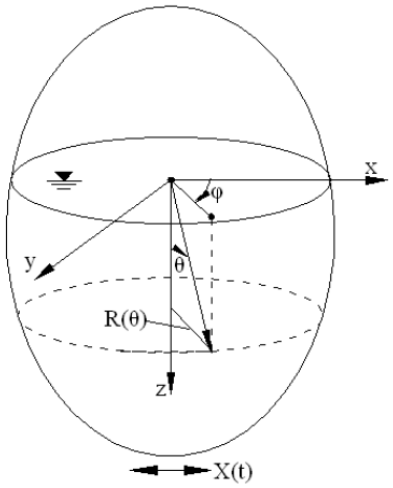

Figure 43. The coordinate system for axisymmetric components

p_I is the impulsive pressure, p_{Cn} is the convective pressure due to sloshing mode n and p_{Am} is the axisymmetric pressure due to axisymmetric mode m. Hence the impulsive pressure is given by:

$$p_1(\phi,\varphi,t) = C_1(\phi)\rho R(\phi)\cos(\varphi)\ddot{x}(t) \tag{97}$$

and convective pressure:

$$p_{Cn_i}(\phi,\varphi,t) = -C_{Cn_i}(\phi)\omega_{Cn_i}^2\rho R(\phi)\cos(\varphi)u_{Cn_i}(t) \tag{98}$$

for each sloshing mode with C_i and C_{ni} being dimensionless pressure profile functions which depend on the tank fill height. The computation of C_i and C_{ni} is based on a series of dynamic mode superposition analyses. Thus, for any fill height, the response of the fluid-structure concentrated mass model to an arbitrary seismic excitation is computed taking into consideration only the 8-th sloshing mode. The resulting hydrodynamic pressure distribution is equal to p_{cn} therefore, the profile functions C_{ni} can be computed using equation (98). Then, a time domain simulation is performed, based on the same seismic excitation as in the dynamic mode superposition analysis, and the total hydrodynamic pressure distribution p is obtained. Finally, the impulsive pressure distribution pi results from equation (96) and the corresponding pressure profile function C_i from equation (97).

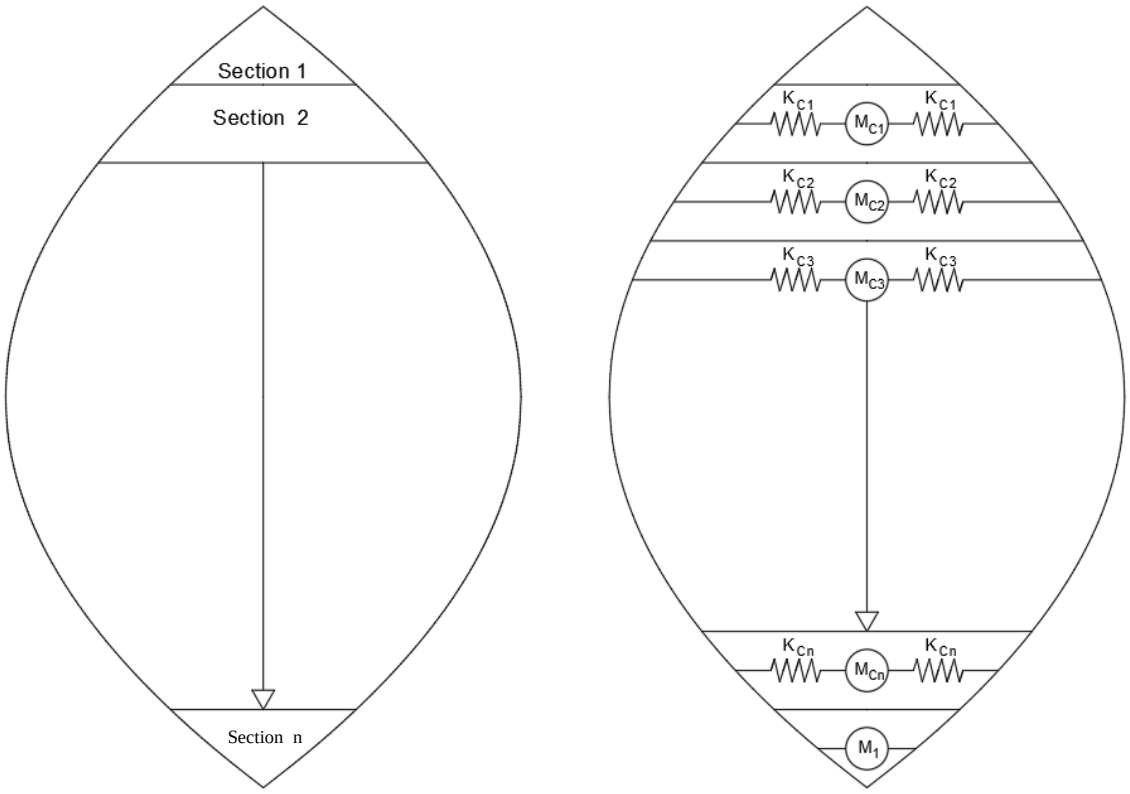

Figure 44. The impulsive-convective idealisation of fluid motion.

The QSD is divided into 10 sections where each section contains a representative mass. Based on the form of the parabolic ogival shell, each mass component is calculated by:

$$m_i = \rho V_i \tag{99}$$

where:

$$V_i = 2\pi \int_{y1}^{y2} \left(\frac{D^2}{4} - 2\frac{D^2}{H^2} y^2 + 4\frac{D^2}{H^4} y^4 \right) dy = 2\pi \left[\frac{D^2}{4} y - \frac{2D^2}{3H^2} y^3 + \frac{4D^2}{5H^4} y^5 \right]_{y_i}^{y_{i+1}} \tag{100}$$

$$= \frac{2\pi}{15} D^2 H$$

Note: D and H are defined in Figure 3b

The spring constants, K_{cn}, is calculated as follows utilising the form of the parabolic ogival shell:

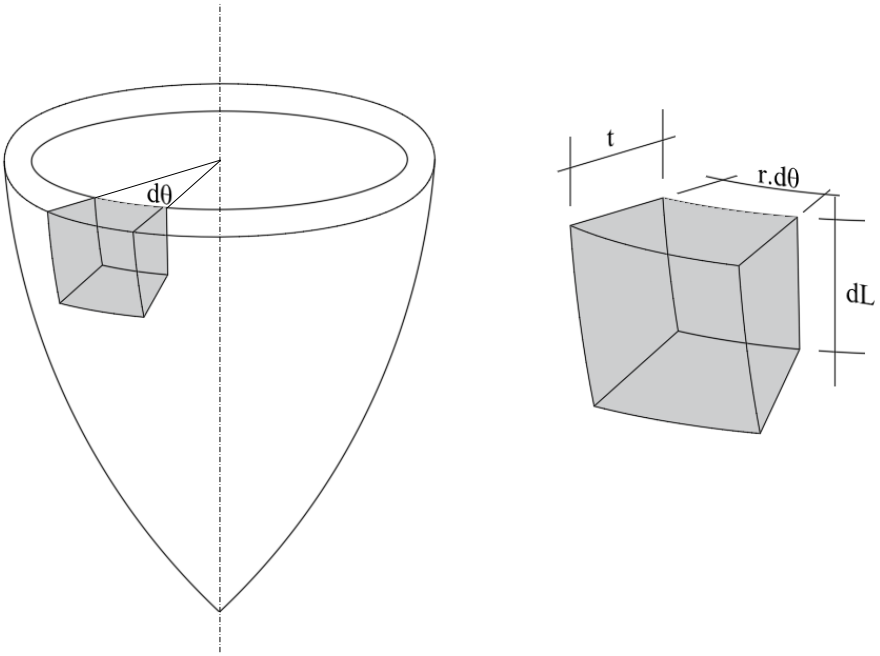

Figure 45. A differential element from the parabolic ogival shell

The stiffness component denoted as:

$$K_{Cn} = \omega_n^2 M_{Cn} \tag{101}$$

From first principles:

$$K = \frac{AE}{L} \tag{102}$$

Where: A is the crossectional area, E is the Young's Modulus and L is the length of the element. Then for the differential element in Figure 45,

$$\Delta K = -\frac{AE}{L^2}\Delta L \tag{103}$$

Where, $A = txd\theta$ and $dL = \sqrt{1+x'^2}\,dy$

Hence,

$$L = -\frac{y\sqrt{1+\frac{16D^2y^2}{H^4}}}{2} - \frac{8H^2 a\sinh\left(\frac{4D}{H^2}y\right)}{D} + \frac{H\sqrt{1+\left(\frac{2D}{H}\right)^2}}{4} + \frac{H^2 a\sinh\left(\frac{2D}{H}\right)}{8D} \tag{104}$$

The stiffness can now be calculated:

$$\begin{aligned} K_i &= -E\int_{\theta=0}^{2\pi}\int_0^{y_i}\frac{tx}{L^2}\sqrt{1+x'^2}\,dy d\theta \\ &= -2\pi E\int_0^{y_i}\frac{tx}{L}\sqrt{1+x'^2}\,dy \\ &= -2\pi E\int_0^{y_i}\frac{tx}{L^2}\sqrt{1+\left(\frac{4y_1}{H^2}\right)^2}\,dy_1 \end{aligned} \tag{105}$$

Where the coordinates:

$$x = D\left(\frac{1}{2} - \frac{2y^2}{H^2}\right) \tag{106}$$

and

$$y_1 = y - \frac{H}{2} \tag{107}$$

By substituting (93)and (104) in (101) ω_i is calculated.

Now the shell stress components can be calculated

$$F_{\theta_j} = p \times \sin(\varphi) \tag{108}$$

and

$$F_{\varphi_j} = p \times \cos(\varphi) \tag{109}$$

The stress components is calculated by dividing the respective forces by the shell thickness, Hence,

$$\sigma_{\theta\, j} = \frac{F_{\theta\, j}}{t_j} \tag{110}$$

And

$$\sigma_{\varphi\, j} = \frac{F_{\varphi_j}}{t_j} \tag{111}$$

3.3.3 Finite Element Modelling of the QSD

3.3.3.1 Introduction

Sloshing, the dynamic behaviour of the liquid's free surface in its retaining structure is of significant importance and is one of the major concerns in the design of liquid retaining structures. As noted by Abramson, H. (1967), for several years, this subject has been a significant concern for scientists, engineers and mathematicians. Any disturbance initiates sloshing to a partially filled liquid container. According to Ibrahim (2006), the free liquid surface can experience different varieties of motion comprising of simple planar, nonplanar, symmetric, asymmetric, rotational, irregular beating, quasi-periodic and chaotic all depending on the type of disturbance and the geometry of the container. When the free liquid surface motion interacts with the elastic support structural dynamics of internal resonance conditions, the free surface modulates. For this investigation, sloshing would be investigated only under seismic excitation.

The difficulty of sloshing involves the assessment and estimation of the hydrodynamic pressure distribution on the container's surface, moments, forces and the natural frequencies of the free liquid surface. Sloshing dynamics has an infinite number of natural frequencies, and the lowest mode is most likely to be excited by concentrated seismic action, which directly affects the dynamic stability and performance of liquid retaining structures. According to Ibrahim (2006), for this reason, previous studies focused on investigating forced harmonic oscillations near the lowest natural frequencies, which are predicted by the fluid field linear equations.

Previous research of sloshing has a long history and presently continues to grasp the importance because of its significance in the application in structural and aerospace engineering. After several decades of research, several practical approaches for researching has been proposed. However, because of its extreme nonlinear effects, solving the dynamics of sloshing is still a great challenge, and a vast amount of work is still essential to develop and confirm theories and fully grasp the understanding sloshing dynamics. Typically, there are three main approaches to analyse the sloshing phenomenon, which are theoretical analytic technique, numerical technique, and experimental technique.

In this section, the research method and methodology is outlined to show how project objectives were accomplished. The section will discuss the collection and interpretation of data, the modelling approach used, and type of analysis. The research aims to provide a QSD design under the sloshing phenomena in the Caribbean under seismic excitations

Examining the effects of the sloshing forces are being investigated based on previous theories developed by other researchers. These theories were utilised to investigate sloshing dynamics within the Caribbean region. Statistical time history acceleration data was obtained to run the dynamic analysis, where the results were used to describe the sloshing phenomena in the different geometry of QSDs, explain the different sloshing modes observed and predict the sloshing phenomena under similitude condition.

3.3.3.2 Data Collection

For this investigation, two types of data were used, namely, seismic maps of the Caribbean and electronic numerical time history acceleration records.

Seismic maps were used to determine the global seismicity of the Caribbean to acquire appropriate time history records. This was done by identifying the earthquake zones, fault type, seismic depth and Peak Ground Acceleration (PGA). The University of the West Indies-Seismic Research Centre (U.W.I. – S.R.C.) and the United States Geologic Survey (U.S.G.S.) were the trusted source used to acquire this information.

Time history acceleration records were the primary type of data utilised to carry out dynamic explicit analysis. These records were used to simulate ground motion of an actual earthquake, which has occurred in the past. By consultation, it was concluded that three were limited records available for the Caribbean. For such, records from another country of similar seismicity to the Caribbean were adopted. These records were obtained from the Pacific Earthquake Engineering Research Center (PEER) website and the United States Geological Survey's Earthquake Hazard Program.

3.3.3.3 Caribbean Tectonics

The Caribbean is an example of an arc system formed at a convergent plate boundary (more specifically, at a subduction zone. This is the leading cause of the volcanic and seismic activity in the Caribbean. When plates move as accumulated energy is released, tectonic earthquakes are generated.

3.3.3.3.1 Seismicity of the Caribbean Region

Extensive diversity of tectonic regimes characterises the perimeter of the Caribbean plate, involving no fewer than four major adjacent plates (North American, South American, Nazca, and Cocos). Inclined zones of deep earthquakes, deep ocean trenches, and arcs of volcanoes clearly indicate subduction of oceanic lithosphere along the Central American and Atlantic Ocean boundaries of the Caribbean plate, while shallow seismicity and focal mechanisms of significant shocks in Guatemala, northern Venezuela, and the Cayman Ridge and Cayman Trench indicate a transform fault and divergent basin tectonics.

The depth profile panels portray earthquakes that extend from the Middle America Trench axis in the west to depths as much as 300 km beneath Guatemala and from the Lesser Antilles Trench axis in the East to depths close to 200 km beneath Guadeloupe and the northeast Caribbean. In contrast, seismicity along the portions of the Caribbean plate margins from Guatemala to Hispaniola and from Trinidad to western Venezuela is suggestive of transform fault tectonics.

Along the northern margin of the Caribbean Plate, the North America plate moves west, relative to the Caribbean plate, at approximately 20 mm/year, resulting in major trans-current faults and troughs. Further east, the North America plate subducts the Caribbean plate which results in surface expression of the deep Puerto Rico Trench. Hence, a zone of intermediate focus earthquakes develops in the subducted slab.

The plate boundary curves around Puerto Rico and the northern portion of the Lesser Antilles where the plate motion vector of the Caribbean plate relative to the North and South American plates is less oblique, resulting in active island-arc tectonics. The North and South America plates subduct the Caribbean plate along the Lesser Antilles Trench at rates of about 20 mm/year; consequently, there are both intermediate focus earthquakes within the subducted South America plate and an array of active volcanoes along the archipelago. The southern Caribbean plate boundary along with the South America plate strikes in an east-west direction across the island of Trinidad and western Venezuela and is characterised by significant strike-slip faults and shallow seismicity, resulting from relative plate movement of about 20 mm/year. Further to the west, a broad zone of convergence move southwest to western Venezuela and central Columbia. Plate boundaries transition from Caribbean/South America convergence in the east to Nazca/South America convergence in the west. The Nazca-Caribbean plate boundary offshore of Columbia is differentiated by convergence at about 65 mm/year. The Cocos plate, along the western coast of Central America, subducts the Caribbean plate at rates of 72–81 mm/year, resulting in a relatively high seismic hazard and a chain of numerous active volcanoes; here intermediate-focus earthquakes occur within the subducted zone of the Cocos plate to depths of nearly 300 km.

3.3.3.4 Time History Acceleration Data

3.3.3.4.1 Time History Acceleration Data Collection

The time history acceleration records used for this research are from Japan. Japan was chosen because it shares seismic similarities with the Caribbean. These include;

- Located within a subduction zone
- Characterised predominantly by shallow seismicity

The primary mechanism for earthquakes in both countries are the reverse fault due to the convergent plate boundary at the subduction zone; and the strike-slip which occurs parallel to the direction of subduction (plate motion).

The time history records were retrieved from PEER-NGA-West2 database. The NGA-West2 consists of an extensive, comprehensive set of time history recorded worldwide in active tectonic regimes. The earthquake used for this investigation is: **Kobe;RSN 1120;Takatori 1995.**

Ground motion information:

i. NGA Record Sequence Number 1120
ii. Magnitude = 6.9
iii. Closest Distance = 1.5 km
iv. Hypocentral Distance = 22.19 km
v. Velocity = 256 m/s
vi. Mechanism = Strike slip
vii. Tp = 1.55 s

PGV = 153.2 cm/s

Figure 46 Figure 47 and Figure 48 shows the time-history acceleration plots used for the study.

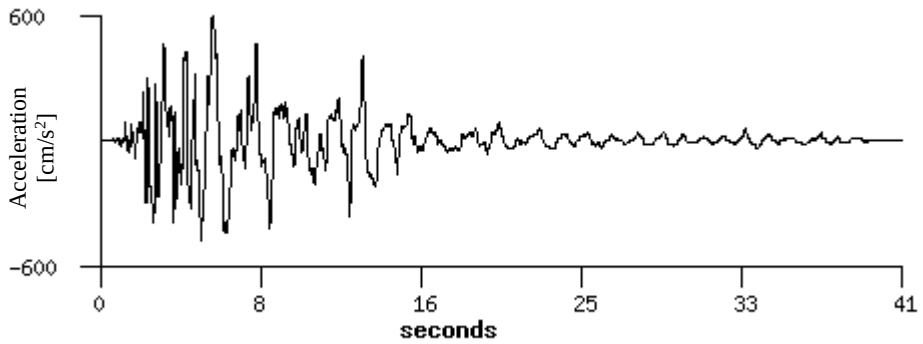

Figure 46. Horizontal (X-Axis) Time-History Acceleration Plot for Kobe; RSN 1120; Takatori 1995

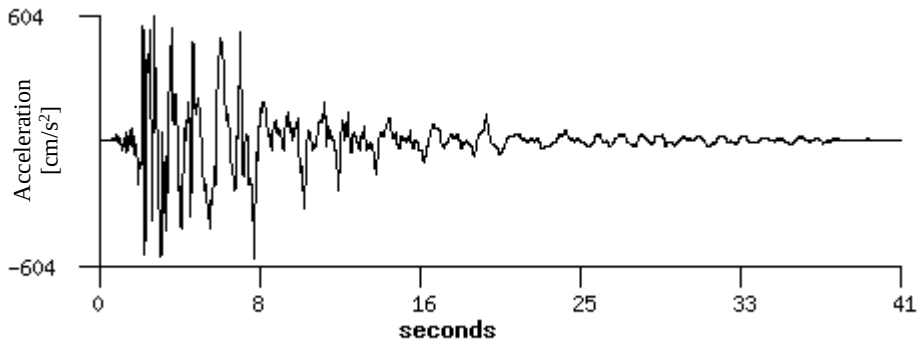

Figure 47. Horizontal (Y-Axis) Time-History Acceleration Plot for Kobe; RSN 1120; Takatori 1995

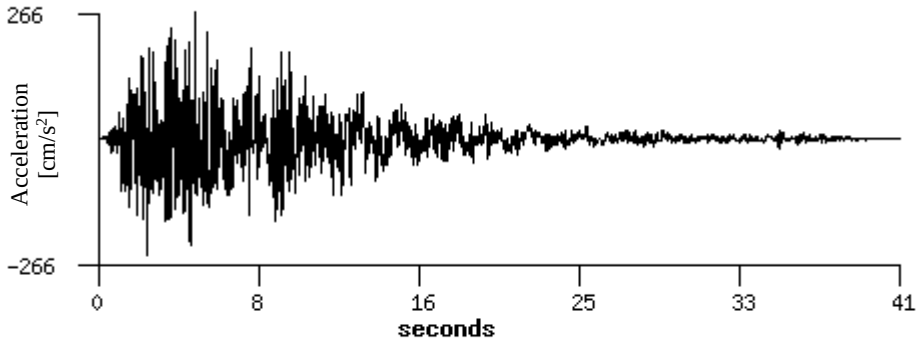

Figure 48. Vertical (Z-Axis) Time-History Acceleration Plot for Kobe; RSN 1120; Takatori 1995

3.3.3.5 Structural Dynamics

Several factors influence the FEA modelling technique. The complexity of the system and the number of influencing parameters need to be determined. This section covers the assumed-modes method, the finite element method, complex analysis using the Fourier transform, as well as the commercial finite element analysis software ABAQUS.

3.3.3.1 Single Degree of Freedom Systems

The fundamental equation in structural dynamics and linear vibration theory a second-order differential equation that relates force to displacement, velocity, and acceleration.

$$m\ddot{x} + c\dot{x} + kx = p(t) \tag{112}$$

This equation of motion represents a single lumped-parameter model and is derived using Newton's laws, see Figure 49.

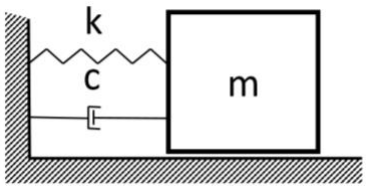

Figure 49. Single-Degree-of-Freedom Lumped Parameter Model

The elements which comprise this model include the mass, the spring, and the damping component. According to the model, an object is placed into motion through the displacement of its mass at a specified distance from a reference. The spring element then goes into tension due to being stretched, and it has the desire to compress and restore the system to equilibrium. The damping component, which occurs when impacted by the spring's restoring motion, dissipates system energy, decreasing the time required to reach equilibrium.

3.3.3.2 Newton's Laws to Lumped-Parameter Models

By connecting several lumped-parameter models, a simple single degree of freedom (SDOF) model can be constructed into a more complex multiple degrees of freedom (MDOF) model. Depending on the complexity of this model, the correct mathematical models can then be developed through the application of Newton's laws and/or the assumed modes method. Newton's laws are best used on simpler models comprised of a few lumped parameter models described by a mass, spring, and damping values. For more complex systems, the assumed modes method is preferred due to the influence of additional parameters on the system.

3.3.3.3 Assumed Modes Method

The assumed modes method, developed by Goodell, (2016) incorporates an extension of the virtual displacement method to produce a generalised parameter model of a continuous system to approximate the deformation of that system. To create the generalised-parameter single-degree-of-freedom model of a continuous system, a single assumed mode is used;

$$v(x;t) = (x)q_v(t) \tag{113}$$

The shape function should represent a single deformation experienced by the structure. The generalised displacement coordinate is defined as qv(t) with the subscript v denoting the generalised coordinate concerning the physical displacement v(x; t). The shape function ψ(x) can be represented by any function. However, a shape representing the deforming structure should be chosen. To generate an MDOF model of a continuous system, equation (113) is expanded to include N shape functions, thus allowing the continuous displacement to be approximated through a finite sum.

$$v(x,t) = \sum_{i=1}^{N} \psi_i\,(x)q_{vi}(t) \tag{114}$$

The assumed-modes method consists of substituting this equation into the expressions for kinetic energy, τ, and strain energy, ν, through a representation of the material by its density, ρ, area A, length L, and modulus of elasticity E, as shown below;

$$\tau = \frac{1}{2}\int_0^L \rho A\,(\dot{u})^2\;dx \tag{115}$$

$$\tau = \frac{1}{2}\int_0^L \rho A\,(\dot{u})^2\;dx \tag{116}$$

$$\nu = \frac{1}{2}\int_0^L EA\,(v')^2\;dx \tag{117}$$

The analyst defines the N^{th} DOF assumed modes through the selection of the shape function. The shape functions must form a linearly independent set and must possess derivatives up to the order appearing in the strain energy, *v*. The shape function must also satisfy all the prescribed BCs.

3.4 Chapter Summary

This chapter outlined the procedures adopted for conducting both numerical and experimental work in the material characterisation of the 3D printed polymers as well as numerical work in examining the behaviour of the QSD. The research methods and methodologies outlined show how project objectives were accomplished. The chapter encompasses discussions of the collection and interpretation of data, the modelling approach used and type of analysis.

The research objectives of the proposed study were to assess and estimate the material characteristics of the 3d Printed polymer as well the hydrodynamic pressure distribution on the QSD shell. The procedures for the solution of the shell forces and natural frequencies of the free liquid surface impacting on the QSDs in the Caribbean seismic zones shows how these factors have a direct consequence on the dynamic stability and performance of stationary liquid in QSDs.

Examining the research problem and the research objectives, the effects of the sloshing forces are being investigated on the basis of previous theories developed. These theories were utilised to investigate sloshing dynamics within the Caribbean region. Statistical time history acceleration data was obtained to run the dynamic analysis, where the results were used to describe the sloshing phenomena in the different geometry of tanks. This research was both qualitative and quantitative in nature.

Seismic maps were used to determine the global seismicity of the Caribbean to acquire appropriate time history records. This was done by identifying the earthquake zones, fault type, seismic depth and Peak Ground Acceleration (PGA). The University of the West Indies-Seismic Research Centre (U.W.I. –

S.R.C.) and the United States Geologic Survey (U.S.G.S.) were the trusted source used to acquire this information.

Time history acceleration records were the primary type of data utilised to carry out dynamic explicit analysis. These records were used to simulate ground motion of an actual earthquake, which has occurred in the past. By consultation, it was concluded that three were limited records available for the Caribbean. For such, records from another country of similar seismicity to the Caribbean were adopted. These records were obtained from the Pacific Earthquake Engineering Research Center (PEER) website and the United States Geological Survey's Earthquake Hazard Program

The next chapter discusses the results obtained from the studies.

4.0 Results

4.1 Introduction

This chapter describes the results from the experimental and numerical studies performed on 3D printed polymers. Results from the first principles analyses are then described followed by those of the finite element analyses.

4.2 3D printed polymer characterisation

4.2.1 Tensile tests and simulations

Figure 50 presents the stress-strain plot comparing experimental tests and numerical simulation results of ABS samples. Average stress and strain values that were plotted to display the stress-strain plot of the specimens printed at (0, 90º) orientations along the longitudinal and transverse directions. The curves for Orientation 1 and 2 (experimental) show similar characteristics to each other confirming Rodríguez (2001) statements of special orthotropic conditions where E1= E2. The transverse direction E3 yields at lower stress compared to longitudinal showing the effect of lower bond strength.

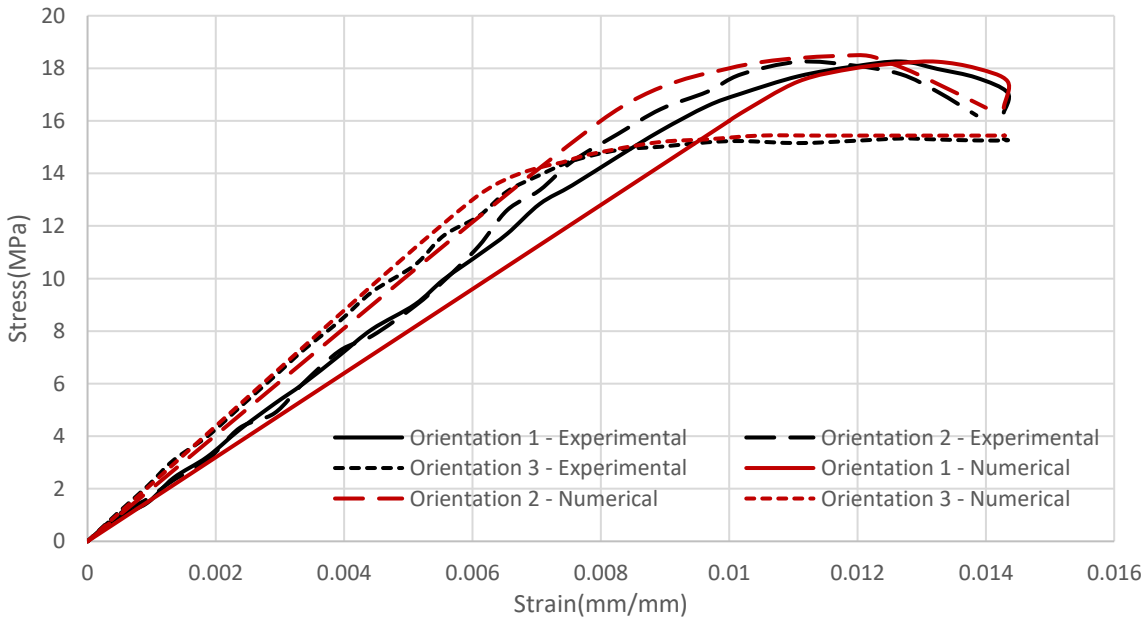

Figure 50. Stress-strain plot comparing experimental tests and numerical simulation results of ABS samples with print orientations 1,2 and 3.

4.2.2 Flexural tests and simulations

Figure 51 presents the load vs deflection curves for specimens constructed longitudinal to the (x, y, z)/ (1, 2, 3) directions. A total of ten (10) specimens per orientation were tested, and the average deflections values at a load of 200N were recorded. For specimens printed longitudinal to the x/1 direction and loaded perpendicularly to that axis showed the highest yielding load compared to the other orientations.

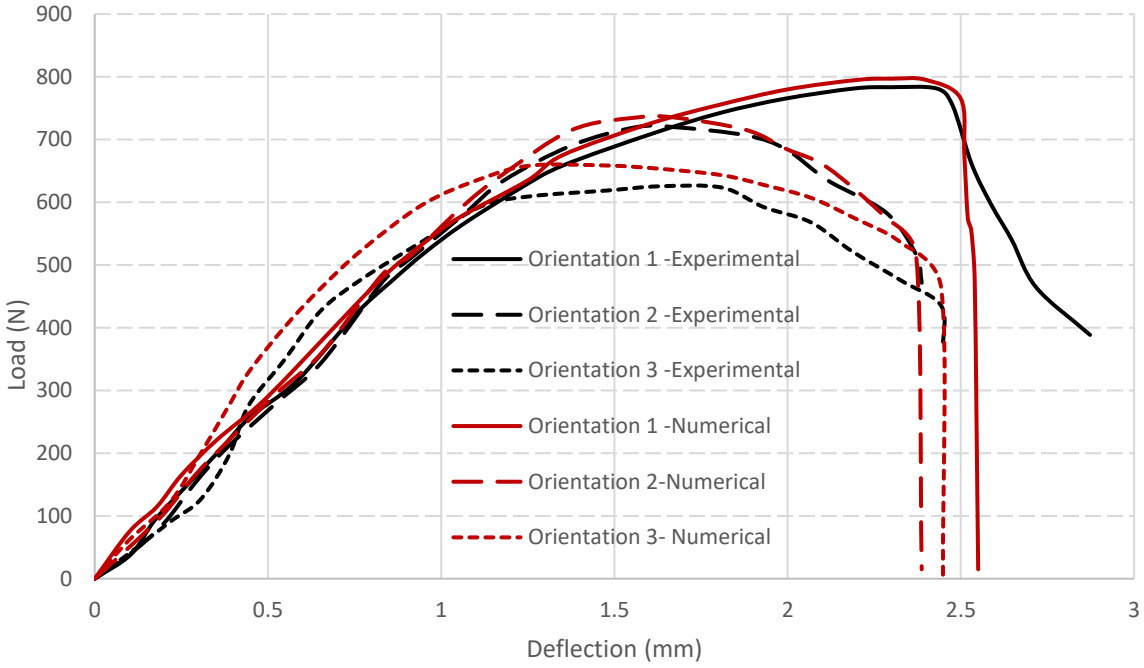

Figure 51. Load-deflection plot comparing experimental tests and numerical simulation results of ABS samples with print orientations 1,2 and 3.

The results from the numerical analysis for the bending test were in close agreement with that from the experimental tests. The load vs deflection graph was obtained from the analysis and shown in figure 53. The data however was only extracted from the deformed section of the geometry and not the entire specimen due to previous mentioned errors. **Error! Reference source not found.** shows some similarities to the experimental and the deflection at 200N were fairly close showing a 4.12% difference in results. The ideal difference desired should fall below 10% as noted in previous studies. Overall, the material properties were predicted accurately.

4.2.3 Torsional property

Figure 52 shows the torsional force against the distance of rotation for the specimens of the three orientation and strain values that were plotted to display the torsional stress vs strain graph of the specimens printed at (0, 90^{o}) orientations along the longitudinal and transverse directions. These graphs were used to obtain the effective shear modulus values used in the construction of the stiffness matrix for the numerical modelling. Orientation 3 was printed along the same axis the shaft rotated about and displayed higher torsional stresses at lower strains than the other orientations. The results from the experiment were taken manually and pre-set intervals. This step provided a lot of room for errors and was compensated according to the instructions given by the manual of the apparatus. As such, the data was first recorded as the torsional force vs the angular displacement. The data was then converted in to torsional stress and strain relations to compare with numerical results.

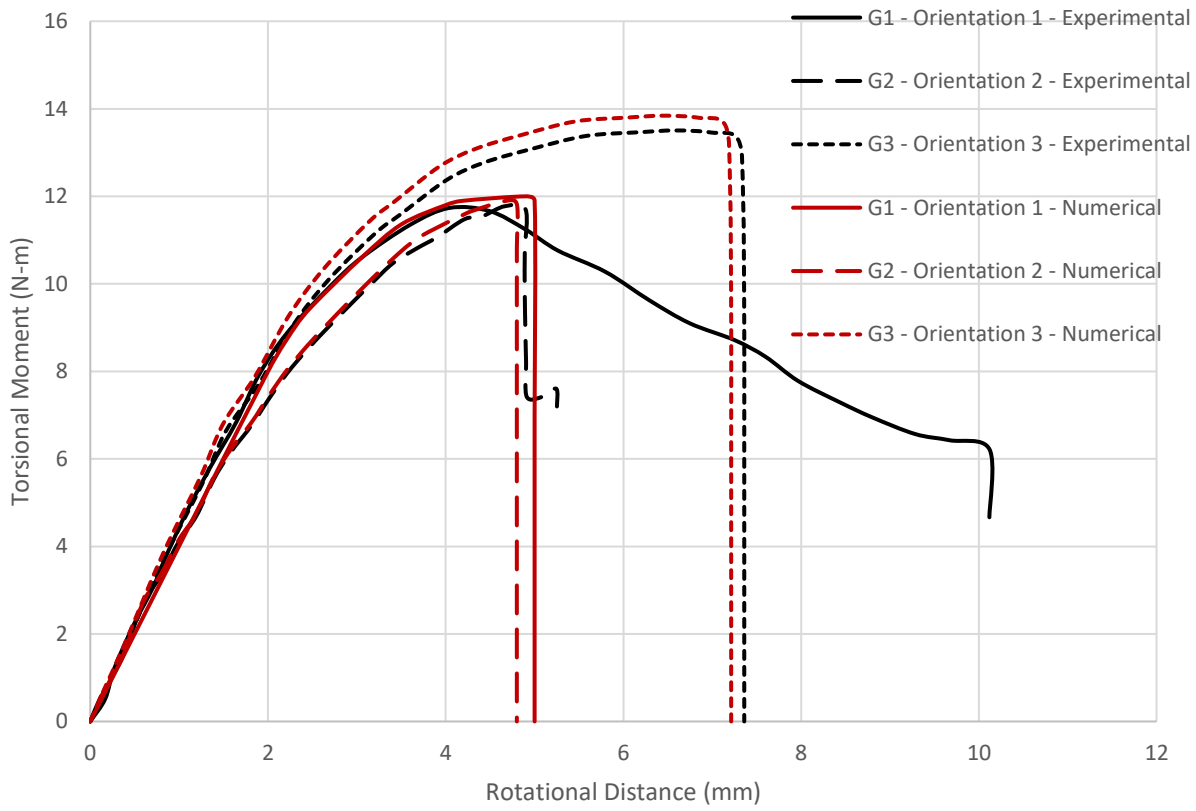

Figure 52. Torsion plot comparing experimental tests and numerical simulation results of ABS samples with print orientations 1,2 and 3.

4.3 First Principles QSD Analyses

The first principles analyses examined a QSD under two (2) conditions. In the first condition, the base is rigidly fixed to the ground, and the second, the QSD is base isolated. The parameters for both simulations of the tank are given in Table 14:

Table 14. Parameters for first principles QSD analyses.

Parameter	**Value**
Height	25 m
Diameter	12.5m
Minimum Shell Thickness	1 m
Maximum Shell Thickness	2 m
Ground excitation (harmonic)	5 Hz
Fill Level	50%

Since the second simulation is base isolated, a plot of the bearing displacement was developed as seen in Figure 53.

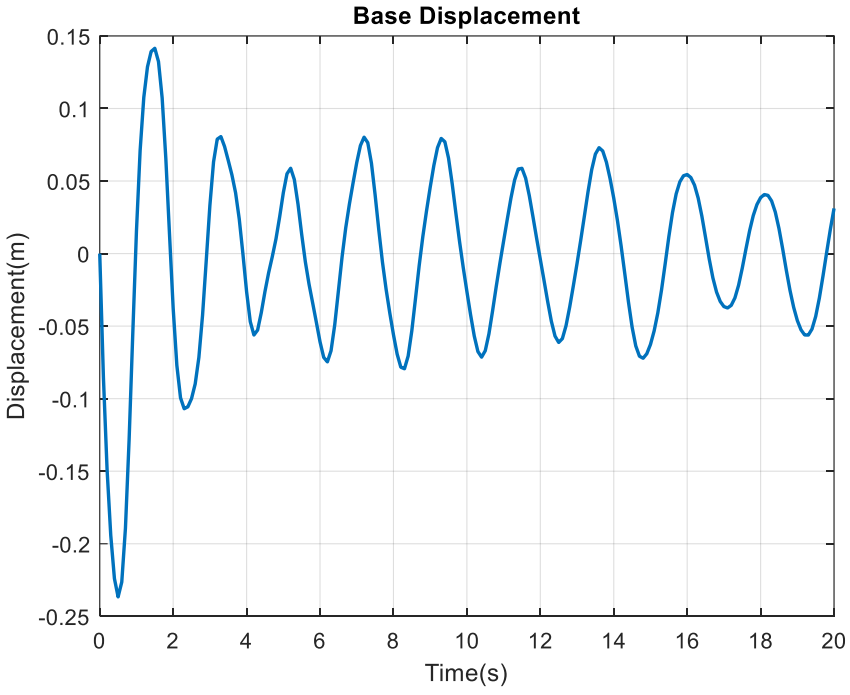

Figure 53. A plot of bearing displacement for base-isolated QSD (5Hz)

The plot shows that the initial seismic impulse has created an initial displacement of 247 mm, which is transient and eventually tapers off to normalised harmonic behaviour. The displacement is dependent on the type of base isolator. A friction-pendulum isolator's range of motion is directly proportional to the mass of its superstructure. Very little is dependent on the friction between the bearing parts (which are usually Teflon coated). Lead- core rubber bearing isolators depend on the stiffness of the rubber layers as well as the lead core. In both cases, Figure 53 displays the typical behaviour of the isolator. Figure 60 and 61 are to be read in accordance with the legend presented in Figure 54.

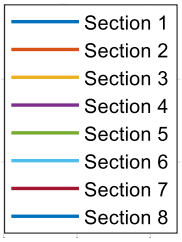

Figure 54. Legend for QSD circumferential section division for the succeeding plots.

4.3.1 Shell Forces

The forces developed in the shell are the hoop or circumferential force, N_θ and the meridional force, N_φ (recall equations (17) and (15) respectively). Upon comparing figures Figure 55a and Figure 56a,

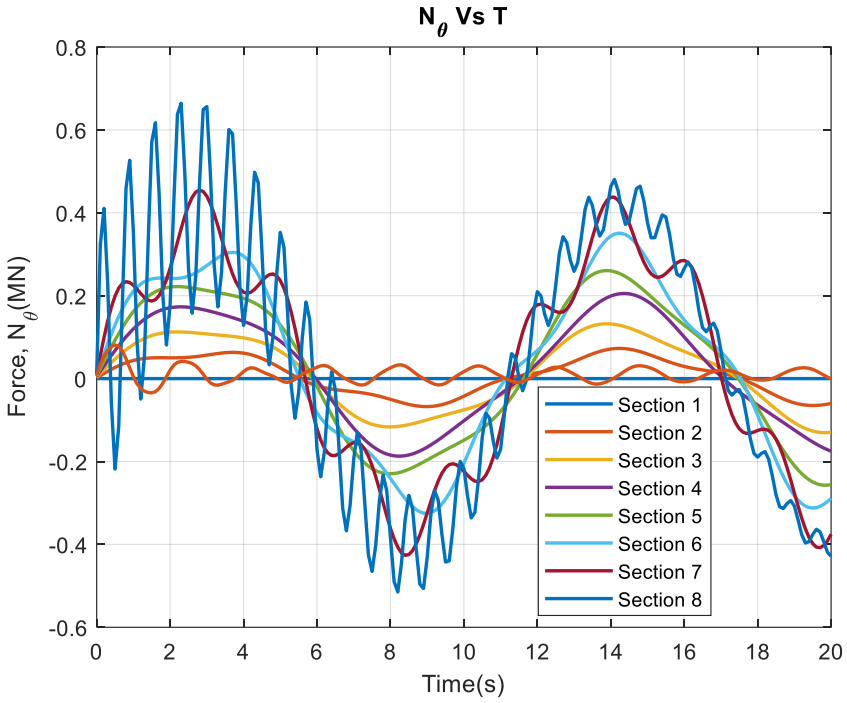

(a)

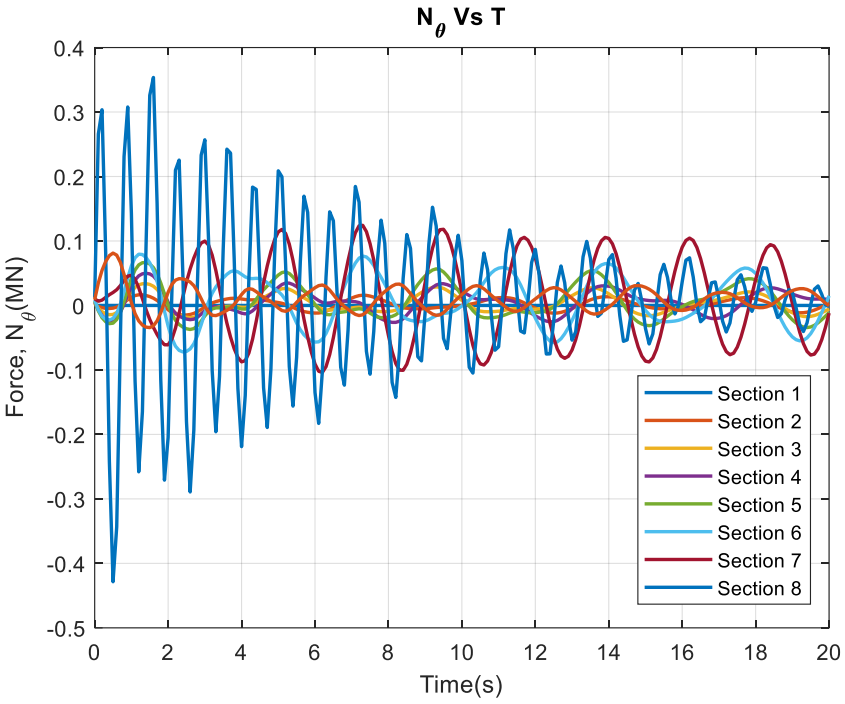

(b)

Figure 55. Circumferential hoop force N_θ in QSD shell, for various sections at 5Hz for (a) Fixed base QSD and (b) Base-isolated QSD

it can be seen that the general shape of the change in the forces follows the overall shape of the input frequency. Although the circumferential shell forces are almost similar, highest circumferential shell forces occur towards the lowest sections of the QSD (sections 7 and 8) while the highest meridional forces also occur in these sections. The highest N_φ values are attributed to the hydrostatic forces that occur in that region. The angular surface movement provides for an increase in meridional force at higher sections. Since the fluid becomes uneven at this section, the circumferential force is translated throughout the region; accordingly, the forces are analogous to those of the lower midsection. Overall, the N_φ is higher than the N_θ by 48.2%.

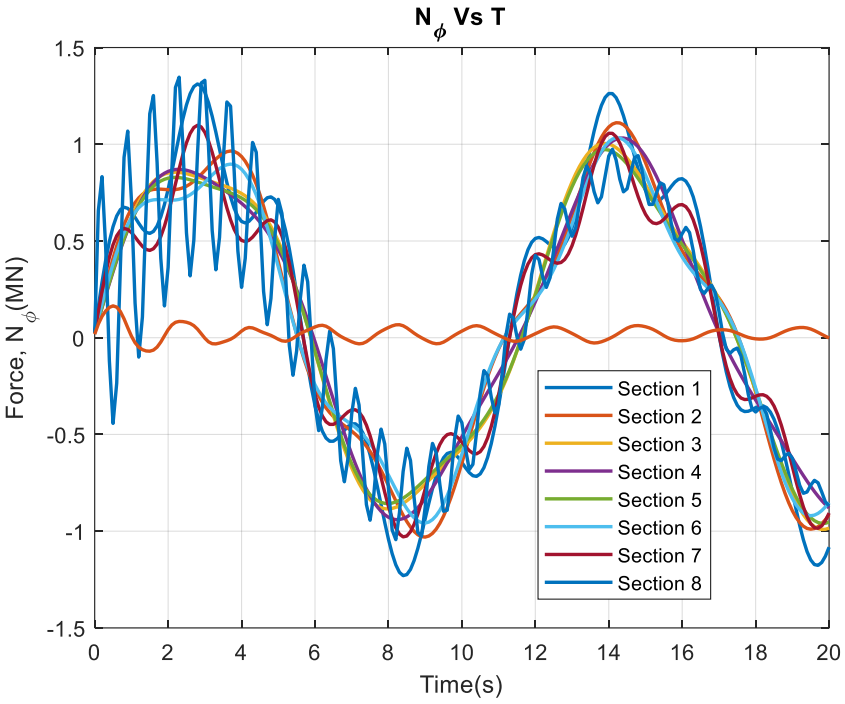

(a)

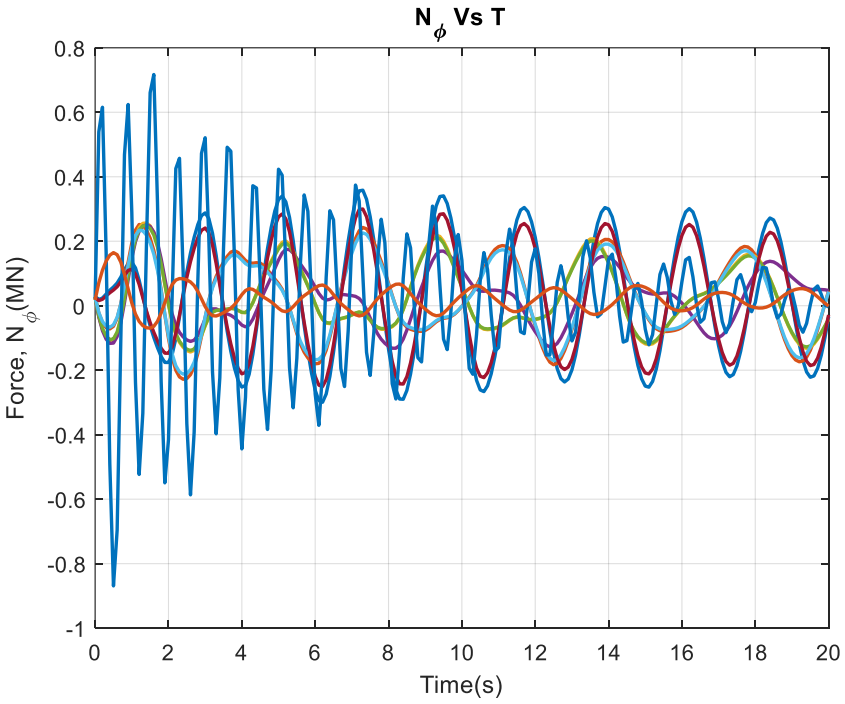

(b)

Figure 56. Meridional force N_φ in QSD shell, for various sections at 5Hz for (a) Fixed base QSD and (b) Base-isolated QSD

The Nθ and Nφ developed due to oscillations from the base isolated model, follow the same mechanical principles as those discussed for the fixed system. The difference is that the period for the frequency is only about 0.2 seconds and follows the general shape of the displacement-bearing plot. The stresses, which were developed by (18), take into account the mechanical properties of the material as well as the cross-sectional thickness at the section where the stress is measured. In and 57 the maximum σ_θ and σ_φ both occur at the base (section 8). It is noticed that section 2 displays some increase in hoop stress.

Figure 58 Figure 57. Circumferential hoop stress σθ in QSD shell, for various sections at 5Hz for (a) Fixed base QSD and (b) Base-isolated QSD

This corresponds to the angular displacement occurring at the free surface of the liquid during the excitation. The base isolated model shows a 10.2% reduction in circumferential stress after the transient behaviour has normalised. The meridional stresses are highest only in the base section of the QSD. This attributed to both the hydrostatic pressure at the base as well as the axial shell loads due to gravity.

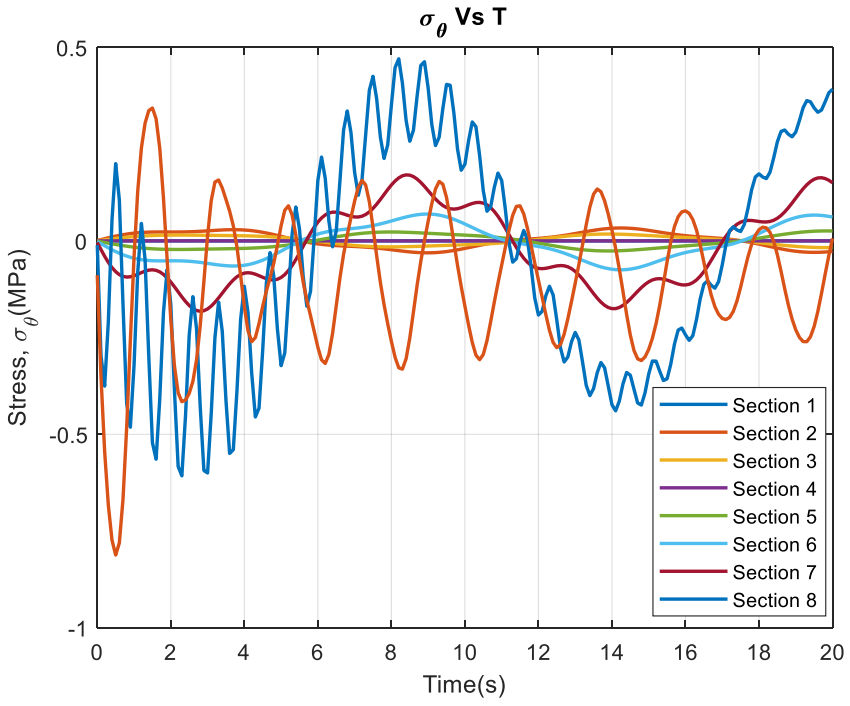

(a)

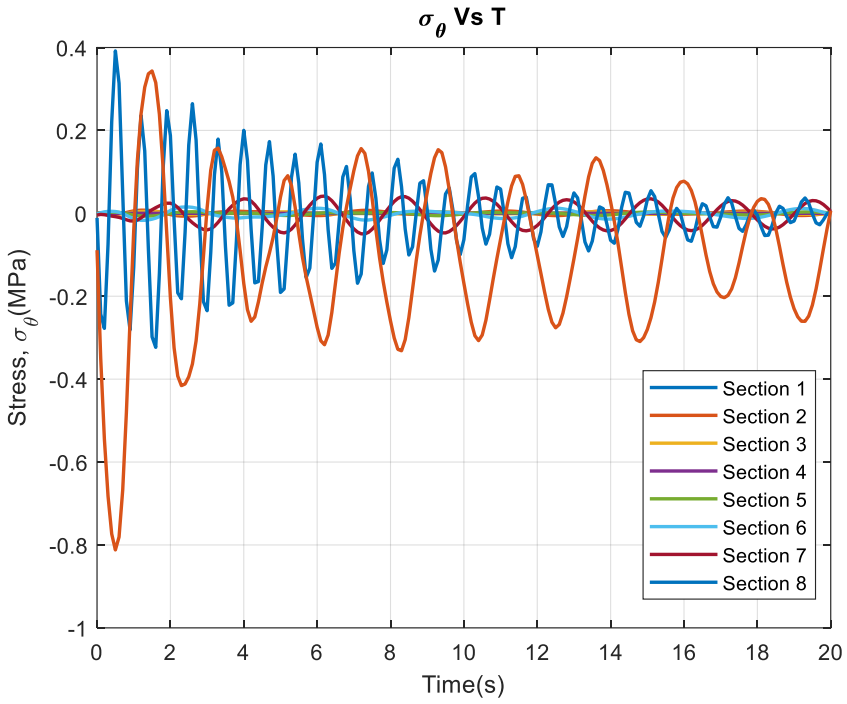

(b)

Figure 58. Meridional hoop stress σ_φ in QSD shell, for various sections at 5Hz for (a) Fixed base QSD and (b) Base-isolated QSD

4.3.2 Comparison of QSD under different fill conditions

Simulations were conducted simultaneously on the QSD outlined in Table 14 above. Each simulation had the same parameters except for the fill levels. Fill levels of 10%, 25%, 50%, 75%, and 90% were each assigned to a separate model.

The peak impulsive displacements varied between each model. The highest impulsive displacement occurred in the QSD with the lowest fill level (10% fill) (see Figure 59). This occurred for both the rigid base and isolated base models because of the smaller volumetric mass coupled with a lighter convective mass. By contrast, the lowest impulsive displacement is at 90% fill. Both plots show that at 3.1 metres from the base of the QSD is where the maximum peak displacement occurs. The base and at heights between 10 and 20 metres have low displacements. The base is rigidly fixed hence the displacement will be small.

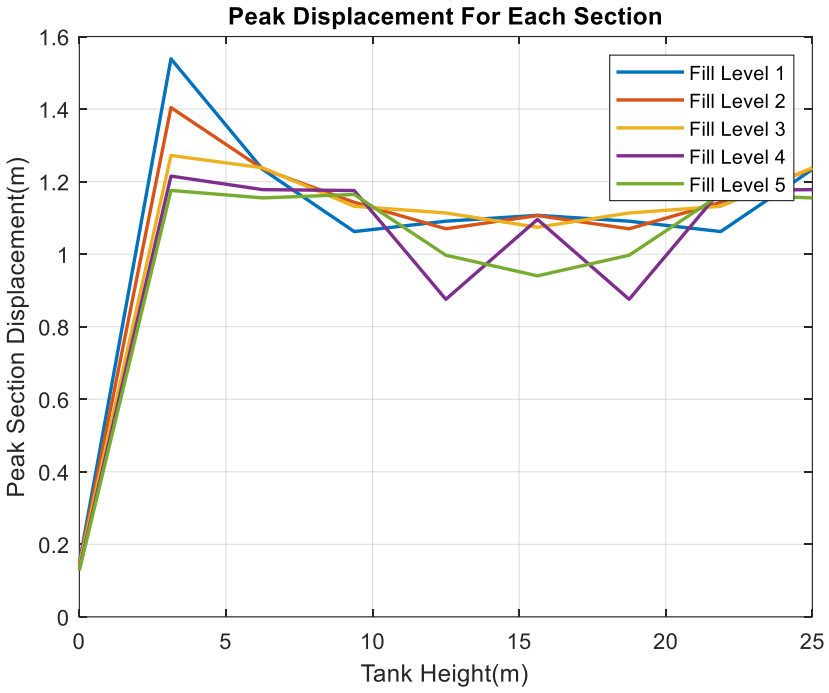

(a)

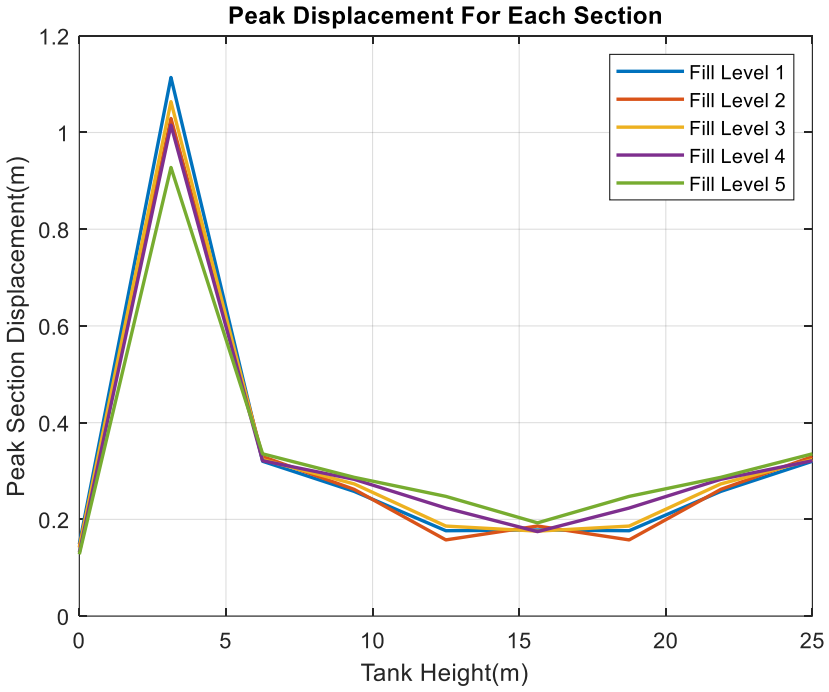

(b)

Figure 59. Comparison of peak impulsive displacement of fluid in QSD, for various fill levels at 5Hz for (a) Fixed base QSD and (b) Base-isolated QSD

Figure 60 and Figure 61 shows comparative relationships for the N_θ and N_φ d among the 5 fill levels. The peak N_θ for the rigid model shows the maximum force in the shell to occur at the 10% fill level while the lowest is at the 90% fill level. This is accurate as the convective mass interacts directly with the internal surface of the shell at that level. The 10% fill level has the lowest value, a reduction of 20% for the same area. The overall N_θ for the base isolate QSD is 50.1% lower than the rigid-base model.

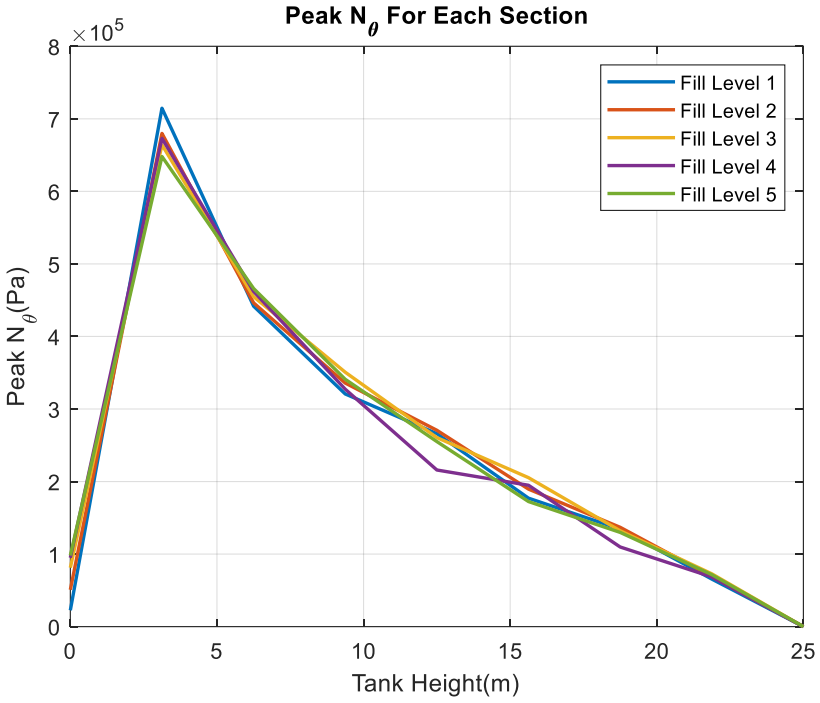

(a)

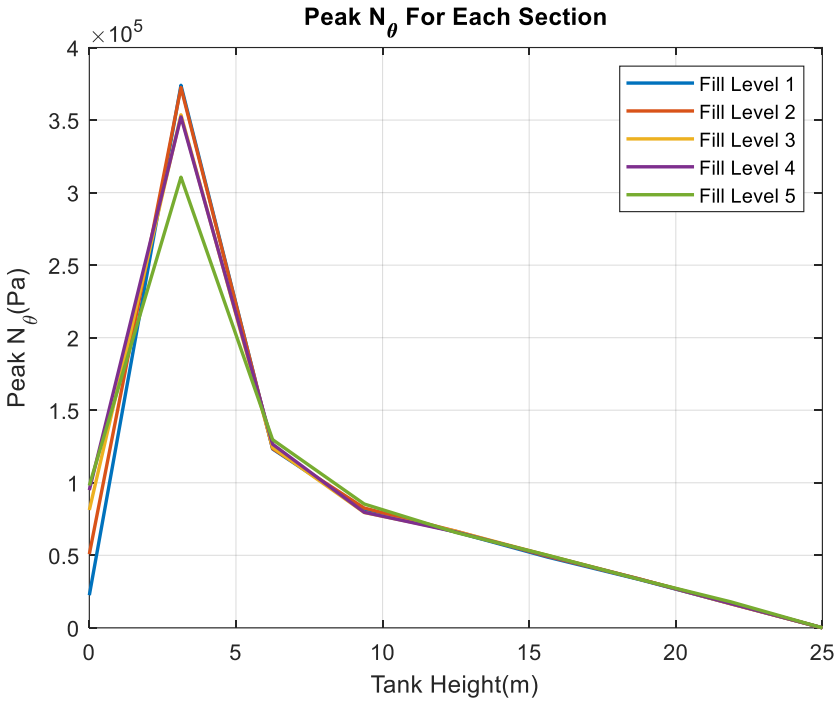

(b)

Figure 60. Comparison of peak circumferential hoop force N_θ in QSD shell, for various fill levels at 5Hz for (a) Fixed base QSD and (b) Base-isolated QSD

The meridional forces along the height of the QSD increase almost linearly towards the base. The base isolated model shows that the 10% fill level impacts the most due to convection of the angular momentum of the free surface to the shell. This is a reduction of 52% of the maximum meridional forces (located at 3.1m from the base). There is an overall reduction of 25% of meridional forces from the 10m height to the apex. This shows that the hydrostatic force governs the sloshing forces.

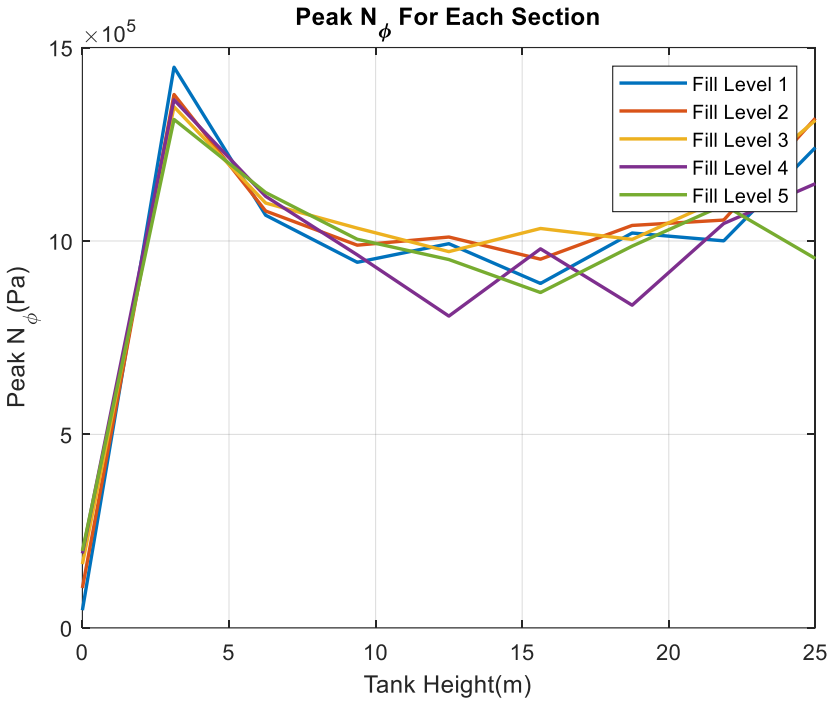

(a)

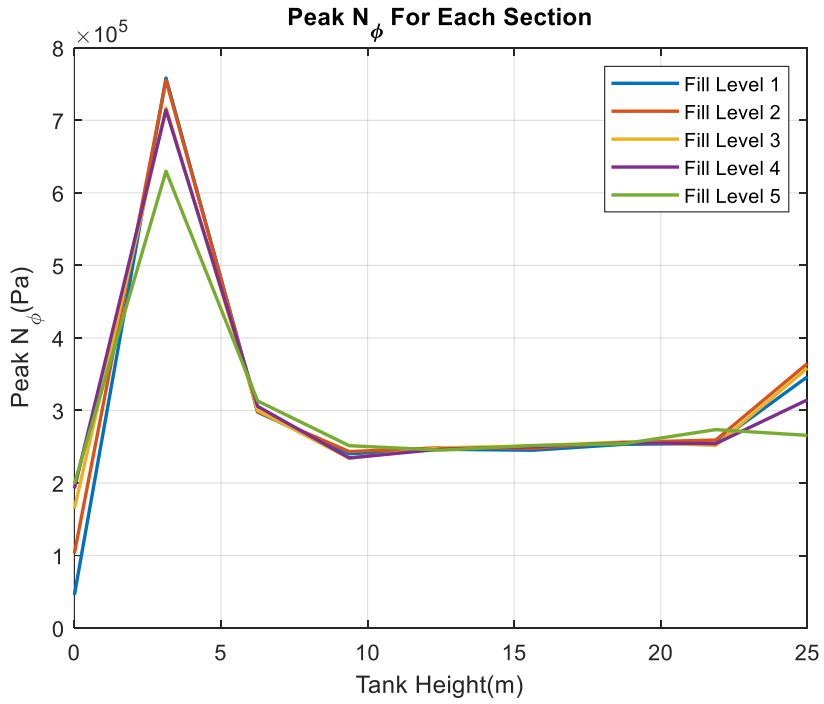

(b)

Figure 61 Comparison of Peak Meridional hoop force N_φ in QSD shell, for various fill levels at 5Hz for (a) Fixed base QSD and (b) Base-isolated QSD

On comparing the peak hoop stresses for the different fill levels, it was found that for the rigid-base model the stress variation was almost negligible. The base isolated QSD displayed a reduction of 36.3%.

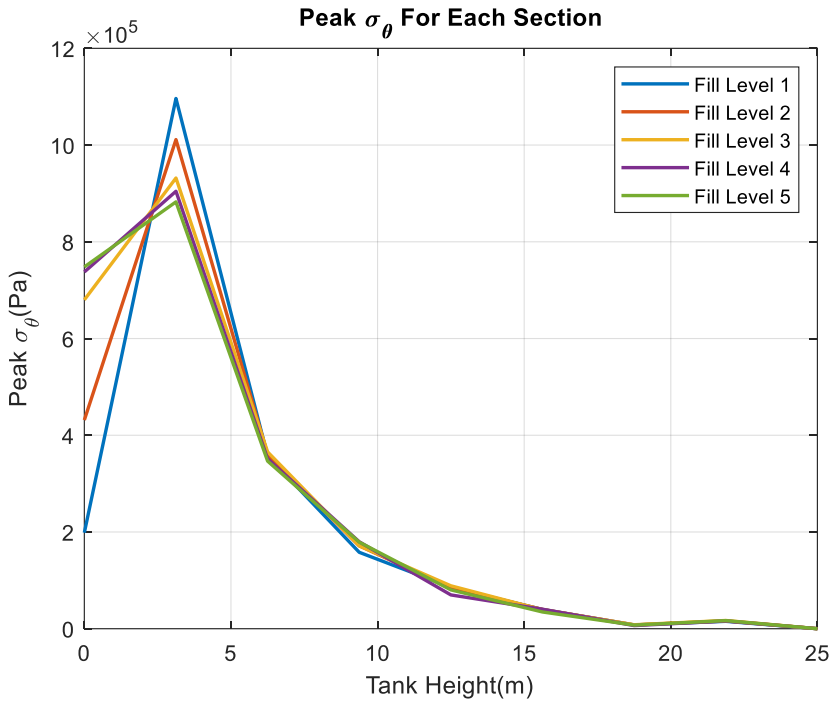

(a)

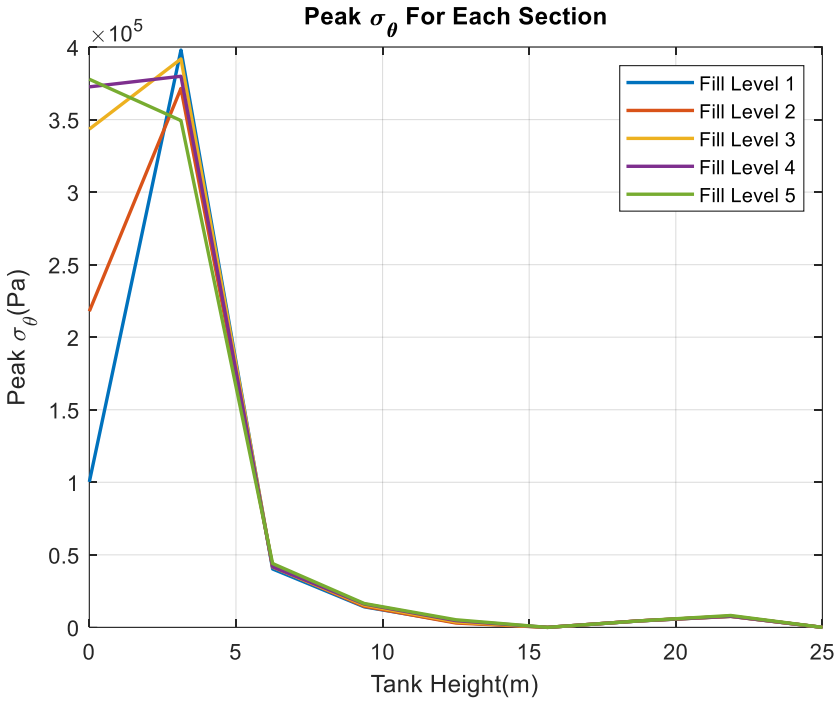

(b)

Figure 62. Comparison of peak circumferential hoop stress σ_θ in QSD shell, for various fill levels at 5Hz for (a) Fixed base QSD and (b) Base-isolated QSD

The peak meridional displayed a similar relationship; however, the maximum stress was at the base.

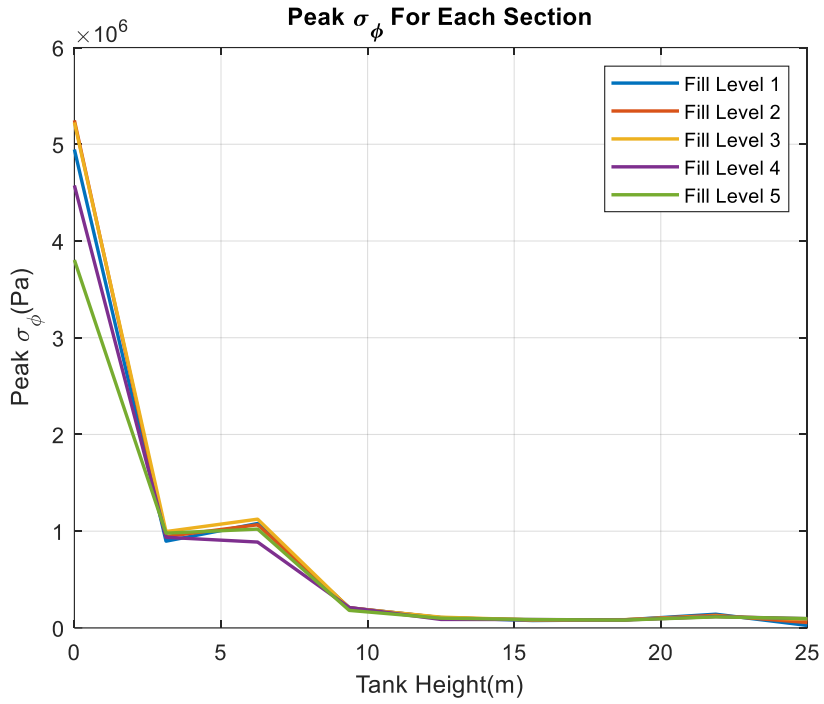

(a)

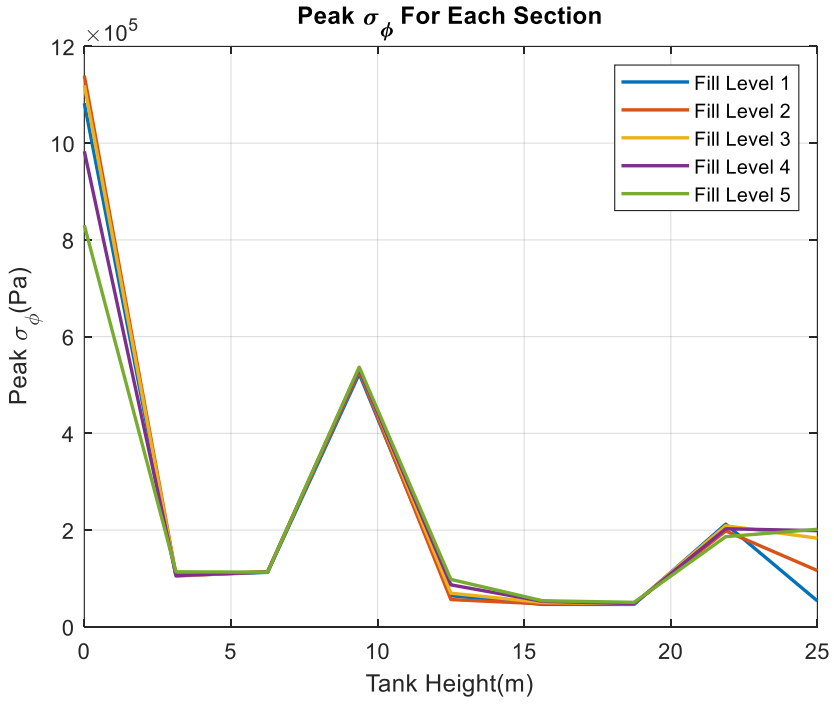

(b)

Figure 63. Comparison of peak meridional hoop stress σ_φ in QSD shell, for various fill levels at 5Hz for (a) Fixed base QSD and (b) Base-isolated QSD

This is due to the hydrostatic force that translates vertically.

4.3.3 Kobe;RSN 1120;Takatori 1995 Time-History Analyses

The first-principles study of the QSD is now extended to include time-history analyses. The models for the QSD were analysed for 10%, 25%, 50%, 75% and 90% fill levels for both fixed base and base isolated models. The parameters for both simulations of the tank are given in Table 15:

Table 15. Parameters for first principles QSD time-history analyses.

Parameter	**Value**
Height	25 m
Diameter	12.5m
Minimum Shell Thickness	1 m
Maximum Shell Thickness	2 m
Ground excitation	Kobe 1995
Fill Level	50%

On examining the results of the analyses, it was evident that the internal stresses in each orthogonal direction were generally in the same range as those of the previous study in section 4.3.3 (see Figure 64 and Figure 65).

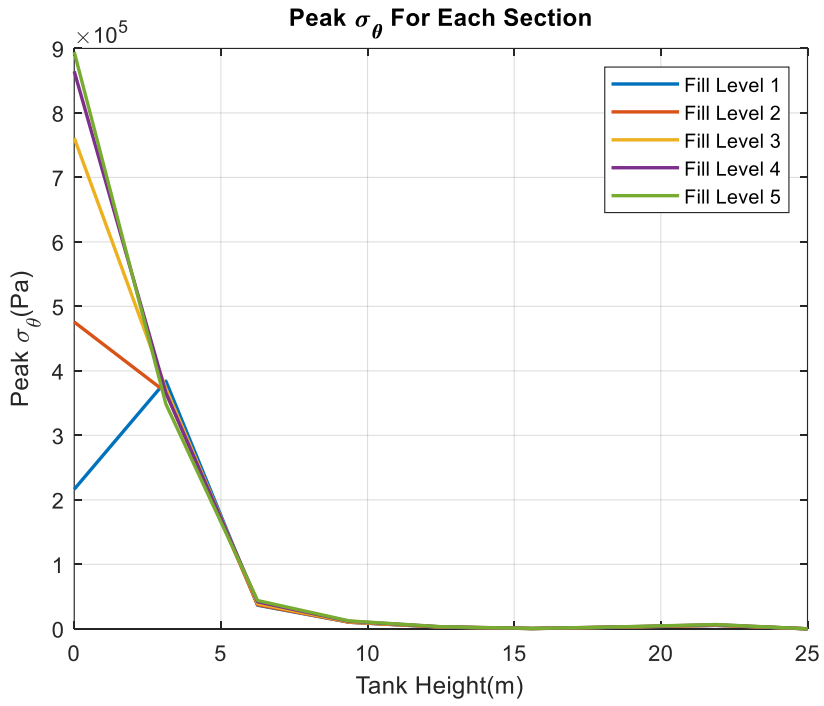

(a)

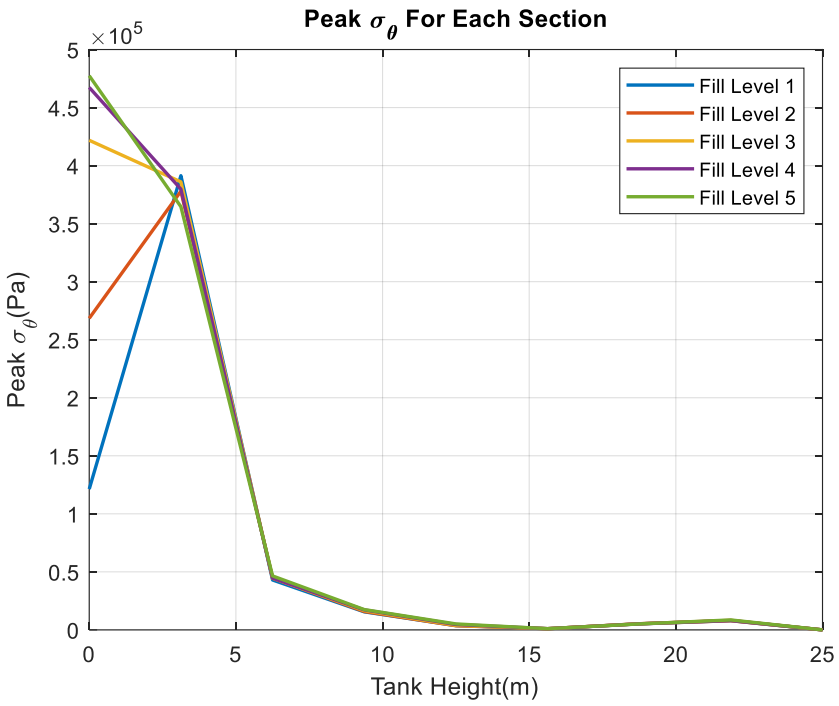

(b)

Figure 64. Comparison of peak meridional hoop stress σφ in QSD shell, for various fill levels analysed with Kobe;RSN 1120;Takatori 1995 time-history data for (a) Fixed base QSD and (b) Base-isolated QSD

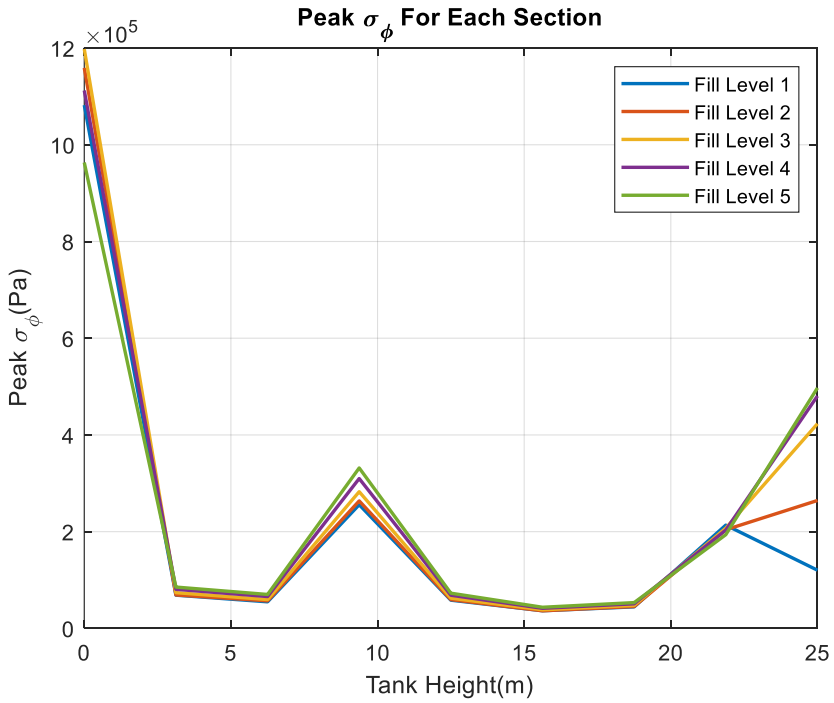

(a)

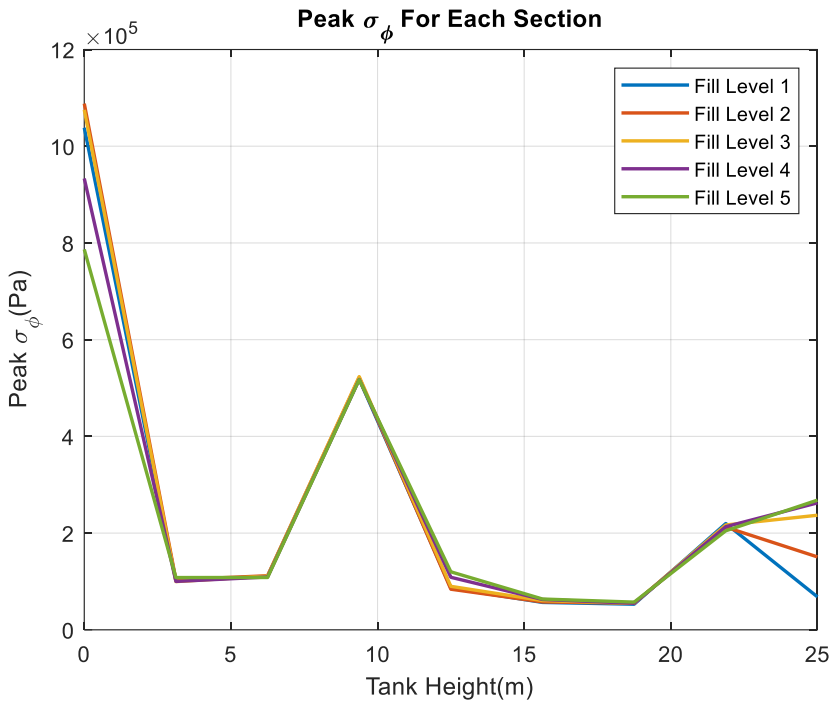

(b)

Figure 65. Comparison of peak meridional hoop stress σφ in QSD shell, for various fill levels analysed with Kobe;RSN 1120;Takatori 1995 time-history data for (a) Fixed base QSD and (b) Base-isolated QSD

4.4 Finite Element QSD Analyses

4.4.1 2D FEA Analysis

The 2-dimensional analyses were grouped into two categories, the first was hydrostatically loaded and the second was dynamically loaded. 25 simulations were conducted for each load case (150 simulations total). The hydrostatic cases proved that the orthogonal stresses increased as the fill level increased (see Figure 66a and Appendix). This stress was reduced as the shell thickness increased. Comparing this with the dynamic cases, the hydrostatic levels produced the most internal stresses in the shell.

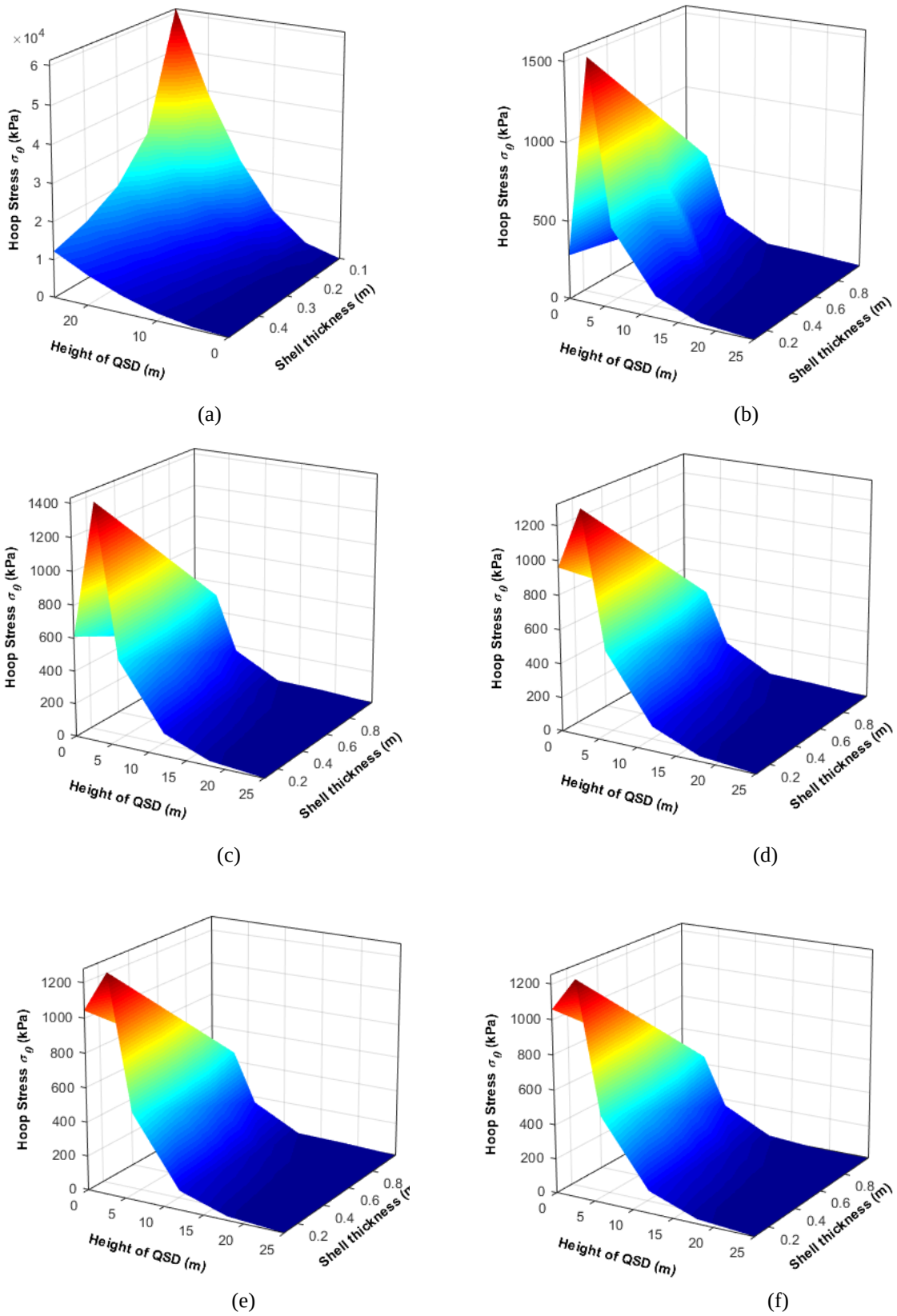

Figure 66. Surface plot results for meridional hoop stress for analyses with varying wall thicknesses for 25m tall QSD for: (a) 90% fill - hydrostatic case, (b) 10% - fill dynamic case (c) 25% fill - dynamic case, (d) 50% fill - dynamic case, (e) 75% fill -dynamic case. (f) 90% fill - dynamic case

The results produced by the 2D FEA analyses were in close agreement with those from the first principle analyses. There was a sharp increase in internal stresses at the 3.1-metre height. This confirms that the impulsive forces coupled with the hydrostatic forces produce an increase in this area. It's also quite noticeable that the lower fill levels have higher stresses at this level. This is due to the convective force produced by the sloshing of the surface in this area the inverted frustum shape at this level, encourages the hydrodynamic movement of the surface to produce a significant sloshing mode. As the fill level increases after the equator, the frustum is inverted and the shape dampens the sloshing at the higher levels. The plan area of the liquid level also decreases which reduces the impulsive force. It was also noted that the impulsive force was gradually replaced with the hydrostatic pressure at the 3.1 m height.

4.4.2 3D FEA Analysis

The 3D FEA SPH simulation was conducted for the 25-metre model. These 6 degree-of-freedom models utilised the Kobe, Takatori 1995 time-history data as the ground motion. 50% fill level was selected since this produced the most significant convective force at the surface. The analysis utilised parallelisation with 16 CPU cores (total of 32 threads). The run time was 419 hours.

The results from the were in good agreement with those from the first principles model as well as the 2D FEA models. Figure 67 and Figure 68 show the hoop stresses and the meridional stresses respectively. The principal stresses (in the S11 direction) range from 0.171 MPa to 4.231 MPa.

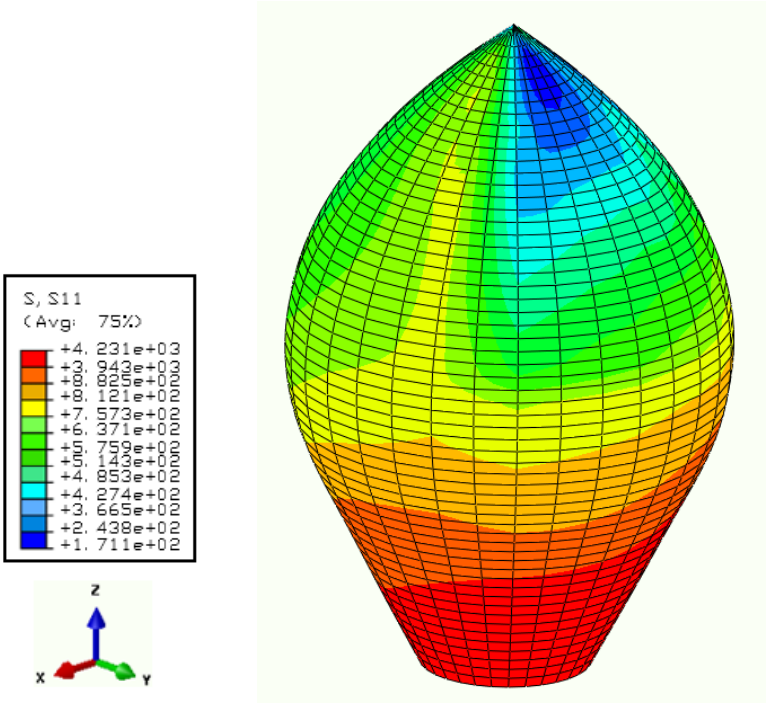

Figure 67. 3D SPH -FE Model output showing S11 stresses

The results show that hydrostatic pressure coupled with the convective surface pressure impacted mainly on the lower third of the shell. The stresses decreased from the middle third section to the apex. This would indicate that the sloshing forces did not have a significant impact on the upper portions of the QSD. The principal stresses (in the S22 direction) range from 0.162 MPa to 5.457 MPa.

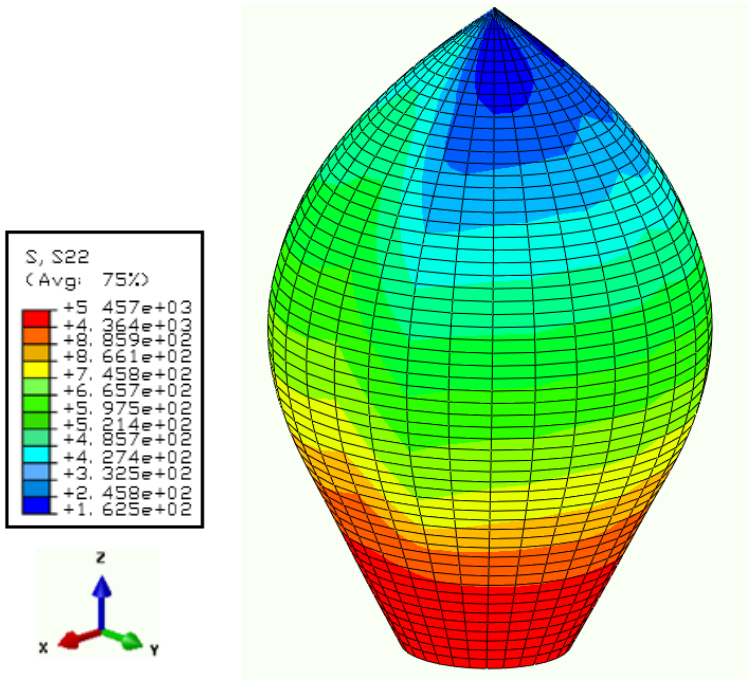

Figure 68. 3D SPH -FE Model output showing S22 stresses

Failure can occur if the Von Mises stress computed is more than the material stress limit. In high magnitude events, high particle velocity would induce high pressures with would interact with the retaining surface and induce high stress which would create small or large displacements and may be in areas that local stress exceeds the material stress and failure occurs. The Von Mises stresses (see

Figure 69) show that the 3D printed FDM ABS can be a viable option for the shell of the QSD since its within range of the material property. The Von Mises stresses range from 2.64 MPa to 22.73 MPa.

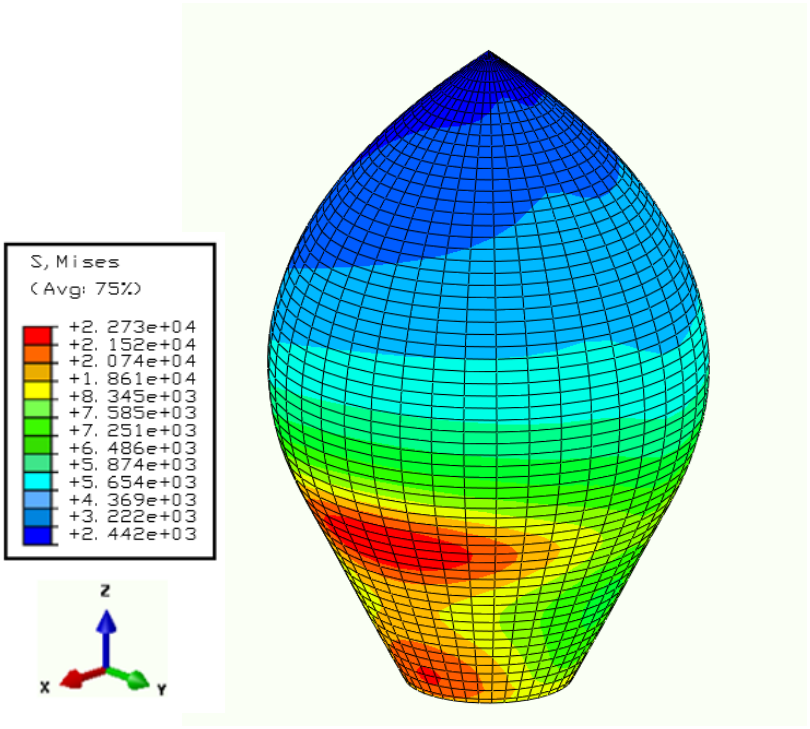

Figure 69. 3D SPH -FE Model output showing Von Mises stresses

4.4.2.1 3D FEA Benchmark

As a benchmark, a concrete version of the 3D printed QSD (using 55 MPa strength) was modelled subjected to the same fill and seismic parameters as the 3D printed version. Smooth particle hydrodynamic analysis was modelled as before, to develop the liquid sloshing within the QSD. The principal stresses in the S11 and S22 directions, as well as the Von Mises stresses were checked. Figure 82 shows the principal stresses (S11) as the tank is subjected to the Takatori 1995 earthquake. As shown in the figure, the maximum principal stress is 3.12 MPa which occurs at the base of the QSD. The minimum stress of 0.142 MPa was concentrated towards the apex. These values were 26% lower than those of the 3D printed version.

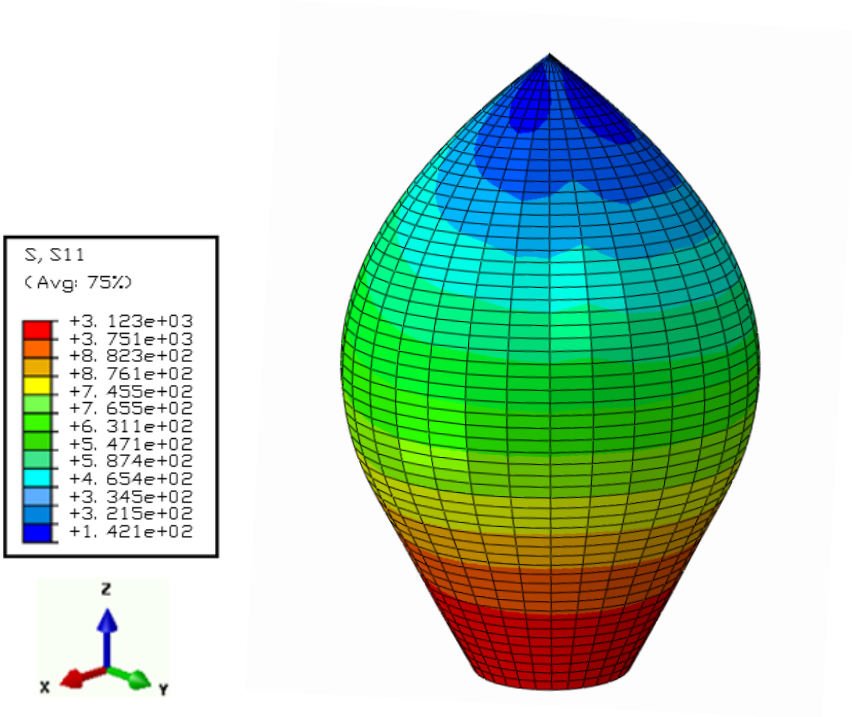

Figure 70. Concrete 3D SPH -FE Model output showing S11 stresses

Figure 70 shows the, the maximum principal stresses in the S22 direction. The maximum is 4.62 MPa which also occurs at the base of the QSD. The minimum stress of 0.132 MPa was barely visible at the apex. These values were 42% lower than those of the 3D printed version.

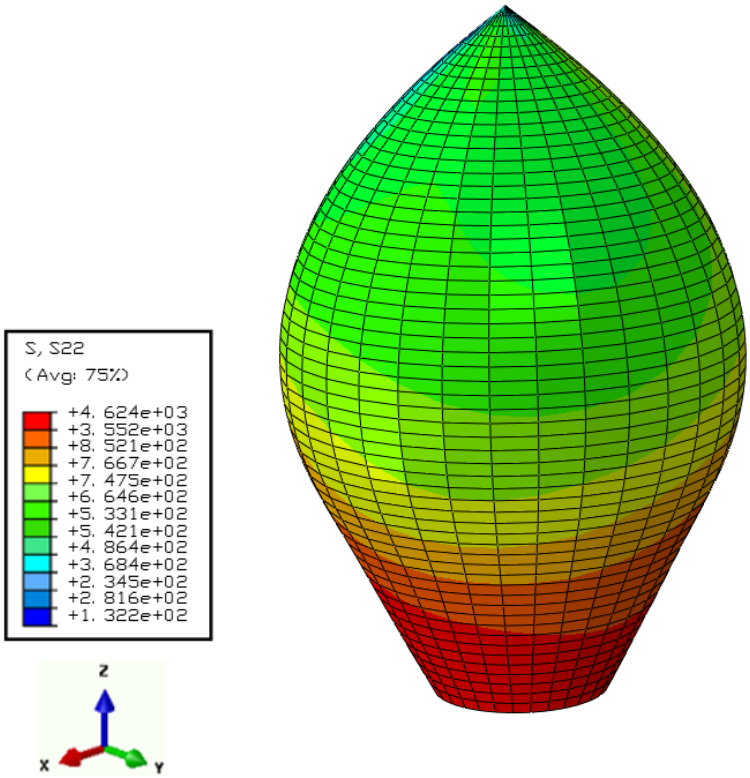

Figure 71. Concrete 3D SPH -FE Model output showing S22 stresses

Figure 72 shows the, Von Mises stresses in the benchmark model. The maximum stress is is 18.71 MPa which occurred at various portions at the base and the apex of the QSD. The minimum stress of 0.121 MPa which dominated the equatorial regions of the model. These values were 17.6% lower than those of the 3D printed version.

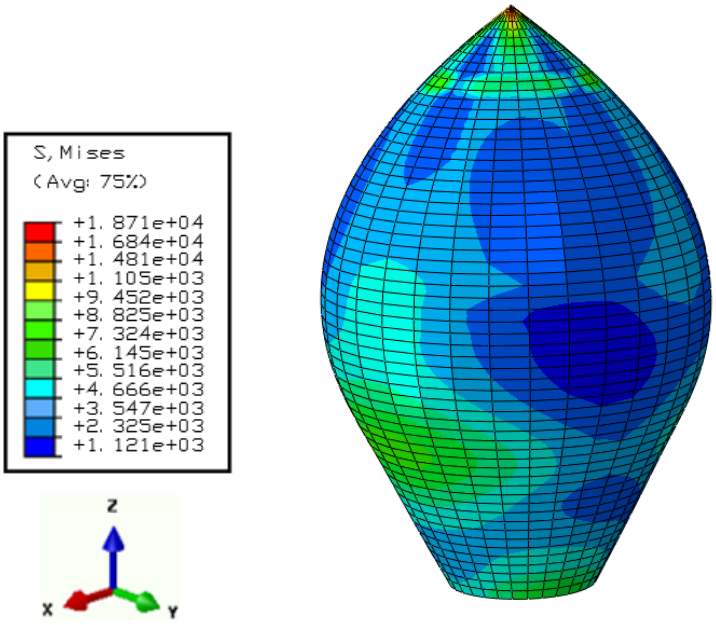

Figure 72. Concrete 3D SPH -FE Model output showing Von Mises stresses

5.0 Discussion

5.0 Discussion

5.1 Introduction

This chapter discusses the results from the experimental and numerical studies performed on 3D printed polymers. Results from the first principles analyses are then discussed followed by those of the finite element analyses. A discussion on the failure criteria is then presented at the end of the chapter.

5.2 3D printed polymer characterisation

5.2.1 Tensile property

The degree of accuracy obtained in the numerical results showed the importance of including the reduction factors for stiffness and strength due to molecular orientation. Overall, the material properties were predicted with similar accuracy to previous studies. The introduction of the ρ_2 value for transverse air void density proved to be a reliable approach to count the potential load-carrying material. However, the bond strength needs to be examined further to determine the true effect on the numerical results. The assumption of anisotropic properties and inputting the data as material constants consider the imperfect bonding which also leads to more accurate results. The assumptions made for the boundary conditions and constraints are applicable for modelling using the FEA software which reduced the computation time of analysis.

Table 16 shows the material properties comparing the experimental results with the numerical results. The modulus of elasticity for orientations E1 and E2 were consistent with a percentage variance of 7.07.

Table 16. Comparison of results of experimental and numerical tests

Property	Experimental	Calculated	% Variance
$E_{1\ (MPA)}$	1636	1528	7.07
$E_{2\ (MPA)}$	1636	1528	7.07
$E_{3\ (MPA)}$	1197	1129	6.02
v_{21}	0.39	0.37	5.41
v_{31}	0.37	0.33	12.12
v_{23}	0.39	0.37	5.41

This is attributed due to the transition melting temperature (270^{o}C) of the 3D printer's extrusion nozzle. As the nozzle temperature increases so too do the glass transition temperature. The cross-sectional geometrical shape of the extruded ABS polymer would become more elliptical; hence, there is a larger contact surface created between layers and thus a stronger bond. As discussed previously, E3 displays lower moduli of elasticities for the tests conducted to that of the first two orientations. This further demonstrated the anisotropicity of the material. The possion's ratios for the two longitudinal orientations (ν_{21} and ν_{23}) showed consistency with a 5.41% variance. The cross-sectional orientation displayed a higher percentage variance of 12.12%. This is also a direct result of the glass transition temperature change coupled with a reduced cross-sectional layer-to-layer bond. Based on figure 52, the average yield stress for the 3D printed ABS in orientations 1 and 2 is 15 MPa. For orientation 3, it is 12.2 MPa.

5.2.2 Flexural property

Error! Reference source not found. presents the load vs deflection curves for specimens constructed longitudinal to the (x, y, z)/ (1, 2, 3) directions. A total of ten (10) specimens per orientation were tested, and the average deflections values at a load of 200N were recorded. For specimens printed longitudinal to the x/1 direction and loaded perpendicularly to that axis showed the highest yielding load compared to the other orientations. This behaviour was expected due the fact that stresses developed within the solid filament rather than the weaker bonds. However, orientation 2 displayed a similar curve that may be due to the similarities in the mesostructure. This curve yielding at a lower loading can be explained by the bond material being weaker causes such failure. It may seem that the reduction factors considered by Rodríguez (2001) should be examined in the numerical analysis for the effective modulus calculations. The shape of the air voids seems to be the most significant factor to take into account when studying the failure of orientation 3. The sharp corners in its air void geometry may initiate cracking that will lead to failure of that type (see Figure 29).

The slack deflection was not taken into account when performing the experimental test due to limited resources. As a result, the numerical results for the bending test may stray from the ones of the

experimental. The deflections of the longitudinal x-axis and the longitudinal z-axis again show similar values with a difference of 6.3%. This could be due to similar mesostructured properties of the two specimens.

Table 17. Deflection at 200N for specimens with orthogonal print orientations.

Specimen Orientation	**1**	**2**	**3**
Deflection @ 200N (mm)	0.5002	0.5151	0.3887
	0.5126	0.4988	0.4651
	0.4987	0.5132	0.3981
	0.512	0.5012	0.4251
	0.4681	0.4235	0.3999
	0.521	0.4251	0.4513
	0.4664	0.4845	0.3848
	0.4743	0.4728	0.3669
	0.4661	0.5103	0.3463
	0.4983	0.4356	0.5001
Average deflection (mm)	0.4918	0.4780	0.4126

The introduction of the ρ2 value for transvers air void density proved to be a reliable approach to count the potential load carrying material. However, the bonds strength needs to be examined further to determine the true effect on the numerical results. The assumption of anisotropic properties and inputting the data as material constants considers the imperfect bonding which also lead to more accurate results. The assumptions made for the boundary conditions and constraints were not practical for modelling using the FEA software.

On comparing the results from the experimental and numerical studies, Table 18 shows the variance percentage for orientations 1 and 2 are almost identical for deflection at 200N.

Table 18. Comparison of results for flexural tests for ABS for specimens with orientations 1,2 and 3.

Deflection at 200N			
Orientation	**Experimental (mm)**	**Numerical (mm)**	**% Variance**
1	0.4918	0.4987	1.40
2	0.478	0.4709	1.51
3	0.4126	0.457	10.76

The percentage variance for orientation 3 is significantly higher. This is due to the air void geometry, as explained previously in this section.

The modulus of rupture for each orientation was calculated based on the results of the experimental tests conducted (see Table 19).

Table 19. Modulus of rupture calculated from the experimental tests.

Modulus of Rupture	**Experimental**
G_{12} (MPA)	645
G_{23} (MPA)	645
G_{31} (MPA)	676

The horizontal orientation (G3), the modulus of rupture is significantly higher. This is attributed to the high bond strength between adjacent layers and hence greater internal shear resistance, hence enabling the sample to fail at a higher load.

4.2.3 Torsional property

The results from the torsion test displayed fair enough results which differ by 7.2% (standard deviation). The data is displayed in the form of torsional stress and strain values. This level of accuracy was not expected due to the manual data collecting process in the experimental stage. As such, the shear modulus prediction versus the experiment was lower than expected. The assumption for the boundary condition seemed practical in duplicating the condition of the experiment. Even though the results fell within the desired range, the location of the deformation was not in the same location. This is due to the fixed conditions applied to one end of the specimen. The results agreed with the anisotropic behaviour of the specimen. The results had to be interpolating from four point of the graph and then log to obtain

the coordinates for the torsional stress and strain. Overall, the material properties were predicted more accurately than other attempts by previous researchers. The introduction of the ρ2 value for transverse air void density proved to be a reliable approach to count the potential load-carrying material. However, the bond-strength needs to be examined further to determine the actual effect on the numerical results. The assumption of anisotropic properties and inputting the data as material constants consider the imperfect bonding which also leads to more accurate results. The assumptions made for the boundary conditions and constraints are applicable for modelling using ABAQUS which reduced the computation time of analysis.

Table 20. Comparison of results for torsional tests for ABS for specimens with orientations 1,2 and 3.

Torsional strain values at 10MPa			
Orientation	Experimental (mm/mm)	Numerical (mm/mm)	% Variance
1	0.0053	0.0049	7
2	0.01	0.0103	3
3	0.0105	0.0113	8

The variance percentage difference between the experimental and numerical torsional tests were less than 10% which indicate good agreement considering the range of environmental temperature conditions that affect the 3D printing process. The air void geometries, which are responsible for the difference, suggest that by increasing the transition glass temperature, the overall cross-sectional area of the void reduces, hence increasing the material torsional property.

4.3 First Principles QSD Analyses

4.3.1 Fluid Behaviour

When the tank is subjected to ground excitation, the inertia properties of the fluid containing within, causes the mass movement of the fluid in the direction of the force. Since a harmonic frequency of 5 Hz was applied to both models (fixed base and base isolated), the convective liquid displacement also followed this sinusoidal pattern (see Figure 73a).

Figure 73b follows a similar pattern however since the convective mass replicates the motion of the

containing structure, the fluid in the base isolated QSD follows a similar pattern to that of the bearing displacement shown in Figure 53. Due to the isolation of the base, the maximum resultant displacement is reduced by 41%. For both models each mass(M_n) component, respective to each section along the QSD height, holds a steady adherence to the general shape of the plot. It can be seen for the middle 50% of the M_n components; the displacement increases linearly. This occurs due to the increase of kinetic energy of the increased lumped mass due to the larger volume (refer to equation (121)) at that section.

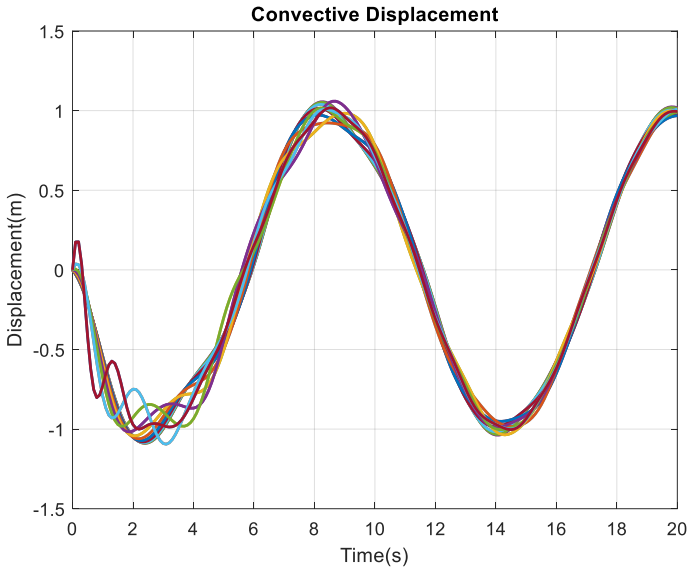

(a)

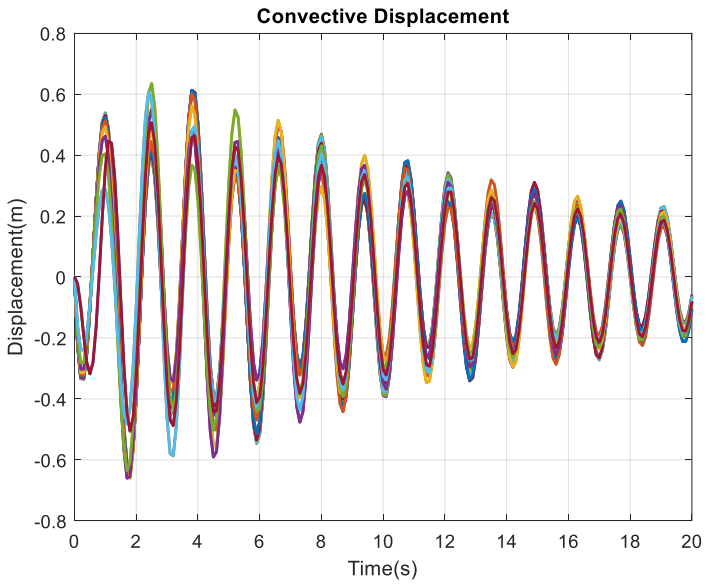

(b)

Figure 73. Convective displacement of fluid in QSD for various sections at 5Hz for (a) Fixed base QSD and (b) Base-isolated QSD

Analogous to the convective displacement of fluid, the fluid mass also develops an impulsive component.

Figure 74a shows an impulsive mass displacement for each section of the tank.

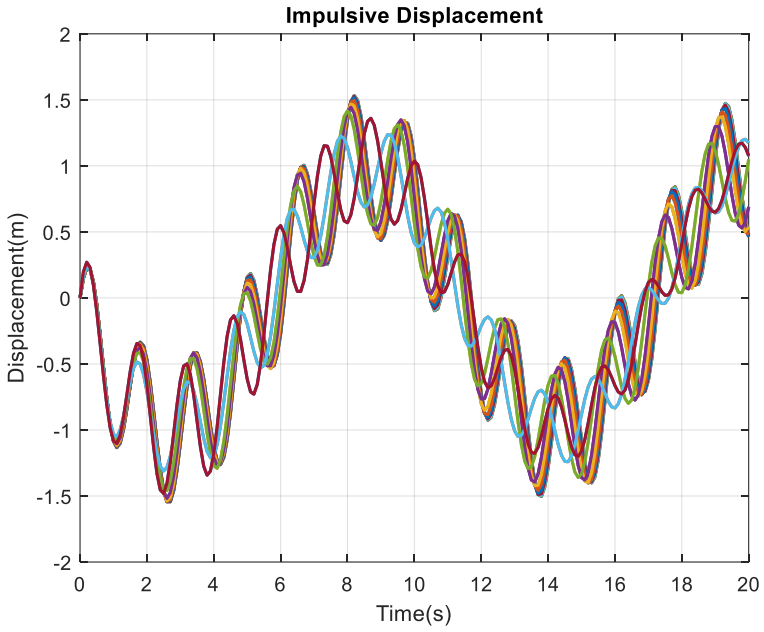

(a)

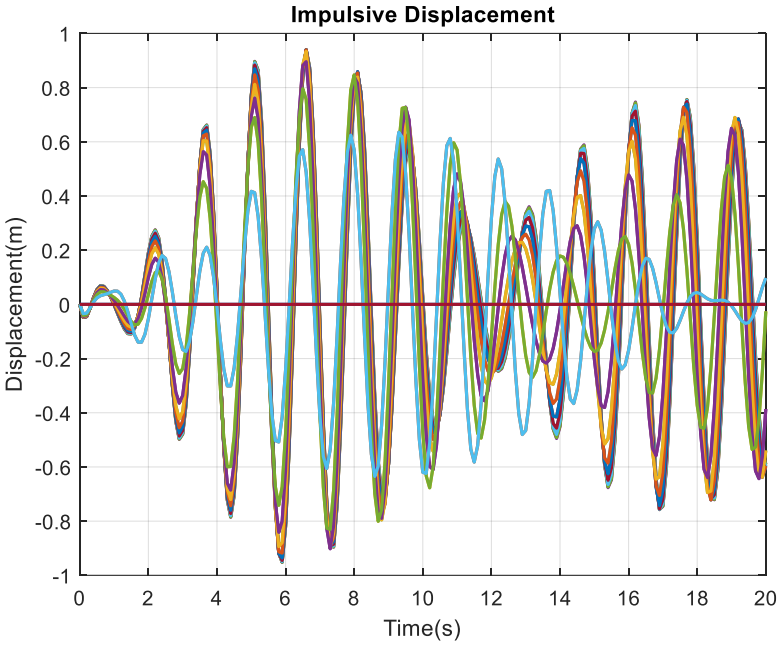

(b)

Figure 74. Impulsive displacement of fluid in QSD for various sections at 5Hz for (a) Fixed base QSD and (b) Base-isolated QSD

The displacement pattern follows a similar sinusoidal pattern as the convective displacement, however due to the increase in velocity of the fluid particles in this section, the fluid shifts alternatingly from the front to the back of the section. This motion transposes throughout the general wave shape for the frequency. The base isolated tank has a unique phenomenon that occurs when excited. The liquid oscillates at same frequency as seen in the convective counterpart. The transient decay becomes a minimum at around 13 seconds, which corresponds to one cycle of the frequency. Here the liquid reverses direction and the impulsive frequency increases for half the cycle. This continues until the overall decay of the harmonic motion ends. The maximum impulsive displacement decreased by 45% when compared to the fixed-based model.

5.4 First Principles QSD Analyses

5.4.1 Shell Forces

The plots in section 4.3.1 shows the variance of shell forces within each section of the QSD during a 20 second period for both fixed based models and base isolated models that were subjected to a frequency of 5Hz. It was noticed that the base isolated models developed a characteristic transient frequency which allowed the shell forces and stresses (both N_{φ} , N_{θ} and σ_{θ} and σ_{φ}) to progressively decay over time. The lowest section (section 8) displayed the largest forces with the highest frequencies both for the fixed base and the base isolated models. This occurred because of the cumulative convective forces coupled with the hydrostatic forces that impact the shell in that area. The corollary is noticed at the apex of the plots (section 1) where the frequency is almost flatlined. This occurs because the liquid inside the QSD does not impact this region. The only factor is the self-weight of the shell which reacts dynamically with the movement from the seismic excitation.

The peak stresses were plotted for each fill level at each section (Figure 61andFigure 62). It was noticeable that the maximum stresses occurred at the lower third of the tank. This is mainly due to the impulsive force coupled with the hydrostatic force being impacted in that region.

The time-history analyses yielded favourable results when compared with the harmonic analyses. This is due to the transient decay of the frequency. The analyses did show an increase in the orthogonal

stresses towards the apex of the tank. This is due to leading forces developed in the tank due to the mass component of the tank at that section and not the liquid fill levels. This can be attributed to the introduction of the vertical component of the time-history data since the base isolation does not consider the vertical damping of the system.

5.5 Finite Element QSD Analyses

5.5.1 2D FEA Analysis

To properly assess the data generated by the 125 dynamic cases, a multiple analysis of variance (ANOVA) was carried out using a software package, Statistical Package for the Social Sciences (SPSS), by only considering the main effects, two way and 3-way interactions of the variables vertical distance, shell thickness, maximum QSD height, and fill levels on the variable stress. The *Estimated Marginal Means* in SPSS tells the mean response for each factor, adjusted for any other variables in the model. The results show that model was significant (p-value < 0.05) in determining the stress. On examination of the separate effects on the dependent variable stress, it was observed that the main effects of height, fill, vertical distance and shell thickness were also seen to be significant factors (p-value < 0.05) for stress. On examination of the two – way interactions, it can be deduced that two-way interactions between distance and thickness, distance and height, distance and fill, thickness and fill and height and fill were also significant factors in assessing the stress. However, the interaction between thickness and height was found to be insignificant (p-value=0.706).

The 3-way interaction between distance, thickness and fill were also found to have a significant effect on the variable stress (p-value <0.05). When the calculated Partial Eta-Squared is greater than 0.5, then the interaction between the variables become significant. The plots for the above analysis can be further supported by the following plots (Figure 75 to Figure 79):

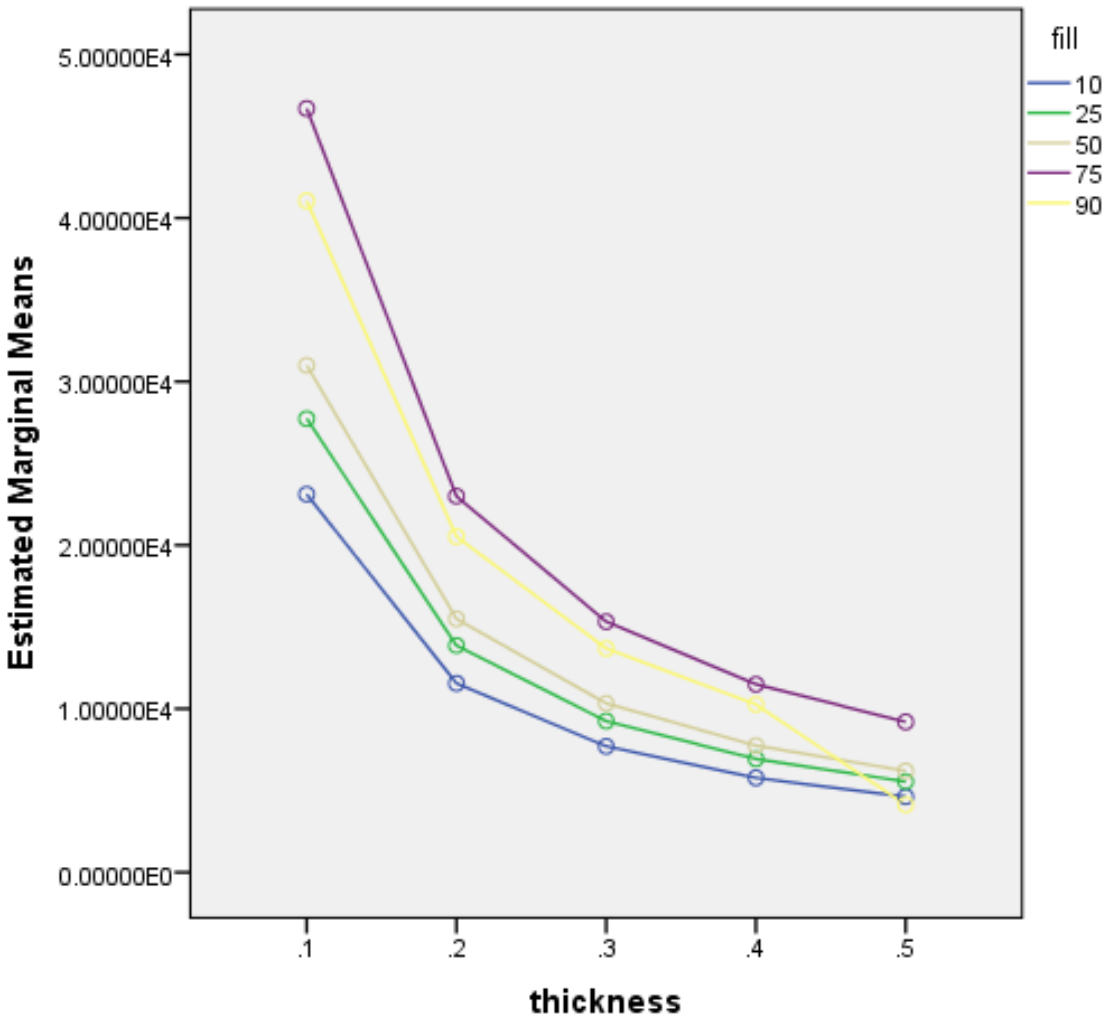

Figure 75. Estimated marginal means of stress for fill levels and thickness

It can be deduced from Figure 75 that thickness did have a significant effect on the stress across the different fill levels. As the thickness increased, the stress decreased. There was no significant effect of fill at higher thicknesses on the stress variable. The interaction effect of thickness and fill was significant and was a medium effect (Partial Eta-Squared =0.617).

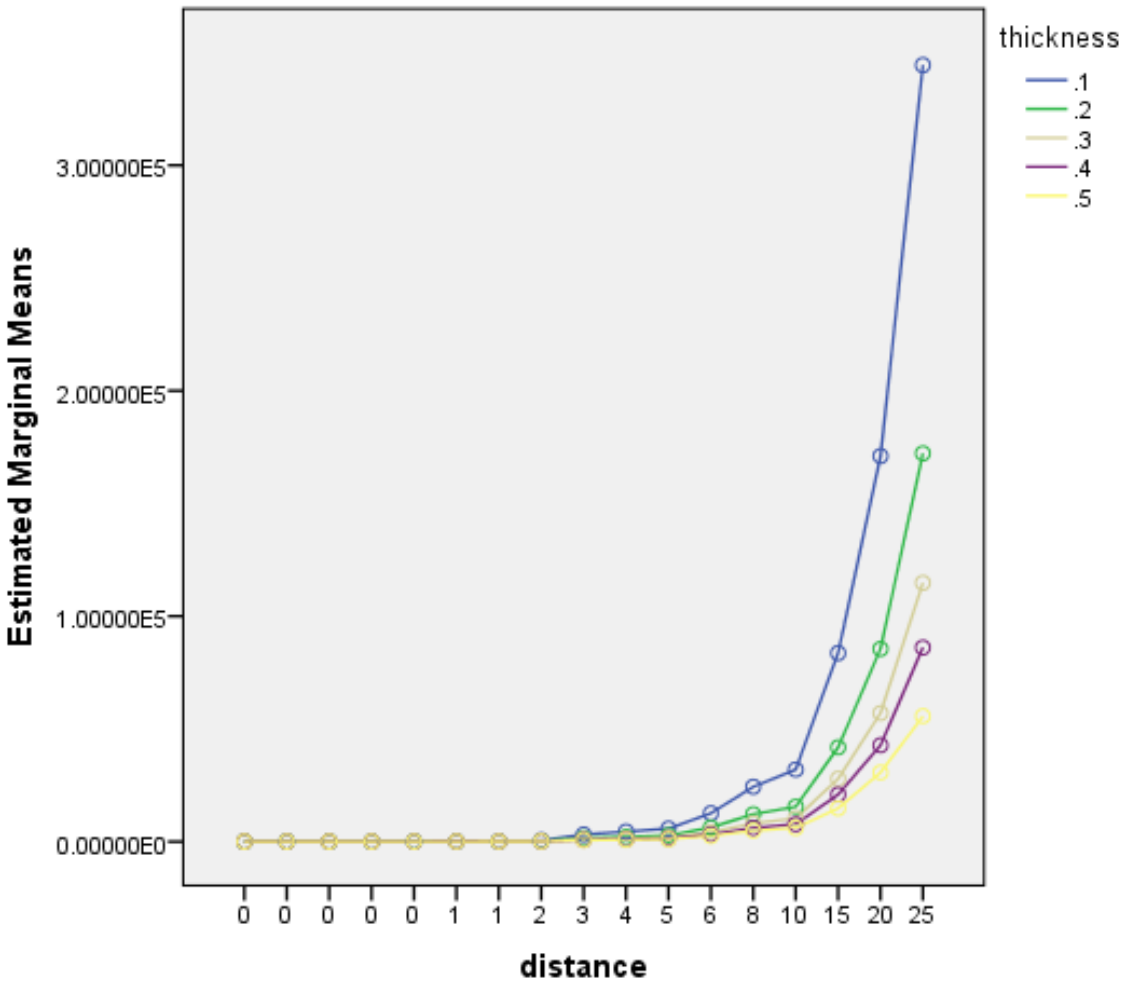

Figure 76. Estimated marginal means of stress for shell thickness and distance

The vertical distance can be seen to have a significant effect on stress at lower values of the thickness (see Figure 76). Both the main effect and interaction effect of distance and thickness was significant with the interaction effect being a strong effect (Partial Eta-Squared = 0.988).

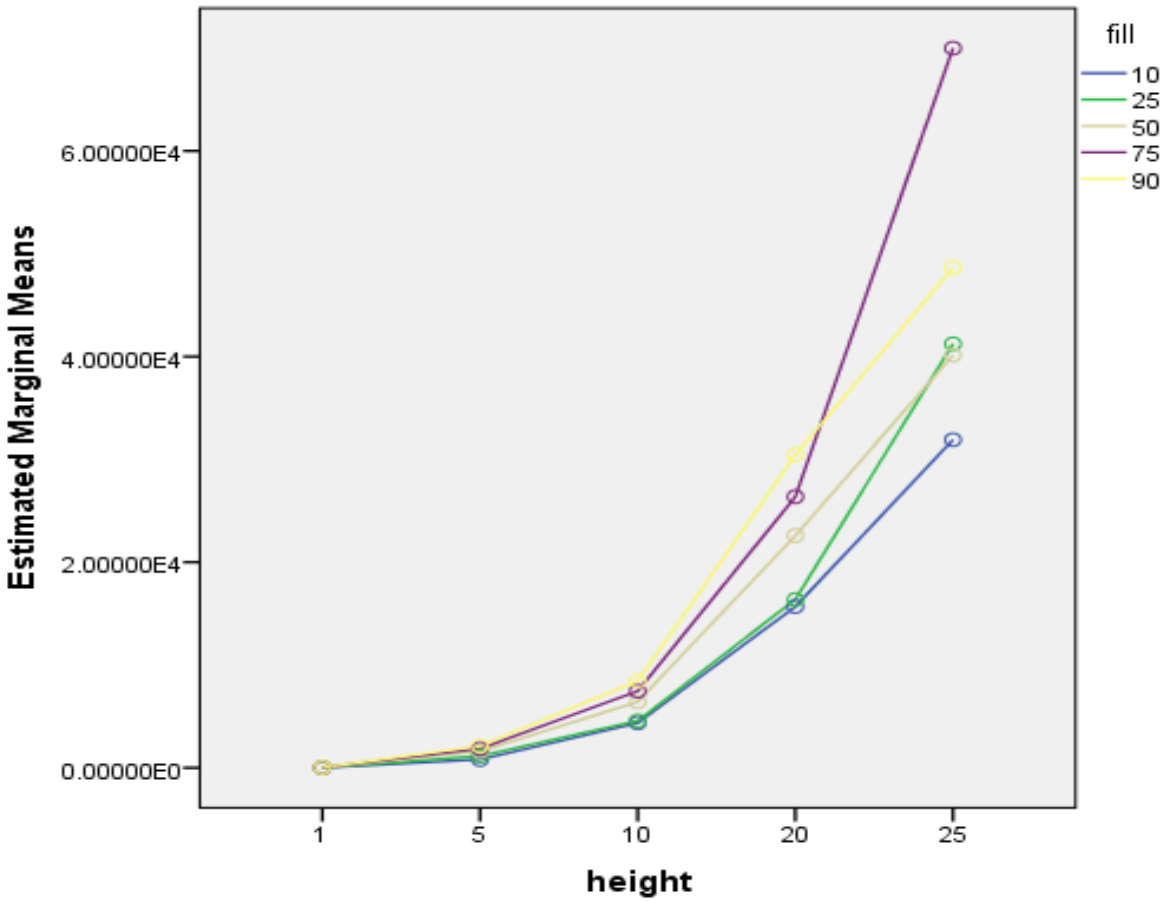

Figure 77. Estimated marginal means of stress for fill levels and QSD height

The analysis revealed that the main effect for height was significant (see Figure 77). There was a drastic increase in stress at the 75% fill level after a height of 20. However, at smaller heights, there was no significant effect on stress due to the fill level. The interaction effect between height and fill was shown to be weak (Partial Eta-squared = 0.268). The main effect on stress was also observed to be a weak effect (Partial Eta-Squared = 0.196).

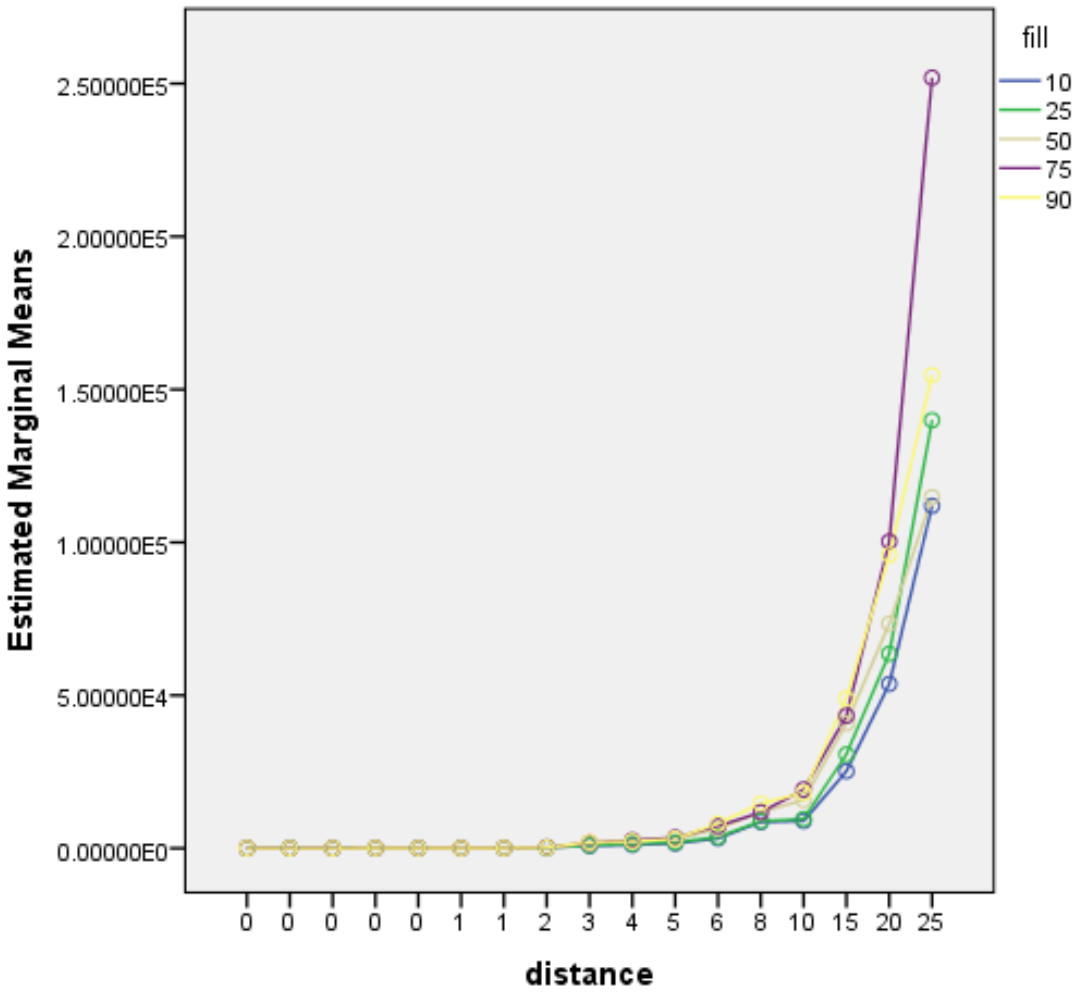

Figure 78. Estimated marginal means of stress for fill levels and distance

Distance was seen to have a significant effect on stress especially at higher values (p-value <0.05). There was a large increase in stress at the greater distances for the fill value of 75%. The interaction effect between distance and fill was observed to be a strong effect (Partial Eta-Squared = 0.951).

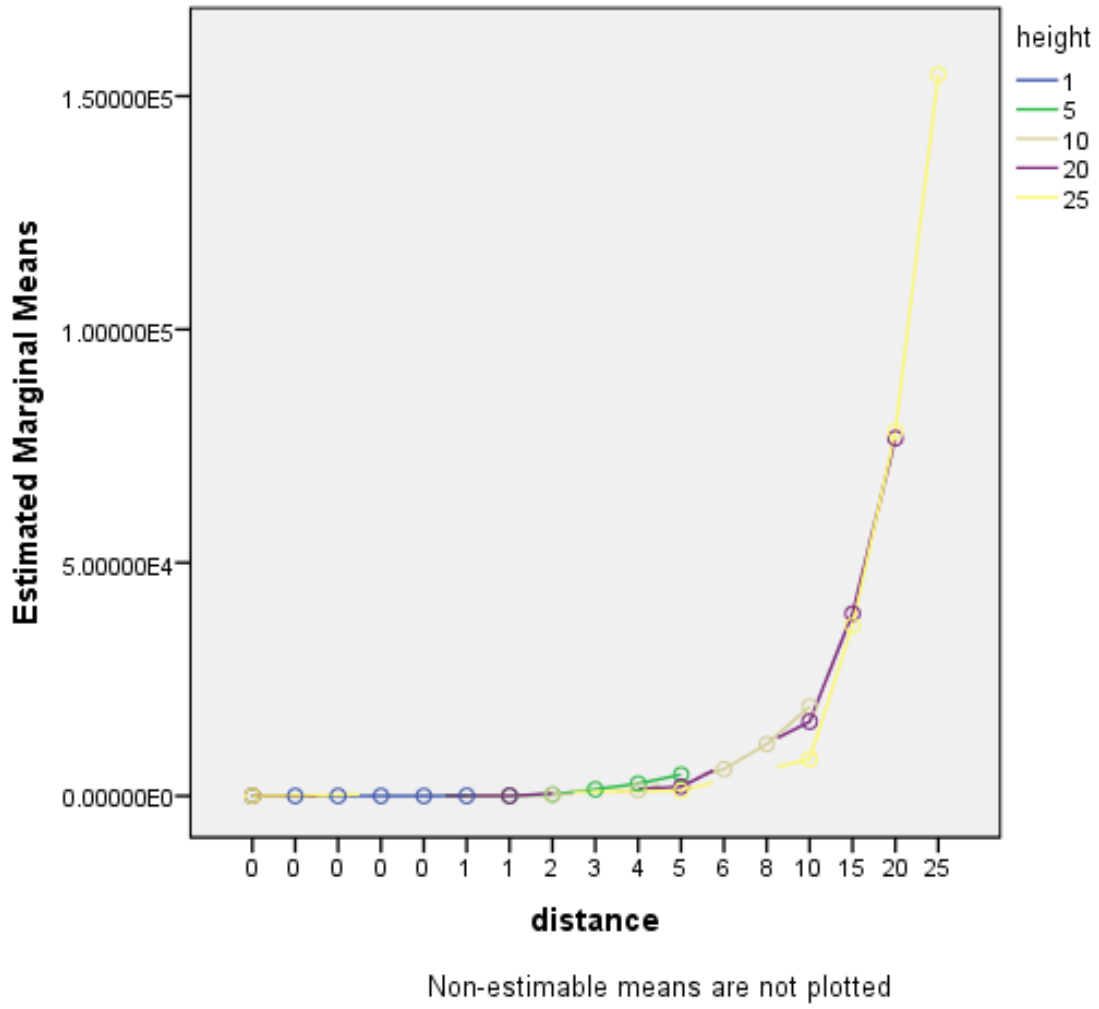

Figure 79. Estimated marginal means of stress for height and distance

Although the interaction effect of distance and height was shown to be significant (p-value <0.05), the effect was a weak one (Partial Eta-Squared = 0.295). There was no significant increase in stress at different distances for the varying heights of 1, 5 and 10m. However, a sharp increase was observed for larger distances at heights of 20 and 25 m.

4.4.2 3D FEA Analysis

The results from 3D finite element analyses conducted on the 25-metre QSD model shows similarity to those from the 2D analyses. The overall principal stresses ranged from 0.162 MPa to 5.457 MPa with the Von Mises stresses ranging from 2.64 MPa to 22.73 MPa. The dynamic excitation from the Kobe, Takatori 1995 earthquake, resulted in sloshing effects developing. The fluid-structure interaction between the resultant impacting sloshing force and QSD shell, resulted in a significant increase in the Von Mises stress. This stress was found to occur just beneath the mid-height equator of the QSD. As the liquid's surface level tends towards the mid-height equator, the surface area increases. This free surface generates impulsive waves during seismic excitation. As a result, the impact forces are increased. When comparing the 2D analyses with the 3D FE analyses, levels that are filled more than 60% of the tank, do not contribute significantly towards the sloshing forces. Hence, it can now be noted that for the worst-case fill level for dynamic analysis, the 50% fill level should be utilised. For the hydrodynamic analysis case, the 90% fill level should be used.

4.4.2 Failure Criteria

In developing the design criteria, the failure criteria must be determined. Figure 80 shows limiting envelopes for the Von Mises stress state as well as the Saint Venant stress state. For the QSD to be safe, the maximum stress must fall within specific boundaries in the diagram.

Considering the material (3D Printed ABS), the yield stress and ultimate tensile stress is now utilised to develop the criteria. Noting that for any FDM 3D printed material, the print orientation is of paramount importance. Orientation 1, provides the best option in terms of strength. It should be noted that the placement of this orientation must be parallel to the most significant in-plane force. For this Orientation, the yield stress was found to be 15 MPa and the maximum tensile stress was 24.4 MPa. Upon comparing these stresses with those from the QSD analyses, it can be seen that for the Serviceability Limit State (SLS) the yield stress of 15MPa can be used. Also, for the Ultimate Limit

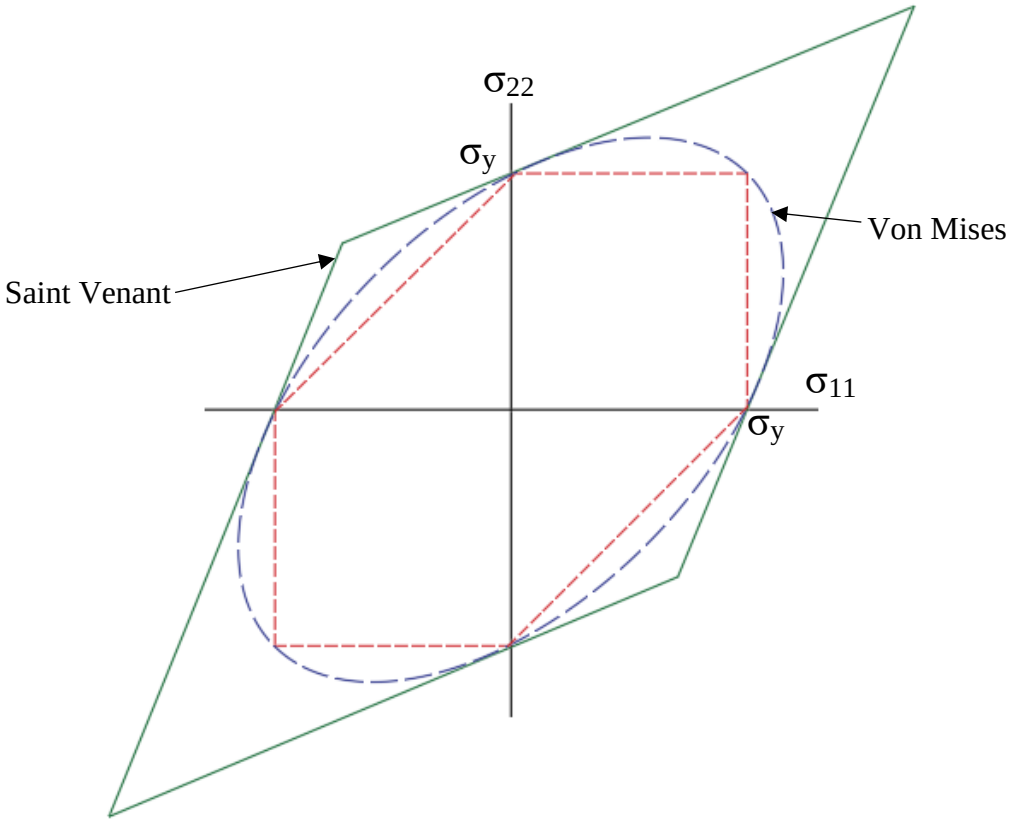

Figure 80. Plot of failure envelopes for various failure modes

State (ULS) the maximum tensile stress can be utilised. The relationship between the material property and the QSD stresses can be written as:

$$\emptyset\sigma_y > \sigma_1, \sigma_2 \rightarrow for\ Serviceablity\ Limit\ State$$

And,

$$\emptyset\sigma_{ult} > \sigma_{VonMises} \rightarrow for\ Ultimate\ Limit\ State$$

Where ∅ is a factor of safety.

6.0 Conclusions and Future Work

6.0 Conclusions and Future Work

6.1 Introduction

This study defined three research objectives and investigated them to successful completion. The first objective examined the mechanical properties of 3D printed ABS polymer. The second investigated the global behaviour of the QSD under hydrostatic and dynamic loads while utilising 3D printed ABS as the main structural material. This finally, determined the behaviour of a 3D printed polymer QSD under seismic conditions for use within the wastewater sector in the Caribbean. These three facets of investigation have employed experimental and numerical research methods to achieve the goals.

6.2 D Printed ABS Polymer

Several simulations and experiments were conducted using ABAQUS to test numerically; tension, flexure and torsion of the 3D printed ABS polymer. The material properties were determined experimentally and compared to the results of the mechanics of material equations as described by Fritch, (1980). These results were in agreement with each other, proving the need to include the factors of stiffness and strength as well as the introduction of ρ_2 void ratio, which counted the potential load-carrying material for the transverse effective properties. However, this was only valid for two orientations (1 & 2) the third orientation of the numerical work was not in close approximation with the experiment. The 8.3% difference observed with the shear modulus prediction in that orientation has been explained as the reason for this occurrence. The deflection predictions for orientation (1 & 2) were in excellent agreement (4.5% & 3.4%) this concludes that the goal of developing numerical models for structural analysis was accomplished.

The examination of the FD-3D polymer material can be classified as moderately ductile when comparing the force with deflection. This type of deflection resembles the characteristics of a steel deflection curve. The goal is to find materials that can be compatible with the FDM platform but display a higher strength to weight ratio than that of steel. However, the behaviour of failure criterion is a significant factor to consider. As the technology is today in its development stage the accuracy of some

industrial platforms makes it possible to print organic scaffolds for cell growth. Hence, the technology can reduce the need for costly construction techniques. As for the material behaviour, it can be applied to QSD shell structures where environmental loads and self-weight are to be considered when conducting structural analyses.

6.3 QSD Analyses

Three groups of analyses were conducted to determine the orthogonal stresses in the shell of the QSD. The first-principles numerical models ran reasonably quickly and many iterations were made during the study. The results showed that they were in within the range 5.34% to 7.2% to 2D FEA simulations. The 3D FEA simulations were within the range of 8.3% to 9.2% to the MATLAB time-history models. This is a good indicator that the first principles numerical models are an excellent timesaving method to predict the behaviour of the QSD under seismic excitation. Upon examining the criteria for the design, analysing the results for the 2D FEA simulations showed that the fill height is not a significant variable with sloshing however, the 3D FEA showed that the hydrostatic pressure is a significant variable. With the maximum tensile stress of the 3D-printed ABS being 24.4 MPa, the overall maximum Von Mises stress of 22.73 MPa, the material can be a viable option for the use of QSD construction.

The failure criteria was found after determining performance of the QSD during static and dynamic loading. For typical service loads, the the maximum principal stresses were found to be 5.457 MPa. Under seismic excitation (either harmonic or dynamic) this range falls well below the yield stress of the 3D printed ABS polymer. Hence, it can be concluded that the yield stress can be the limiting criterion for failure in the serviceability limit state. Similarly, the Von Mises stress was can be used as the limiting criterion for the Ultimate Limit State when designing the QSD.

6.4 Summary of conclusions

The following is summary of conclusions for this study:

1. The orientations 1 and 2 for the 3D printed ABS polymer have been found to be suitable for use as a construction material, particularly in the case of shells.

2. The 3D printed ABS polymer with Orientation 1 (parallel to the axial force) has an ultimate tensile strength of 24.4 MPa and a yield strength of 15 MPa.
3. The numerical simulations in ABAQUS have proven to be a good indicator for determining the mechanical properties.
4. The results from 2D FEA SPH models are close to 3D 6DOF FEA models. However, they reduce the computation time significantly.
5. The parabolic ogival shell form with a height to diameter ratio of 2.5 is excellent for adoption for the 3D printed ABS QSD.
6. The fill level does not dictate the design criteria when compared to sloshing produced from external dynamic loading.
7. The criteria for failure is defined as:

$$\emptyset\sigma_y > \sigma_1, \sigma_2 \rightarrow for\ Serviceablity\ Limit\ State$$

And,

$$\emptyset\sigma_{ult} > \sigma_{VonMises} \rightarrow for\ Ultimate\ Limit\ State$$

Where $\emptyset$ is a factor of safety.

6.5 Future Work

This study has provided insight into the novel concept of utilising 3D printed FDM ABS polymers for use in QSD construction. As FDM techniques and 3D printing technologies are rapidly advancing, new methods and materials for construction can be explored. For example the use of composite FDM polymers. Composite FDM polymers are reinforced within the air voids created during the extrusion process. Material strengths can be increased significantly, thus allowing for more elegant design shell thicknesses.

An experimental study can be conducted whereby scaled models are constructed and tested using a 6 DOF setup. Accelerometers and strain gauges are positioned at several elevations around the

circumference of the QSD, and hydraulic actuators cycle a scaled pre-defined time history. This experimental setup can further validate the numerical simulations presented in this study.

For ease of manufacturing and construction, the QSD can now be designed as modular elements that would be fabricated offsite in a factory setting. These modular parts would have to be added to the numerical simulations and further tested via an experimental setup as described above. Parametric optimisation can then carried out to refine the QSD into a final product.

Financial studies for manufacturing, erecting, and maintenance can be done to ensure the product is marketable. Integration studies into existing wastewater treatment plants and maintenance schemes are other avenues in which this study can be furthered.

Publications

Conference Papers

Tota-Maharaj K. and Ramroop, N., (2016) Feasibility of Novel Quadric (Egg-Shaped) Sludge Digesters within Wastewater Treatment Plants Hydraulic Infrastructure across the Caribbean. *Caribbean Water and Wastewater Association Technical Conference 2016: Port of Spain, Trinidad and Tobago*

Ramroop, N. and Tota-Maharaj K., (2018) Parametric Stress Distribution in 3D Printed Polymer Quadric-Surfaced Sludge Digesters for Sustainable Wastewater Infrastructure. *CWWA 27th Annual Conference and Exhibition: Montego Bay, Jamaica*

Ramroop, N. and Tota-Maharaj K., (2018) Parametric Stress Distribution in 3D Printed Polymer Quadric-Surfaced Sludge Digesters for Sustainable Wastewater Infrastructure. *5th International Association of Hydro-Environment Engineering and Research (IAHR) Europe Congress-New Challenges in Hydraulic Research and Engineering: University of Trento, Italy*.

Published Journal Articles

Tota-Maharaj K. and Ramroop, N., (2020) Numerical Modelling of Quadric-Surfaced Sludge Digesters (QSD) within Wastewater Infrastructure using 3-D Printing Techniques. *Instutue of Water*.

Journal Articles Under Review

Tota-Maharaj K. and Ramroop, N., (2019) Mechanical Characterisation of 3D-printed polymers through Finite Element Analysis (FEA) with Fused Deposition Technology. *Archives of Civil and Mechanical Engineering*.

Seminars

University of Greenwich Post-graduate Seminar: Structural Dynamics of Novel Quadric Surfaced Sludge Digesters for use in Waste Water Treatment Works in Small Island Developing States (SIDS). February 9th 2016. University of Greenwich. Kent. UK,

UWE Bristol IWSN Post-graduate Winter Conference: Seismic Response of Novel Quadric Surfaced Sludge Digesters for use in Waste Water Treatment Works. January 17th 2018. Arnolfini Centre. Bristol. UK.

UWE Bristol IWSN Post-graduate Winter Conference: Development of the Design Criteria for 3D-Printed Quadric Surfaced Sludge Digesters. January 15th 2019. Arnolfini Centre. Bristol. UK.

References

Abramson, H. (1961). Representation of Fuel Sloshing in Cylindrical Tanks by an Equivalent Mechanical Model. *ARS Journal.*

Abramson, H. (1967). *The dynamic behavior of liquids in moving containers, with applications to space vehicle technology*. Washington: Govt. Pr.

Abramson, H. and Garza, L. (1965). Liquid frequencies and damping in compartmented cylindrical tanks. *Journal of Spacecraft and Rockets.*

Ahn, S., Montero, M., Odell, D., Roundy, S. and Wright, P.K. (2002). Anisotropic material properties of fused deposition modeling ABS. *Rapid Prototyping*, 8(4), 248-257.

Allaire, G., Jouve, F. and Toader, A-M. (2002). A level-set method for shape optimization. *Comptes Rendus Mathematique*, 334(12), 1125–1130.

ASTM Standard, (1991). *C39/C39M-14 Standard test method for compressive strength of cylindrical concrete specimens.* West Conshohocken, ASTM International.

ASTM Standard, (2002). *D638-02 Standard for tensile testing of rigid plastics*, West Conshohocken, ASTM International.

ASTM Standard, (2008). *D618-08 Standard Practice for Conditioning Plastics for Testing*. West Conshohocken, ASTM International.

Axelrad, E. L., (1987). *Theory of Flexible Shells*. Elsevier Science Ltd.- New York, U.S.A.

Balendra, T. and Nash, W. (1978). *Earthquake analysis of a cylindrical liquid storage tank with a dome by finite element method*. Amherst, Mass.: Dept. of Civil Engineering, University of Massachusetts at Amherst.

Barnyak, M. and Barnyak, O. (1996). Normal oscillations of viscous liquid in a horizontal channel. *International Applied Mechanics.*

Bauer, H. (1964). Discussion: Breathing Vibrations of a Partially Filled Cylindrical Tank ”Linear Theory” *Journal of Applied Mechanics*.

Bauer, H. and Eidel, W. (1999). Frictionless liquid sloshing in circular cylindrical container configurations. *Aerospace Science and Technology*.

Belytschko, T., Liu, W. and Moran, B. (2014). *Nonlinear finite elements for continua and structures*. Chichester: Wiley.

Bengoubou-Valerius, M., Bazin, S., Bertil, D., Beauducel, F. and Bosson, A. (2008). A new seismological data center for the French Lesser. *Seismol*, 79(1), 90-102.

Berman, B. (2015). 3-D printing: The new industrial revolution. *Business Horizons*, 55(2), 155-162.

Berlot, R. (1960). Closure to Discussions of Production of Rotation in a Confined Liquid Through Translational Motion of the Boundaries (1960, ASME J. Appl. Mech., 27, p. 365). *Journal of Applied Mechanics*

Bozzoni, F., Corigliano, M., Lai, C.G., Salazar, W., Scandella, L., Zuccolo, E., Latchman, J., Lynch, L. and Robertson, R. (2011). Probabilistic Seismic Hazard Assessment at the Eastern Caribbean Islands. *Seismological Society of America*, 106(5), 2499–2521.

Brackbill, J., Kothe, D. and Ruppel, H. (1988). Flip: A low-dissipation, particle-in-cell method for fluid flow. *Computer Physics Communications*.

Brooks, J. (1959). *Dynamics of fluids in moving containers*. Ft. Belvoir: Defense Technical Information Center.

Brookshaw, L. (2003). Smooth particle hydrodynamics in cylindrical coordinates. *ANZIAM Journal*.

Budiansky, B. (1958). *Sloshing of liquids in circular canals and spherical tanks*. Ft. Belvoir: Defense Technical Information Center.

Chester, W. (1964). Resonant oscillations in closed tubes. *Journal of Fluid Mechanics*.

Cirak, F. and Radovitzky, R. (2005). A Lagrangian “Eulerian shell “fluid coupling algorithm based on level sets. *Computers & Structures*.

Colagrossi, A., Graziani, G. and Pulvirenti, M. (2014). Particles for fluids: SPH versus vortex methods. *Mathematics and Mechanics of Complex Systems*.

Cooper, R. and Doroff, S. (1974). *Symposium on Naval Hydrodynamics (10th), Hydrodynamics for*

Safety Fundamental Hydrodynamics. Ft. Belvoir: Defense Technical Information Center.

Currie, J. (2004). Advances in egg-shaped digester design enhance life cycle benefits. *Water and Wastewater International*, 19(4), 38-40.

Dao, M. and Asaro, R. J. (1999). A study on failure prediction and design criteria for fiber composites under fire degradation. *Composites*, 30(2), 123-131.

Doyle, J. F., (2007). *Nonlinear Analysis of Thin-Walled Structures*. Springer-Verlag New York, U.S.A.

Fritch, L.W. (1980), Injection molding ABS for properties, *Conference Proceedings*, Conference of the Society of Plastic Engineers, Los Angeles, California, 184-216.

Gates T.S., Veazie, D.R. and Brinson, C.L. (1996). A Comparison of Tension and Compression Creep in a Polymeric Composite and the Effects of Physical Aging on Creep. *NASA Technical Memorandum*, 1-33.

Gibson, A.G., Wu, Y.S., Evans, J.T. and Mouritz, A.P. (2006). Laminate theory analysis of composites under load in fire. *Journal of Composite Materials*. 40(7), 639-658.

Gibson, G., (1965). *Linear Elastic Theory of Thin Shells*: The Commonwealth and International Library: Structures and Solid Body Mechanics Division (Commonwealth Library). Pergamon, U.S.A.

Godderidge, B., Turnock, S. and Tan, M. (2012). A rapid method for the simulation of sloshing using a mathematical model based on the pendulum equation. *Computers & Fluids*.

Godderidge, B., Turnock, S. and Tan, M. (2012). Evaluation of a rapid method for the simulation of sloshing in rectangular and octagonal containers at intermediate filling levels. *Computers & Fluids*.

Goldstein, S. A., Wilson, D. L., Sonstegard, D. A. and Matthews, L. S., (1983). The mechanical properties of human tibial trabecular bone as a function of metaphyseal location. *Journal of Biomechanics*, 16(12), 965-969.

Gray IV, R.W., Baird, D.G. and Bohn, J.H., (1998). Effects of processing conditions on short TLCP fiber reinforced FDM parts. *Rapid Prototyping Journal*, 1(4), 4–25.

Graham, E. and Rodriquez, A. (1951). *The Characteristics of Fuel Motion which Affect Airplane Dynamics*. Ft. Belvoir: Defense Technical Information Center.

Guillénb, T., Zhang, Q.H., Tozzi, G., Ohrndorf, A., Christ, H.J. and Tong, J. (2011). Compressive behaviour of bovine cancellous bone and bone analogous materials, microCT characterisation and FE analysis. *Journal of The Mechanical Behaviour of Biomedical Materials*, 4(1), 1452-1461.

Guo, X.E., McMahon, T.A., Keaveny, T.M., Hayes, W.C. and Gibson, L.J. (1994). Finite element modeling of damage accumulation in trabecular bone under cyclic loading. Journal of biomechanics, 2(27), 145-155.

Harris, A. (2007). *Viscous Morphologies*. London, Bedford Press, 1-60.

Hayes, W.C. (1993). Theoretical analysis of the experimental artifact in trabecular bone modulus. *Journal of Biomechanics*, 26(4), 599-607.

Head, P.R. (1996). Advance composites in civil engineering. Montreal: a critical overview at this high interest, low use stage of development. *Conference 0Proceedings*, Proceedings of the 2nd International Conference on Advanced Composite Materials in Bridges and Structures, Montreal, Canada, 3-15.

Higgins, T. and Moran, M. (1968). Similitude: Theory and applications. *Journal of the Franklin Institute*.

Hossain, M.S., Ramos, J., Espalin, D., Perez, M. and Wicker, R. (2013). Improving tensile mechanical properties of FDM-manufactured specimens via modifying build parameters. *Conference Proceedings*. 24th International Solid Freeform Fabrication Symposium - An Additive Manufacturing Conference, Austin, Texas, 380-392.

Hughes, T. R. J. (1987). *The Finite Element Method: Linear Static and Dynamic Finite Element Analysis.* Englewood Cliffs, New Jersey: Prentice-Hall

Hutchinson, A. (2010). Rain Water Harvesting – Case Studies from the Barbados Experience. *Conference Proceedings*. Caribbean Waste Water Association Conference, Grenada. 1-14

Ibrahim, R. (2006). *Liquid sloshing dynamics*. Cambridge: Cambridge University Press.

Ibrahim, R., Yoon, Y. and Evans, M. (1990). Random excitation of nonlinear coupled oscillators. *Nonlinear Dynamics*.

Isaacson, M. and Ryu, C. (1998). Earthquake-Induced Sloshing in Vertical Container of Arbitrary Section. *Journal of Engineering Mechanics*.

Ibrahim, G. and Ganghoffer, J-F. (2014). 3D plastic collapse and brittle fracture surface models of trabecular bone from asymptotic homogenization method. *International Journal of Engineering Science*, 87, 58-82.

Johnson, G., Stryk, R. and Beissel, S. (1996). SPH for high velocity impact computations. *Computer Methods in Applied Mechanics and Engineering*.

Jones, I.C., Banner, J. L. and Mwansa, B.J. (1998). Geochemical Constraints on Recharge and Groundwater Evolution: The Pleistocene Aquifer of Barbados. *Conference Proceedings*, Third Annual Symposium on Water Resources. Barbados. 9-14

Kadir, R.A.M., Syahrom, A. and Öchsner, A. (2010). Finite element analysis of idealised unit cell cancellous structure based on morphological indices of cancellous bone. *Medical & Biological Engineering & Computing*, 48(5), 497-505.

Kaufmann, R. and Juselius, K. (2016). Testing competing forms of the Milankovitch hypothesis: A multivariate approach. *Paleoceanography*.

Keaveny, T.M., Borchers, R.E., Gibson, L.J. and Hayes, W.C. (1993). Trabecular bone modulus and strength can depend on specimen geometry. *Journal of Biomechanics*, 26(8), 991-1000.

Keaveny, T.M., Guo, X.E., Watchel, E.F., McMahon, T.A., Hayes, W.C. (1994). Trabecular bone exhibits fully linear elastic behavior and yields at low strains. *Journal of biomechanics*, 9(27), 1127-1136.

Khennane, A. (2013). Introduction to finite element analysis using MATLAB and Abaqus. New York, CRC Press.

Kline, S. (2012). *Similitude and approximation theory*: Springer.

Kowalczyk, P. (2003). Elastic properties of cancellous bone derived from finite element models of parameterized microstructure cells. *Journal of Biomechanics*, 36(7), 961-972.

Kratochvil, P. (1989). Structure and Properties of Polymers and Rawlings, R.D (ed.) *Material Science and Engineering.*, Oxford. Encyclopaedia of Life Support Systems,135-156.

Lamb, H. (1995). *Hydrodynamics*. Cambridge: Univ. Pr.

Lamb, J. and Mcneill, W. (1970). Fundamental sloshing frequency for an inclined, fluid-filled right circular cylinder. *Journal of Spacecraft and Rockets*.

Lawrence, H., Wang, C. and Reddy, R. (1958). Variational Solution of Fuel Sloshing Modes. *Journal of Jet Propulsion*.

Leonard, H. and Walton, W. (1961). *An investigation of the natural frequencies and mode shapes of liquids in oblate spheroidal tanks*. Ft. Belvoir: Defense Technical Information Center.

Liu, G. and Liu, M. (2009). *Smoothed particle hydrodynamics*. Singapore [etc.]: World Scientific.

Lia, J., Chen, H-M. and Chen, J-B. (2007). Studies on seismic performances of the prestressed egg-shaped digester with shaking table test. *Engineering Structures*, 29(4), 522-566.

Li, L., Sun, Q., Bellehumeur, C. and Gu, P. (2001). Composite modeling and analysis of FDM prototypes for design and fabrication of functionally graded parts. *Conference Proceedings*. 22th, Solid freeform fabrication symposium; Austin, Texas, 187-194.

Lucy, L. (1977). A numerical approach to the testing of the fission hypothesis. *The Astronomical Journal*.

Mamadapur, M. S., Zhang, Y. and Wang, J. (2015). Constitutive modelling for fused deposition modelling of acrylonitrile butadiene styrene (ABS) under elastic response. *International Journal of Rapid Manufacturing*, 5(1), 76-94.

Martens, M., Audekercke R.V., Delport, P., de Meester, P. and Mulier, J.C. (1983). The mechanical characteristics of cancellous bone at the upper femoral region. *Journal of Biomechanics*, 16(12), 971-983.

Masood S, H., Mau, K. and Song W.Q. (2010). Tensile properties of processed FDM polycarbonate. *Materials Science Forum*, 654, 2556-2559.

McIver, P. and McIver, M. (1993). Sloshing frequencies of longitudinal modes for a liquid contained in a trough. *Journal of Fluid Mechanics*.

Morse, P. and Feshbach, H. (1999). *Methods of theoretical physics*. Boston, Mass.: McGraw-Hill.

Nemat-Nasser, S. and Hori, M. (1993). Overall Properties of Heterogeneous Materials and Achenbach, D. (ed). *Micromechanics, 37(1)*,11.

Parkinson, I. H. and Fazzalari, N. L. (2013). Characterisation of Trabecular Bone Structure. *Stud Mechanobiol Tissue Eng Biomater*, 5, 31-51.

Perilli, E., Baleani, M., Ohman, C., Fognani, R., Baruffaldi, F. and Viceconti, M. (2008). Dependence of mechanical compressive strength on local variations in microarchitecture in cancellous bone of proximal human femur. *Journal of biomechanics*, 41(2), 438-446.

Proudman, J. and Lamb, H. (1925). Hydrodynamics. *The Mathematical Gazette*.

PTI, (2006). *Post-Tensioning Manual*. 6th edition. Phoenix, Post-Tensioning Institute.

Rodriguez, J. F., Thomas, J. P. and Renaud, J. E. (2001). Mechanical behavior of acrylonitrile. *Rapid Prototyping Journal*, 7(3), 148-58.

Rodriguez, J. F., Thomas, J. P. and Renaud, J. E. (2003). Mechanical behavior of acrylontrile butadiene styrene fused deposition materials modelling. *Rapid Prototyping Journal*, 9(4), 219-230.

Rodriguez, J.F., Thomas, J.P. and Renaud, J. E. (2001). "Mechanical behavior of acrylonitrile butadiene styrene (ABS) fused deposition materials. Experimental investigation. *Rapid Prototyping Journal*, 7(3), 148 - 158.

Rogowsky, D.M. and Marti, P. 1(996). *Detailing for Post Tensioning*. Bern, Switzerland: VSL International Ltd.

Feih, S., Mathys, Z., Gibson, A.G. and Mouritz, A.P. (2006). Modelling the tension and compression strengths of polymer laminates in fire. Composites Science and Technology, 67(3), 552-564.

Sayre, R. (2014). *A Comparative Finite Element Stress Analysis of Isotropic and Fusion Deposited 3D Printed Polymer,* unpublished thesis (M.Sc.), Rensselaer Polytechnic Institute.

Schimd, K. and Kalpakjian, S. (2008). *Manufacturing Processes for Engineering Materials,* 5th edition. Hoboken, New Jersey, Pearson Education.

Shaffer, S., Yang, K.J., Vargas, J., Di Prima, M.A. and Voit, W. (2014). On reducing anisotropy in 3D printed polymers via ionizing radiation. Polymer, 55(23), 5969–5979.

Shofner, M.L., Lozano, K., Rodríguez-Macías, F.J. and Barrera, E.V. (2003). Nanofiber-reinforced polymers prepared by fused deposition modeling. Journal of Applied Polymer Science, 89(11), 3081-3090.

Shrimali, M. and Jangid, R. (2002). Seismic response of liquid storage tanks isolated by sliding bearings. *Engineering Structures*.

Sixt, H. and Wilderer, P. A. (1983). Design and performance of egg-shaped digesters for combined sludge and industrial wastewater treatment. *Conference Proceedings*, Proceedings of the 38th Industrial Waste Conference. West Lafayette, Indiana, 627-636

Sood, A.K., Ohdar , R.K. and Mahapatra, S.S. (2010). Parametric appraisal of mechanical property of fused deposition modelling processed parts. *Materials and Design*, 31(1), 287-295.

Stansbury, J.W. and Idacavage, M.J., (2015). 3D printing with polymers. challenging among expanding options. Dental Materials, 32(1), 54-64.

Stava, O., Vanek, J., Benes, B., Carr, N. and Mech, R. (2012). Stress Relief: Improving Structural Strength of 3D Printable Objects. *ACM Transactions on Graphics*, 31(4), 1-11.

Stephens, D. (1965). *Experimental investigation of liquid impact in a model propellant tank*. Washington, DC: National Aeronautics and Space Administration.

Stephens, D. (1965). *Experimental investigation of liquid impact in a model propellant tank*.

Washington, DC: National Aeronautics and Space Administration.

Sutter, G. (1996). Specialized formwork for symmetrical concrete structures. *Concrete International*, 18(10). 50–53.

Tekinalp, H.L., Kunc, V., Velez-Garcia, G.M., Duty, C.E. and Love, L.J. (2014). Highly oriented carbon fiber–polymer composites via additive. *Composites Science and Technology*, 105(5), 144-150.

Trembath, N. (1957). *Fluid sloshing in tanks of arbitrary shape*. Ft. Belvoir: Defense Technical Information Center.

Trotsenko, V. (1967). On free vibrations of liquid in a cylinder with annular ribs. *Soviet Applied Mechanics*.

Torrado, A.R., Shemelya, C.M., English, J.D. and Lin, Y. (2015). Characterizing the effect of additive to ABS on the mechanical anisotropy of specimens fabricated by material extrusion 3D-printing. *Additive Manufacturing*, 6, 16-29.

Wang, H., Liu, S.X., Zhou, B., Wang, J., Ji, B., Huang, Y., Hwang, K. and Guo, X.E. (2013). Accuracy of individual trabecula segmentation based plate and rod finite element models in idealized trabecular bone microstructure. *Journal of Biomechanical Engineering*, 135(4), 1393-1398

Wang, J., Zhou, B., Stein, E., Shi, X., Adams, M., Shane, E., Liu, S.X. and Guo, X.E. (2013). Fast Trabecular Bone Strength Predictions of HR-pQCT and Individual Trabeculae Segmentation–Based Plate and Rod Finite Element Model Discriminate Postmenopausal Vertebral Fractures. *Journal of Bone and Mineral Research*, 28(7),1666-1678.

Weiss, H. and Rogge, T. (1965). *A nonlinear analysis for sloshing forces and moments on a cylindrical tank*. [Washington]: National Aeronautics and Space Administration.

Widmayer, E. and Reese, J. (1953). *Moment of inertia and damping of fluid in tanks undergoing pitching oscillations*. Washington, D.C.: National Advisory Committee for Aeronautics.

Wu, H. C. 2006. *Advanced civil infrastructure materials*. Sawston, Cambridge, Woodhead Publishing Limited. 271-273.

Zhong, W., Lia, F., Zhang, Z., Song, L. and Li, Z. (2001). Short fiber reinforced composites for fused deposition. *Journal of Material Engineering Science*, 301(2), 125–130.

Zhu, H. X., Knott, J. F. and Mills, N. J. (1997). Analysis of the elastic properties of open-cell foams with tetrakaidekahedral cells. *Journal of the Mechanics and Physics of Solids*, 45(3), 319-343.

Zingoni, A. (2001). Stresses and deformations in egg-shaped sludge digesters: Membrane effects. Engineering Structures, 23(11), 1365-1372.

Zingoni, A. (2002). Parametric stress distribution in shell-of-revolution sludge digesters of parabolic ogival form. *Thin-walled Structures*, 40(7), 691-702.

Zingoni, A. (2004). Shell forms for egg-shaped concrete sludge digesters: A comparative study on structural efficiency. *Structural Engineering and Mechanics*, 19(3), 321-336.

APPENDICES

APPENDIX I

QUADRIC SURFACE SLUDGE DIGESTER DESIGN GUIDE

1. Given the volume of sludge to be treated, the dimensions can be deduced from the following:

$$D = \sqrt{\frac{15V}{2\pi H}} \quad \text{or} \quad H = \frac{15V}{2\pi D^2}$$

Where V = internal volume of the QSD x 10% of volume of sludge to be treated.

2. Using Figure A1, deduce overall dimensions of the QSD.

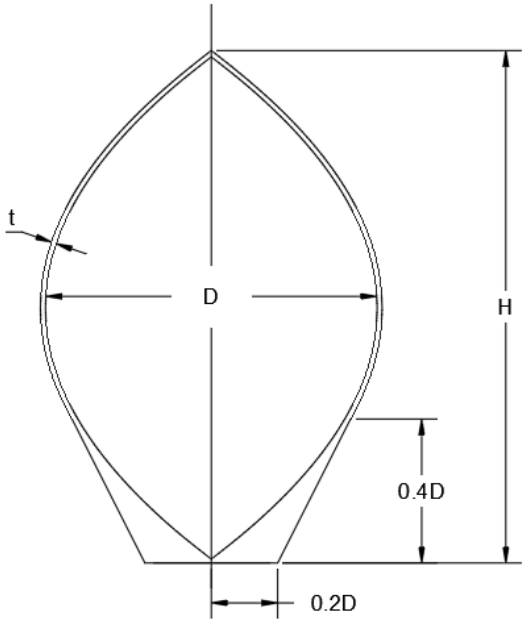

Figure A1. General design dimensions of the QSD

3. Choose an arbitrary thickness, t > 400mm.
4. Use 3D FDM material ensuring tool extrusion path is always parallel to the tangent of the circumference of the shell.
5. Analyse the QSD using appropriate FEA software to determine the stresses
6. Ensure that:

$$\emptyset\sigma_y > \sigma_1, \sigma_2 \rightarrow for\ Serviceablity\ Limit\ State$$

And,

$$\emptyset\sigma_{ult} > \sigma_{VonMises} \rightarrow for\ Ultimate\ Limit\ State$$

Where $\emptyset$ =0.60

σ_y is the yield stress of 3D Printed ABS

σ_1, σ_2 are the principal stresses in the longitudinal and cross-sections respectively.

σ_{ult} is the ultimate tensile stress

$\sigma_{VonMises}$ is the Von Mises stress

7. If $\emptyset\sigma_y < \sigma_1, \sigma_2$ then revise thickness t.
8. If $\emptyset\sigma_{ult} > \sigma_{VonMises}$ then revise thickness t.

APPENDIX II

FIRST PRINCIPLES MATLAB CODE

```
%%%%%%%%%%%%%%%%%%%
% QSD MATLAB CODE %
%%%%%%%%%%%%%%%%%%%


clc
global ugdd n time
%GUI Inputs:
%-----------
sel1 = questdlg('What is the required input type?', ...
                         'Input Type Selection', ...
                         'Frquency Input','History Data','Frquency Input');
switch sel1
    case 'Frquency Input'
        prompt={'Tank Height(m):','Tank Diameter(m):','Tank Min
Thickness(m):','Tank Max Thickness(m):','Tank Modulus of
Elasticity(GPa):',...
            'Tank Wall Density(Kg/m3):','Ground Frequency(Hz):'};
        name='Inputs:';
        numlines=1;
        defaultanswer={'25','10','0.5','2','1.636','1052','5'};
        answer=inputdlg(prompt,name,numlines,defaultanswer);
        fg=str2double(answer{7});                          %Ground motion
frequency
        %Ground Motion calculations:
        %---------------------------
        A=1;                                                %Amplitude
        dt=0.1;                                             %Time step
        t=0:dt:20;                                          %simulation time
        ug=A.*sin(2.*pi.*pi.*fg.*t./180);                   %ground
displacement
        dugdt=diff(ug)./diff(t);                            %Ground velocity
        d2ugdt2=diff(dugdt)./diff(t(1:end-1));              %Ground
acceleration
        ugdd=mean(d2ugdt2);                                 %Mean ground
acceleration
    case 'History Data'
        prompt={'Tank Height(m):','Tank Diameter(m):','Tank Min
Thickness(m):','Tank Max Thickness(m):','Tank Modulus of
Elasticity(GPa):',...
            'Tank Wall Density(Kg/m3):'};
        name='Inputs:';
        numlines=1;
        defaultanswer={'25','12.5','0.5','2.5','1.636','1052','5'};
        answer=inputdlg(prompt,name,numlines,defaultanswer);
        %Ground Motion calculations:
        %---------------------------
        DATA=xlsread('ADJUSTED-Kobe;RSN 1120;Takatori 1995 Time History
Data.xlsx');
        t=DATA(:,1);                                        %Time data
        [t, order]=sort(t);                                 %Sorting time
vector in ascending order
```

```
        ugdd=DATA(:,2);                                         %ground
acceleration data
        ugdd=ugdd(order);                                       %sorting
acceleration with respect to time
        ug=ugdd./(2*(pi^2)*(50^2));                             %ground
displacement
        ug=transp(ug);
        ugdd=mean(ugdd);                                        %Mean ground
acceleration

end
time=t;

H=str2double(answer{1});                                %Tank Height
D=str2double(answer{2});                                %Tank Center Diameter
tmin=str2double(answer{3});                             %Tank minimum
thickness
tmax=str2double(answer{4});                             %Tank maximum
thickness
E=str2double(answer{5})*(10^9);                         %Tank modulus of
elasticity
rhos=str2double(answer{6});                             %Tank material density
n=8;                                                    %Number of sections



prompt={'Fill Level 1:','Fill Level 2:','Fill Level 3:','Fill Level
4:','Fill Level 5:'};
name='Fill Levels Comparison Inputs (%):';
numlines=1;
defaultanswer={'10','25','50','75','90'};
answer=inputdlg(prompt,name,numlines,defaultanswer);

%Tank type selection:
%--------------------
sel = questdlg('What is the required tank type?', ...
                        'Tank Type Selection', ...
                        'Base Isolated','Fixed','Base Isolated');

FL=zeros(5,1); Ub=zeros(length(t),5);
Uc=zeros(n+1,length(t),5); Uc_m=zeros(n+1,5);
Fn=zeros(n+1,length(t),5); Fn_m=zeros(n+1,5);
Ft=zeros(n+1,length(t),5); Ft_m=zeros(n+1,5);
Segn=zeros(n+1,length(t),5); Segn_m=zeros(n+1,5);
Segt=zeros(n+1,length(t),5); Segt_m=zeros(n+1,5);
for i=1:5
    switch answer{i}
        case 'N/A'
            FL(i)=0;
        otherwise
            FL(i)=str2double(answer{i})/200;

[Uc(:,:,i),Uc_m(:,i),Ub(:,i),Fn(:,:,i),Ft(:,:,i),Fn_m(:,i),Ft_m(:,i),Segn(:
,:,i),Segt(:,:,i),Segn_m(:,i),Segt_m(:,i)]=...
                LSTSolFun(H,D,tmin,tmax,E,rhos,FL(i),sel,n,t,ug,ugdd);
    end
end
```

```
%Plotting:
%-----------
for j=1:n+1
    figure(1)
    plot(t,Uc(j,:,1),'LineWidth',1.5), xlabel('Time(s)'),
ylabel('Displacement(m)'), title('Section Displacement'), grid on, hold on
    figure(2)
    plot(t,Fn(j,:,1).*(10^-6),'LineWidth',1.5), xlabel('Time(s)'),
ylabel('Force, N_{\theta}(MN)'), title('N_{\theta} Vs T'), grid on, hold on
    figure(3)
    plot(t,Ft(j,:,1).*(10^-6),'LineWidth',1.5), xlabel('Time(s)'),
ylabel('Force, N_{\phi}(MN)'), title('N_{\phi} Vs T'), grid on, hold on
    figure(4)
    plot(t,Segn(j,:,1).*(10^-6),'LineWidth',1.5), xlabel('Time(s)'),
ylabel('Stress, \sigma_{\theta}(MPa)'), title('\sigma_{\theta} Vs T'), grid
on, hold on
    figure(5)
    plot(t,Segt(j,:,1).*(10^-6),'LineWidth',1.5), xlabel('Time(s)'),
ylabel('Stress, \sigma_{\phi}(MPa)'), title('\sigma_{\phi} Vs T'), grid on,
hold on

end
switch sel
    case 'Base Isolated'
        figure(6)
        plot(t,Ub(:,1),'LineWidth',1.5), xlabel('Time(s)'),
ylabel('Displacement(m)'), title('Base Displacement'), grid on
end
figure(1)
legend('Section 1','Section 2','Section 3','Section 4','Section 5','Section
6','Section 7','Section 8','Location','NorthEast')
figure(2)
legend('Section 1','Section 2','Section 3','Section 4','Section 5','Section
6','Section 7','Section 8','Location','NorthEast')
figure(3)
legend('Section 1','Section 2','Section 3','Section 4','Section 5','Section
6','Section 7','Section 8','Location','NorthEast')
figure(4)
legend('Section 1','Section 2','Section 3','Section 4','Section 5','Section
6','Section 7','Section 8','Location','NorthEast')
figure(5)
legend('Section 1','Section 2','Section 3','Section 4','Section 5','Section
6','Section 7','Section 8','Location','NorthEast')

TH=zeros(n+1,1);
for j=0:n
    TH(j+1)=(j/n)*H;
end
TH=flip(TH);
for i=1:5
    figure(8)
    plot(TH,Uc_m(:,i),'LineWidth',1.5), xlabel('Tank Height(m)'),
ylabel('Peak Section Displacement(m)'), title('Peak Displacement For Each
Section'), hold on, grid on
    figure(9)
    plot(TH,Fn_m(:,i),'LineWidth',1.5), xlabel('Tank Height(m)'),
ylabel('Peak N_{\theta}(Pa)'), title('Peak N_{\theta} For Each Section'),
hold on, grid on
    figure(10)
```

```
    plot(TH,Ft_m(:,i),'LineWidth',1.5), xlabel('Tank Height(m)'),
ylabel('Peak N_{\phi}(Pa)'), title('Peak N_{\phi} For Each Section'), hold
on, grid on
    figure(11)
    plot(TH,Segn_m(:,i),'LineWidth',1.5), xlabel('Tank Height(m)'),
ylabel('Peak \sigma_{\theta}(Pa)'), title('Peak \sigma_{\theta} For Each
Section'), hold on, grid on
    figure(12)
    plot(TH,flip(Segt_m(:,i)),'LineWidth',1.5), xlabel('Tank Height(m)'),
ylabel('Peak \sigma_{\phi}(Pa)'), title('Peak \sigma_{\phi} For Each
Section'), hold on, grid on
end
hold off all
figure(8)
legend('Fill Level 1','Fill Level 2','Fill Level 3','Fill Level 4','Fill
Level 5')
figure(9)
legend('Fill Level 1','Fill Level 2','Fill Level 3','Fill Level 4','Fill
Level 5')
figure(10)
legend('Fill Level 1','Fill Level 2','Fill Level 3','Fill Level 4','Fill
Level 5')
figure(11)
legend('Fill Level 1','Fill Level 2','Fill Level 3','Fill Level 4','Fill
Level 5')
figure(12)
legend('Fill Level 1','Fill Level 2','Fill Level 3','Fill Level 4','Fill
Level 5')

function
[Uc,Uc_m,Ub,Fn,Ft,Fn_m,Ft_m,Segn,Segt,Segn_m,Segt_m]=LSTSolFun(H,D,tmin,tma
x,E,rhos,HL,sel,n,t,ug,ugdd)
global Mt g mew
%Other Inputs:
%-------------
rhow=1000;                          %Liquid density
zetac=0.5/100;                      %Convective damping ratio
zetai=2/100;                        %Impulsive damping ratio
zetab=10/100;                       %Bearing damping ratio
Tb=2;                               %Bearing period of isolation
Tt=20;                              %Total time of simulation
Mt=2*pi*(D^2)*H*rhow/15;            %Total mass
g=9.81;                             %Gravitational acceleration
mew=0.01;                           %Coeff. of friction

%Output to command window:
%--------------------------
fprintf('H/D ratio = %g\n',H/D)
fprintf('NOTE: Section (1) is top of the tank and section (n) is bottom of
the tank\n\n')

%Tank Geometrical Calculations:
%------------------------------
global R j
R=zeros(ceil((n+1)/2),1);                       %Radius vector
initialization
for j=1:ceil((n+1)/2)                           %For loop
    R(j)=(D/2)-((2*D/(H^2))*((j*H/n)-H/n)^2);     %Radius calculation for
each section in lower half
end
R(end)=0.2;
```

```
R2=flip(R);                                          %Mirroring radius for
upper half
R=[R2(1:end-1);R];                                    %Vector assembly
phai=linspace(0,30,n+1).*pi/180;

th=zeros(n+1,1);                                    %Thickess
Hd=round(n+1/4);                                    %Decision height
for j=1:Hd
    th(j)=tmax-(((tmax-tmin)/0.25)*(j/n));          %Variable thickness
end
for j=Hd+1:n+1
    th(j)=tmin;                                     %Constant thickness
end

%Mass, Stiffness, and Damper calculations:
%-----------------------------------------
global Mcc Kcc Ccc Kb Cb Mr Mtot
Mc=zeros(n,1); Mi=zeros(n,1);
%Mass Initialization
Kc=zeros(n,1); Ki=zeros(n,1);
%Stiffness Initialization
Cc=zeros(n,1); Ci=zeros(n,1);
%Damper Initialization
P=zeros(n,1);  wi=zeros(n,1); wc=zeros(n,1);
%Natural frequency
Mr=Mt*(-0.01599+(0.86356*HL/R(1))-
(0.30941*(HL/R(1))^2)+(0.04083*(HL/R(1))^3));
%Rigid mass calculation
for j=1:n
    Mc(j)=Mt*(1.01327-(0.87578*HL/R(j))+(0.35708*(HL/R(j))^2)-
(0.06692*(HL/R(j))^3+(0.00439*(HL/R(j))^4))); %Convective mass for each
section
    Mi(j)=Mt*(-0.15467+(1.21716*HL/R(j))-
(0.62839*(HL/R(j))^2)+(0.14434*(HL/R(j))^3-(0.0125*(HL/R(j))^4)));
%Impulsivemass for each section
    P(j)=0.07726+(0.17563*HL/R(j))-
(0.106*(HL/R(j))^2)+(0.02609*(HL/R(j))^3)-(0.0025*(HL/R(j))^4);
%Dimensionless parameter
    wc(j)=sqrt(1.84*(g/R(j))*tanh(H/R(j)));
%Convective natural frequency
    wi(j)=(P(j)/H)*sqrt(E/rhos);
%Impulsive natural frequency
    Kc(j)=Mc(j)*(wc(j))^2;
%Convective stiffness
    Ki(j)=Mi(j)*(wi(j))^2;
%Impulsive stiffness
    Cc(j)=2*zetac*Mc(j)*wc(j);
%Convective damping
    Ci(j)=2*zetai*Mi(j)*wi(j);
%Impulsive damping
end
Mcc=Mc+Mi;
Ccc=Cc+Ci;
Kcc=Kc+Ki;
Mcct=sum(Mcc);
Mtot=Mr+Mcct;
Mct=sum(Mc);
%Total convective mass
Mit=sum(Mi);
%Total impulsive mass
```

```
wb=2*pi/Tb;
%Base natural frequency
Kb=(Mct+Mit+Mr)/((Tb/(2*pi))^2);
%Base stiffness
Cb=zetab*2*wb*(Mct+Mit+Mr);
%Base damper


%Displacement calculation:
%------------------------------
Uc=zeros(n,length(t));
Ucd=zeros(n,length(t));
%Acceleration Initialization
Uc_m=zeros(n+1,1);
y0=zeros(n+1,1);
dy0=0.1.*ones(n+1,1);
yini=[y0;dy0];
[~,y] = ode45(@ODEsolver,t,yini);                                   %Ode
Solver
for j=1:n
    Uc(j,:)=transp(y(:,j));                                         %Section
Displacement
end
Ub=transp(y(:,n+1));                                                %Bearing
Displacement
jj=1;
for j=n+2:2*n+1
    Ucd(jj,:)=transp(y(:,j));                                       %Section
Acceleration
end

for j=1:n
    switch sel
        case 'Fixed'
            Uc(j,:)=Uc(j,:)-ug;                                        %Fixed
Tank case
        case 'Base Isolated'
            Uc(j,:)=Uc(j,:)-Ub;                                        %Base
Isolated Tank case
    end
end

Uc=[Uc;Ub];
size(Uc)
for j=1:n+1
    Uc_m(j)=max(Uc(j,:));
end


%Force Calculation:
%------------------
Fs=zeros(n+1,length(t));
Fn=zeros(n+1,length(t));
Ft=zeros(n+1,length(t));
Fn_m=zeros(n+1,1);
Ft_m=zeros(n+1,1);
Pr=(10^5).*((2.*H.*D.*sin(phai))-((H^2).*cos(phai))./(4.*D.*sin(phai));

for j=1:n
```

```
    Fs(j,:)=-(Mcc(j).*(Uc(j,:)+ugdd));
%Sloshing Force Calculation
    Fn(j,:)=Fs(j,:).*sin(phai(j));
%Normal Force
    Ft(j,:)=Fs(j,:).*cos(phai(j));
%Tangential Force
    Fn_m(j)=max(Fn(j,:));
    Ft_m(j)=max(Ft(j,:));
end
Fs(n+1,:)=-(Mr.*(Uc(n+1,:)+ugdd));
%Sloshing Force Calculation
Fn(n+1,:)=Fs(n+1,:).*sin(phai(n));
%Normal Force
Ft(n+1,:)=Fs(n+1,:).*cos(phai(n));
%Tangential Force
Fn_m(n+1)=max(Fn(n+1,:));
Ft_m(n+1)=max(Ft(n+1,:));

%Stress Calculation:
%-------------------
Segn=zeros(n+1,length(t));
Segt=zeros(n+1,length(t));
Segn_m=zeros(n+1,1);
Segt_m=zeros(n+1,1);
for j=1:n
    Segn(j,:)=Fn(j,:)./(R(j))*(th(j));
%Normal Stresses Calculation
    Segt(j,:)=Ft(j,:)./(R(j)*th(j));
%Tangential Stresses Calculation
    Segn_m(j)=max(Segn(j,:));
    Segt_m(j)=max(Segt(j,:));
end
Segn(n+1,:)=Fn(n+1,:)./(R(n+1))*(th(n));
%Normal Stresses Calculation
Segt(n+1,:)=Ft(n+1,:)./(R(n+1)*th(n));
%Tangential Stresses Calculation
Segn_m(n+1)=max(Segn(n+1,:));
Segt_m(n+1)=max(Segt(n+1,:));

end


function dydt=ODEsolver(t,y)
%Function called to solve ODE Equations
global ugdd Cb Kb Ccc Mcc Kcc Mtot
s1=-ugdd-(Ccc(8)*y(1)/Mcc(8))-(Kcc(8)*y(10)/Mcc(8));
s2=-ugdd-(Ccc(7)*y(2)/Mcc(7))-(Kcc(7)*y(11)/Mcc(7));
s3=-ugdd-(Ccc(6)*y(3)/Mcc(6))-(Kcc(6)*y(12)/Mcc(6));
s4=-ugdd-(Ccc(5)*y(4)/Mcc(5))-(Kcc(5)*y(13)/Mcc(5));
s5=-ugdd-(Ccc(4)*y(5)/Mcc(4))-(Kcc(4)*y(14)/Mcc(4));
s6=-ugdd-(Ccc(3)*y(6)/Mcc(3))-(Kcc(3)*y(15)/Mcc(3));
s7=-ugdd-(Ccc(2)*y(7)/Mcc(2))-(Kcc(2)*y(16)/Mcc(2));
s8=-ugdd-(Ccc(1)*y(8)/Mcc(1))-(Kcc(1)*y(17)/Mcc(1));
s9=-ugdd-(Mcc(8)*y(1)/Mtot)-(Mcc(7)*y(2)/Mtot)-(Mcc(6)*y(3)/Mtot)-
(Mcc(5)*y(4)/Mtot)-(Mcc(4)*y(5)/Mtot)-(Mcc(3)*y(6)/Mtot)-
(Mcc(2)*y(7)/Mtot)-(Mcc(1)*y(8)/Mtot)-(Cb*y(9)/Mtot)-(Kb*y(18)/Mtot);
dydt=[s1;s2;s3;s4;s5;s6;s7;s8;s9;y(1);y(2);y(3);y(4);y(5);y(6);y(7);y(8);y(
9)];

end
```

```
%%%%%%%%%%%%%
% END OF CODE %
%%%%%%%%%%%%%
```

APPENDIX III

MATLAB CODE TO GENERATE SURFACE PLOTS

```
%%%%%%%%%%%%%%%%%%%%%%%%%%%%%%%%%%%%%%%%
% MATLAB CODE TO GENERATE SURFACE PLOT%
%%%%%%%%%%%%%%%%%%%%%%%%%%%%%%%%%%%%%%%%

plot3(x,y,z,'.-')
tri = delaunay(x,y);
plot(x,y,'.')
%%
 [r,c] = size(tri);
disp(r)
%% Plot it with TRISURF
h = trisurf(tri, x, y, z);
axis vis3d

%l = light('Position',[-140 25 10])
%set(gca,'CameraPosition',[40 -1.5 5])
view ([30 18])
%p perspective
lighting phong
shading interp
%colorbar EastOutside
colormap('jet');
set(gca, 'projection', 'perspective', 'box', 'on')

%AXIS OPTIONS
axis on
axis tight
xlabel('Height of QSD (m)', 'fontsize', 10, 'fontweight', 'bold', 'color',
[0 0 0],'HorizontalAlignment','right')
ylabel('Shell thickness (m)', 'fontsize', 10, 'fontweight', 'bold',
'color', [0 0 0],'HorizontalAlignment','left')
zlabel('Hoop Stress \sigma_{\theta} (kPa)', 'fontsize', 10, 'fontweight',
'bold', 'color', [0 0 0],'HorizontalAlignment','center')

xh = get(gca,'xLabel'); % Handle of the x label
set(xh, 'Units', 'Normalized')
pos = get(xh, 'Position');
set(xh, 'Position',pos.*[1.1,2,1],'Rotation',-14)

xh = get(gca,'yLabel'); % Handle of the y label
set(xh, 'Units', 'Normalized')
pos = get(xh, 'Position');
set(xh, 'Position',pos.*[.85,6,1],'Rotation',40)


%%%%%%%%%%%%%%%
% END OF CODE %
%%%%%%%%%%%%%%%
```

APPENDIX IV

FIRST PRINCIPLES TIME-HISTORY PEAK FORCE VALUES FOR 25M QSD

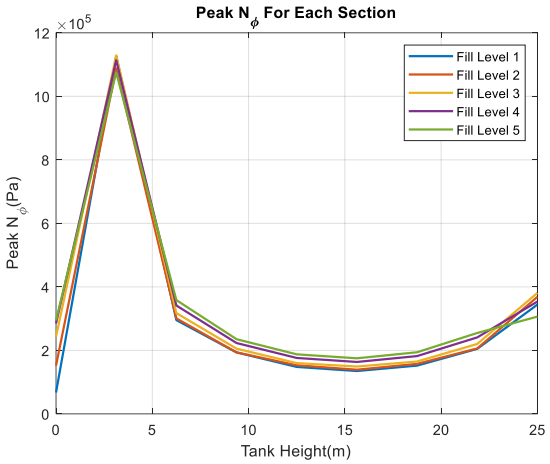

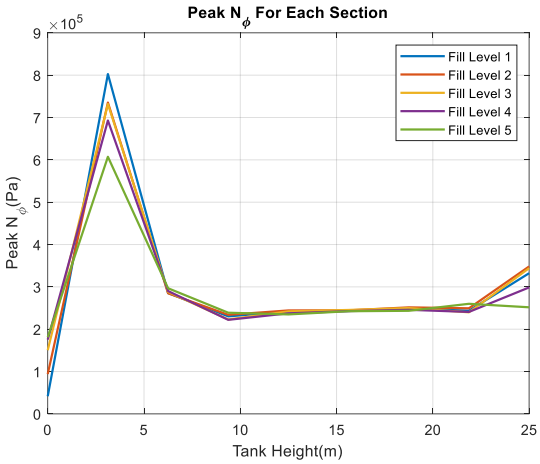

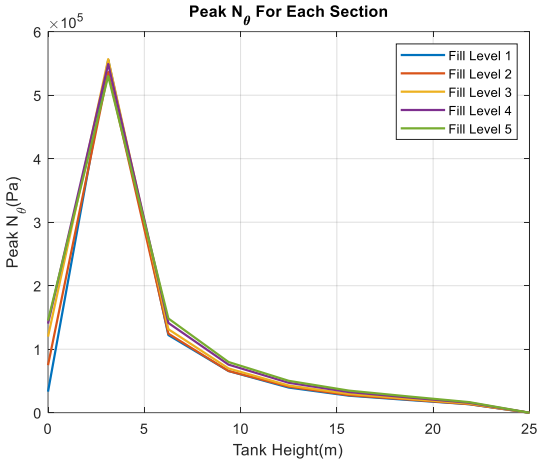

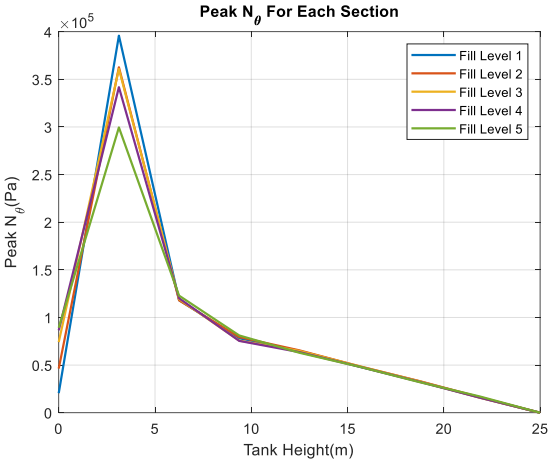

APPENDIX V

MULTUPLE ANOVA TAKE OF DEPENDENT VARIABLES

Tests of Between-Subjects Effects

Dependent Variable: stress

Source	Type III Sum of Squares	df	Mean Square	F	Sig.	Partial Eta Squared
Corrected Model	1376059256617.017[a]	605	2274478110.111	387.849	.000	.999
Intercept	232951078714.270	1	232951078714.270	39723.290	.000	.996
distance	586221646990.637	16	36638852936.915	6247.731	.000	.999
thickness	100069074523.248	4	25017268630.812	4265.995	.000	.992
height	730919580.095	4	182729895.024	31.159	.000	.464
fill	15090267631.675	4	3772566907.919	643.306	.000	.947
distance * thickness	251772514347.423	64	3933945536.678	670.824	.000	.997
distance * height	1252575562.454	9	139175062.495	23.732	.000	.597
distance * fill	57851088633.782	64	903923259.903	154.139	.000	.986
thickness * height	207636308.127	16	12977269.258	2.213	.007	.197
thickness * fill	4820718701.193	16	301294918.825	51.377	.000	.851
height * fill	1093784338.991	16	68361521.187	11.657	.000	.564
distance * thickness * height	616951848.016	36	17137551.334	2.922	.000	.422
thickness * height * fill	370860971.181	64	5794702.675	.988	.511	.305
distance * thickness * fill	26411821419.023	256	103171177.418	17.593	.000	.969
distance * height * fill	2146651118.759	36	59629197.743	10.168	.000	.718
Error	844465684.477	144	5864345.031			
Total	1552219946362.578	750				
Corrected Total	1376903722301.494	749				

a. R Squared = .999 (Adjusted R Squared = .997)

APPENDIX VI

SURFACE PLOTS FOR HYDROSTATIC CASE

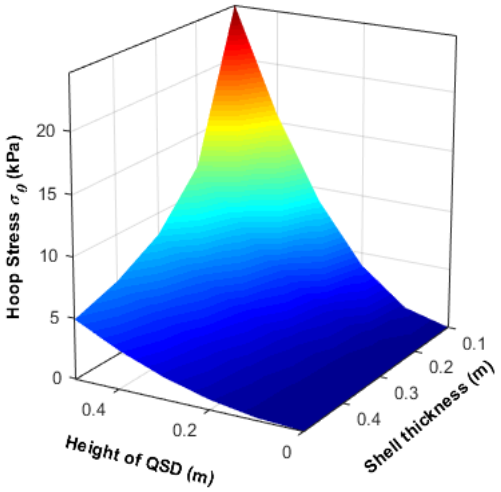

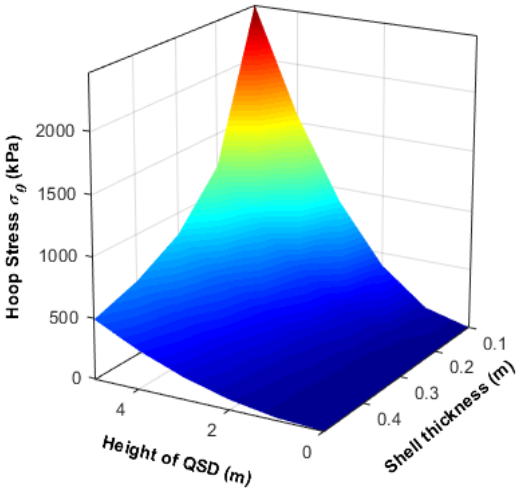

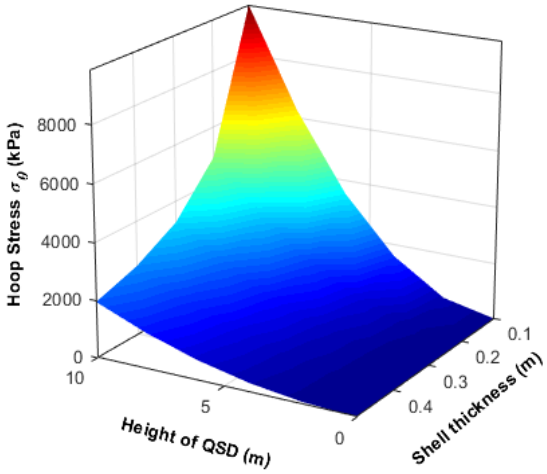

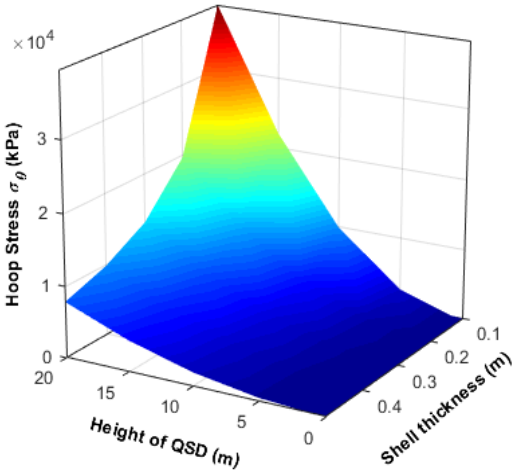

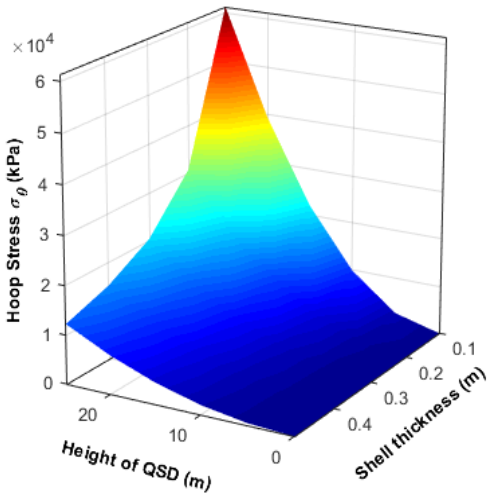

SURFACE PLOTS FOR DYNAMIC CASE -10% FILL LEVEL

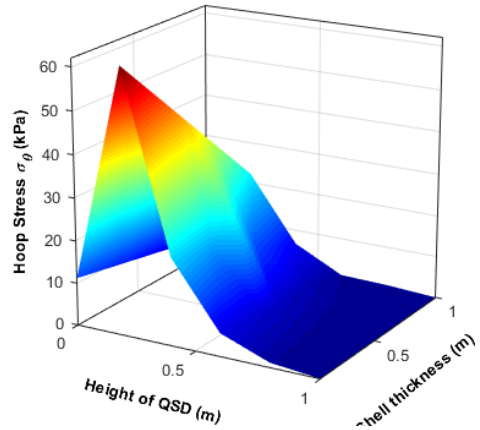

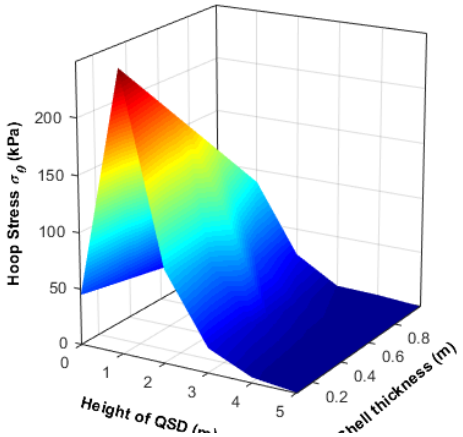

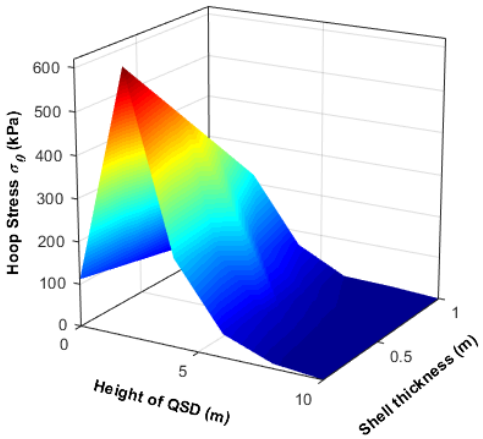

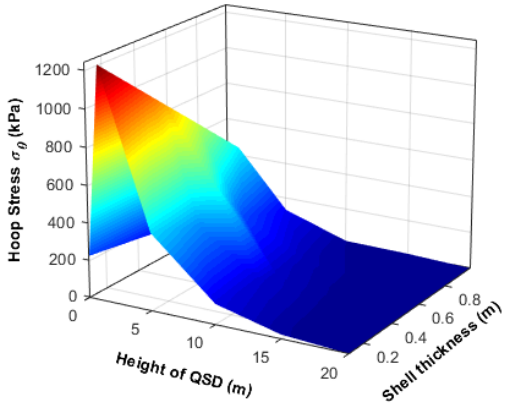

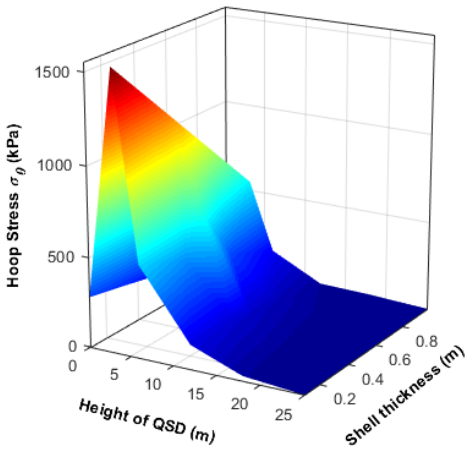

SURFACE PLOTS FOR DYNAMIC CASE -25% FILL LEVEL

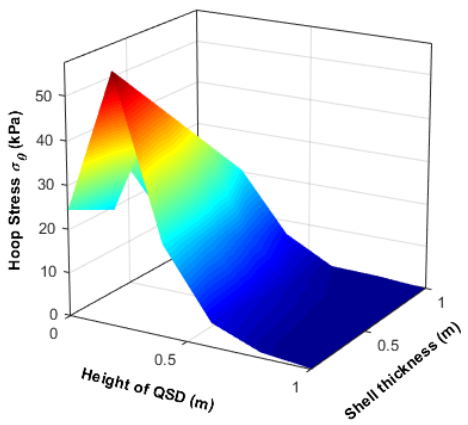

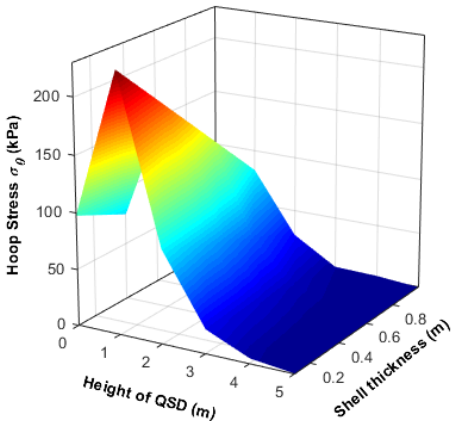

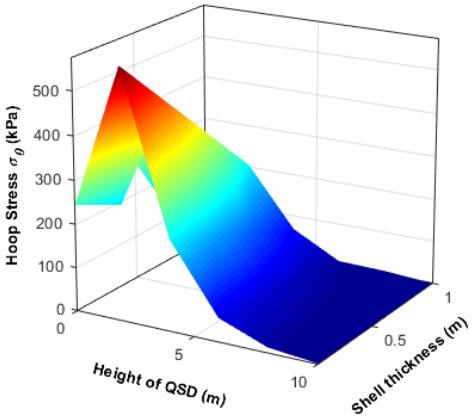

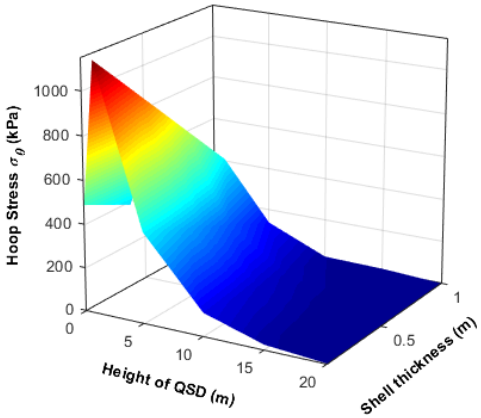

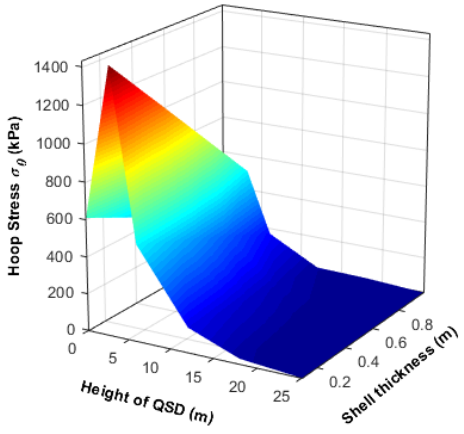

SURFACE PLOTS FOR DYNAMIC CASE -50% FILL LEVEL

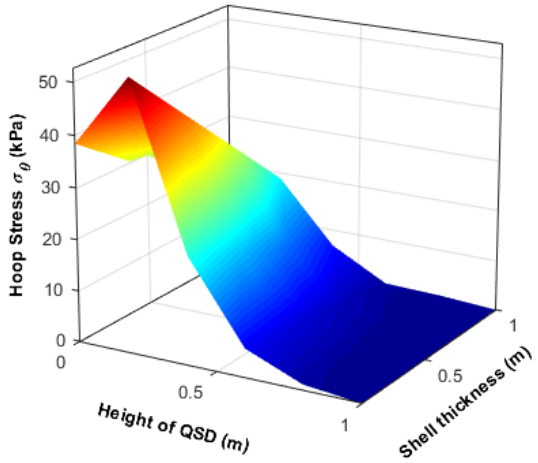

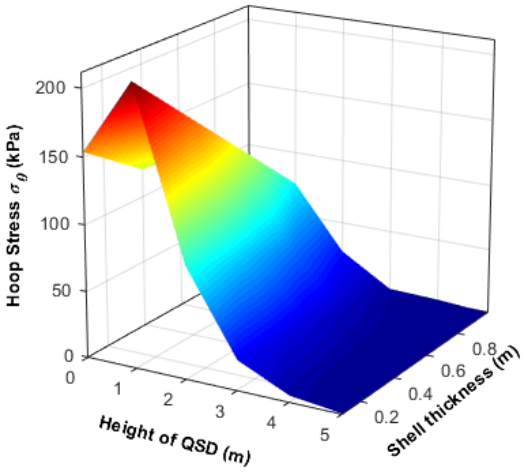

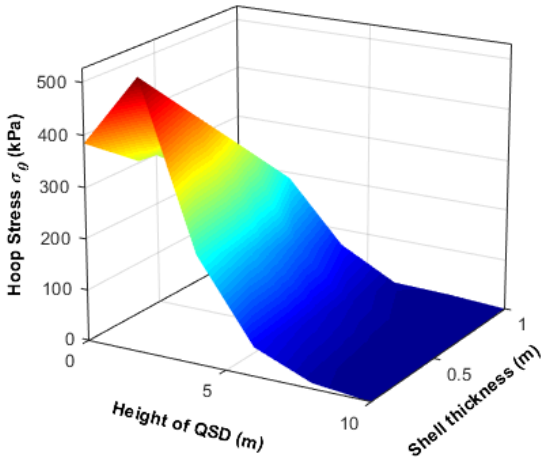

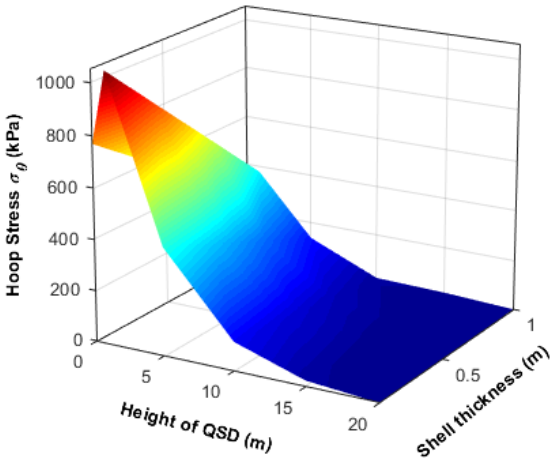

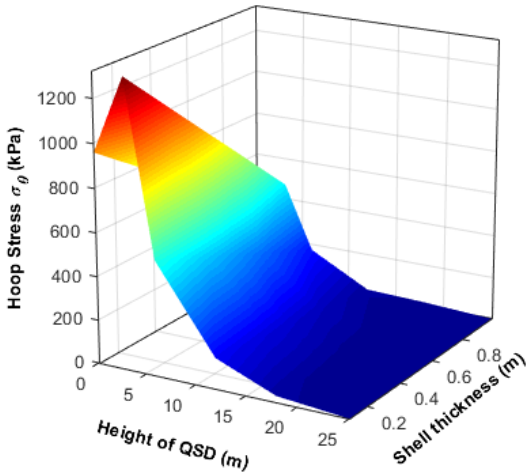

SURFACE PLOTS FOR DYNAMIC CASE -75% FILL LEVEL

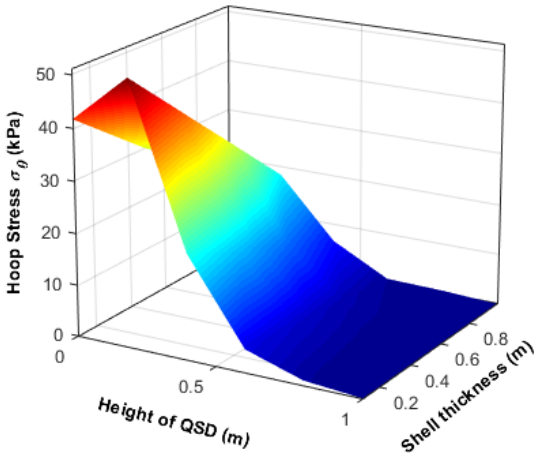

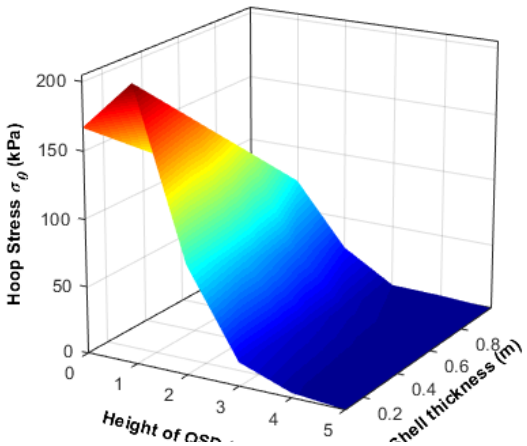

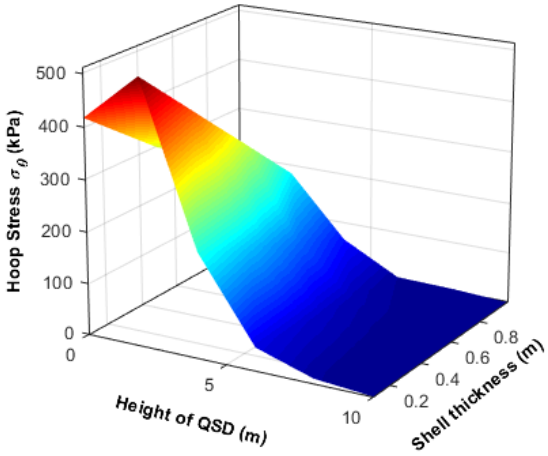

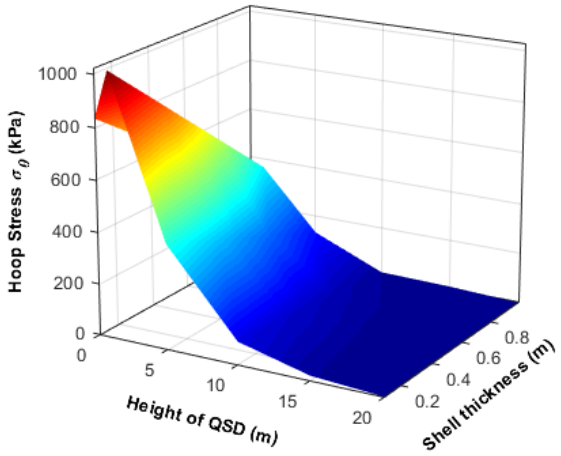

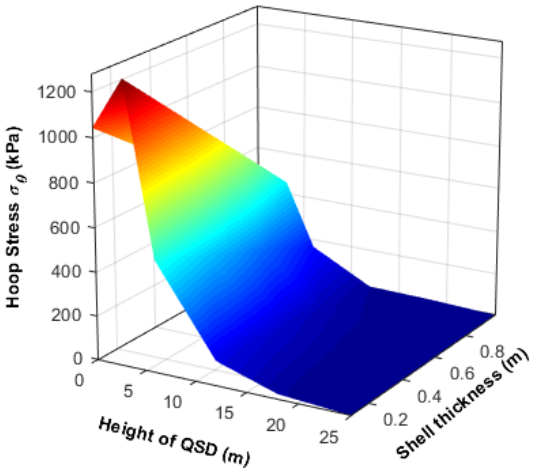

SURFACE PLOTS FOR DYNAMIC CASE -90% FILL LEVEL

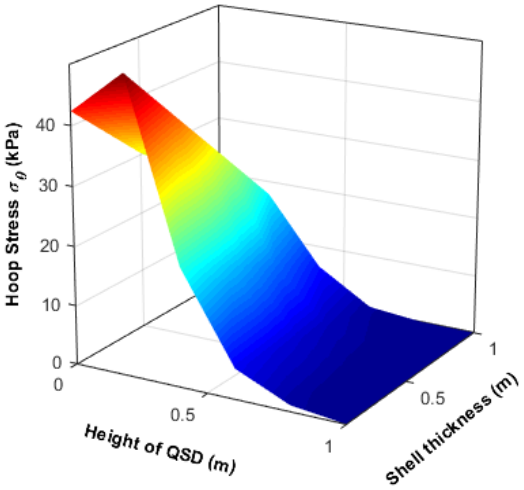

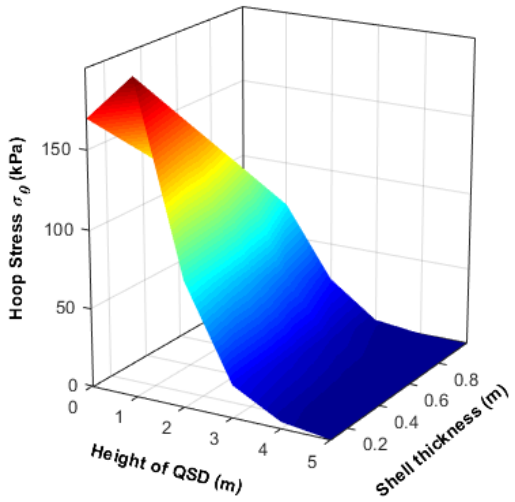

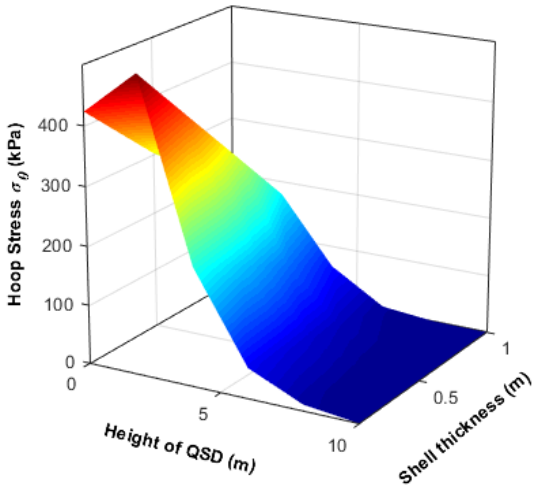

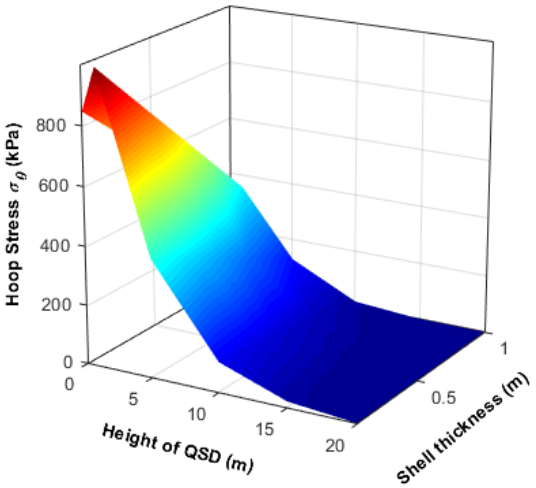

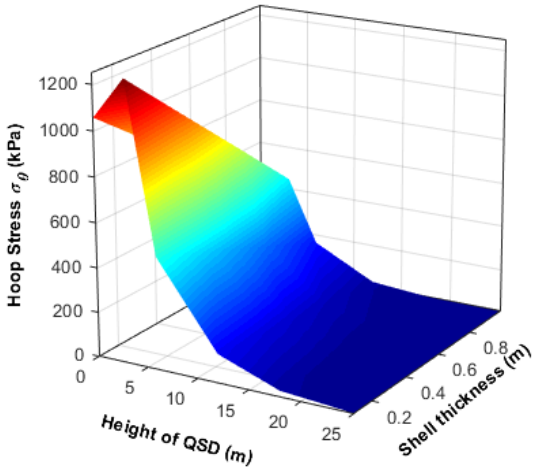

APPENDIX VII

MODELLING INFORMATION ABOUT ABAQUS

ABAQUS

ABAQUS is a commercial finite element analysis software application from *Dassault Systemes*. It provides product simulation to engineers to vary and simulate various design attributes. The ABAQUS Unified FEA product suite offers robust and complete solutions for both routine and sophisticated engineering problems covering a vast range of industrial applications. The user can gain access to these analysis tools through ABAQUS/CAE. CAE stands for Complete ABAQUS Environment and provides the modelling, managing, and monitoring for performing analysis and visualisation of results. The CAE user interface allows for the creation of application-specific systems through a graphical user interface and dialogue boxes. ABAQUS utilises three steps to develop, perform, and present the results for each finite element model. The first step is the pre-processing or modelling stage. It involves the creation of an input file which contains the design of the system, the system parameters, and the analysis to be performed. The second step is the processing of the model. The final step is post-processing where analysis results are generated in the form of an output file. ABAQUS CAE provides the capability for pre-processing, post-processing, and monitoring of the processing stage.

ABAQUS Procedure

ABAQUS defines an analysis history by:

i. Dividing the problem history into steps;
ii. Specifying an analysis procedure for each step
iii. Prescribing loads, BCs, base motions, and output requests for each step.

The essential idea in ABAQUS can isolate the issue history into steps. A step is any appropriate period of the analysis. In its most straightforward way, a step can be the case with a static analysis in

ABAQUS/Standard of a load adjustment starting with one magnitude then onto the next. ABAQUS enables clarification of each progression that shows the information (.dat) record.

For each step created, this decision characterises the sort of analysis to be performed during the step: static stress investigation, dynamic stress investigation, eigenvalue buckling, transient heat exchange analysis. A single methodology is permitted per step. Concerning ABAQUS/Standard or ABAQUS/Explicit, any mix of accessible methodology can be utilised from step to step.

General Analysis Steps vs Linear Perturbation (LP) Steps

ABAQUS defines two types of steps: general analysis steps, which analyses the linear or nonlinear responses, and linear perturbation steps, which analyses linear problems. General analysis steps are incorporated in an ABAQUS/Standard or ABAQUS/Explicit analysis; LP analysis steps are accessible only in ABAQUS/Standard. ABAQUS/Standard linear analysis considered to be LP analysis about the state at the time when the linear analysis practice is introduced. This LP methodology permits general submission of linear analysis methods in cases where the linear response depends on preloading or on the nonlinearity of the response history of the model. In general analysis steps ABAQUS/Standard computes the result for a single set of applied loads. This is also the default for the LP steps. However, for static, direct steady-state dynamic and SIM-based steady-state dynamic LP steps, it is possible to find solutions for various load cases.

General Analysis Steps

A general analysis step is used where the effects of any nonlinearities existing in the model are included. Steps occur in linear succession where the starting condition for a particular step forms from the end condition of the step preceding it as the model evolves throughout the history of the general analysis steps, as it responds to its respective loading history. If the initial step of the analysis is general, the initial conditions for the step can be quantified directly.

ABAQUS takes into consideration the total time to increase throughout a general analysis. Each step also has its own time, which begins at zero for each step. If the analysis procedure for the step property has the order of a real-time scale, as in a dynamic analysis, the step time must be consistent to that real-

time. Otherwise, step time is any convenient time-scale. The step times of all the general steps accumulate into the total computational time. Any steps that do not have a physical time-scale would, therefore, be of an insignificantly small step time, which would be associated with the steps in which a real time scale does exist.

Sources of nonlinearity

Nonlinear stress analysis complications can encompass up to three sources of nonlinearity.

i. Material nonlinearity
ii. Geometric nonlinearity
iii. Boundary nonlinearity.

Material Nonlinearity

Many of the materials are history-dependent meaning that the material's response at any time depends on what has occurred at previous times. Thus, the solution must be acquired by following the actual loading arrangement.

Geometric Nonlinearity

In ABAQUS, a problem is defined as “small-displacement” analysis, which means that geometric nonlinearity is ignored in the element calculations. The kinematic relationships are linearised. By default, large displacements and rotations, in contact constraints, are accounted for even if the small-displacement element formulations are used for the analysis. In the reference (original) arrangement, the elements in a small-displacement analysis are formulated, using original nodal coordinates. The errors in such an estimate are of the order of the strains and rotations compared to unity. The estimate also eliminates any possibility of capturing bifurcation buckling, which is sometimes a critical aspect of a structure's response.

The substitute to a “small-displacement” analysis in ABAQUS is to include large-displacement effects. In this case, most elements are formulated using existing nodal positions. Elements, therefore, distort their shapes as the deformation increases. With satisfactorily large deformations, the elements may become so distorted that they are no longer appropriate for use. In this situation, ABAQUS issues a

warning message indicating the problem. In addition, ABAQUS/Standard reduces the time increment before making further attempts to continue the solution.

Almost all of the elements in ABAQUS utilises fully, nonlinear formulation. The exceptions are the cubic beam elements and the small-strain shell elements (those shell elements other than S3/S3R, S4, S4R, and the axisymmetric shells) where the cross-sectional thickness change is ignored. Hence, these elements are appropriate only, for large rotations and small strains.

Linear Perturbation Analysis Steps

Linear perturbation analysis steps are accessible only in ABAQUS/Standard. The response in a linear analysis step is the LP response about the base state. The base state is the existing state of the model at the end of the last general analysis step before the LP step. The base state is established from the initial conditions provided that the perturbation step is the initial step of an analysis.

LP analyses can be executed from time to time during a nonlinear analysis by including the LP steps between the general response steps. The LP response does not affect as the general analysis is continued. The step time of LP steps, which is taken arbitrarily to be a minimal number, is never accumulated into the total time. After each of these steps, the frequencies can then be obtained in an LP analysis step.

If geometric nonlinearity is included in the general analysis upon which an LP investigation is based, stress stiffening or softening effects and load stiffness effects are included in the LP analysis.

ABAQUS Explicit Analysis

The explicit dynamics analysis procedure in ABAQUS/Explicit is established upon the implementation of an explicit integration rule together with the use of diagonal or “lumped” element mass matrices. The equations of motion for the body are integrated using the explicit Central Difference Time Integration (CDTI) rule.

$$\dot{u}^{\left(i+\frac{1}{2}\right)} = \dot{u}^{\left(i-\frac{1}{2}\right)} + \frac{\Delta t^{(i+1)} + \Delta t^{(i)}}{2}\ddot{u}^{(i)} \tag{118}$$

$$u^{(i+1)} = u^{(i)} + \Delta t^{(i+1)} \dot{u}^{\left(i+\frac{1}{2}\right)} \tag{119}$$

where

$\dot{u}$ – Velocity

$\ddot{u}$ – Acceleration The superscript (i) refers to the increment number and $i - \frac{1}{2}$ and $i + \frac{1}{2}$ refer to mid-increment values.

The CDTI operator is explicit in that the kinematic state can be advanced using known values of $\dot{u}^{\left(i-\frac{1}{2}\right)}$ and $\ddot{u}^{(i)}$ from the previous increment. The explicit integration rule is quite simple but by itself does not provide the computational efficiency associated with the explicit dynamics method.

Stability

The explicit method integrates through time by using several minor time increments. The CDTI operator is conditionally stable and the stability limit for the operator (with no damping) is given in terms of the highest eigenvalue in the system as shown in Equation 130.

$$\Delta t \leq \frac{2}{\omega_{max}} \tag{120}$$

The time incrementation arrangement in ABAQUS/Explicit is fully automatic and requires no user interference. An adaptive algorithm is used that resolves the conservative bounds for the highest element frequency. An approximation of the highest eigenvalue in the system can be acquired by determining the maximum element dilatational mode of the mesh. The stability limit is based upon this highest element frequency is conservative in that it gives a smaller stable time increment than the actual stability limit that is based upon the maximum frequency of the entire model. In general, constraints such as BCs and contact have the result of compressing the eigenvalue spectrum, which the element-by-element approximations do not take into account. ABAQUS/Explicit contains a global estimation procedure, which governs the maximum frequency of the entire model. This procedure continuously updates the estimate for the maximum frequency.

ABAQUS/Explicit initially uses the element-by-element approximations. As the step proceeds, the stability limit will be established from the global estimator once the procedure determines that the accuracy of the global estimation is acceptable. A trial stable time increment is calculated for each element in the mesh using Equation (121).

$$\Delta t = \frac{2}{{\omega_{max}}^{element}} \tag{121}$$

where ${\omega_{max}}^{element}$ is the element maximum eigenvalue. A conservative estimate of the stable time increment is given by the minimum taken over all the elements. The above stability limit can be re-written as Equation (122).

$$\Delta t = \min\left(\frac{L_e}{c_d}\right) \tag{122}$$

where L_e is the characteristic element dimension and c_d is the current effective, dilatational wave speed of the material. The characteristic element dimension is derived from an analytic upper bound expression for the maximum element eigenvalue.

The explicit procedure requires no iterations and no tangent stiffness matrix. Based on these fundamentals, an explicit model was created. The fluid mesh element is taken from the explicit element library, and it is named the C3D8R element and the tank mesh element named S4R. Three "dynamic/explicit" steps are defined to correspond to the x,y,z acceleration respectively.

Natural Frequency and Mode Shape Extraction

The frequency extraction procedure:

i. Performs eigenvalue extraction to calculate the natural frequencies and the corresponding mode shapes of a system;

ii. Will include initial stress and load stiffness effects due to preloads and initial conditions if geometric nonlinearity is accounted for in the base state so that small vibrations of a preloaded structure can be modelled;

iii. Will compute residual modes if requested;

iv. It is a LP procedure;

v. Can be performed using the traditional Abaqus software architecture or if appropriate, the high-performance SIM architecture;

vi. Solves the Eigen frequency problem only for symmetric mass and stiffness matrices; the complex Eigen frequency solver must be used if unsymmetrical contributions, such as the load stiffness, are needed.

Eigenvalue Extraction

The eigenvalue problem for the natural frequencies of an un-damped finite element model is presented in equation (123)

$$(-\omega^2 M^{MN} + K^{MN})\emptyset^N = 0 \qquad (123)$$

where

- M^{MN} – is the mass matrix (which is symmetric and positive definite);
- K^{MN} – is the stiffness matrix (which includes initial stiffness effects if the base state included the effects of nonlinear geometry);
- $\emptyset^N$ – is the eigenvector (the mode of vibration);
- M and N are degrees of freedom.

When K^{MN} is positive definite, all eigenvalues are positive. Rigid body modes and instabilities cause K^{MN} to be indefinite. Rigid body modes produce zero eigenvalues. Instabilities produce negative eigenvalues and occur when you include initial stress effects. ABAQUS/Standard solves the Eigen frequency problem only for symmetric matrices.

Structural-Acoustic Coupling

Structural-acoustic coupling affects the natural frequency response of systems. In ABAQUS only the Lanczos Eigen solver fully includes this effect. In ABAQUS/AMS and the subspace Eigen solver, the effect of coupling is neglected for the purpose of computing the modes and frequencies; these are computed using natural BCs at the structural-acoustic coupling surface. An intermediate degree of consideration of the structural-acoustic coupling operator is the default in ABAQUS/AMS and the Lanczos Eigen solver. The coupling is projected onto the modal space and stored for later use.

Structural-Acoustic Coupling using the Lanczos Eigen solver without the SIM architecture.

If structural-acoustic coupling is present in the model and the Lanczos method not based on the SIM architecture is used, ABAQUS/Standard extracts the coupled modes by default. Because these modes fully account for coupling, they represent the mathematically optimal basis for subsequent modal procedures. The effect is most noticeable in strongly coupled systems such as steel shells and water. However, coupled structural-acoustic modes cannot be used in subsequent random response or response spectrum analyses. Coupling can be defined using either acoustic-structural interaction elements or the surface-based tie constraint. It is possible to ignore coupling when extracting acoustic and structural modes; in this case the coupling boundary is treated as traction-free on the structural side and rigid on the acoustic side.

Acoustic interface elements

Acoustic interface elements:

i. Can be used to couple a model of an acoustic fluid to a structural model containing continuum or structural elements;
ii. Couple the accelerations of the surface of the structural model to the pressure in the acoustic medium;
iii. Can be used in dynamic and steady-state dynamic procedures;
iv. Must be defined with the nodes shared by the acoustic elements and the structural (or solid) elements;

v. Can be used only in small-displacement simulations and are not intended for use in nonlinear or hydrostatic fluid-structure interactions;

vi. Are ignored in Eigen frequency extraction analyses if the subspace iteration Eigen solver is used; and

vii. If necessary, can be degenerated into triangular elements.

For most problems, the surface-based, structural-acoustic capabilities provide a more general and easy to use methods for modelling the interaction between an acoustic fluid and a structure. User-specified acoustic interface elements give increased control over the coupling specification, at the expense of the convenience of the surface-based procedures.

Appropriate Element

The order of the underlying acoustic and structural elements usually dictates which acoustic interface element should be used. The general acoustic interface element, ASI1, can be used in any coupled acoustic-structural simulation; however, normally it is used only with the acoustic link elements (AC1D2 and AC1D3).

The Normal Direction of the Acoustic-Structural Interface

The connectivity of the acoustic interface elements and the right-hand rule define the normal direction of the acoustic-structural interface. It is essential that this normal point into the acoustic fluid, as shown in Figure 81.Normal directions for two-dimensional and axisymmetric acoustic-structural interface elements. and Figure 82.

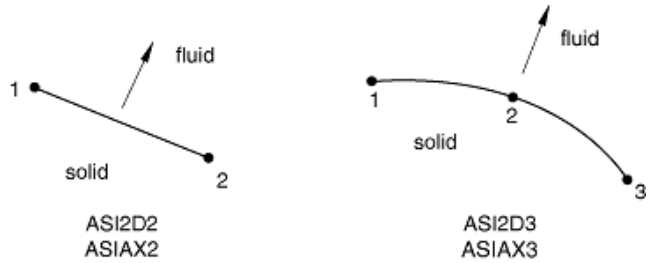

Figure 81.Normal directions for two-dimensional and axisymmetric acoustic-structural interface elements.

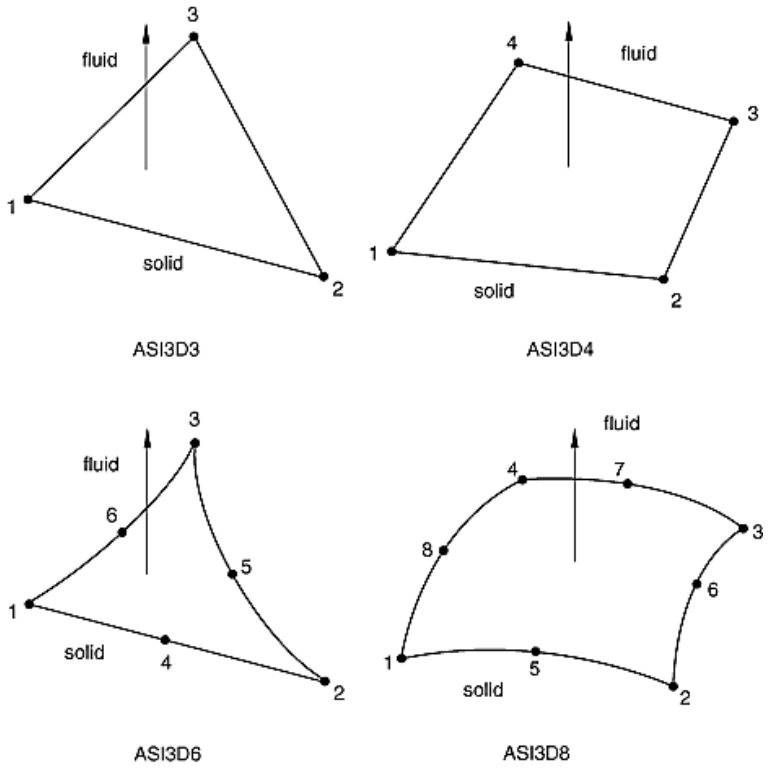

Figure 82. Normal directions for three-dimensional acoustic-structural interface elements.

Mesh Elements

Characterising Elements

Five aspects of an element characterise its behaviour:

i. Family
ii. Degrees of freedom
iii. Number of nodes
iv. Formulation
v. Integration

Each element in ABAQUS has a unique name, e.g. T2D2, S4R, C3D8I, or C3D8R etc. The element name identifies each of the five characteristics of an element.

Family

One of the significant distinctions between different element families is the geometry that each family assumes. The first letter or letters of an element's name indicate to which family the element belongs. For example, S4R is a shell element, CINPE4 is an infinite element, and C3D8I is a continuum element.

Degrees of Freedom (DOF)

The DOF is the fundamental variables calculated during the analysis. For a stress/displacement simulation the DOF are the translations and, for shell, pipe, and beam elements, the rotations at each node.

Number of Nodes and Order of Interpolation

Displacements or other DOFs are calculated at the nodes of the element. At any other point in the element, the displacements are obtained by interpolating from the nodal displacements. Usually, the number of nodes used in the element determines the interpolation order.

Elements that have nodes only at their corners, such as the 8-node brick shown in Figure 83(a), use linear interpolation in each direction and are often called linear elements or first-order elements.

In ABAQUS/Standard elements with mid-side nodes, such as the 20-node brick shown in Figure 83(b), use quadratic interpolation and are often called quadratic elements or second-order elements.

Modified triangular or tetrahedral elements with mid-side nodes, such as the 10-node tetrahedron shown in Figure 83(c), use a modified second-order interpolation and are often called modified or modified second-order elements.

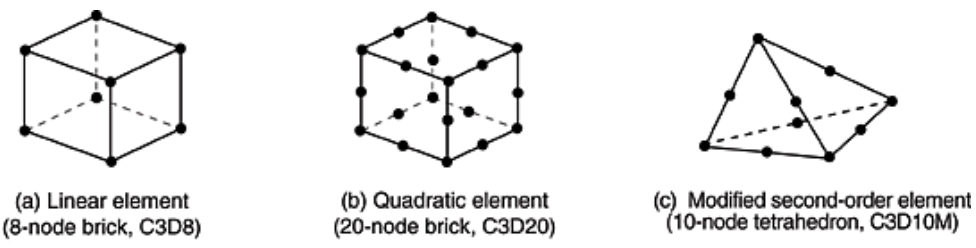

Figure 83. Brick elements used in ABAQUS

Typically, the number of nodes in an element is clearly identified in its name. The 8-node brick element is called C3D8, and the 4-node shell element is called S4R.

Formulation

An element's formulation denotes the mathematical theory used to define the element's behaviour. In the Lagrangian (also known as material) description of behaviour, the element distorts with the material. In the alternative Eulerian (also known as spatial) description elements are fixed in space as the material flows through them. Eulerian methods are used commonly in fluid mechanics simulations. ABAQUS/Explicit offers multi-material Eulerian elements for use in stress/displacement analyses. Adaptive meshing in ABAQUS/Explicit combines the features of pure Lagrangian and Eulerian analyses and allows the motion of the element to be independent of the material. All other stress/displacement elements in ABAQUS are based on the Lagrangian formulation. In ABAQUS/Explicit the Eulerian elements can interact with Lagrangian elements through general contact.

To accommodate different types of behaviour, some element families in ABAQUS include elements with several different formulations. In addition, ABAQUS also offers continuum shell elements, which have nodal connectivity's like continuum elements but are formulated to model shell behaviour with as few as one element through the shell thickness.

Some ABAQUS/Standard element families have a standard formulation as well as some alternative formulations. An additional character at the end of the element name identifies elements with alternative formulations. For example, the continuum, beam, and truss element families include members with a hybrid formulation (to deal with incompressible or inextensible behaviour); these elements are identified by the letter H at the end of the name (C3D8H or B31H).

ABAQUS/Standard uses the lumped mass formulation for low-order elements; ABAQUS/Explicit uses the lumped mass formulation for all elements. Consequently, the second mass moments of inertia can deviate from the theoretical values, especially for coarse meshes.

ABAQUS/CFD uses hybrid elements to circumvent well-known div-stability issues for incompressible flow. ABAQUS/CFD also permits the addition of degrees of freedom based on procedure settings such as the optional energy equation and turbulence models.

Integration

ABAQUS uses numerical techniques to integrate various quantities over the volume of each element, thus allowing complete generality in material behaviour. Using Gaussian quadrature for most elements, ABAQUS evaluates the material response at each integration point in each element. Some continuum elements in ABAQUS can use full or reduced integration, a choice that can have a significant effect on the accuracy of the element for a given problem.

ABAQUS uses the letter R at the end of the element name to label reduced-integration elements. For example, CAX4R is the 4-node, reduced-integration, axisymmetric, solid element.

Modelling Approach

A complete ABAQUS analysis usually consists of three distinct stages: pre-processing, simulation, and post-processing. These three (3) stages are linked together by files as illustrated in **Error! Reference source not found.**.

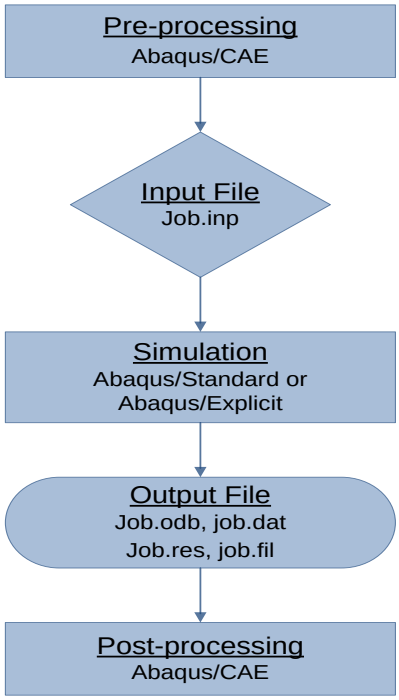

ABAQUS Basic Analysis Process

Pre-processing (ABAQUS/CAE)

In this stage, the model of the physical problem is defined, and an ABAQUS input file is created. The model is created graphically using ABAQUS/CAE, although the ABAQUS input file for a simple analysis is created directly using the text editor.

Simulation (ABAQUS/Standard or ABAQUS/Explicit)

The simulation is the stage in which ABAQUS/Standard or ABAQUS/Explicit solves the numerical problem defined in the model. Depending on the complexity of the problem being analysed and the processing speed of the computer CPU being used, it may take anywhere from seconds to days to complete a single analysis run.

3.3.3.8.1.6.3 Post-processing (ABAQUS/CAE)

From the results obtained, the simulation will display the fundamental variables that were requested to be calculated. The evaluation is done interactively using the Visualisation module of ABAQUS/CAE. The Visualisation module reads the neutral binary output database file and has a variety of options for displaying the results, including colour contour plots, animations, deformed shape plots, and X–Y plots.

ABAQUS Modelling Solution

ABAQUS Units

Before starting to define any model, the system of units that is being utilised must be certain. ABAQUS has no built-in system of units. All input data must be specified in consistent units. Some common systems of consistent units are shown in Table 21. The SI system of measurements was utilised throughout this project.

Table 21. ABAQUS Basic Analysis Process

Quantity	SI Unit
Length	m
Force	N
Mass	kg
Time	s
Stress	Pa (N/m^2)
Energy	J
Density	kg/m^3

QSD Tank Simulation (ABAQUS/Explicit Analysis)

Modelling of the QSD

To accurately model the seismic excitation, an independent dynamic explicit step for each direction of displacement was created. This method of modelling approach was done and the results were analysed. The three dynamic explicit steps allowed the gravity load to be added simultaneously applying a directional acceleration and propagated it to the other two steps with a change in the direction of acceleration. When applying the BCs, the respective degree of freedom was suggested and applied with respect to the acceleration data for that direction. The same was done for the two following two steps under the one boundary condition. By propagating the steps with respect to the boundary condition, this allowed the x,y,z direction to be run simultaneously to simulate the seismic behaviour of the tank.

The ABAQUS/Explicit method was adopted to analyse tanks with fill levels of 10%, 25%, 50%, 75% and 90%. The sloshing loads were examined and modelled in 2 categories; 5 Hz harmonic excitation and the Kobe 1995-time history seismic excitation. The SPH method was used to convert the solid

homogenous part to particles; the only type of analysis that ABAQUS allowed to carry out this task was the dynamic explicit.